Design and Analysis of Hydraulic Hybrid Passenger Vehicles

A THESIS
SUBMITTED TO THE FACULTY OF THE GRADUATE SCHOOL
OF THE UNIVERSITY OF MINNESOTA
BY

Kai Loon Cheong

IN PARTIAL FULFILLMENT OF THE REQUIREMENTS
FOR THE DEGREE OF
Doctor of Philosophy

Prof. Perry Y. Li and Prof. Thomas R. Chase

September, 2015

Acknowledgements

This material was based on work performed within the Center for Compact and Efficient Fluid Power (CCEFP) supported by the National Science Foundation (EEC-0540834). Special thanks to Polaris for donating a off-road all terrain vehicle (Polaris Ranger) to the Center for Compact and Efficient Fluid Power (CCEFP)

Abstract

The research described in this dissertation focuses on the development of computationally efficient design methodology to optimize the hydraulic hybrid power-split transmission for fuel efficiency, acceleration performance and robustness against powertrain uncertainties. This research also involve experimental implementation of a three-level hierarchical control approach on two test beds, requiring powertrain control design and fine-tuning. Hybrid powertrains have the potential to benefit the fuel efficiency of highway and off-highway vehicles. Hydraulic hybrid has high power density. Hydraulic power-split architecture is chosen in this study for its flexibility in operation and combined advantage of series and parallel architecture.

An approach for optimizing the configuration and sizing of a hydraulic hybrid power-split transmission is proposed. Instead of considering each mechanical configuration consisting of combinations of gear ratios, a generalized kinematic relation is used to avoid redundant computation. The Lagrange multiplier method for computing the optimal energy management control is shown to be 450 times more computationally efficient for use in transmission design iterations. To exploit the benefit of high power density of hydraulics, a classical multi-objective solver is utilized to incorporate the acceleration performance criteria into the transmission design optimization. By considering worst-case uncertainty, the transmission design is optimized to be robust against powertrain uncertainties and insensitive to operating condition variations, and yet fuel efficient.

The Generation I and II vehicles are experimental platforms built to implement controls and to validate the fuel efficiency gain for power-split transmission. The powertrain for the platforms are modeled to predict the potential fuel efficiency improvement by different energy management strategies. Results show maximum of 74% fuel efficiency gain by optimizing engine management from CVT to full optimal hybrid operation. The three-level control strategy is implemented on the Generation I vehicle. This control strategy segregates the tasks of the drive-train into three layers that respectively 1) manages the accumulator energy storage (high level); 2) performs vehicle level optimization (mid-level); and 3) attains the desired vehicle operating condition (low level). Results validated the modularity and effectiveness of this control structure.

Contents

List of Tables

List of Figures

Chapter 1

Introduction

Hybrid powertrain systems are defined as vehicle propulsion systems with two or more power sources on-board. The primary power source is generally an internal combustion engine due to its high power and energy density. The secondary power source can be either hydraulic, pneumatic, electric or even mechanical machines, equipped with energy storage. Hybrid drivetrain systems have been studied and developed intensively in recent years. Hybrid drivetrain systems are designed to be fuel efficient and to reduce harmful emissions in order to address concerns about energy availability and environmental impacts.

In parallel with research on more efficient components, overall hybrid drivetrain systems have been a major focus to improve the fuel economy of not only highway vehicles but also utility and agricultural vehicles. Another important characteristic of hybrid powertrain systems is the capability of storing energy for later use. Hybridization allows engine power to be different from vehicle power. This feature enables regenerative braking and engine management. Furthermore, the engine could potentially be downsized due to the secondary source of power [1]. Design, analysis and control of power-split transmissions for hydraulic hybrid passenger vehicles are the research foci in this dissertation.

The rest of this chapter will be organized as follows: Section 1.1 discusses the current technology of conventional non-hybrid transmissions and their limitations that leads to the motivation of designing hybrid transmissions. Section 1.2 motivates the application

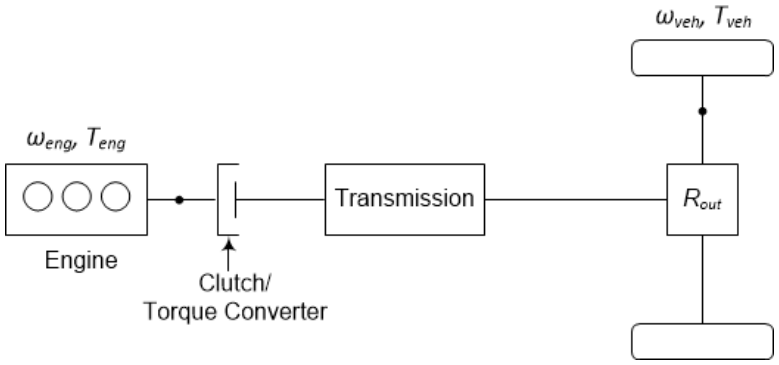

Figure 1.1: Conventional powertrain structure.

of hydraulic hybrid powertrain systems in passenger sized vehicles. Characteristics, advantages, and disadvantages of different hybrid transmission architectures are described in Sec. 1.3. Section 1.4 briefly introduces the test hardware utilized for case studies and experimental validation in this dissertation. Section 1.5 presents the overview made in this dissertation.

1.1 Conventional Powertrain

The traditional type of propulsion system is shown in Fig. 1.1, which consists of an internal combustion engine, a clutch or torque converter, and a discrete geared transmission (manual or automatic transmission). The clutch or torque converter is to allow the vehicle to launch from zero speed without stalling the engine. The transmission or gearbox is to shift the engine speed relative to the vehicle speed. Due to the constraint of all the vehicle power must be supplied by the engine, the engine's operating point can not be varied arbitrarily, losing the potential to improve fuel efficiency. However, transferring power through a mechanical shaft is efficient. Especially with the state-of-the-art seven-speed dual-clutch transmissions (Fig. 1.2(a)), operation smoothness is comparable with a belt-type Continuous Variable Transmission (CVT) (Fig. 1.2(b)) with superior torque capability and fast response [2, 3, 4].

Nevertheless, these conventional powertrains are only efficient on the highway, where the vehicle can be run at steady speed and stopping is infrequent. In a city driving scenario, frequent acceleration and deceleration of the vehicle requires the engine to

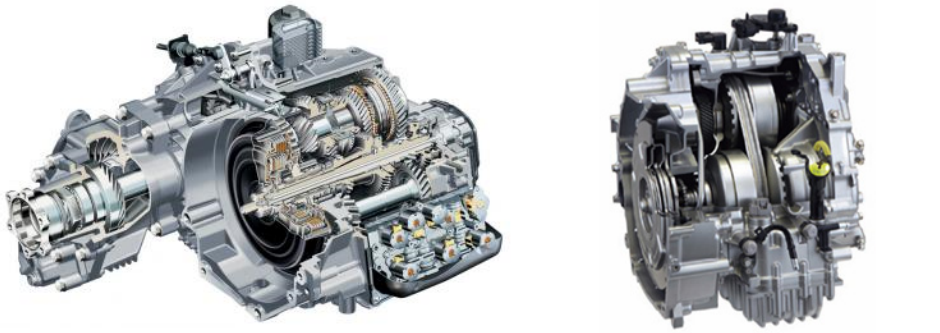

(a) Dual clutch transmission
(Courtesy of Volkswagen Group)

(b) Honda belt type CVT
(Courtesy of Honda Automotive)

Figure 1.2: Examples for non-hybrid transmissions.

operate at high speed low torque condition. A significant fraction of this power is eventually wasted through heat in friction braking, causing the powertrain to operate inefficiently.

1.2 Why Hydraulic Hybrid Powertrains?

Hydraulic hybrid powertrains utilize hydraulic pump/motors as secondary movers and accumulators to store energy. Hydraulic hybrid powertrains are selected as the focus of this research for the following reasons. Hybrid electric passenger vehicles are available in the automotive market. Meanwhile, hydraulic hybrid powertrains have been mostly applied to heavy duty vehicles, for instance delivery trucks [5], refuse trucks, city transit buses, etc. Hydro-mechanical power-split transmissions (HMT) are also widely applied for off-highway vehicles, especially agricultural tractors [6], but not compact-sized passenger vehicles.

Hydraulic hybrid vehicles (HHV) have several unique advantages over electric hybrid vehicles. High power density is a key reason for converting heavy-duty trucks into hydraulic hybrids instead of electric hybrids. The high power density of hydraulics allows superior regenerative braking efficiency over electric regenerative braking (approximately 70% compared to 40% braking energy recovery [7]), as electrical batteries

usually requires charge-sustaining to prolong batteries' life while hydraulic accumulators have no such limitation. While increasing the overall efficiency of the powertrain, hydraulic hybrids do not significantly sacrifice the acceleration performance of the vehicle compared to electric hybrids. For example, the EPA-developed full series HHV in a passenger car test chassis in [8] achieved 0 to 60 mph in 8 seconds using a 1.9 liter diesel engine, as compared to Toyota Prius that achieved 9.7 seconds.

The cost of building a hydraulic hybrids is also potentially lower than electric vehicles. Constructing high efficiency electric motors demands high quality conductors, or even in some cases, rare and exotic earth materials like permanent magnets. Moreover, the lifetime of a battery is generally shorter than that of a hydraulic accumulator, incurring environmental impact and increased maintenance for electric hybrid vehicles. On the other hand, hydraulic components typically have a design operation life of 20 years without significant degradation. Thus, they provide short and long-term cost-saving benefits to power transmission sector.

However, hydraulics hybrids have several fundamental disadvantages compared to electric hybrids. Energy density is a major shortcoming associated with storing energy in hydraulic accumulators. As shown in Fig. 1.3, hydraulic accumulators have the advantage of higher power density but energy density is several orders lower than batteries. This is the main reason why electric plug-in vehicles exist but not hydraulic plug-ins. Typically, a Toyota Prius Plug-in in Electric Vehicle (EV) mode can travel 11 miles. Due to this characteristic of hydraulic accumulators, the operation of a hydraulic hybrid powertrain should be different from an electric hybrid powertrain. On the other hand, hydraulics are generally considered to be noise, vibration and harshness (NVH) unfriendly due to high pitched noise and fluid leakage. These issues, however, are considered less of a challenge as internal combustion engines suffer similar problems that have been successfully mitigated.

1.3 Hybrid Architectures

Several types of hybrid architectures are currently available. The three most common hybrid architectures in the market are series, parallel and power-split hybrids, and each has its uniqueness and advantage. Series and power-split architectures are capable of

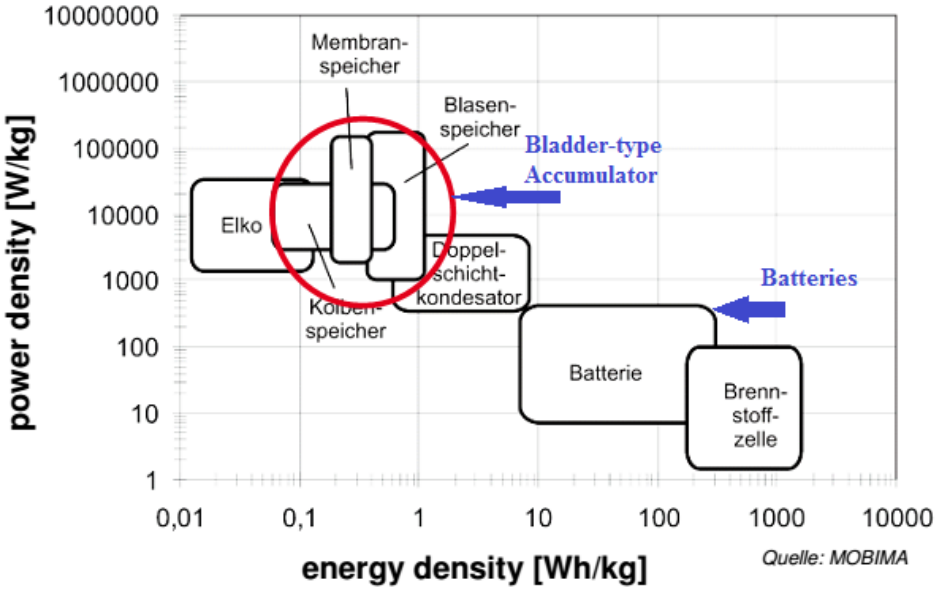

Figure 1.3: Power density and energy density comparison. (Courtesy of HYDAC International)

operating without energy storage.

1.3.1 Series Architecture

A series hybrid eliminates the need of any mechanical linkage between the engine and the wheels, as shown in Fig. 1.4. This entirely transforms the propulsion structure, potentially reducing drivetrain weight and improving the driving performance. The lack of a mechanical coupling between the engine and wheels allows the engine to run at any desired operating point or at constant speed, thus increasing fuel efficiency. A hydro-static transmission is essentially a series architecture transmission without energy storage capability. Figure 1.5 illustrates the engine management achievable by this transmission architecture. Non-hybrid operating mode shifts engine operation from the mechanical point[1] `(1)` to a higher efficiency point `(2)` along the constant power curve. In contrast, the hybrid operating mode shifts engine operation from the mechanical

[1] Mechanical point is the engine operating point mapped from the transmission output condition with only mechanical gears, without using electric or hydraulic machines.

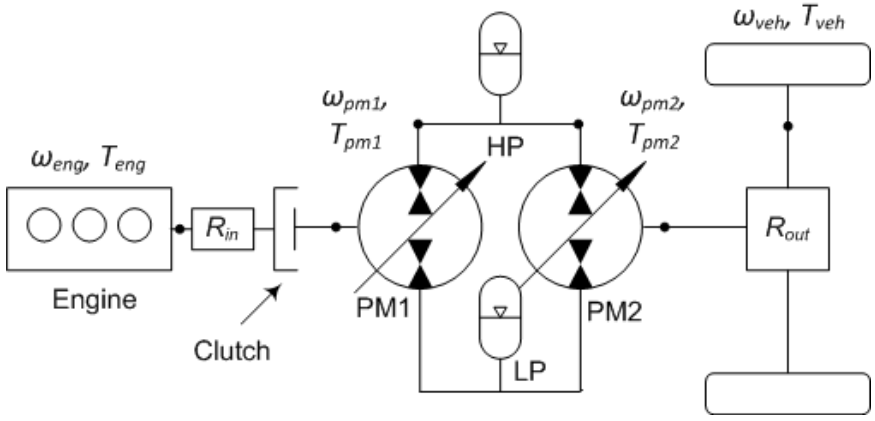

Figure 1.4: Hydraulic series hybrid architecture.

point (1) to the maximum efficiency point (3), with excessive or deficit power is being allocated to the accumulator. This type of hybrid, however, suffers from double energy conversion loss, i.e. from mechanical to secondary mover, and then from secondary mover back to mechanical. Since all power must pass through the secondary movers, the overall drivetrain efficiency is highly sensitive to the secondary mover's efficiency.

A series hybrid vehicle example developed by joint effort from the Environmental Protection Agency (EPA) and industry is the UPS 'package car' series hydraulic hybrid delivery vehicle [7] that utilizes a set of highly efficient large angle hydro-static pump/motors. This vehicle achieved 60-70% improvement in fuel economy. Parker Hannifin's RunWise hybrid drive system developed for Class 8 heavy duty vehicles (e.g. refuse trucks) is claimed to achieve 50% fuel economy improvement. In the 1990s, the EPA successfully demonstrated a series HHV in a passenger car test chassis that represents a large car platform, like a Ford Taurus and Chevrolet Impala [8]. The developers claimed 80+ mpg on combined EPA city/highway drive cycle, and 0-60 mph acceleration in 8 seconds was achieved with a 1.9 liter diesel engine without using expensive lightweight materials.

1.3.2 Parallel Architecture

The parallel hybrid architecture is illustrated in Fig. 1.6. It transfers the majority of power from the engine to the wheels through a highly efficient mechanical shaft. Only

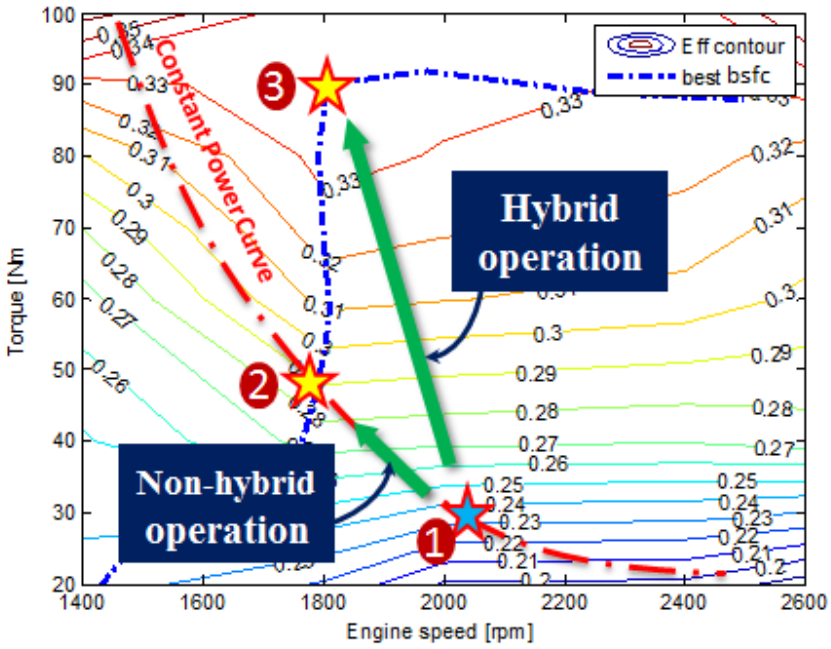

Figure 1.5: Comparison between CVT and full hybrid engine management operating modes for series and powersplit architectures.

one secondary machine is required in order to augment engine output torque or perform regenerative braking. This configuration is relatively simple for retrofitting into an ordinary vehicle but the engine cannot be completely decoupled from the wheel speed requirement, limiting engine management capability, despite the efficient mechanical path. To depict the limitation on engine management of a parallel hybrid transmission, Fig. 1.7 shows the engine torque can be augmented using the pump/motor from the mechanical point `(1)` to a higher efficiency point `(2)`.However, augmenting the engine torque from mechanical point `(3)` to lower efficiency `(4)` is not beneficial.

A commercially available automotive example of a parallel hybrid is the Honda Integrated Motor Assist (IMA) system. Industrial usage examples include Eaton's Hydraulic Launch Assist (HLA) system [9] and Bosch's Hydraulic Flywheel (HFW) system [10]. Fuel saving mechanisms implemented by these designs are mainly engine load leveling and regenerative braking.

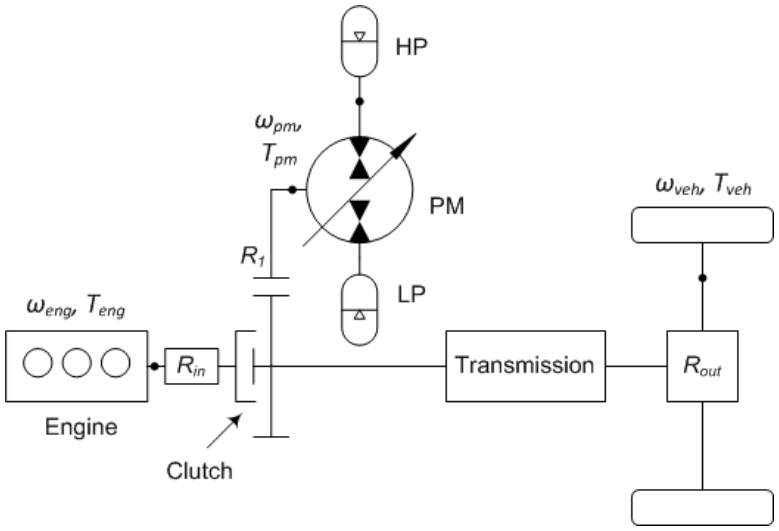

Figure 1.6: Hydraulic parallel hybrid architecture.

1.3.3 Power-split Architecture

Power-split hybrids shown in Fig. 1.8 leverage the advantages of both the series and parallel hybrids. In addition to being able to decouple engine operation from vehicle load/speed requirements, they also transfer a flexible fraction of power through the efficient mechanical shaft, hence the name power-split, or hydro-mechanical transmissions (HMT) for hydraulic versions. This architecture preserves the full engine management capability of a series hybrid, and yet it is less susceptible to hydraulics efficiency, similar to the parallel architecture.

As first proposed in [11] and will be discussed in Ch. 2, by locking up or free-spinning individual secondary machine units, a power-split configuration can be operated as a series or a parallel hybrid. This flexibility offers full engine management as in a series hybrid, and efficient mechanical transmission as in a parallel hybrid. This advantageous feature yields an attractive configuration that will be the focus of this research. A survey in [12] has demonstrated that a hydro-mechanical transmission with average pump/motor efficiency of 93% or lower achieves better fuel economy than series hybrid architecture.

Z. Du et al. [13] describe similar results. Three hybrid architectures are compared

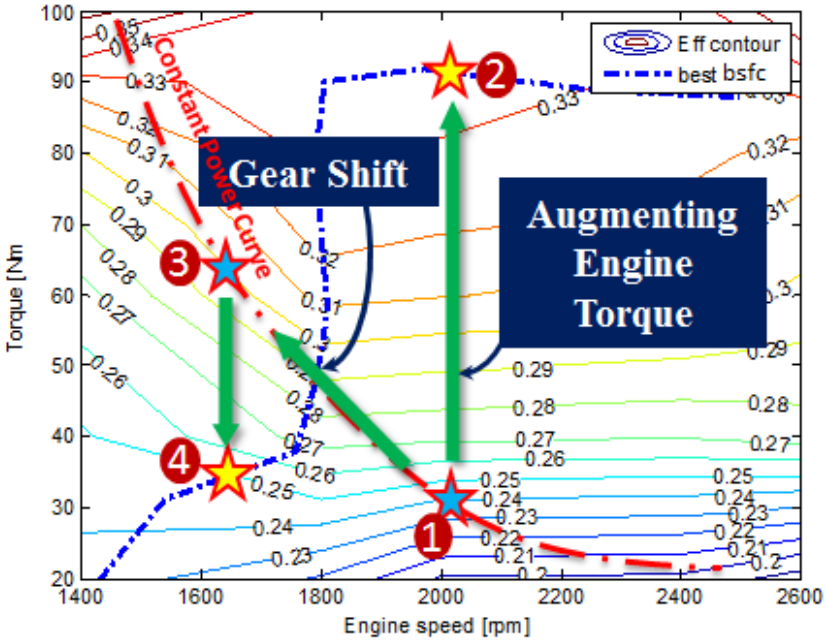

Figure 1.7: Engine management for parallel architecture.

with varying mean hydraulic efficiency, showing powersplit architectures have the advantage of less sensitivity to hydraulic efficiency but parallel architectures would have comparable efficiency if gear-shift ratios are available. The overall power efficiency of different architectures is approximated by [13][2] :

$$\eta_{pwrtrn} = \eta_{eng} / \left(\frac{\%_{hyd}}{\eta_{hyd}} + \frac{(1 - \%_{hyd})}{\eta_{mech}} \right) \tag{1.1}$$

where η_{pwrtrn} is the overall powertrain efficiency, η_{eng} is the mean engine efficiency, η_{hyd} is the mean hydraulic component efficiency, η_{mech} is the mechanical efficiency, and $\%_{hyd}$ is the average fraction of engine energy transmitted through the hydraulic path. Figure 1.9 were generated using the assumption that $\%_{hyd} = 1$ for series architecture and $\%_{hyd} = 0.6$ for power-split and parallel architectures; $\%_{hyd}$ will depend on control strategy. Series and power-split architectures assume $\eta_{eng} = 0.33$. Since parallel architectures have limited engine management, η_{eng} is assumed to be 10% lower. Hydraulic

[2] Regenerative braking energy is neglected in this illustration for simplicity

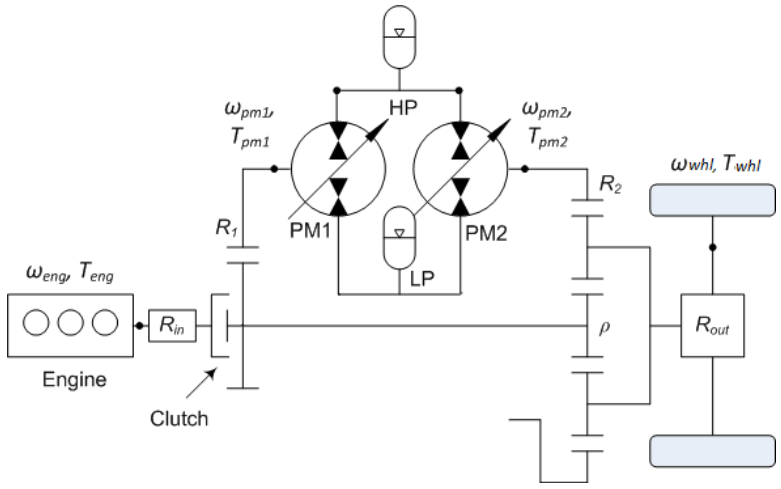

Figure 1.8: A example of hydraulic power-split hybrid architecture.

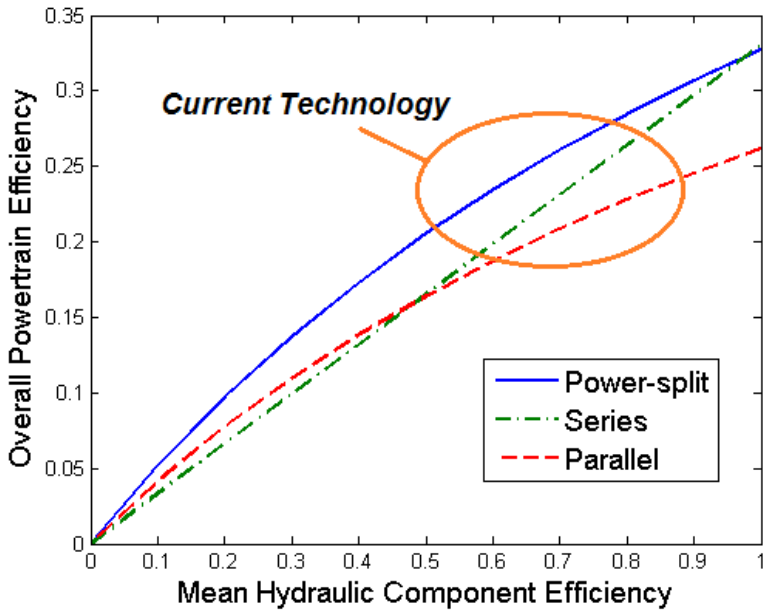

Figure 1.9: Comparison of overall powertrain efficiencies as a function of mean hydraulic efficiency for the three hybrid architectures [13]. The curves depend on assumptions on efficiency and powertrain operation, which are explained in the text.

components operated throughout a duty cycle could potentially achieve 50∼80% efficiency under current technology. This indicates that power-split architectures pose the highest potential for fuel savings.

Power-split transmissions can be operated without energy storage capabilities, in which case non-hybrid transmissions operate as continuously variable transmissions (CVT), providing a wide range of speed ratios from the engine to wheel. The mechanism of a power-split system is to vary the fraction of power being transferred through the continuously variable unit (CVU) and the mechanical shaft. Figure 1.5 illustrates the engine management achievable by this transmission architecture. CVT operating mode shifts engine operation from the mechanical point `(1)` to a higher efficiency point `(2)` along the constant power curve. Hybrid operating mode shifts engine operation from the mechanical point `(1)` to maximum efficiency `(3)`, with excessive or deficit power is allocated to the accumulator.

Examples of power-split hybrids are the Toyota Hybrid System (THS), Ford Hybrid System (FHS), GM Voltec powertrain, and GM 2-Mode Hybrid. For more examples of commercialized hybrid electric vehicle power-split systems, please refer to [14]. Hydromechanical transmissions include the John Deere IVT [15], and Bosch Hydromechanical Variable Transmission (HVT) [16], that are used in agricultural and construction vehicles. Peugeot Hybrid Air [17] resembles series-parallel hybrid architecture for on-highway vehicles.

1.4 Hydraulic Hybrid Powertrains Test Beds

The work described here is part of Project 'Test bed 3' (TB3) of the Center for Compact and Efficient Fluid Power (CCEFP) [18]. TB3 aims to develop efficient and high power hydraulic powertrains for passenger-sized vehicles. Two test beds are associated with this project (see Fig. 1.10). The first test bed, Generation I, was built in-house at the University of Minnesota (UMN) using a Polaris Ranger off-road all-terrain vehicle,[3] as the vehicle platform. The second test bed, Generation II, is a full size pickup truck, with its original 6-speed automatic transmission replaced with a hydro-mechanical transmission built by Folsom Technologies International (FTI).

[3] The Polaris Ranger vehicle is donated by Polaris Industries.

Figure 1.10: Generation I and II test bed platforms.

Genration I: The Generation I Hydraulic Hybrid Passenger Vehicle (HHPV) test bed is a hydro-mechanical hydraulic hybrid vehicle built in-house at the University of Minnesota (UMN). The engine is a 1.5 liter 4 cylinder engine with peak power of 26.5kW at 314.2 rad/s and peak torque of 94Nm at 188.5 rad/s. The transmission is designed to fit into a single unit gearbox (see Fig. 1.11), using standard off-the-shelf components including planetary gears and helical gears. Two 28cc bent-axis axial piston pump/motors are coupled to the transmission. The components were sized using design optimization in [19], which will be discussed in Ch. 2. The research in this dissertation will focus on Generation I vehicle.

Generation II: The Generation II test bed emphasizes on medium-duty hybrid hydro-mechanical transmission. An F-150 full-size pickup truck[4] is used as the Generation II platform. Using a Folsom hydraulic transmission[5] , the vehicle is reconfigured from the conventional transmission to a HMT. By adding valves, and a low and a high pressure accumulator, the truck is further developed into a hydraulic hybrid vehicle.

In its original configuration, the hydraulic transmission was used as a CVT. As explained in Sec. 1.3.3, energy storage makes engine management more flexible and enables operation at a more optimal spot independent of the power output demand. Energy lost through friction braking can now be recovered into the high pressure accumulator,

[4] The F-150 vehicle was donated by Ford Motor Company to the University of Minnesota.
[5] The Generation II hydraulic transmission was donated by Folsom Technology International (FTI).

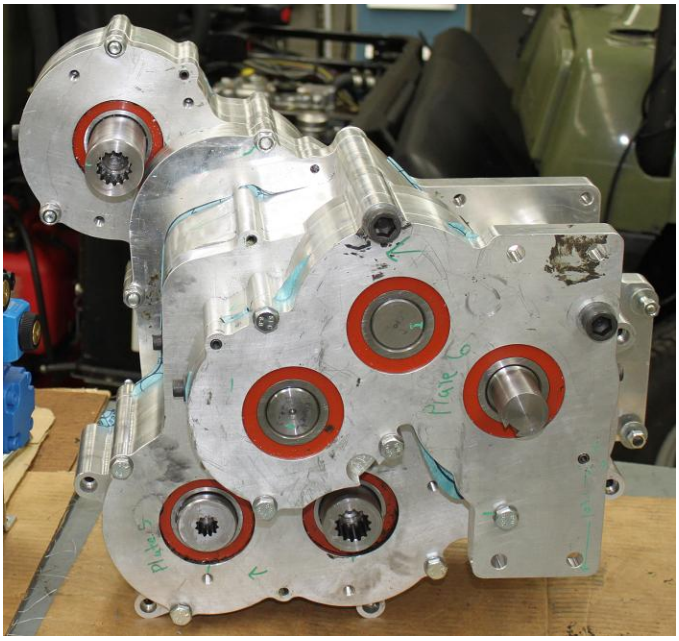

Figure 1.11: UMN-built Generation I power-split gearbox.

and used for vehicle launch and engine management.

The main power source of the F-150 truck is a 4.6 liter 24-valve V8 gasoline engine with 218kW peak power at 597 rad/s and 430Nm peak torque at 419 rad/s. The differential at the rear splits the power between the two wheels with a final drive ratio of 3.31. Hybrid vehicle control strategies developed in Generation I will be adopted for use on this test bed.

1.5 Dissertation overview

The research presented in this dissertation focuses on the development of passenger-sized vehicles with hydraulic hybrid power-split powertrains. This dissertation extends the methods in [11, 12, 19] to optimize the transmission design, powertrain control strategy, and analysis of the hydraulic hybrid powertrain performance and efficiency. The major contributions in this research can be divided into (i) analysis and optimization of the hydraulic hybrid transmission design, and (ii) modeling, controls and experimental implementation of both the Generation I and II vehicles. The analytical side of this

research mainly includes optimization of the hydraulic hybrid transmission design to improve the fuel efficiency, acceleration performance, and robustness against powertrain uncertainties. The experimental side of this study includes powertrain controller design and implementation to prove the effectiveness of the controllers.

This dissertation can be divided into two major sections: design optimization of the hydraulic hybrid transmission which will be discussed in Ch. 2, 3 and 4, and experimental testing with controls design in Ch. 5 to 9. The ultimate goal of this research is to investigate the improvement in fuel economy that can be gained from converting conventional transmissions into hydraulic hybrid transmissions. The chapters in the dissertation are organized as follows:

Chapter 2 focuses on deterministic transmission design optimization developed in order to systematically improve the performance and efficiency of the powertrain design. A generalized kinematic relation modeling technique is presented to allow continuous search within the design set regardless of the transmission architecture. A time-efficient algorithm is proposed to synthesize an energy management strategy to evaluate the fuel economy of the powertrain. With this algorithm, the performance index of each design can be evaluated rapidly to optimize the transmission design iteratively. Same methodology is applied to hybrid electric vehicle (HEV) for comparison.

Chapter 3 discusses the evaluation of the powertrain's acceleration performance. For deterministic design optimization, acceleration of the designed vehicle is included as another objective function for the overall transmission design. The original design optimization problem is then re-formulated into a multi-objective optimization. By using a weighted sum approach to the multi-objective optimization, a set of optimal trade-off solutions called the Pareto frontier of the optimization problem is generated, and yet the overall optimal design algorithm remains time-efficient.

Chapter 4 further extends the studies of transmission optimization methodology to include the variation of the powertrain losses and operating conditions. By formulating the stochastic variation of the powertrain losses into worst-case variation for the powertrain losses, the transmission design is optimized to be robust against powertrain uncertainties, insensitive to operating condition variations, and fuel efficient.

Chapter 5 introduces the Generation I test bed, and presents the modeling, system identification and analysis of individual components of the Generation I powertrain.

Chapter 6 presents the controls and analysis of the Generation I test bed. Chapter 7 presents the experimental results of the Generation I vehicle, and a discussion on the fuel economy achieved and challenges from the tests.

Chapter 8 introduces the Generation II vehicle, presents the modeling and design optimization of the FTI transmission, and discusses the potential fuel efficiency improvement by optimizing the FTI transmission. Chapter 9 discussed the design and challenges of the controls for the FTI transmission, and presents some preliminary test results and potential fuel economy improvements of Generation II platform.

Chapter 10 contains concluding remarks, and a summary of the research and contributions presented in this dissertation. Recommendations for future work and hardware upgrades are also discussed.

Chapter 2

Deterministic Transmission Optimal Design

From Ch. 1, hydraulic hybrid powertrains have shown great potential to improve fuel efficiency from conventional powertrains. However, the hydraulic components are inherently less efficient than mechanical gears. Thus, the design of a hydraulic transmission must be carefully optimized in order to exploits its advantages.

In this chapter, a systematic and computationally efficient methodology to optimize the hydraulic hybrid power-split transmission is proposed and will be discussed in detail. The methodology utilizes the insight that there are many design configurations that are mechanically distinct but kinematically equivalent. Thus, evaluation of redundant configurations during optimization process can be avoided by considering only the kinematic relation between various components.

The transmission design is based on physical model optimization, and is applied in a deterministic fashion, in which every major components will be described by a mathematical model or static map. Component sizing plays a significant role in a hydraulic hybrid vehicle as it not only fulfills certain performance requirements but also determines the overall efficiency of the powertrain throughout a standard duty cycle. This study focuses only on deterministic optimization where the powertrain components' model and drive cycles are known without any randomness and uncertainties involved.

The rest of this chapter will be organized as follows: Section 2.1 presents a review

for hybrid hydro-mechanical transmissions and transmission design optimization. Modeling of basic architectures of Hydro-Mechanical Transmission (HMT) is discussed in Sec. 2.2. Section 2.3 presents a generalized modeling approach for a compound architecture HMT. A computationally efficient framework using Lagrange Multiplier to synthesize the optimal energy management is proposed in Sec. 2.4. Section 2.5 summarizes the transmission's deterministic optimization procedures. The proposed design methodology is applied to optimize the design of Generation I vehicle in Sec. 2.6. Section 2.7 applies the same optimization methodology to optimize Hybrid Electric Vehicles (HEVs). Section 2.8 contains some concluding remarks for this deterministic optimization chapter.

2.1 Review of Hydraulic Hybrid Hydro-Mechanical Transmissions and Transmission Design Optimization

Power-split transmissions can take two different forms, (i) **Non-hybrid** transmission is where energy storage is not present and vehicle is propelled entirely by the engine, and (ii) **Hybrid** transmission is a power-split transmission equipped with a pair of hydraulic accumulators for energy storage.

As described in [20], non-hybrid hydrostatic power splitting transmissions have a great potential of providing high flexibility in vehicle operation and maintaining high torque capability. In this article, different basic architectures of hydro-mechanical transmissions, i.e. input coupled, output coupled and compound architectures are discussed and analyzed[1] . This investigation concluded that design flexibility of power-split hydrostatic transmissions is significant, considering the variety of different systems, the use of fixed or variable displacement hydraulic units, and the versatile use of planetary gearsets to generate an enormous variety of configurations. Despite the complexity of a power-split system as compared to pure mechanical or pure hydrostatic systems, it has potential to improve the efficiency of a powertrain system by exploring different possibilities of design. Thus, the research in this chapter will focus on optimizing the design of power-split transmissions.

Study in [21] investigated the operational characteristics, performance and efficiency

[1] Different architectures of power-split will be discussed in details in Sec. 2.2.2, 2.2.3 and 2.3.

of four different non-hybrid hydro-mechanical power-split architectures, i.e. the output coupled, compound coupled, input coupled and dual stage input coupled, for a heavy-duty truck. Thus, the transmission design is sized towards peak power and maximum speed instead of being fuel efficient, and the gear ratio and pump/motor units are sized based on maximum engine torque, maximum wheel torque and maximum vehicle speed. Moreover, the engine is constrained to operate at a fixed speed, which is applicable to a diesel engine but not necessarily a gasoline engine on a passenger vehicle. By this method of designing the hydro-mechanical transmission, the output coupled architecture appears to be superior in efficiency, whereas the dual stage input coupled architecture has better compactness. Instead of constraining the engine speed, this chapter will explore how engine management can further improve the overall powertrain efficiency.

There are also designs of HMT that use a pair of high angle 45 degree bent axis hydrostatic pump/motors with advanced displacement control mechanism to achieve high efficiency and robustness in [6]. Even though in [6], the pump/motors are designed to achieve high efficiency, combinations of gear ratios and pump/motor sizes are not optimized based on a specific drive cycle, for a specific vehicle. Most importantly, energy storage is not considered in these cases, which could offer the powertrain further improvement in fuel efficiency. The research in this chapter will show that having energy storage could transform the transmission design and pump/motors sizing entirely, such that the hybrid powertrain is more fuel efficient.

Hybridizing a transmission using a set of accumulators for energy storage offers advantages over non-hybrid transmissions in efficiency, flexibility, and also controls. Despite the additional energy storage, the basic structure of hydro-mechanical transmission for both configurations are identical. As mentioned in Sec. 1.3.3, the core idea of hybrid powertrain optimization is to shift operating points of all components to high efficiency regions [12]. Due to the transmission's rudimentary powertrain control and oversized hydraulic units in [12], the pump/motors are operated in the inefficient low fractional displacement region. Hence, the hybrid drivetrain design requires optimization and the control strategy must be significantly improved. Nevertheless, hydro-mechanical drivetrains show potential for high fuel economy in a passenger sized vehicle. This chapter will address the design and control issues in [12] and propose a systematic and time-efficient transmission design methodology.

Optimization methods are proposed for hydraulic hybrid passenger vehicles in [11, 22]. The study in [22] optimized the gear ratio by assuming the engine's highest efficiency operating point is mapped to the low speed centroid of the drive cycle operating points, allowing higher overall engine efficiency operation to improve fuel economy. Volumetric sizing of the pump/motors units is done to fulfill torque requirements. Results in [11] show an improvement of 20% in fuel economy by optimizing the pump/motor sizes and gear ratios using this approach. The fuel efficiency can be further improved by allowing the pump/motors to be locked up. This study also presented a hierarchical approach to divide the controls into three levels. Control approach will be adopted in this dissertation while the method to optimize the transmission gear ratios and pump/motor sizes are further improved.

In [23], a systematic and comprehensive methodology to design an optimal hydraulic hybrid power-split transmission for a delivery truck is presented. The transmission in this study consists of two planetary gearsets and two clutches to construct the transmission, where the additional planetary gearset and clutches are utilized to achieve gear shifting. This methodology involves searching all possible gear connection configurations and screening all possibilities through mechanical feasibility check. Different connection combinations between the two planetary gearset, engine, and two pump/motors yields 1,152 potential candidate configurations[2] . Only 20 configurations remains valid after the mechanical feasibility check. The optimal performance of the design is evaluated by driving through simplified driving schedules. This optimization methodology applies a power management algorithm similar to Equivalent Consumption Minimization Strategy (ECMS) [24] to speed up computation. Note that engine, pump/motors and final drive ratio are not optimized in this study. This three-step-methodology requires exhaustive search through all possibilities and the amount of configurations increases exponentially with the number of planetary gearsets being used. A more computationally efficient approach is proposed in this chapter to design hydraulic hybrid power-split transmissions, which includes sizing of the gear ratios and pump/motor sizes. Instead of searching through a large number of design candidates as in [23], a generalized modeling approach is utilized to summarize all design candidates into one transmission kinematic

[2] This number of candidates is speculated based on 6 nodes for both planetary gearsets, (Engine)6x(Pump)4x(Motor)3x(Vehicle)2x(Connection between planetary gearsets)4x(Clutch)2=1152

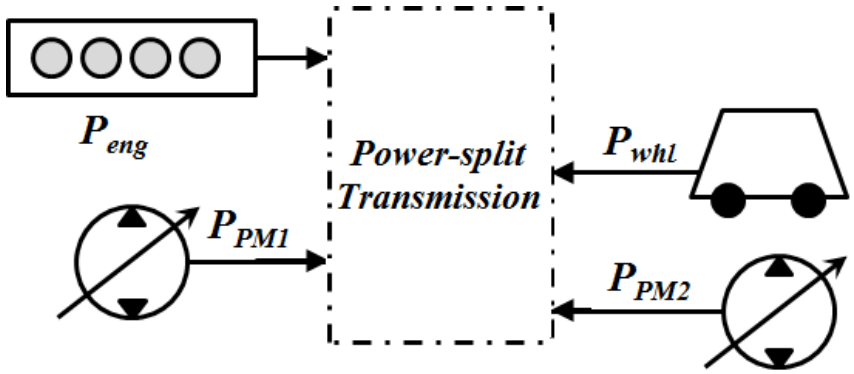

Figure 2.1: A generic representation model of a power-split transmission as a four-port device.

matrix. The Lagrange Multiplier method is used to synthesize the energy management strategy to reduce computation overhead.

2.2 Modeling of Power-split Transmission

Modeling of the two basic power-split architectures, i.e. the input coupled and the output coupled architectures will be presented in this section.

2.2.1 Power-split Transmission as a Four-Port System

A power-split transmission uses a pair of pump/motors and at least one planetary gearset to realize the power-split feature. Additional planetary gearsets and clutches can also be used to achieve discrete gear shifts, similar to a conventional automatic transmission. However, for simplicity they are not considered in this section. There are two basic power-split configurations, i.e. input coupled and output coupled transmissions. Despite the differences in architecture, a power-split transmission can be interpreted as a four-port device (Fig. 2.1) with power flows between the engine, wheel and the two pump/motors [25].

Due to power conservation by referring to Fig. 2.1 and by defining the power into the transmission as positive, the power flow of the four port device is:

$$\omega_{eng}T_{eng} + \omega_{whl}T_{whl} + \omega_{pm1}T_{pm1} + \omega_{pm2}T_{pm2} = 0 \tag{2.1}$$

where $P_{eng} = \omega_{eng} T_{eng}$ is the engine power, ω_{eng}, T_{eng} are the engine speed and torque, $P_{whl} = \omega_{whl} T_{whl}$ is the wheel power, ω_{whl}, T_{whl} are the wheel speed and torque, $P_{pm1/2} = \omega_{pm1/2} T_{pm1/2}$ is the pump/motors' power, and $\omega_{pm1/2}, T_{pm1/2}$ are the pump/motors' speed and torque.

Suppose that $(\omega_{pm1}, \omega_{pm2})$ and $(\omega_{eng}, \omega_{whl})$ are related by a kinematic matrix $G_\omega \in \Re^{2\times 2}$ such that:

$$\begin{pmatrix} \omega_{pm1} \\ \omega_{pm2} \end{pmatrix} = G_\omega \begin{pmatrix} \omega_{eng} \\ \omega_{whl} \end{pmatrix} \tag{2.2}$$

Then the torques (T_{pm1}, T_{pm2}) and (T_{eng}, T_{whl}) are related by the torque matrix G_T such that:

$$\begin{pmatrix} T_{pm1} \\ T_{pm2} \end{pmatrix} = G_T \begin{pmatrix} T_{eng} \\ T_{whl} \end{pmatrix} \tag{2.3}$$

Combining Eq. (2.1) together with Eq. (2.2) and Eq. (2.3) yields:

$$\begin{aligned} \begin{pmatrix} \omega_{eng} & \omega_{whl} \end{pmatrix} \begin{pmatrix} T_{eng} \\ T_{wlh} \end{pmatrix} + \begin{pmatrix} \omega_{pm1} & \omega_{pm2} \end{pmatrix} \begin{pmatrix} T_{pm1} \\ T_{pm2} \end{pmatrix} &= 0 \\ \begin{pmatrix} \omega_{eng} & \omega_{whl} \end{pmatrix} \left(I + G_\omega^\intercal G_T \right) \begin{pmatrix} T_{eng} \\ T_{whl} \end{pmatrix} &= 0 \\ \text{This implies that } \left(I + G_\omega^\intercal G_T \right) &= 0 \\ \text{Hence, } G_T &= -G_\omega^{-\intercal} \end{aligned} \tag{2.4}$$

Hence, the speed and torque kinematic matrices are related by Eq. (2.4).

2.2.2 Input coupled architecture

An input coupled transmission (Fig. 2.2) splits the power from the engine into a mechanical and a hydraulic transmission path. The hydraulic path is modulated by the accumulator and the resultant power is recombined with the mechanical power via a planetary power combination device. According to Eq. (2.4), the kinematic relationship between the speed and torque of the pump/motors $(\omega_{pm\,1/2}, T_{pm\,1/2})$ with those of the

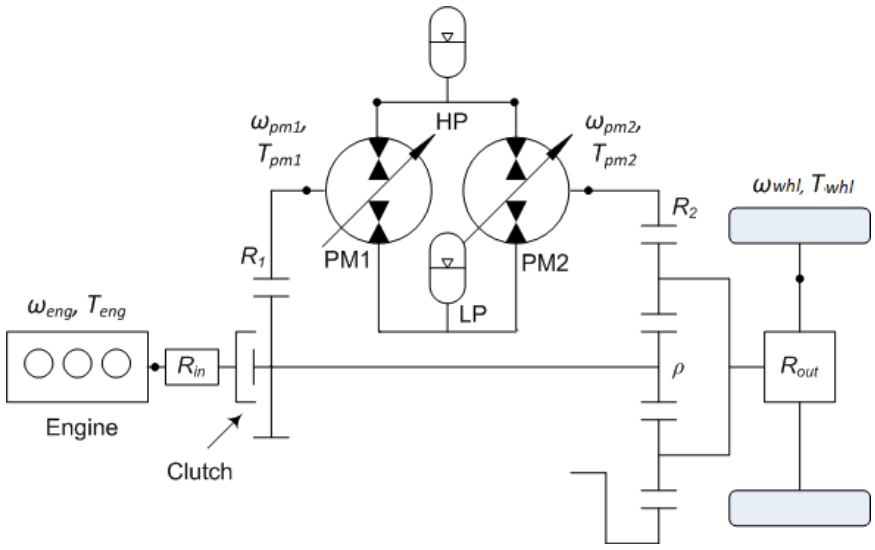

Figure 2.2: Hydraulic input coupled power-split hybrid architecture.

engine (ω_{eng}, T_{eng}) and of the vehicle (wheel) (ω_{whl}, T_{whl}) can be expressed as follows:

$$\begin{pmatrix} \omega_{pm1} \\ \omega_{pm2} \end{pmatrix} = \underbrace{\begin{pmatrix} r_{11} & 0 \\ r_{21} & r_{22} \end{pmatrix}}_{G_\omega} \begin{pmatrix} \omega_{eng} \\ \omega_{whl} \end{pmatrix} \tag{2.5a}$$

$$\begin{pmatrix} T_{pm1} \\ T_{pm2} \end{pmatrix} = \underbrace{\begin{pmatrix} -1/r_{11} & r_{21}/(r_{11}r_{22}) \\ 0 & -1/r_{22} \end{pmatrix}}_{G_T} \begin{pmatrix} T_{eng} \\ T_{whl} \end{pmatrix} \tag{2.5b}$$

where the gear ratios can be physically decomposed into $r_{11} = R_1 R_{in}$, $r_{21} = -R_2 R_{in}\rho$, $r_{22} = R_2 R_{out}(1+\rho)$ and $R_1 = r_{pm1}/r_{in}$ is the fixed gear ratio from Unit 1 to the transmission input shaft, $R_2 = r_{pm2}/r_\rho$ is the fixed gear ratio from Unit 2 to the planetary gearset, $R_{in} = r_{eng}/r_{in}$ is the fixed gear ratio from engine to the transmission input shaft, and $R_{out} = r_{whl}/r_{out}$ is the final drive ratio from the transmission output shaft to the wheels, and ρ is the radius-ratio of the sun and ring of the planetary gear (r_{sun}/r_{ring}, such that $\rho < 1$). The parametrization will preserve redundancy, allowing the sign and value of each element of matrix G_ω to be arbitrary.

Unit 1 is the 'torquer' as it adds torque to or subtracts torque from the engine as

shown in Eq. (2.5b). Unit 2 is the 'speeder' as it modifies the wheel speed from some fixed ratio of the engine speed as shown in Eq. (2.5a).

2.2.3 Output coupled architecture

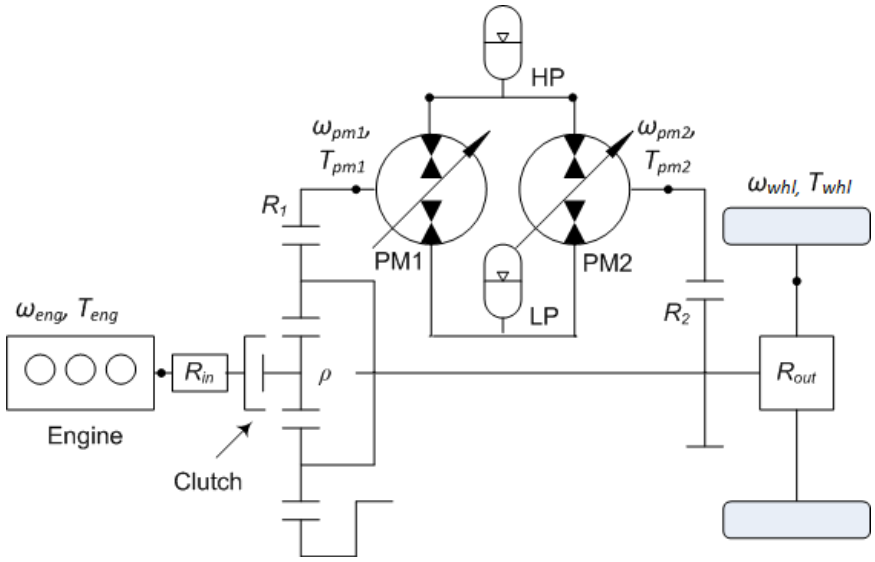

Figure 2.3: Hydraulic output coupled power-split hybrid architecture.

An output coupled transmission (Fig. 2.3) is configured in a reversed arrangement to the input coupled architecture. Engine power is split with the planetary power-split device into hydraulic and mechanical paths, and power from the engine and hydraulic pump/motors is recombined at the output shaft. The power in the hydraulic path is again modulated by the accumulator power. Its kinematic relationship is represented by:

$$\begin{pmatrix} \omega_{pm1} \\ \omega_{pm2} \end{pmatrix} = \underbrace{\begin{pmatrix} d_{11} & d_{12} \\ 0 & d_{22} \end{pmatrix}}_{G_\omega} \begin{pmatrix} \omega_{eng} \\ \omega_{whl} \end{pmatrix} \tag{2.6a}$$

$$\begin{pmatrix} T_{pm1} \\ T_{pm2} \end{pmatrix} = \underbrace{\begin{pmatrix} -1/d_{11} & 0 \\ d_{12}/(d_{11}d_{22}) & -1/d_{22} \end{pmatrix}}_{G_T} \begin{pmatrix} T_{eng} \\ T_{whl} \end{pmatrix} \tag{2.6b}$$

where $d_{11} = -R_1 R_{in} \rho$, $d_{12} = R_1 R_{out}(1+\rho)$, $d_{22} = R_2 R_{out}$, $R_1 = r_{pm1}/r_\rho$ is the fixed

gear ratio from Unit 1 to the planetary gear, $R_2 = r_{pm2}/r_{out}$ is the fixed gear ratio from Unit 2 to the transmission output shaft, and $\rho = r_{sun}/r_{ring}$ is the radius-ratio of the sun and ring of the planetary gear, similar to input coupled configuration. In contrast with input coupled transmission, Unit 1 is the 'speeder' while Unit 2 is the 'torquer'.

2.3 Generalized Transmission Modeling

As mentioned earlier, despite the differences between the two configurations of the power-split transmission, it can be interpreted as a four-port device connecting the power flows between the engine, wheels, and the two pump/motors. In a typical process for designing a power-split hybrid transmission such as in [11, 23], a specific architecture (e.g. input coupled, output coupled) or the connection between the gear sets [23] is chosen first and then the gear ratios and pump/motor sizes are optimized to achieve specified performance and / or overall system efficiency. In this dissertation, we consider a generalized transmission's kinematic relationship:

$$\begin{pmatrix} \omega_{pm1} \\ \omega_{pm2} \end{pmatrix} = \underbrace{\begin{pmatrix} g_{11} & g_{12} \\ g_{21} & g_{22} \end{pmatrix}}_{G} \begin{pmatrix} \omega_{eng} \\ \omega_{whl} \end{pmatrix} \tag{2.7}$$

$$\begin{pmatrix} T_{pm1} \\ T_{pm2} \end{pmatrix} = -G^{-T} \begin{pmatrix} T_{eng} \\ T_{whl} \end{pmatrix} \tag{2.8}$$

where $G \in \Re^{2\times 2}$ is nonsingular and the elements of the matrix are arbitrary. The lower and upper triangular matrices in Eq. (2.5a) and (2.6a) for the input coupled and output coupled configurations can be considered as special cases. The torque relationship Eq. (2.8) is derived from power conservation discussed earlier in Eq. (2.4).

An important question to ask is whether an arbitrary kinematic relationship in Eq. (2.7) can indeed be realized mechanically. The following proposition guarantees at least one possible realization of an arbitrary design.

Proposition 1. *An arbitrary nonsingular kinematic relation G in Eq.*(2.7) *can be realized by a cascade connection of an input coupled and an output coupled transmission.*

Proof: This result can be shown by LU factorizing G as a product of an upper and a

lower triangular matrix:

$$\begin{pmatrix}\omega_{pm1}\\ \omega_{pm2}\end{pmatrix} = \underbrace{\begin{pmatrix}r_{11} & 0\\ r_{21} & r_{22}\end{pmatrix}}_{\text{Input coupled}} \underbrace{\begin{pmatrix}d_{11} & d_{12}\\ 0 & d_{22}\end{pmatrix}}_{\text{Output coupled}} \begin{pmatrix}\omega_{eng}\\ \omega_{whl}\end{pmatrix} \tag{2.9}$$

The lower diagonal matrix corresponds to an input coupled configuration in Eq. (2.5a). And the upper diagonal matrix corresponds to an output coupled configuration shown in Eq. (2.6a). Consequently, Eq. (2.9) can be realized by connecting the pump/motor shafts of the output coupled transmission to the input/output (i.e. engine and vehicle) shafts of an input coupled transmission, as seen in the top section of Fig. 2.4. And the pump/motors are connected to input coupled transmission's pump/motor shaft ports. This is illustrated in bottom section of Fig. 2.4. ◇

LU factorization is not unique if specific values are not imposed on the diagonal elements of a triangular matrix [26]. This non-uniqueness preserves some extra degrees of freedom in realizing the G matrix in order to satisfy other design constraints.

The mechanical realization in Fig. 2.4 can be further simplified to a compound planetary transmission. One possibility is shown in Fig. 2.5. Here, the matrix G for the configuration in Fig. 2.5 is physically realized as

$$\begin{aligned} G &= \begin{pmatrix} -R_1R_{in}\rho_1 & R_1R_{out}K(1+\rho_1)\\ R_2R_{in}(1+\rho_2) & -R_2R_{out}\rho_2 \end{pmatrix}\\ &= \begin{pmatrix} R_1 & 0\\ 0 & R_2 \end{pmatrix}\begin{pmatrix} -\rho_1 & K(1+\rho_1)\\ (1+\rho_2) & -\rho_2 \end{pmatrix}\begin{pmatrix} R_{in} & 0\\ 0 & R_{out} \end{pmatrix} \end{aligned} \tag{2.10}$$

where the middle matrix represents the radius-ratios (ρ_1, ρ_2) of the sun and ring of the planetary gearsets, and the ratio of the connecting gears (K) between the ring of the first and the sun of the second planetary gearset, and the first and last matrices are the fixed gear ratios on the pump/motors (R_1, R_2), and the engine and final drive ratio (R_{in}, R_{out}).

Notice that an arbitrary G can be realized with some choices of the parameters. The number of gears selected is to preserve some redundancy, allowing the sign of each

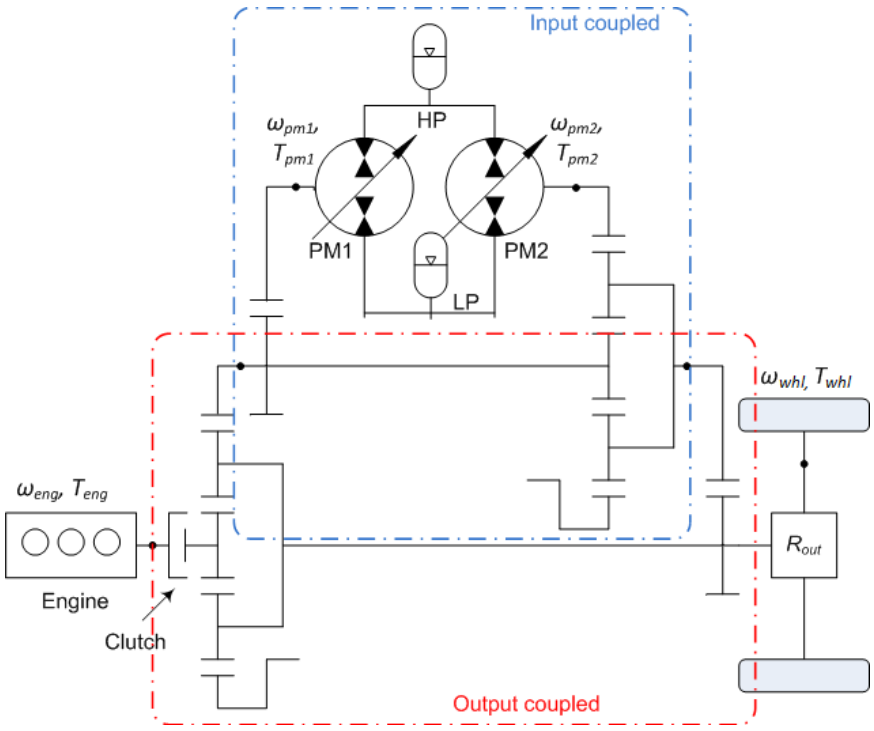

Figure 2.4: Combined input-output power-split configuration

element of matrix G to be arbitrary[3] , and to satisfy other geometric constraints. For the compound configuration with $n = 4$ elements in matrix G, the number of gears required is $2n - 1 = 7$ for arbitrary matrix, with at least 3 gears for each element. Similarly, for input and output coupled configurations with $n = 3$ elements in matrix G, $2n-1 = 5$ gears are required for arbitrary matrix, with at least 2 gears for each element. In this realization, both planetary gear sets perform power combination/split functions instead of one of them being used for discrete gear shifts as described in [21, 23].

As special cases, the generalized power-split model represented by Eq. (2.10) reduces to an input coupled or an output coupled architecture by setting $\rho_1 = -1$ and $\rho_2 = -1$ respectively.

$$G = \begin{pmatrix} R_1 R_{in} & 0 \\ R_2 R_{in}(1+\rho_2) & -R_2 R_{out}\rho_2 \end{pmatrix} \qquad \rho_1 = -1 \quad \text{Input coupled} \tag{2.11}$$

$$G = \begin{pmatrix} -R_1 R_{in}\rho_1 & R_1 R_{out} K(1+\rho_1) \\ 0 & R_2 R_{out} \end{pmatrix} \qquad \rho_2 = -1 \quad \text{Output coupled} \tag{2.12}$$

As shown in Eqs. (2.11) and (2.12), the generalized kinematic matrix G is reduced back into the form in Eqs. (2.5a) and (2.6a). These results shows that at least one solution exists for arbitrary G, whether G is a full matrix for compound architecture, $G_{1,2} = 0$ for input coupled, or $G_{2,1} = 0$ for output coupled. Again, due to the redundancy of the gear ratios[4] , the matrices G in Eqs. (2.11) and (2.12) can have non-unique values and sign.

Although a kinematic relation G in Eq. (2.7) can be realized in many ways, they affect the operation of the pump/motors, engine and the vehicle in the same way. Because of this, using G as a continuous design parameter to be optimized avoids many redundant computations in discrete configuration design. Compared to the exhaustive search method in [23], the generalized power-split model has the advantage of model simplicity and computational efficiency. From a different perspective, the two planetary gearsets in [23] are not configured as a compound architecture but to achieve gear shifting. This implies two distinct G matrices are needed to model the two different gear ratios in [23]. In other words, if gear shifting is not implemented, then the kinematic

[3] Negative sign of the gear ratio implies internal gear.

[4] Number of gear ratios $(R_{in}, R_1, ...)$ is larger than the number of elements in G (3 elements)

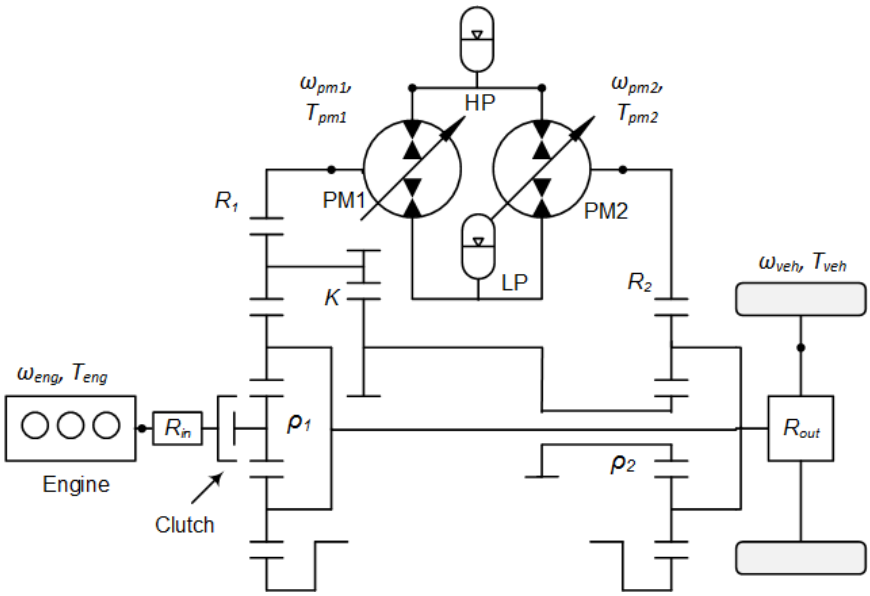

Figure 2.5: Compound power-split configuration

relation G captures all the design candidates considered in the study conducted in [23].

2.4 Optimal Control Synthesis

Fuel economy under a prescribed drive cycle is the optimization performance index for a specific transmission design. In order to evaluate the fuel economy of a specific transmission design, it is necessary to develop the controller that optimizes its performance due to its flexibility from energy storage. A hybrid power-split architecture allows arbitrary engine operation (ω_{eng}, T_{eng}) while fulfilling the vehicle speed and torque (ω_{whl}, T_{whl}). This feature provides the freedom to (i) choose the accumulator flow $Q_{acc}(t)$, and (ii) optimize total powertrain loss associated with the desired Q_{acc}.

Before synthesizing the optimal energy management controller, losses of the powertrain are defined for a specific engine (ω_{eng}, T_{eng}) and vehicle condition (ω_{whl}, T_{whl}). The engine loss $Loss_{eng}$ is a function of engine operation (ω_{eng}, T_{eng}). The pump/motor's loss $Loss_{pm\,i}$ is dependent on its volumetric displacement $(x_{pm\,i}) \in [-1, 1]$, speed $(\omega_{pm\,i})$, and system pressure (P_{sys}). The torque and flow characteristics of the pump/motor are

given by:

$$\begin{aligned} T_{pm\,i}(t) &= \frac{P_{sys}(t)D_{max\,i}}{2\pi}x_{pm\,i}(t) - sgn(\omega_{pm\,i})\cdot Loss_{mech,pm\,i}(x_{pm\,i},\omega_{pm\,i},P_{sys}) \\ Q_{pm\,i}(t) &= \frac{\omega_{pm\,i}D_{max\,i}}{2\pi}x_{pm\,i}(t) + Loss_{vol,pm*}(x_{pm\,i},\omega_{pm\,i},P_{sys}) \end{aligned}$$

where $Loss_{mech,pm\,i}$ is the pump/motor's torque loss, $Loss_{vol,pm\,i}$ is the pump/motor's flow loss. The pump/motor is motoring when $x_{pm\,i}, \omega_{pm\,i}, P_{sys}$ are positive. The pump/motor operation is constrained to fulfill the transmission's kinematic relation described in Eqs. (2.7) and (2.8):

$$\begin{pmatrix}\omega_{pm1}\\ \omega_{pm2}\end{pmatrix} = G_\omega \begin{pmatrix}\omega_{eng}\\ \omega_{whl}\end{pmatrix}, \qquad \begin{pmatrix}T_{pm1}\\ T_{pm2}\end{pmatrix} = G_T \begin{pmatrix}T_{eng}\\ T_{whl}\end{pmatrix}$$

The pump/motor's power loss is defined as:

$$Loss_{pm\,i}(x_{pm\,i},\omega_{pm\,i},P_{sys}) = P_{sys}Loss_{vol,pm\,i} + sgn(\omega_{pm\,i})\omega_{pm\,i}Loss_{mech,pm\,i} \quad (2.13)$$

In order to constrain the operation of components within their operating ranges, we define $Loss_{pm\,i} = \infty$ for $|\omega_{pm\,i}(t)| > \omega_{pm,max}$ or $|x_{pm\,i}(t)| > 1$. The high pressure accumulator as energy storage can be described as:

$$P_{hi}(t) = \frac{P_{pr}V_0}{V_0 - V_{acc}(t)} \quad (2.14)$$

$$\dot{V}_{acc}(t) =: Q_{acc}(t) = -\sum_{i=1}^{2} Q_{pm\,i}(\omega_{eng}, T_{eng}, \omega_{whl}, T_{whl}) \quad (2.15)$$

where P_{pr} is the pre-charge pressure of the accumulator, V_0 is the accumulator volume, V_{acc} is the hydraulic fluid volume in the accumulator, and Q_{acc} is the flow into the accumulator. With the low pressure P_{lo} assumed to be constant, the system pressure is defined as $P_{sys} =: P_{hi} - P_{lo}$[5] .

Thus, the total powertrain loss as a function of engine operation (ω_{eng}, T_{eng}) and

[5] As stated at the end of this section, accumulator pressure is instead assumed to be constant in order to apply the Lagrange Multiplier method for many of the simulations performed in this chapter.

vehicle conditions (ω_{whl}, T_{whl}) is expressed as:

$$\begin{aligned} &Loss(\omega_{eng}, T_{eng}, \omega_{whl}, T_{whl}, P_{sys}) = \\ &Loss_{eng}(\omega_{eng}, T_{eng}) + \sum_{i=1}^{2} Loss_{pm\,i}(x_{pm\,i}, \omega_{pm\,i}, P_{sys}) \end{aligned} \tag{2.16}$$

where $Loss_{eng}$ is the engine loss, $Loss_{pm\,i}$ is the pump/motors' loss, where the pump/motor displacements are specified as the vehicle's speed and torque (ω_{whl}, T_{whl}) are fulfilled.

The high level controller to manage the energy storage optimally throughout a prescribed drive cycle is formulated as follows:

$$\begin{aligned} J^* = \min_{(\omega_{eng}, T_{eng})} & \int_{t_0}^{t_f} Loss(\omega_{eng}, T_{eng}, \omega_{whl}(t), T_{whl}(t), P_{sys}(t))dt \\ \text{subject to } & \int_{t_0}^{t_f} P_{sys}(t) \cdot Q_{acc}(\omega_{eng}, T_{eng}, \omega_{whl}(t), T_{whl}(t))dt = 0 \\ & \underline{V_{acc}} \leq V_{acc}(t) \leq \overline{V_{acc}} \end{aligned} \tag{2.17}$$

where J^* is the optimal cost, (ω_{whl}, T_{whl}) are given for a specific drive cycle, ω_{whl} is the vehicle wheel rotational speed ($\omega_{whl} > 0$ means driving forward), T_{whl} is the vehicle wheel torque ($T_{whl} < 0$ means driving forward, $T_{whl} > 0$ means braking), P_{sys} is the system pressure, Q_{acc} is the accumulator volumetric net flow, V_{acc} is the accumulator liquid volume, and $\underline{V_{acc}}$ and $\overline{V_{acc}}$ are the lower bound and upper bound of the accumulator liquid volume. The terminal constraint ensures that the accumulator ends with the same energy with which it started.

An example of a prescribed drive cycle is the EPA combined drive cycle as shown in Fig. 2.6, that is a combination of the Urban and Highway drive cycle [27].

Typically, the optimal control problem expressed in Eq. (2.17) is solved using Dynamic Programming (DP) [28] to obtain global optimality. Solving Eq. (2.17) with V_{acc} as the only dynamic state will require computational time of approximately 5 hours[6] . However, as an optimal control problem must be solved for each iteration during the design optimization process, a computationally efficient approach is needed.

The rest of this section will be organized as follows: Section 2.4.1 lays out different

[6] On a standard 2.6GHz dual core computer.

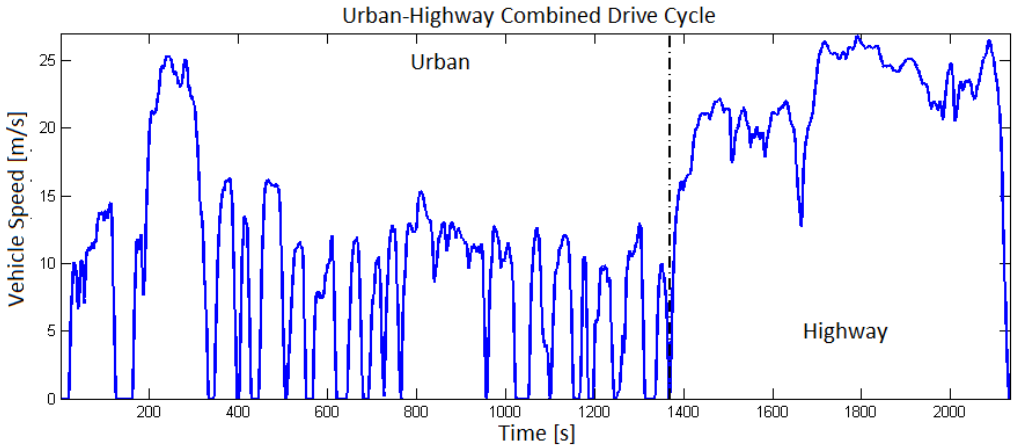

Figure 2.6: Combined urban and highway drive cycle.

transmission operating modes that simplify the optimization process and potentially operate the powertrain more efficiently. Section 2.4.2 discusses the Lagrange Multiplier Method that is the core methodology to this transmission design optimization.

2.4.1 Hybrid Transmission Operating Modes

Operating modes for the hydraulic hybrid powertrain are defined as the continuous powertrain operation being constrained to a finite number of operating points, and each constrained operating point is referred to as a `mode`. The engine operation for each operating mode is restricted a priori. Operating modes are introduced here to reduce computational effort for solving the optimization problem in Eq. (2.17). Two additional assumptions are made here: (i) the system pressure is constant and (ii) the accumulator capacity is unconstrained.

In normal power-split operation, the engine and both hydraulic pump/motors are working cooperatively to achieve the driver's demand. By constraining the powertrain operation to only several operating modes, the high level decision variable is reduced from the continuous set of engine operation (ω_{eng}, T_{eng}) in Eq. (2.17) into a finite set of discrete operating modes $\texttt{mode}(t)$, substantially reducing computational overhead.

Each operating mode involves de-clutching the engine (and shutting down the engine[7]) or locking up/free-spinning individual pump/motors whenever these actions

[7] Ideally the engine would be shut down but this is not in the scope of the experiments performed

would reduce losses. The pump/motor is considered lossless when locked-up or free-spinning.

`HMT` mode operates the engine at the maximum efficiency point $(\omega^*_{eng}, T^*_{eng})$, with the pump/motors working cooperatively to achieve demanded wheel speed and torque. The powertrain loss for `HMT` mode is defined as:

$$\begin{aligned} Loss_{mode}(t, \texttt{HMT}) &= Loss_{eng}(\omega^*_{eng}, T^*_{eng}) \\ + \sum_{i=1}^{2} Loss_{pm\,i}(\omega^*_{eng}, T^*_{eng}, \omega_{whl}(t), T_{whl}(t)) & \end{aligned}$$

where the pump/motor conditions $(\omega_{pm1}, T_{pm2}), (\omega_{pm2}, T_{pm1})$ are related to the engine and vehicle conditions by:

$$\begin{pmatrix} \omega_{pm1} \\ \omega_{pm2} \end{pmatrix} = G_\omega \begin{pmatrix} \omega^*_{eng} \\ \omega_{whl} \end{pmatrix}, \qquad \begin{pmatrix} T_{pm1} \\ T_{pm2} \end{pmatrix} = G_T \begin{pmatrix} T^*_{eng} \\ T_{whl} \end{pmatrix}$$

and the accumulator flow Q_{acc} is expressed as

$$Q_{acc}(\texttt{HMT}(t)) = -\sum_{i=1}^{2} Q_{pm\,i}(\omega^*_{end}, T^*_{eng}, \omega_{whl}(t), T_{whl}(t))$$

`Parallel-1` modes operate the engine at maximum torque $T_{eng,max}$ with either one of the pump/motors locked-up. Similarly, the powertrain loss for `parallel` mode is defined as:

$$\begin{aligned} Loss_{mode}(t, \texttt{parallel}) = Loss_{eng}(\omega_{eng}(\omega_{whl}(t)), T_{eng,max}) \\ + Loss_{pm\,i}(\omega_{eng}, T_{eng,max}, \omega_{whl}(t), T_{whl}(t)) \end{aligned}$$

where either P/M-1 or P/M-2 is locked-up ($\omega_{pm\,i} = 0$). If P/M-1 is locked up, the ω_{pm2} and ω_{eng} can be determined by

$$\begin{pmatrix} 0 \\ \omega_{pm2} \end{pmatrix} = G_\omega \begin{pmatrix} \omega_{eng} \\ \omega_{whl} \end{pmatrix}$$

in this dissertation.

If P/M-2 is locked up, the ω_{pm1} and ω_{eng} can be determined by

$$\begin{pmatrix} \omega_{pm1} \\ 0 \end{pmatrix} = G_\omega \begin{pmatrix} \omega_{eng} \\ \omega_{whl} \end{pmatrix}$$

and (T_{pm1}, T_{pm2}) can be determined by:

$$\begin{pmatrix} T_{pm1} \\ T_{pm2} \end{pmatrix} = G_T \begin{pmatrix} T_{eng,max} \\ T_{whl} \end{pmatrix}$$

`Parallel-2` modes operate the engine at maximum efficiency speed ω^*_{eng} with either one of the pump/motors free-spinning. Similarly, the powertrain loss for `parallel` mode is defined as:

$$\begin{aligned} Loss_{mode}(t, \texttt{parallel}) = Loss_{eng}(\omega^*_{eng}, T_{eng}) \\ + Loss_{pm\,i}(\omega^*_{eng}, T_{eng}, \omega_{whl}(t), T_{whl}(t)) \end{aligned}$$

where either P/M-1 or P/M-2 is free-spinning ($T_{pm\,i} = 0$). If P/M-1 is free-spinning ($T_{pm1} = 0$), the $(\omega_{pm1}, \omega_{pm2})$ can be determined by

$$\begin{pmatrix} \omega_{pm1} \\ \omega_{pm2} \end{pmatrix} = G_\omega \begin{pmatrix} \omega^*_{eng} \\ \omega_{whl} \end{pmatrix}$$

and (T_{pm2}, T_{eng}) can be determined by:

$$\begin{pmatrix} 0 \\ T_{pm2} \end{pmatrix} = G_T \begin{pmatrix} T_{eng} \\ T_{whl} \end{pmatrix}$$

If P/M-2 is free-spinning ($T_{pm2} = 0$), the (T_{pm1}, T_{eng}) can be solved by

$$\begin{pmatrix} T_{pm1} \\ 0 \end{pmatrix} = G_T \begin{pmatrix} T_{eng} \\ T_{whl} \end{pmatrix}$$

and the accumulator flow Q_{acc} is expressed as

$$Q_{acc}(\texttt{parallel}(t)) = -Q_{pm\,1/2}(\omega_{eng}, T_{eng}, \omega_{whl}(t), T_{whl}(t))$$

`P/M-1 only` or `P/M-2 only` modes de-clutch the engine, with the vehicle running solely on accumulator power, and one of the pump/motors is locked-up or free-spinning. The powertrain loss for `P/M-1` or `P/M-2` modes is defined as:

$$Loss_{mode}(t, \texttt{P/M} - \texttt{1/2}) = Loss_{pm\,i}(\omega_{whl}(t), T_{whl}(t))$$

For example, if P/M-2 is locked up ($\omega_{pm2} = 0$) and $T_{eng} = 0$, then ω_{pm1}, T_{pm1} can be solved by

$$\begin{pmatrix} \omega_{pm1} \\ 0 \end{pmatrix} = G_\omega \begin{pmatrix} \omega_{eng} \\ \omega_{whl} \end{pmatrix}, \qquad \begin{pmatrix} T_{pm1} \\ T_{pm2} \end{pmatrix} = G_T \begin{pmatrix} 0 \\ T_{whl} \end{pmatrix}$$

and the accumulator flow Q_{acc} is expressed as

$$Q_{acc}(\texttt{P/M} - \texttt{1/2}(t)) = -Q_{pm\,1/2}(\omega_{whl}(t), T_{whl}(t))$$

where $Loss_{eng} = 0$ for `P/M-1 only` or `P/M-2 only` modes.

Also, $Loss_{mode}(t, \texttt{mode}, P_{sys}) = \infty$ if the pump/motor's operating displacement, speed or pressure is out-of-range.

Table 2.1 summarizes all possible operating modes available for the 3 power-split architectures. Only four modes, `HMT, P/M-1 only, P/M-2 only` and the `parallel` using the "torquer" pump/motor, are considered for all architectures. The remaining modes are neglected because they will likely not be efficient. These are chosen to maximize powertrain efficiency and are found to be valid from preliminary studies [11]. For example, the `parallel` mode using the "speeder" pump/motor leads to operating the engine at low torque as "speeder" can only modify engine speed. This will not allow the engine to operate as efficiently (engine low speed and high torque operation is generally more efficient); and the `P/M-1&2 only` mode will incur inefficiencies due to power recirculation or low pump/motor displacements.

With total loss of each operating mode defined, the original optimization problem

Input coupled	Modes	Comments
mode 1*	HMT	Power-split, engine on
mode 2*	Parallel-1	Lock-up P/M-2, engine on
mode 3	Parallel-2	Freespin P/M-1, engine on
mode 4*	P/M-1 only	Lock-up P/M-2, engine off
mode 5*	P/M-2 only	Lock-up P/M-1, engine off
mode 6	P/M-1&2 only	Generally not used, engine off
Output coupled	Modes	Comments
mode 1*	HMT	Power-split, engine on
mode 2	Parallel-1	Freespin P/M-2, engine on
mode 3*	Parallel-2	Lock-up P/M-1, engine on
mode 4*	P/M-1 only	Lock-up engine, engine off
mode 5*	P/M-2 only	Freespin P/M-1, engine off
mode 6	P/M-1&2 only	Generally not used, engine off
Compound	Modes	Comments
mode 1*	HMT	Power-split, engine on
mode 2*	Parallel-1a	Lock-up P/M-2, engine on
mode 3	Parallel-1b	Freespin P/M-2, engine on
mode 4	Parallel-2a	Lock-up P/M-1, engine on
mode 5	Parallel-2b	Freespin P/M-1, engine on
mode 6*	P/M-1a only	Lock-up P/M-2, engine off
mode 7	P/M-1b only	Freespin P/M-2, engine off
mode 8*	P/M-2a only	Lock-up P/M-1, engine off
mode 9	P/M-2b only	Freespin P/M-1, engine off
mode 10	P/M-1&2a only	Generally not used, engine off
mode 11	P/M-1&2b only	Generally not used, engine off

Table 2.1: Modes for different architectures (* used in this dissertation)

from Eq. (2.16) is simplified into the following form:

$$Loss_{mode}(t, \texttt{mode}) = \begin{cases} Loss_{mode}(t, \texttt{HMT}), & \text{if } \texttt{mode} = \texttt{HMT} \\ Loss_{mode}(t, \texttt{parallel}), & \text{if } \texttt{mode} = \texttt{parallel} \\ Loss_{mode}(t, \texttt{P/M} - \texttt{1}), & \text{if } \texttt{mode} = \texttt{P/M} - \texttt{1} \\ Loss_{mode}(t, \texttt{P/M} - \texttt{2}), & \text{if } \texttt{mode} = \texttt{P/M} - \texttt{2} \end{cases} \tag{2.18}$$

Drivability test is conducted in the HMT mode for each design iteration, where the

transmission design must be feasible throughout the drive cycle whenever forward driving torque is required using this mode. Hence, feasibility is defined when $Loss_{mode}(t, \texttt{HMT})$ is finite, for all $t_0 \leq t \leq t_f$ throughout the specific drive cycle.

$$Loss_{mode}(t, \texttt{HMT}) \neq \infty, \qquad \text{for all } t_0 \leq t \leq t_f \tag{2.19}$$

This is to ensure the transmission outputs sufficient positive torque assuming minimum accumulator charge.

Replacing the engine operation (ω_{eng}, T_{eng}) in Eq. (2.17) with modal operation `mode` and including the two assumptions defined earlier, the high-level (energy management) control in Eq. (2.17) is re-formulated as[8] :

$$\begin{aligned} \min_{\texttt{mode}(\cdot)} J_{mode} = \min_{\texttt{mode}(\cdot)} & \int_{t_0}^{t_f} Loss_{mode}(t, \texttt{mode}(t))dt \\ \text{subject to } & \int_{t_0}^{t_f} P_{sys}Q_{acc}(t, \texttt{mode}(t))\, dt = 0 \end{aligned} \tag{2.20}$$

where $Loss(t, \texttt{mode})$ is the total of loss of each `mode` in Eq. (2.18), and $P_{sys}Q_{acc}(t, \texttt{mode})$ is the accumulator power, if an operating `mode` is applied to satisfy the drive-cycle speed and torque at time t.

2.4.2 Lagrange Multiplier Method

As mentioned earlier, to avoid using time-consuming DP to synthesize the energy management strategy for each transmission design, the two assumptions (i) the system pressure is constant and (ii) the accumulator capacity is unconstrained are made. By adjoining the terminal constraint into the cost function in Eq. (2.20), the constrained optimization problem can be solved by use of the scalar Lagrange Multiplier $\lambda \in \Re$ as [11, 28]:

$$J_{mode}(\lambda) = \min_{\texttt{mode}(\cdot)} \int_{t_0}^{t_f} (Loss_{mode}(t, \texttt{mode}(t)) + \lambda \cdot P_{sys}Q_{acc}(t, \texttt{mode}(t)))dt \tag{2.21}$$

[8] $(\cdot)$ indicates the arguments of the specific variable is arbitrary.

The cost function $J_{mode}(\lambda)$ for the minimization in Eq. (2.21) for all $\lambda \in \Re$ is upper bounded by the optimal cost J^* from the constrained optimization problem in Eq. (2.20).

Let $\texttt{mode}^*$ be the solution to the constrained optimization problem in Eq. (2.20). Since $\texttt{mode}^*(\cdot)$ is also a feasible solution, where $\int_{t_0}^{t_f} P_{sys}Q_{acc}(\texttt{mode}^*)dt = 0$, for the unconstrained capacity optimization problem in Eq. (2.21), optimization of Eq. (2.21) will not be larger than J^*. Thus, for all $\lambda \in \Re$, $J_{mode}(\lambda) \leq J^*_{mode}$. If regularity conditions are satisfied, we can also show that $\max_\lambda J_{mode}(\lambda) = J^*$ [29, 30].

Thus, assuming regularity conditions are satisfied, Eq. (2.20) can be solved by

$$J^*_{mode} = \max_{\lambda} \int_{t_0}^{t_f} \min_{\texttt{mode}(t)} [Loss_{mode}(t, \texttt{mode}(t)) + \lambda \cdot P_{sys}Q_{acc}(t, \texttt{mode}(t))]dt \qquad (2.22)$$

This is significantly more computationally efficient than DP because the inner minimization can be done inside the integral for every time instance, while the outer maximization is only one-dimensional. The optimal λ^* is a constant scalar that is a function of the distribution and statistics of the drive cycle (ω_{cyc}, T_{cyc}), but not dependent on the sequence of the drive cycle.

In summary, Eq. (2.22) for a specific transmission design can be solved numerically by (1) initializing λ, (2) computing the powertrain loss for every `mode` at every t of the drive cycle, and searching for the `mode` that has the least loss for each t, and summing the least loss for all t to compute $J_{mode}(\lambda)$, (3) outer maximization: finding λ that gives the maximum $J_{mode}(\lambda) \rightarrow J^*_{mode}$.

2.5 Transmission Parameterization, Design Optimization, and Dynamic Programming Verification

In this optimization study, we determine the hydraulic hybrid power-split transmission design that maximizes fuel economy. The vehicle weight, engine (size and efficiency map), and drive-cycles are assumed to be given. The hydraulic hybrid power-split transmission will be parameterized by $(G, D_{max,1}, D_{max,2})$ which are the kinematic relation $G \in \Re^{2\times 2}$ in Eq. (2.7) and the maximum displacements of the two pump/motors. In this study, the engine size and vehicle parameters (weight, drag coefficients, etc.) are not optimized.

2.5.1 Parameterization and Design Optimization

In order to compare different power-split architectures, three separate cases are considered: input coupled (G is lower triangular in Sec. 2.2.2), output coupled (G is upper triangular in Sec. 2.2.3), and compound (G is a full matrix in Sec. 2.3) architectures.

The transmission design optimization is to find $(G, D_{max,1}, D_{max,2})$ that yields the best fuel economy for a given drive cycle. While the hybrid powertrain operates in four different modes, the Lagrange Multiplier method is used to decide the best choice of `mode` to achieve high fuel economy at each discrete time step and fulfill the terminal constraint.

Using the optimal energy management strategy presented in Sec. 2.4.2, the particular transmission design is guaranteed to achieve high efficiency throughout a prescribed drive cycle. The focus is then shifted back towards optimizing the design of the transmission. The transmission optimal design is to *minimize the total powertrain loss by varying the design parameter υ while operating the powertrain most optimally for a prescribed duty cycle.* This design optimization can be expressed as:

$$\min_{\upsilon} J^*_{mode}(\upsilon) \tag{2.23}$$

where $\upsilon = (G, D_{max1}, D_{max2})$ are the design parameters, and J^*_{mode} is the optimal cost function using the defined operating modes throughout the drive cycle.

The optimized transmission design is then validated using Dynamic Programming to ensure simplifying assumptions of constant system pressure and unconstrained capacity have minimal effect on the performance of the optimized design. Dynamic programming is used to synthesize the energy management for the defined operating modes, by including the pressure dynamic and finite accumulator capacity.

This optimization procedure utilizes a standard optimization algorithm provided in Matlab's `fminsearch`, which applies the Nelder-Mead simplex direct search algorithm [31]. The optimization process is similar to that described in [32, 33]. The process is shown in flowchart form in Fig. 2.7 and is summarized in tabular form below:

1. Initialize transmission kinematics and pump/motor sizes (G, D_{max1}, D_{max2}).
2. Calculate system losses for each operating mode at each time point throughout the drive cycle, and solve optimal control problem in Eq. (2.22).

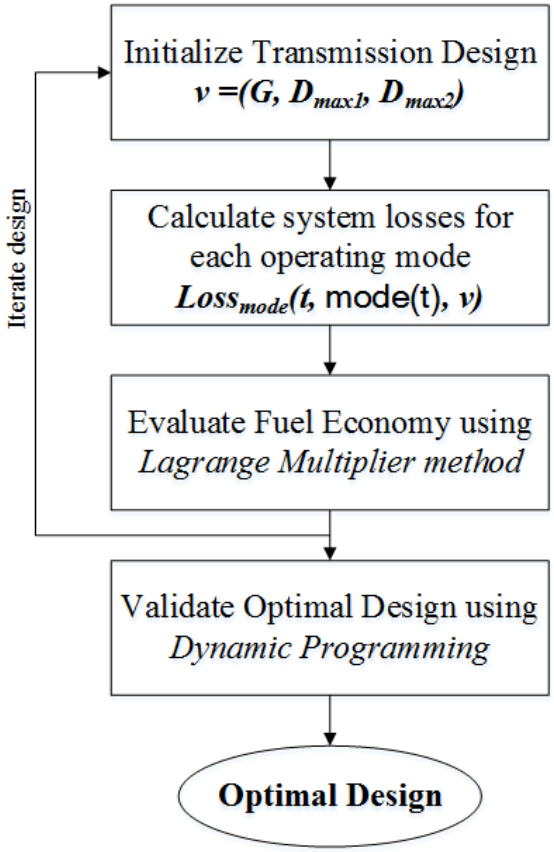

Figure 2.7: Flowchart summarizing the hydraulic hybrid transmission design.

3. Check `HMT` mode drivability requirements in Eq. (2.19). Goto Step 5 if fails.
4. Evaluate the achieved fuel economy.
5. Generate new (G, D_{max1}, D_{max2}) using standard optimization algorithm (Matlab's `fminsearch`). Repeat Steps 2, 3, and 4 until convergence.
6. Verify transmission design using Dynamic Programming.

As mentioned earlier, the optimized transmission design is validated using Dynamic Programming to ensure simplifying assumptions of constant system pressure and unconstrained capacity have minimal effect on the performance of the optimized design. Dynamic programming will be discussed in the following section.

2.5.2 Verification using Dynamic Programming (DP)

Dynamic programming [34, 35] is a numerical optimization method for solving optimal control problems. This method transforms a complex problem into a sequence of simpler problems. Its essential characteristic is the multistage nature of the optimization procedure.

Consider the finite-horizon $t \in [t_0, t_f]$ optimization problem in Eq. (2.20),

$$\begin{aligned} J^*_{mode} &= \min_{\texttt{mode}(\cdot)} \int_{t_0}^{t_f} Loss_{mode}(t, \texttt{mode}(t), P_{sys}(t))dt \\ \text{subjected to} \quad & \int_{t_0}^{t_f} P_{sys} Q_{acc}(t, \texttt{mode}(t))dt \\ & \underline{V_{acc}} \leq V_{acc}(t) \leq \overline{V_{acc}} \end{aligned} \tag{2.24}$$

Theorem 1. *Suppose* $\texttt{mode}^*(t)$ *is the optimal policy that minimizes Eq.* (2.24)*, and* J^*_{mode} *is the optimal cost. For any* $t = t_k$ *throughout the horizon, such that* $t_0 \leq t_k \leq t_f$*, the optimal policy* $\texttt{mode}^*(\tau), \tau \in [t_k, t_f]$ *minimizes*

$$J^*_{mode}(t_k, \texttt{mode}(\cdot), P_{sys}(t_k)) = \min_{\texttt{mode}(\cdot)} \int_{t_k}^{t_f} Loss_{mode}(t, \texttt{mode}(t), P_{sys}(t))dt$$

Hence, the policy $\texttt{mode}^*(\tau), \tau \in [t_k, t_f]$ *is optimal over the interval of* $[t_k, t_f]$*. This is referred to as the* principle of optimality*.*

By utilizing the *principle of optimality* and discretizing the system, the optimization

problem in Eq. (2.24) can be solved iteratively from $t = t_f$ to $t = t_0$, where each minimization sub-problem from t_k to t_{k-1} is solved to find the optimal policy:

$$\begin{aligned} \texttt{mode}^*(t_{k-1}) = \arg \min_{\texttt{mode}(t_{k-1})} [& \int_{t_{k-1}}^{t_k} Loss_{mode}(t, \texttt{mode}(t), P_{sys}(t)) dt \\ & + J^*_{mode}(t_k, \texttt{mode}^*(t_k), P_{sys}(t_k))], \\ & t \in [t_{k-1}, t_k] \end{aligned} \tag{2.25}$$

where the optimal cost $J^*_{mode}(t_k, \texttt{mode}^*(t_k), P_{sys}(t_k))$ is referred to as the cost-to-go function at time t_k. Solving the optimization problem in Eq. (2.24) using Dynamic Programming can be summarized as, (1) for every initial state $P_{sys}(t_{k-1})$, compute the optimal policy $\texttt{mode}^*(t)$ for the minimization sub-problem for $t \in [t_{k-1}, t_k]$ according to Eq. (2.25), (2) for every state $P_{sys}(t_{k-1})$, compute the optimal cost $J^*_{mode}(t_k, \texttt{mode}(\cdot), P_{sys}(t_k))$, (3) repeat Step 1 and 2 until $t = t_0$, with $\texttt{mode}^*(t)$ and $J^*_{mode}(t, \texttt{mode}(\cdot), P_{sys})$ recorded.

Dynamic programming can be employed to solve wide varieties of optimization problems and the cost function of the optimization need not be convex. However, this method becomes computationally intensive with increasing number of states. In this study, the optimality of J^*_{mode} due to operating modes restrictions will not be investigated.

2.6 Case study: Generation I HHPV

The work done so far has been to develop a design procedure for hydraulic hybrid transmissions. Assuming a 1000kg compact vehicle (including 300kg for the hybrid transmission excluding engine and differential), similar to the one presented in [11], paired with a 21kW diesel engine, the proposed transmission design approach described in Sec. 2.5 is applied to design a hydraulic hybrid powersplit transmission that can achieve high fuel economy. The combined EPA urban and highway cycle is used to optimize the transmission design for fuel economy (Fig. 2.6). Following the design of the transmission, its fuel economy for the EPA urban, highway, and combined cycles are evaluated. A constant system pressure of 13.8MPa (2000psi) is assumed.

The rest of this section is organized as follows: The optimization results of different architectures are shown in Sec. 2.6.2. Section 2.6.3 discusses the effects of the two assumptions (constant pressure and unconstrained accumulator capacity) made on the

powertrain operating behavior. Section 2.6.4 investigates the effects of both constraints on the powertrain by using dynamic programming (DP). Lastly, Sec. 2.6.5 discusses the computational advantage of the design methodology.

2.6.1 Vehicle Modeling

In order to apply model based optimization, the mathematical model of each component in the powertrain is presented in this section. The vehicle is mainly separated into five parts, i.e. the vehicle chassis (aero-dynamic and rolling resistance characteristics), vehicle's inertial dynamics, engine, transmission (includes geartrains, hydraulic pump/motor units), and energy storage (hydraulic accumulators).

Vehicle Chassis

The reference vehicle used in this study is based on a modified utility vehicle described in [11]. The vehicle is assumed to weigh $M = 1000\ kg$. The road load[9] of the vehicle, consisting of rolling resistance and aero-dynamic drag, can be modeled as [36]:

$$RL = M \cdot g \left(f_0 + (3.24 \cdot f_s \frac{2.237}{100} v)^{2.5} \right) + \frac{1}{2} C_D A_f \rho_{air} v^2 \tag{2.26}$$

where RL is the road load of the vehicle in N, $g = 9.81\ m/s^2$ is the gravitational constant, $\rho_{air} = 1.29\ kg/m^3$ is the air density, and v is the vehicle speed in m/s. The rolling resistance characteristics of the tires on regular road pavement contains the coefficients $f_0 = 0.0095, f_s = 0.0035$. The aerodynamic drag characteristics of the vehicle consist of an aerodynamic drag coefficient (C_D) of 0.5 and a frontal area (A_f) of 1.784 m^2. $v = \omega_{whl} R_{tire}$ where $R_{tire} = 0.31m$ is the effective wheel radius. These properties mimic a lightweight compact size passenger highway vehicle.

Engine Model

A selected model-based 1.1L diesel reference engine map $\eta_{eng}(\omega_{eng}, T_{eng})$ (shown in Fig. 2.8) is used as a quasi-static fuel consumption model. This engine has a peak power of 21kW and peak efficiency of 29.3% at 272 rad/s (2600 rpm), and 70 Nm

[9] Road load is the vehicle propulsion resistance if driven on the road, including tire rolling resistance and aero-dynamic drag.

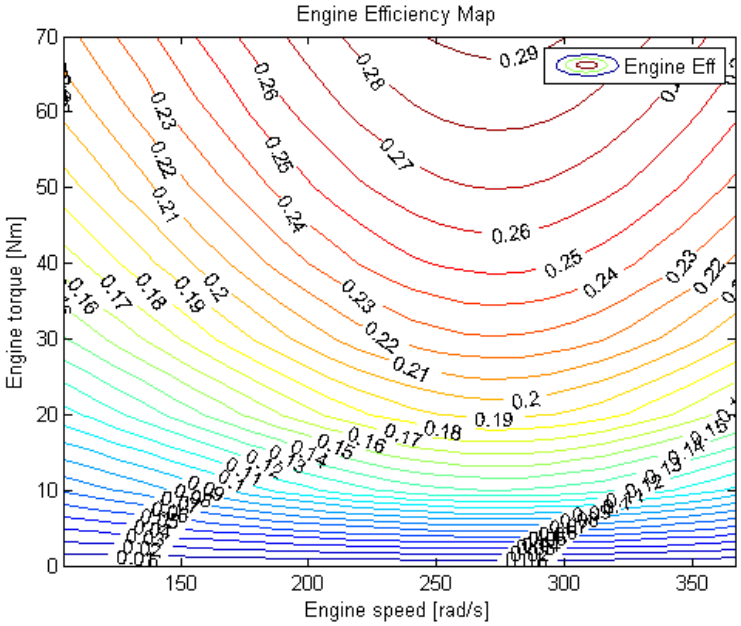

Figure 2.8: Reference diesel engine efficiency map approximated using Willan's line model.

torque. The engine efficiency is generated by adopting the Willan's line model [37], using fuel consumption for specific engine speeds provided by a manufacturer[10] . Also, it is assumed that a clutch is available between the engine and the transmission so that the engine can be disengaged from the drivetrain whenever this action would be deemed beneficial. The $Loss_{eng}$ for Eq. (2.16) can be determined by:

$$Loss_{eng}(\omega_{eng}, T_{eng}) = \omega_{eng} T_{eng} \left(\frac{1}{\eta_{eng}(\omega_{eng}, T_{eng})} - 1 \right) \tag{2.27}$$

Hydraulic Pump/Motors

The hydraulic units' size are to be optimized in this study. A set of scalable baseline torque and flow characteristic maps as a function of fractional displacement, pump/motor speed and system pressure $(x_*, \omega_{pm*}, P_{sys})$ are used. The characteristic maps are based

[10] Only 6 fuel consumption points at maximum torque are provided.

on those for a 28cc bent-axis variable displacement pump/motors obtained from a manufacturer. The torque and flow are assumed to scale linearly with the maximum displacements (D_{max1},D_{max2}) for a given pressure. This generates a series of pump/motor models that assumes the efficiency maps of the pump/motors are invariant with respect to the normalized torque and flow. The scaling of the torque and flow characteristic map is expressed as:

$$T_{pm*} = \eta_{mech}(x_*, \omega_{pm*}, P_{sys})\frac{P_{sys}}{2\pi}D_{max*}x_* \quad \text{for motoring} \tag{2.28}$$

$$T_{pm*} = \frac{1}{\eta_{mech}(x_*, \omega_{pm*}, P_{sys})}\frac{P_{sys}}{2\pi}D_{max*}x_* \quad \text{for pumping} \tag{2.29}$$

$$Q_{pm*} = \eta_{vol}(x_*, \omega_{pm*}, P_{sys})\frac{\omega_{pm*}}{2\pi}D_{max*}x_* \quad \text{for pumping} \tag{2.30}$$

$$Q_{pm*} = \frac{1}{\eta_{vol}(x_*, \omega_{pm*}, P_{sys})}\frac{\omega_{pm*}}{2\pi}D_{max*}x_* \quad \text{for motoring} \tag{2.31}$$

where the subscript '$*$' represents 1 or 2, P_{sys} is the system pressure, η_{mech} is the mechanical efficiency, η_{vol} is the volumetric efficiency, $x_* \in [-1, 1]$ is the pump/motors fractional displacement, and T_{pm*} and Q_{pm*} are the scaled torque and flow of the pump/motor. The pump/motor loss $Loss_{pm*}(x_*, \omega_{pm*}, P_{sys})$ can be determined from scaling the baseline power loss map.

Accumulators

Gas-charged isothermal accumulators are assumed as energy storage in this study. A pair of high and low pressure accumulators of $38L$ ($10gal$) are connected to the high and low pressure lines respectively. In this study, the low pressure is assumed to be maintained constantly at $P_{lo} = 1.4MPa$ (200psi) for simplicity. More detailed accumulator modeling can be found in [38][11] . Hence, the high pressure is modeled as shown in Eq. (2.15), with the pre-charge pressure of the accumulator of $P_{pr} = 10.3MPa(1500psi)$, and the accumulator volume of $V_0 = 38L$. The system pressure is $P_{sys} = P_{hi} - P_{lo}$. The accumulator model presented here is only used during the validation of the optimal transmission design using dynamic programming in Sec. 2.6.4.

[11] The accumulator model in [38] takes heat transfer losses into account. Alternatively, the accumulator pressure can be described with the Benedict-Webb-Rubin equation [39].

2.6.2 Optimization Results

Table 2.2 shows the optimal input coupled, output coupled and compound power-split designs, with assumed constant system pressure of 13.8MPa (2000psi). The fuel economies presented are evaluated using Lagrange Multiplier, and the validation of the optimal design using DP will be presented in Sec. 2.6.3 and 2.6.4. As expected, the compound architecture achieves the highest fuel economy, the input coupled design achieves $\sim 0.5\%$ less, and the output coupled achieves $\sim 5\%$ less. The kinematics matrix G of the compound design is very close to that of the optimal input-coupled design. The combined pump/motor sizes of the compound design is smaller, 13% and 21% less than the input coupled and output coupled designs, which physically can be translated to approximately 10kg weight reduction[12] . This weight reduction is offset by the extra planetary gearset needed for compound configuration that weighs approximately 5kg. On the other hand, the drivability test poses a lower bound constraint on the pump/motor sizing. If the drivability test is omitted, both pump/motors' size will be 11% smaller for compound configuration.

Compared to the ideal transmission[13] , the compound architecture transmission achieves fuel economy 24% lower in the Urban drive cycle, 12% lower in the Highway drive cycle, and 16% lower in the combined drive cycle. The compound transmission achieves closest fuel economy to ideal transmission in Highway drive cycle. This shows the full engine management is less significant, where the regenerative braking is also less beneficial.

Meanwhile, the highway fuel efficiency presented in Tab 2.2 is lower than the urban drive cycle, even though efficient mechanical path is expected for the highway drive cycle. This indicates that the pump/motors are operating at high efficiency, capable of recovering majority of the braking energy during the Urban drive cycle. This also suggest that the optimized design emphasized on improving the fuel economy for the Urban drive cycle. The pump/motor's efficiency map used maybe significantly more efficient than realistically feasible, as will be discussed in Ch. 5.

Table 2.3 shows two possible realizations of the optimized G matrix for the compound

[12] The weight variation is assumed to scale linearly according to an example pump catalogue.

[13] Ideal transmission case assumes the transmission is assumed lossless and the engine is operating at maximum efficiency of 29.3%, setting the highest efficiency achievable by the selected engine.

Table 2.2: Optimal Designs for the 3 Power-split Architectures and fuel economies using Lagrange Multiplier approach at 13.8MPa (2000psi).

Architecture	Ideal Transmission
City/Highway/Combined	2.24/3.68/3.07 [L/100km] 104.9/63.9/76.5 [mpg]
Architecture	Input coupled
Matrix G	$\begin{pmatrix} 1.0175 & 0 \\ 2.0660 & -8.3570 \end{pmatrix}$
P/Ms' size	P/M-T=27.7cc P/M-S=28.8cc
City/Highway/Combined	2.99/4.19/3.66 [L/100km] 78.6/56.1/64.2 [mpg]
Architecture	Output coupled
Matrix G	$\begin{pmatrix} 1.2768 & -4.0424 \\ 0 & 4.7239 \end{pmatrix}$
P/Ms' size	P/M-S=23.9cc P/M-T=39.1cc
City/Highway/Combined	3.23/4.28/3.84 [L/100km] 72.7/54.9/61.2 [mpg]
Architecture	Compound
Matrix G	$\begin{pmatrix} 0.9810 & 0.6400 \\ 2.0573 & -8.3764 \end{pmatrix}$
P/Ms' size	P/M-1=24.5cc P/M-2=24.7cc
City/Highway/Combined	2.96/4.19/3.65 [L/100km] 79.5/56.1/64.5 [mpg]

power-split design according to Fig. 2.5. As seen, non-uniqueness of the matrix G realization allows the selection of one gear to be offset by another. For example, R_{in} in *Design 1* can be simplified from 0.5 to 1 by offsetting R_1, R_2 and R_{out} into *Design 2*, reducing the gear to a direct connection[14] .

Figure 2.9 shows the optimal distribution, throughout the drive cycle, of the operating modes for the compound power-split design in Table 2.2. The "engine-on" modes (i.e. `HMT` and `parallel`) occur mainly at high vehicle speeds. This accounts for ∼33% of the cycle time, consistent with the engine power at peak efficiency of 29.3% and the mean vehicle power requirement throughout the drive cycle. At lower vehicle speeds and during braking, "hydraulic-only" modes are preferred. "(S)peeder" pump/motor

[14] If the nearly 50:1 gear ratio of K is problematic, other ratios can be changed to adjust K.

Table 2.3: Two realizations of the optimal compound design according to Fig. 2.5. Negative ratios imply internal gears or using idler gear between two external gears.

Ratios	ρ_1	ρ_2	R_1	R_2	R_{in}	R_{out}	K
Design 1	0.75	0.75	-2.62	2.35	0.50	4.75	-0.029
Design 2	0.50	0.75	-1.96	1.18	1.00	9.50	-0.023

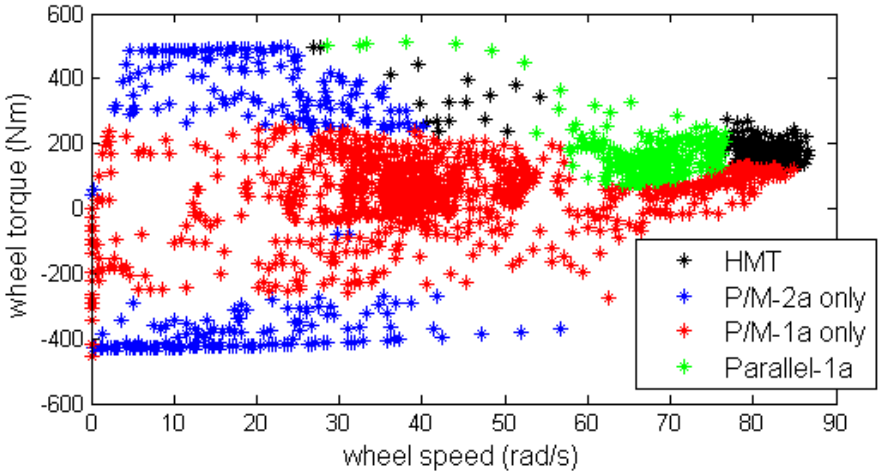

Figure 2.9: Compound power-split modes distribution

(P/M-2) only is preferred at high torques whereas "(T)orquer" pump/motor (P/M-1) only mode is preferred at lower torques.

Figure 2.10 shows the optimal distribution of the operating modes for the input coupled power-split design in Table 2.2 under the Combined drive cycle. The operating behavior of the input coupled architecture is very similar to the compound power-split. This similarity in operation is caused by the similar transmission G matrix and pump/motor sizes.

Figure 2.11 shows the output coupled architecture modes distribution throughout the drive cycle. As seen, the `HMT` mode occurs at high vehicle torque and low braking torque. The `parallel` mode is preferred at high vehicle speeds with relatively low torque. While `T-only` (P/M-2) mode occurs over a wide range of vehicle speeds and torques, `S-only` (P/M-1) mode is used only at the maximum braking torque with zero

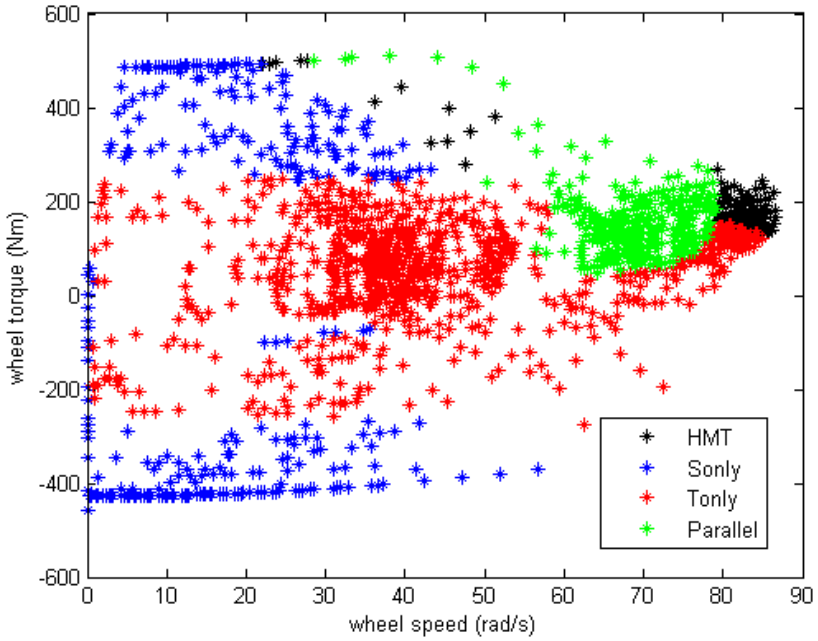

Figure 2.10: Input coupled power-split modes distribution

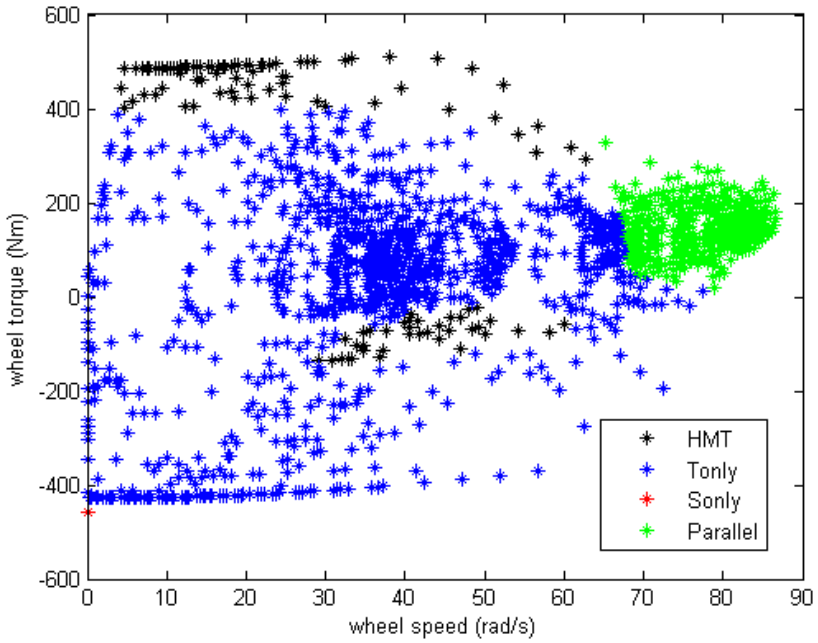

Figure 2.11: Output coupled power-split modes distribution

speed.

In reality, system pressure would vary from the lowest (assumes pre-charge pressure 10.3MPa (1500psi)) to the maximum pressure of the accumulator (assumed to be 34.5MPa (5000psi) in this study) throughout the entire drive cycle, as the accumulator is charged and discharged. Using the lower pressure limit of 13.8MPa (2000psi) to optimize the transmission design is to ensure that the pump/motor displacements are sized conservatively. Higher system pressure leads to operating the pump/motors at lower displacements. The fuel economy performance is evaluated again, using the same transmission parameters, but different pressures, to show how fuel economy of the optimal transmission design is affected. Results are shown in Fig. 2.12. Since the hydraulic pump/motor units assumed are inherently inefficient at low displacement, fuel economy of the transmission tends to be lower as the system pressure increases, setting the lower bound for the specific design. Thus, in actual driving conditions, the fuel mileage should lie between the bounds depicted in Fig. 2.12.

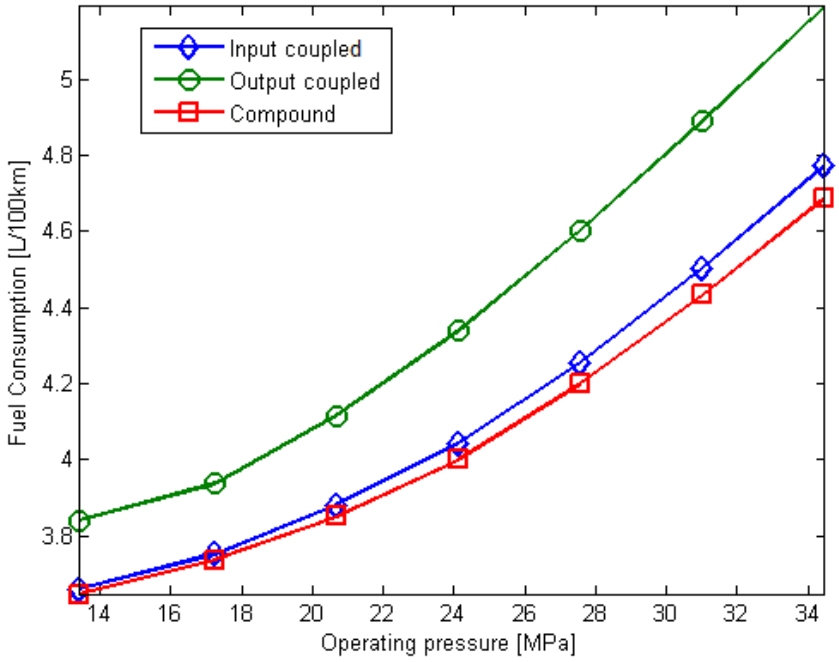

Figure 2.12: Fuel economy of different architectures under Combined drive cycle at various system pressures.

2.6.3 Constraint on Energy Storage Capacity

The optimization procedure assumes constant system pressure and unconstrained accumulator capacity in order to reduce computational burden. Figure 2.13(a) shows state-of-charge (SOC) of the unconstrained accumulator. The accumulator is discharged nearly continuously in the City cycle and recharging nearly continuously during the Highway cycle. This accumulator behavior is attributed to the unconstrained accumulator capacity assumption made in order to apply Lagrange Multiplier method. This leads to an impractical size of 2.5MJ accumulators (equivalent to volume of 209 liters based on a pre-charge pressure of 10.3MPa and a maximum pressure of 34.5MPa).

The Lagrange Multiplier method is computationally efficient and able to ensure the accumulator returns to its original state. To ensure the assumption on accumulator size does not significantly affect the efficiency of the drivetrain, dynamic programming (DP) is performed for the optimal compound design in Table 2.2 with a reasonable 150kJ accumulator capacity (approximately 13 liters volume) constraints. The system pressure is still assumed to be constant 13.8MPa (2000psi) and identical 4-mode operation is applied. For compound power-split, the fuel consumption only increases from 3.65L/100km (64.5mpg) to 3.73L/100km (63.1mpg). Figure 2.13(b) shows that with the constraint, the accumulator is discharged and recharged repeatedly throughout the drive-cycle to stay within the limits.

2.6.4 Effect of accumulator pressure dynamics

Recall that the constant pressure assumption used in the Lagrange multiplier method has neglected the actual accumulator dynamics that pressure decreases as energy depletes. To evaluate the effect of accumulator pressure dynamics, Dynamic Programming is applied to the optimal compound design in Table 2.2 coupled with an isothermal accumulator modeled in Sec. 2.6.1. DP in this case applies the same modal operation, and pressure states are discretized at $1.38MPa$ ($200psi$). The SOC over the drive-cycle is shown in Fig. 2.13(c). The fuel consumption increases from $3.65L/100km$ ($64.5mpg$), estimated for a constant low system pressure, unconstrained capacity case, to $3.73L/100km$ ($63.0mpg$). Although the accumulator pressure is allowed to reach $34.5MPa$, the DP result in Fig. 2.13(c) tends to keep the accumulator pressure low, so

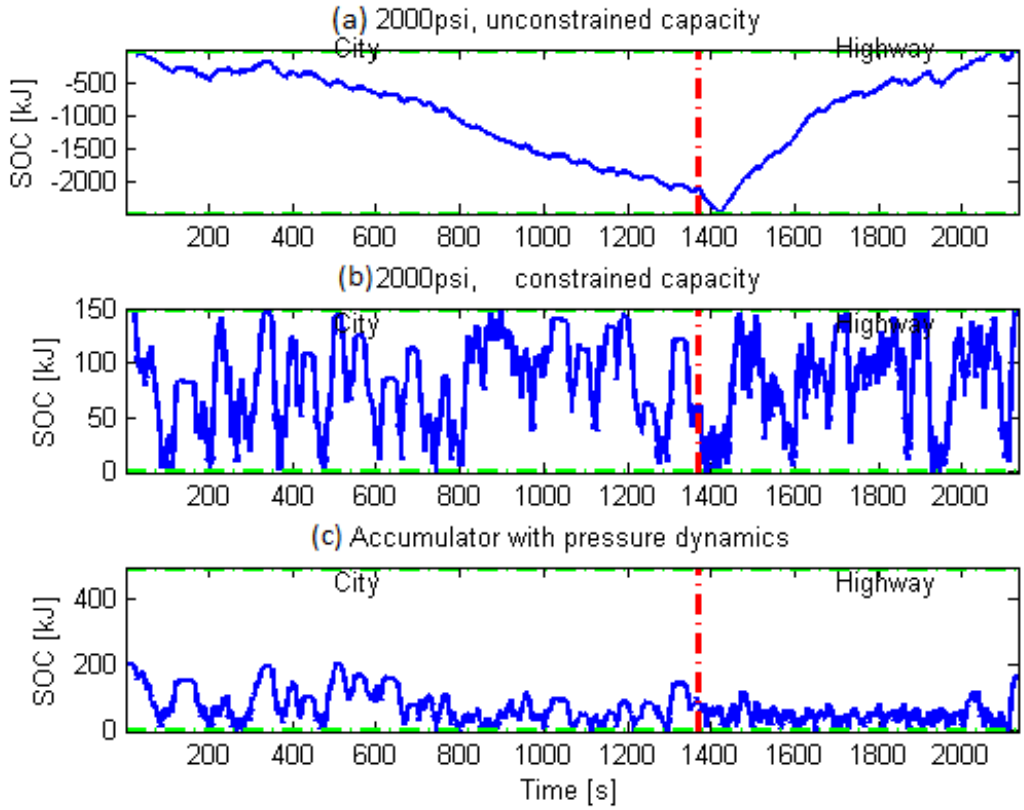

Figure 2.13: Accumulator SOC over the combined drive cycle for the compound design in Table 2.2: (a) at constant pressure with unconstrained accumulator capacity; (b) at constant pressure with 150kJ accumulator capacity constraint; (c) with an isothermal accumulator

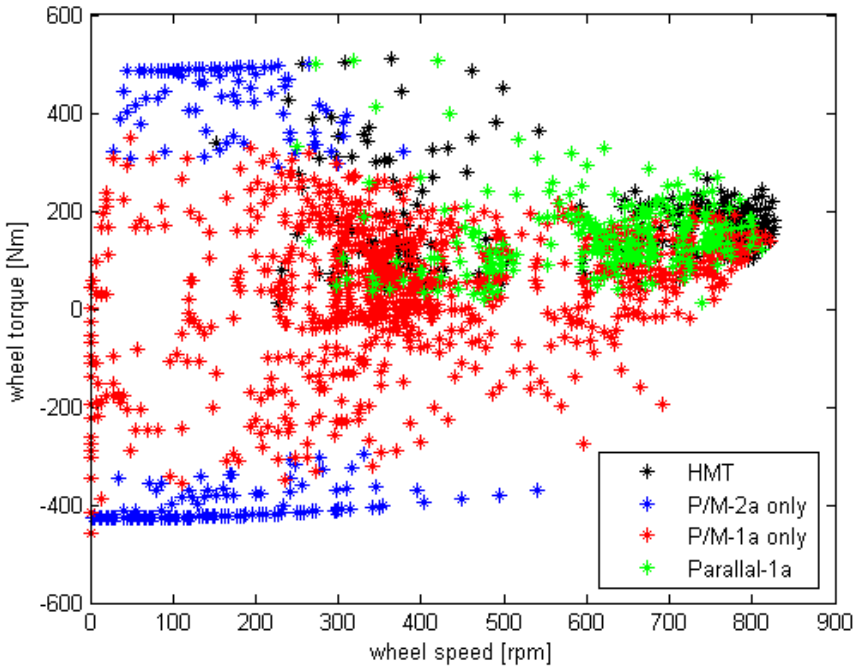

Figure 2.14: Compound power-split modes distribution using Dynamic Programming energy management with isothermal accumulator.

the fuel economy is closer to the low pressure estimate rather than the high pressure case in Fig. 2.12.

Figure 2.14 shows the optimal distribution under Dynamic Programming strategy using isothermal accumulators, throughout the drive cycle, of the operating modes for the compound power-split design in Table 2.2. Despite the difference in energy management and the variation in pressure, the operating modes from DP is similar to Lagrange Multiplier method, except that DP operating modes are not distinctively segmented. Particularly, the `parallel` mode also occurs at lower speeds and torques as compared to Lagrange Multiplier method.

Results shown so far in this study assumes modal operation for the hybrid powertrain to reduce computational overhead. However, penalties are not considered for switching between `modes` or turning the engine on/off. Moreover, the pump/motors are assumed to be lossless when free-spinning or locked up. However, due to the restricted engine

operation, fuel economies presented here are expected to under-estimate compared to globally optimal fuel economy. However, the core idea of this study is to understand the fuel efficiency improvement achievable by optimizing the transmission design.

2.6.5 Computation Times

This optimization methodology and the simplifying assumptions offers significant improvement in computational efficiency. On a basic PC, it takes only approximately 2 seconds to synthesize the optimal control and evaluate a design. In contrast, dynamic programming in Sec. 2.6.4 would take over 15 minutes for each transmission design. Moreover, the analysis presented previously in Sec. 2.6.4 suggests that the assumptions made in Sec. 2.4 have minimal impact on fuel economy estimation as compared to dynamic programming. Compared to solving the original optimization problem Eq. (2.17) that takes 5 hours of computation time, the Lagrange Multiplier method is approximately 450 times faster.

In contrast with the study in [23], fuel economy evaluation of each design requires approximately 1 minute, excluding the time needed to filter the pool of design candidates. Moreover, this study does not optimize the pump/motor sizes. In addition, the methodology proposed in this chapter focuses on optimizing the kinematic matrix G of the transmission while leaving the gear ratios realization until after G is optimized.

2.7 Hybrid Electric Transmission Optimization and Comparison

Hybrid Electric Vehicles (HEV) are generally perceived to be highly efficient. It is imperative to compare the fuel efficiency between the HEVs and HHVs in order to understand the potential of hydraulic hybrids. The same design methodology used to optimize the HHV should be applied to the HEV to ensure a fair comparison. The optimization approach described in Sec. 2.5 is not restricted only to hydraulic hybrid vehicles. In optimizing and analyzing hybrid electric vehicle (HEV) power-split transmissions, similar procedures can be utilized by replacing the hydraulic power unit with

electric machines, and the hydraulic accumulator with a battery.[15]

Similar to optimizing the HHV, this study utilizes four modes of operation for the hybrid electric powertrain, and the energy management is also synthesized using the Lagrange Multiplier method. Using a battery as energy storage, the operating voltage is assumed constant at 300V, with electric current flowing into the battery as it charges. The vehicle attributes are identical as described in Sec. 2.6.1.

The reference engine used here is identical to the one described in Sec. 2.6.1. The baseline motor/generators are selected from ADVISOR [40]. A scalable baseline efficiency map for permanent magnet motor/generators rated to 49kW is used. The selected electric motor/generators have similar peak efficiency compared to the hydraulic pump/motors (approximately 96%). The overall efficiency of electric motor/generator is higher because the efficiency remains above 90% over a broad range. The battery for energy storage is a NiMH battery pack rated to 30kW at 300V nominal voltage. Other components and parameters remain identical to the hydraulic hybrid case.

Table 2.4: HEV configurations comparison

Fuel Economy	Input Coupled	Output Coupled
City	2.85 L/100km 82.4 mpg	2.82 L/100km 83.5 mpg
Highway	4.02 L/100km 58.5 mpg	4.06 L/100km 57.9 mpg
Combined	3.53 L/100km 66.8 mpg	3.53 L/100km 66.8 mpg
Matrix G	$\begin{pmatrix} 0.6956 & 0 \\ 5.1986 & 13.5767 \end{pmatrix}$	$\begin{pmatrix} 9.6034 & 0.14141 \\ 0 & 0.18567 \end{pmatrix}$
M/G sizes	M/G-1: 29.4 kW M/G-2: 65.0 kW	M/G 1: 14.2 kW M/G 2: 64.2 kW

Results show HEVs and HHVs have comparable fuel economies. HEVs are approximately 4% more fuel efficient than HHVs on the combined drive cycle despite the wide range of high efficiency associated with electric motor/generators. Component sizing results are summarized in Tab. 2.4. Compared to HHV designs where the P/M-1,2

[15] For each configuration, the pump/motors P/M-1,2 are replaced by the electric motor/generators M/G-1,2.

sizes are similar, the HEV designs have M/G-1 sized to be substantially smaller than M/G-2. This is caused by the high baseline maximum torque of 270Nm provided by M/Gs at 300V, compared to the baseline maximum torque of 61Nm provided by P/Ms at 13.8MPa. Thus, smaller M/G-1 is required to absorb engine torque. Interestingly, this analysis has generated a set of of optimal components that is comparable to the Toyota Prius design [41, 42]. This study focuses on light-weight vehicles, therefore regenerative braking has significantly less impact on optimal hybrid operation due to less kinetic energy being available for recovery.

For the HEV to achieve the fuel economy in Tab. 2.4, the batteries need to be sufficiently large to absorb and provide the power needed (≈30kW in this case). This would require a battery pack that is 50% larger than the one in the Toyota Prius (which is capable of 21kW). The weight of the battery is projected to increase from 40kg to 60kg. This translates to higher cost and weight. Since HEV's battery is sized for power whereas accumulator is sized for energy capacity, the power requirement on the battery would be more severe if the vehicle weight is larger or a more stringent acceleration requirement is imposed. This issue, however, does not arise with a hydraulic accumulator due to the high power density of hydraulic systems. This analysis also shows that an optimized drivetrain design and a well-designed energy management strategy is crucial, as it allows the engine to operate mainly in the most efficient region, substantially increasing the mean engine efficiency throughout the drive cycle.

2.8 Concluding Remarks

This chapter has presented an efficient approach for optimizing the configuration and pump/motor sizes of a hydraulic hybrid power-split transmission. It utilizes a generalized kinematic relationship of the transmission to avoid redundant computation of mechanically different but kinematically equivalent configurations. A full kinematic matrix is shown to be realizable by a compound configuration. Modal vehicle operations are proposed to reduce loss. By neglecting the pressure dynamics and accumulator size constraints, the Lagrange multiplier method can be used to solve the optimal control problem necessary to evaluate each design. Simulations show that these simplifications have minor impacts on the estimated fuel economies of the optimized designs.

A case study on a compact sized vehicle indicates that the optimized compound power-split and input coupled power-split have better fuel economy and require smaller pump/motors than an optimized output coupled power-split. Dynamic programming is applied to the optimized transmission design, validating the transmission design is feasible, and constant system pressure and unconstrained accumulator capacity has minor effect on fuel economy.

Further studies are required not only to compare different architectures but also the effects of various parameters that have not been considered in this investigation; for example, vehicle sizes, weights, duty cycles and engine sizes. In particular, the specified drive cycle will affect the optimal sizing of the powertrain, which in turn potentially alters its operational characteristics. The same optimization method is also applied to hybrid electric vehicles.

Chapter 3

Optimal Design with Acceleration Performance

As mentioned earlier, hydraulics have the advantage of power density over electrical machines. Hence, acceleration is another important performance index to be considered during the design of the transmission. Time to accelerate from 0 to 100 km/h is a common metric to compare powertrains' acceleration performance, and it is reasonable to consider the 0 to 100 km/h time as one of the cost functions during the transmission design optimization. The purpose of this chapter is to optimize the design of the hybrid transmission, considering both the fuel economy and acceleration performance.

This chapter will discuss acceleration performance of the hydraulic hybrid powertrain system in detail. A simplified method to evaluate the hybrid powertrain's acceleration performance is proposed and validated. By applying a classical multi-objective solver, the objective of optimizing acceleration performance can be incorporated into the design optimization procedure for fuel economy presented in Ch. 2 without sacrificing the computational efficiency. With this systematic methodology, transmission design with different trade-offs for both fuel efficiency and acceleration objectives can be accomplished.

This rest of this chapter is organized as follows: A review of evaluating hybrid powertrain acceleration performance is presented in Sec. 3.1. Section 3.2 introduces a simplified approach to evaluate the acceleration performance of each hybrid powertrain

design. Section 3.3 presents and explains the formulation of a classical multi-objective optimization problem, and solutions for the fuel economy and acceleration performance optimization. A case study of optimizing the Generation I hybrid powertrain design by incorporating the acceleration performance is presented in Sec. 3.4. Conclusions regarding the deterministic optimization with acceleration considered are discussed in Sec. 3.5.

3.1 Review of Hybrid Powertrain Acceleration Performance Optimization

A study of a continuously variable power split transmission is conducted in [43]. This study focuses on evaluating the acceleration time from rest to 100kph of the transmission that uses a V-belt CVT combined with a planetary gearset. The continuously variable power split transmission performance is compared to a conventional manual and automatic transmission. Unlike the hybrid transmission investigated in this chapter, the transmissions do not involve energy storage, hence this study focused on selecting the transmission ratio.

A method to optimize the gear shift operations of an automatic transmission is proposed in [44]. This study is to improve the shifting performance of the automatic transmission, while respecting the passengers comfort. This gear-shift optimization problem is formulated into a multi-objective optimization, and solved using objective weighting method (also known as Weighted-sum method). The multi-objective formulation will be utilized in this chapter to optimize both fuel economy and acceleration performance into the transmission design optimization.

The design of hybrid electric power-split vehicle is described in [45]. Apart from developing a systematic design methodology using a single planetary gearset, this study also evaluates the acceleration performance (0 to 100kph time) for the transmission design. The evaluation of the acceleration performance uses engine wide-open-throttle control (maximum engine torque). In this chapter, the engine also considers operating at maximum torque condition to evaluate the acceleration performance.

An automated modeling and screening process to design a double planetary gear

power split hybrid transmission is developed in [46]. While this study focused on designing the transmission for plug-in hybrid electric vehicles, it also mentioned that adding a clutch to the planetary gearset is beneficial for acceleration. However, the method to evaluate the acceleration performance assumes no battery power limitation. In this chapter, the acceleration of the vehicle will rely on the limited stored energy in the accumulator instead.

The design methodology in [47] is separated into light-load and full-load analyses. While the light-load analysis assesses the fuel efficiency of the transmission design, the full-load analysis computes the 0 to 100kph time and optimizes the design to improve acceleration performance. Similar to [45], maximum engine torque is assumed and vehicle acceleration is maximized. Maximum engine torque and maximum vehicle output torque strategy will be considered to evaluate the 0 to 100kph acceleration time in this chapter.

The studies in [45, 46, 47] involve evaluating the 0-100kph acceleration performance for hybrid vehicles, and [47] optimized the transmission design to improve acceleration performance. However, these studies did not incorporate the acceleration performance directly into the transmission design optimization for fuel efficiency. This motivates the study in this chapter to connect transmission design optimization for fuel efficiency and acceleration performance.

3.2 Acceleration Performance Evaluation

Unlike conventional powertrains where the engine has to provide all of the power, hybrid powertrains can utilize power from the accumulators to improve the 0-100kph acceleration time (t_{100kph}) performance. In the 0-100kph acceleration duty cycle, the accumulator charge is not required to return to its initial state for comparison. Due to the extra degree-of-freedom of a hybrid powertrain, the 0-100kph acceleration time optimization problem is formulated as follows:

$$\min_{(T_{whl}(\cdot),Q_{acc}(\cdot))} t_{100kph}(\omega_{eng}, T_{eng}) = \int_{t_0}^{t_f} 1dt \tag{3.1}$$

subjected to the constraints of:

$$\begin{aligned} v(t_0) &= 0m/s \\ v(t_f) &= 27.8m/s(100kph) \end{aligned}$$

and vehicle dynamic (in Sec. 2.6.1):

$$M\dot{v} = \frac{T_{whl}}{R_{tire}} - M \cdot g \left(f_0 + (3.24 \cdot f_s \frac{2.237}{100} v)^{2.5} \right) - \frac{1}{2} C_D A_f \rho_{air} v^2 \tag{3.2}$$

$$v = \omega_{whl} R_{tire} \tag{3.3}$$

and hybrid transmission is the input coupled power-split with kinematics (in Sec. 2.3):

$$\begin{aligned} \begin{pmatrix} \omega_{pm1} \\ \omega_{pm2} \end{pmatrix} &= \begin{pmatrix} r_{11} & 0 \\ r_{21} & r_{22} \end{pmatrix} \begin{pmatrix} \omega_{eng} \\ \omega_{whl} \end{pmatrix} \\ \begin{pmatrix} T_{pm1} \\ T_{pm2} \end{pmatrix} &= \begin{pmatrix} -1/r_{11} & r_{21}/(r_{11} r_{22}) \\ 0 & -1/r_{22} \end{pmatrix} \begin{pmatrix} T_{eng} \\ T_{whl} \end{pmatrix} \end{aligned} \tag{3.4}$$

and pump/motor torque and flow characteristics are given by:

$$\begin{aligned} T_{pm\,i}(t) &= \frac{P_{sys}(t) D_{max\,i}}{2\pi} x_{pm\,i}(t) - sgn(\omega_{pm\,i}) \cdot Loss_{mech,pm\,i}(x_{pm\,i}, \omega_{pm\,i}, P_{sys}) \\ Q_{pm\,i}(t) &= \frac{\omega_{pm\,i} D_{max\,i}}{2\pi} x_{pm\,i}(t) + Loss_{vol,pm*}(x_{pm\,i}, \omega_{pm\,i}, P_{sys}) \end{aligned}$$

and accumulator dynamic (in Eq. (2.15)):

$$\begin{aligned} P_{hi}(t) &= \frac{P_{pr} V_0}{V_0 - V_{acc}(t)} \\ P_{hi}(t_0) &= P_{hi,0} \\ \dot{V}_{acc}(t) &=: Q_{acc}(t) = -(Q_{pm1}(t) + Q_{pm2}(t)) \\ \underline{V_{acc}} &\leq V_{acc}(t) \leq \overline{V_{acc}} \end{aligned}$$

where t_{100kph} is the total time required for the vehicle to accelerate from rest to $100kph$, T_{whl} is the transmission output torque, Q_{acc} is the net flow into the accumulator, v is the vehicle speed in m/s, M is the vehicle mass, R_{tire} is the effective tire radius, $g = 9.81$

Parameter	Value
G	$\begin{pmatrix} 1.0175 & 0 \\ 2.0660 & -8.3570 \end{pmatrix}$
M	1000 kg
R_{tire}	0.31 m
f_0	0.0095
f_s	0.0035
C_D	0.5
A_f	1.784 m^2
$P_{pr,hi}$	11.0 MPa
$V_{0,hi,lo}$	38 L
$D_{max\,1,2}$	28.1 cc

Table 3.1: Reference vehicle parameters for acceleration evaluation example.

m/s^2 is the gravitational constant, $\rho_{air} = 1.29\ kg/m^3$ is the air density, $x_{pm\,i} \in [-1, 1]$ is the pump/motors' volumetric displacement, $\omega_{pm\,i}$ is the pump/motors' speed, P_{sys} is the system pressure, $Loss_{mech,pm\,i}$ is the pump/motor's torque loss, $Loss_{vol,pm\,i}$ is the pump/motor's flow loss, $P_{hi,0}$ is the initial condition for the high pressure accumulator, and V_{acc} is the hydraulic fluid volume in the accumulator. The low pressure is assumed to be constant of 1.38MPa (200psi). The system pressure is defined as $P_{sys} = P_{hi} - P_{lo}$.

To illustrate the behavior of the powertrain during the acceleration, an input coupled power-split hydraulic hybrid vehicle is selected as a reference hydraulic hybrid vehicle, and the attributes of the vehicle are described in Tab. 3.1. The engine model is as described in Sec. 2.6.1.

Assumptions made in this study are: (i) the high pressure accumulator is initially charged to its maximum capacity; i.e. 34.5 MPa (5000 psi) and its pre-charged pressure is 11.0MPa (1600psi), (ii) the desired engine speed is achieved instantaneously, and (iii) the engine is operating along the engine's maximum torque curve, $T_{eng} = T^*_{eng}(\omega_{eng})$, for any engine speed. Since fuel consumption is not optimized here, the engine is expected to operate at maximum torque. The accumulator capacity is 38L, sized to achieve high fuel efficiency in Ch. 2.

In order to evaluate the t_{100kph} in Eq. (3.1), the time-consuming DP solver is usually applied as will be discussed in Sec. 3.2.1. To address the computational overhead issue,

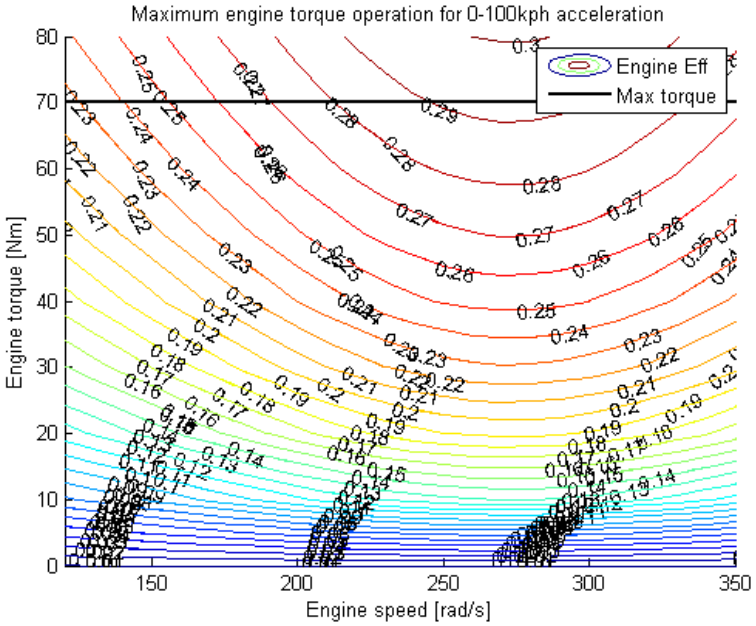

Figure 3.1: Engine maximum torque curve for evaluating acceleration performance.

a maximum output torque strategy in Sec. 3.2.2 is devised that significantly reduces the computation time. A constant engine power strategy is proposed in Sec. 3.2.3 to further simplify the acceleration time evaluation, and this strategy will be used to incorporate acceleration performance into the hybrid powertrain design optimization. The vehicle described in Tab. 3.1 will be used to compare the three different strategies.

3.2.1 Dynamic Programming (DP) Strategy

Dynamic programming is commonly used to solve the minimization problem in Eq. (3.1). Unlike the optimization problem in Ch. 2, the terminal time t_f of the 0-100kph acceleration duty cycle is unknown and needs to be optimized.

Consider the optimization problem in Eq. (3.1) re-formulated into a family of final vehicle speed optimization problems where the final time t_f increases from t_0:

$$\begin{aligned} \max_{T_{whl}(\cdot),Q_{acc}(\cdot)} \quad & \int_{t_0}^{t_f} \dot{\omega}_{whl}(T_{whl}, Q_{acc}, \omega_{whl}, P_{sys}, t)dt \\ \text{subjected to} \quad & \underline{V_{acc}} \leq V_{acc}(t) \leq \overline{V_{acc}} \end{aligned} \tag{3.5}$$

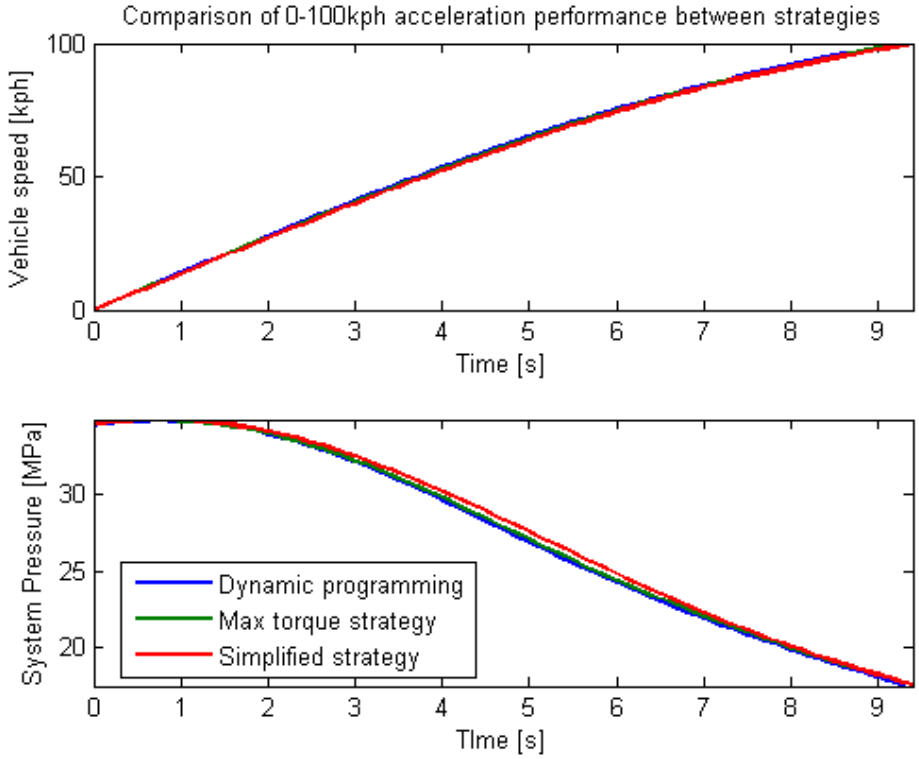

Figure 3.2: Comparison of 0-100kph acceleration performance between the three strategies.

The original problem in Eq.(3.1) is solved when the solution has reached t_f when the desired velocity is a feasible solution. Accumulator state-of charge and vehicle velocity are the two states involved in this dynamic programming. With this modification, regular dynamic programming can be applied forward in time by solving Eq. (3.5) iteratively from $t = t_0$ to increasing final times.

Figure 3.2 shows the optimal vehicle speed trajectory and accumulator charge usage solved using DP, achieving 0-100kph acceleration in 9.3 seconds. As seen in the figure, the accumulator is charged for approximately 1 sec due to the low vehicle speed and high engine power, and then discharged for maximum output torque. This DP problem is discretized with 0.1 sec sampling time and 0.014MPa (2 psi) accumulator pressure grid. Solving this problem using DP requires approximately 2 hours and 6 minutes to evaluate the best 0-100 kph acceleration time for each transmission design.

3.2.2 Maximum output torque strategy

As demonstrated previously, using DP to solve the minimization problem in Eq. (3.1) is very time-consuming, and acceleration performance is required to be evaluated for every design iteration. In order to rapidly evaluate the best t_{100kph}, the optimization problem is reduced to maximizing the instantaneous output torque. The original acceleration optimization in Eq. (3.1) is formulated into the following static optimization:

$$\max_{(\omega_{eng}, x_T, x_S)} T_{whl}(\omega_{eng}, T^*_{eng}(\omega_{eng}), x_T, x_S, P_{sys}(t), t) \tag{3.6}$$

where $T^*_{eng}(\omega_{eng})$ is the maximum engine torque for a specific engine speed, $P_{sys}(t)$ is the system pressure, and T_{whl} is the vehicle output torque. This strategy fully utilizes the accumulator energy storage to maximize the output torque of the transmission, achieving 0-100kph acceleration in 9.3 seconds. As seen in Fig. 3.2, the max-torque strategy has similar behavior in accumulator charge usage and similar vehicle speed trajectory compared to the DP strategy. The maximum output torque strategy computation requires approximately 2 seconds to complete, substantially faster than DP.

3.2.3 Constant engine power strategy

To further reduce the computational requirement to solve Eq. (3.1), the engine operating condition is constrained to constant engine speed and engine torque. The engine operating point is selected as $\bar{\omega}_{eng} = 251 rad/s$ and $\bar{T}_{eng} = 70 Nm$ based on the average engine speed and torque results obtained from max-torque strategy.

$$\max_{x_T, x_S} T_{whl}(\bar{\omega}_{eng}, \bar{T}_{eng}, x_T, x_S, P_{sys}(t), t) \tag{3.7}$$

Once again, Fig. 3.2 compares all three different strategies to achieve 0-100kph, and the accumulator charge usage for constant engine power strategy deviates only a maximum of $90 psi$ from the DP strategy. The constant engine power strategy achieves 0-100kph acceleration in 9.4 seconds, and requires 0.8 second of computation time. This strategy is only applicable if the same engine is used and not being optimized, and the transmission design is not significantly different from the reference transmission in Tab. 3.1.

3.3 Multi-objective Optimization

To exploit the power density advantage of hydraulics in automotive transmissions, the intuitive approach is to increase the pump/motors size to improve the 0-100kph performance, and sacrifice fuel efficiency in the meantime. Under such circumstances, a balanced trade-off between fuel economy and acceleration performance is crucial to guarantee both objectives are within acceptable performance for a specific transmission design.

In order to incorporate the acceleration performance (in Sec. 3.2) into the optimal fuel efficiency hybrid powertrain design in Chap. 2, a multi-objective (MO) optimization approach is utilized to solve design problems that contain conflicting objectives. A generic *multi-objective optimization problem* can be expressed in the following form:

$$\begin{aligned} \min_{\mathbf{x}} \quad & [J_1(\mathbf{x}), ..., J_k(\mathbf{x})] \\ \text{subjected to} \quad & \mathbf{x} \in S \end{aligned} \tag{3.8}$$

where $J_i : \Re^n \rightarrow \Re (i = 1, ..., k)$ is the objective functions, $\mathbf{x} \in \Re^n$ is the decision (variable) vector, and the set of feasible decision vectors is denoted as S. The *Pareto optimality* based on the problem in Eq. (3.8) is defined as [48, 49, 50]:

Definition 1. *A decision (variable) vector* $\mathbf{x}^* \in S$ *and an objective vector* $J(\mathbf{x}^*)$ *etc. is considered as* Pareto Optimal *if there does not exist another decision vector* $\mathbf{x} \in S$ *such that* $J_i(\mathbf{x}) \leq J_i(\mathbf{x}^*)$ *for all* $i = 1, ..., k$ *and* $J_i(\mathbf{x}) < J_j(\mathbf{x}^*)$ *for at least one index* j.

Definition 2. *The optimization problem Eq.* (3.8) *is* convex *in objective space if it satisfy the inequality*

$$J_i(\alpha x + \beta y) \leq \alpha J_i(x) + \beta J_i(y)$$

for all i, *all* $x, y \in \Re^n$ *and all* $\alpha, \beta \in \Re$ *with* $\alpha + \beta = 1$, $\alpha \geq 0$ *and* $\beta \geq 0$.

It is important to note that the goal of using multi-objective optimization in this study is not to find a single best design solution. Instead, it is to find a set of non-inferior designs that have different performance for the multiple objectives. In this powertrain design optimization problem, the goal is to generate the Pareto Frontier that satisfies the optimality of the objectives of minimizing the fuel economy J_{FE} and 0 to 100 km/h

acceleration time J_{100kph}. Any transmission design included within the generated Pareto Frontier is considered optimal.

The original multi-objective design problem of the transmission determines the design parameters $\nu = (G, D_{max1}, D_{max2})$ such that:

$$\begin{cases} \max_{\nu} J_{FE} & \text{in Sec. 2.4.2} \\ \min_{\nu} J_{100kph}(\nu) = t_{100kph}(\nu) & \text{in Sec. 3.2.3} \end{cases} \tag{3.9}$$

where the first objective function, J_{FE}, is the optimal fuel economy achieved by the powertrain for a design ν utilizing the optimized modes $\texttt{mode}^*$ and accumulator utilization as explained in Sec. 2.4.2.

While the second objective function, $J_{100kph}(\nu)$, as determined by the constant engine power, maximum output torque strategy in Sec. 3.2.3.

Unlike single objective (SO) problems that seek a single optimal solution, multi-objective problems involve finding a set of feasible optimal trade-off solutions, called the Pareto Frontier. External information is needed to decide which Pareto optimal solution is the 'preferred' solution. To solve multi-objective problems, various numerical methods are commonly used, for example converting the objectives into a single weighted function, genetic algorithm (GA), particle swarm optimization, Directed Search Domain (DSD), Pareto Surface Generation, etc ([49, 50, 51, 52]). Approaches such as genetic algorithms involve Monte Carlo simulations, which could be difficult and time-consuming. Here, two classical multi-objective optimization approaches, i.e. Weighted-Sum and ϵ-Constraint methods, are selected in this dissertation.

3.3.1 Weighted-Sum Method

In the *Weighted-Sum method* [49, 53], the multi-objective problem in Eq. (3.8) is converted to:

$$\begin{aligned} \min_{\mathbf{x}} \quad & \sum_{i=1}^{k} \omega_i J_i(\mathbf{x}) \\ \text{subjected to} \quad & \mathbf{x} \in S \end{aligned} \tag{3.10}$$

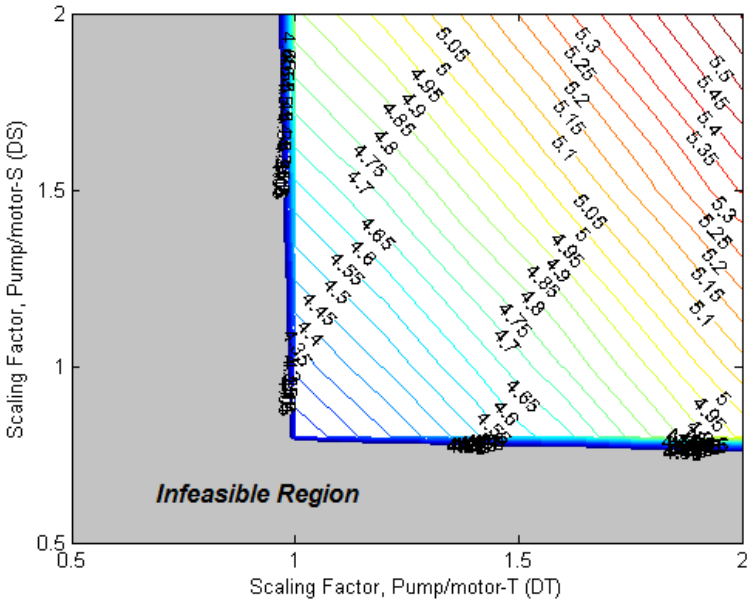

Figure 3.3: Fuel consumption [L/100km] through EPA combined drive cycle variation with different pump/motor sizes.

where $\omega_i \geq 0$ for all $i = 1, ..., k$ is the weighting factors, $\sum_{i=1}^{k} \omega_i = 1$, and $J_i(\mathbf{x})$ is the normalized objective functions. As proven in [49], the solution of Eq. (3.10) can be shown to be a unique Pareto optimal solution[1] :

Theorem 2. *If* $\mathbf{x}^*$ *is the Pareto optimal solution of the convex multi-objective problem in Eq.* (3.8)*, there exists non-zero positive weighting factors* $\omega_i \geq 0$, $\sum_{i=1}^{k} \omega_i = 1$ *such that* $\mathbf{x}^*$ *is the solution to Eq.* (3.8)*.*

The theorem shows that all Pareto solutions can be found by using the Weighted-Sum method if the multi-objective optimal problem in Eq. (3.8) is convex in the objective space. Also, it is highly advisable to normalize the objective functions such that different magnitudes of the objectives do not confuse the method, causing the method to bias certain objectives. Using a set of uniformly distributed weighting factors in this method does not guarantee uniformly distributed Pareto solutions, i.e. $J_i(x_k) \neq J_i(x_{k+1})$.

[1] A unique Pareto solution means there is no identical solution throughout the set of Pareto Frontier solutions.

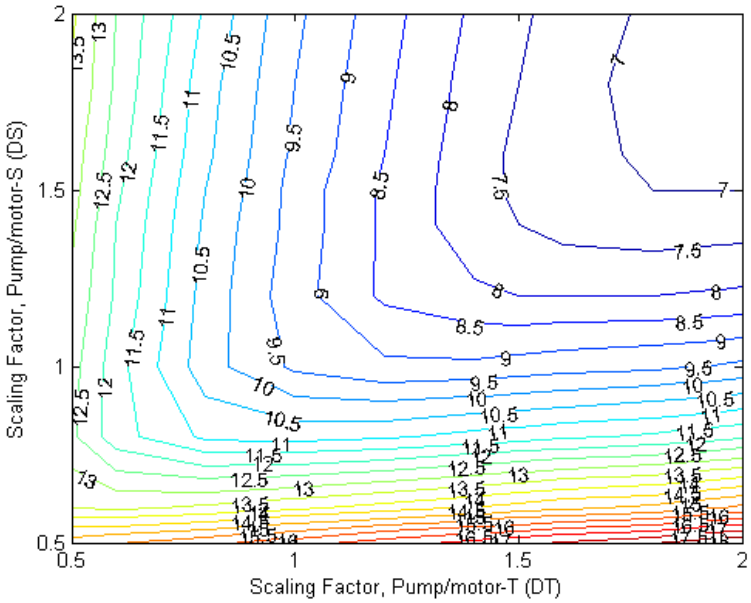

Figure 3.4: t_{100kph} [sec] variation with different pump/motor sizes.

A simplified case to optimize only the pump/motor sizes (D_{max1}, D_{max2}) of the transmission is investigated. As discussed in Ch. 2, the Lagrange Multiplier method assumes accumulator capacity is unconstrained and constant system pressure of 13.8MPa (2000psi). For each design (D_{max1}, D_{max2}), the Lagrange Multiplier method discussed in Ch. 2 is used to evaluate the fuel efficiency of the powertrain, and the constant engine power strategy in Sec. 3.2 is used to evaluate the acceleration performance. The effects of the pump/motors' sizing on fuel economy and acceleration performance are presented in Fig. 3.3 and 3.4, where the axes are showing the scaling factor of the reference pump/motor size of 28cc.

Expectedly, as shown in Fig. 3.3, the smaller the displacement of the pump/motors, the more efficient is the transmission. However, the sizing becomes infeasible when P/M-T is smaller than 28cc and P/M-S smaller than 22.4cc. The lower bound pump/motor sizes are influenced by the feasibility to follow the prescribed drive cycle. In contrast, using the method presented in Sec. 3.2, the acceleration performance improves as the pump/motor sizes increase. These conflicting objectives with respect to the design space provide an ideal application for the multi-objective optimization solvers. Figure 3.4 also

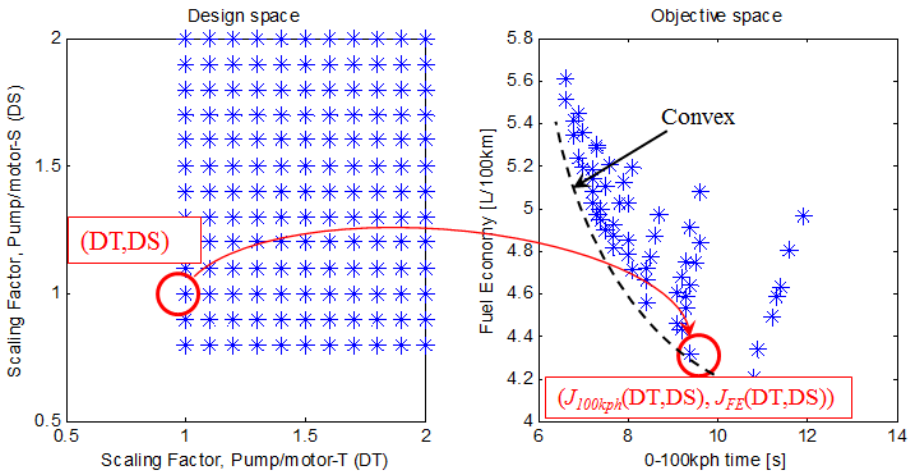

Figure 3.5: Mapping of the design space (DT, DS) to the objective space (J_{100kph}, J_{FE}).

shows that the feasible transmission design space for optimizing fuel economy and 0-100kph acceleration time can be different.

Figure 3.5 illustrates the mapping of the design space (DT, DS) from Fig. 3.3 and 3.4 to the objective space $(J_{100kph}(DT, DS), J_{FE}(DT, DS))$. Figure 3.5 indicates the objective space is convex, and the goal is to utilize the Weighted-Sum method to find the Pareto Frontier from the objective space.

In the Weighted-sum method, the problem in Eq. (3.9) is re-formulated into:

$$\min_{\nu} J_{WS}(wf) = \min_{\nu} \left[-(1 - wf) \cdot \frac{J_{FE}(\nu)}{nf_1} + wf \cdot \frac{J_{100kph}(\nu)}{nf_2} \right] \tag{3.11}$$

where for each wf, $J_{WS}(wf)$ is the weighted-sum of the two objective functions, weighting factor $wf \in [0, 1]$, and $nf_{1,2}$ are the normalizing factors for each objective. Normalizing factors are generally selected to be the largest feasible value of each cost function achievable.[2] By definition, the weighted-sum cost function J_{WS} is a convex combination[3] of both original objective functions. In this study, $nf_1 = 56.0$ and $nf_2 = 18.5$ from the pre-calculated objective cost in Fig. 3.3 and 3.4. Since all objective cost within the design space is computed, the minimization in Eq. (3.11) can be solved by direct

[2] The negative sign for J_{FE} is to convert maximization of the objective function into minimization.
[3] Geometrically, a convex combination is a linear combination of points where all coefficients are non-negative.

search for each wf[4] .

The optimization result of Eq. (3.11) is presented Fig. 3.6, showing this method is capable of generating the Pareto Frontier for this specific multi-objective problem within the design space. Note that several sample points are labeled with a range of wf values. This results from discretization of the design space: multiple choices for wf may yield the same design. To illustrate the meaning of Pareto Frontier in transmission optimization, the design space shown are feasible designs in Fig. 3.3. The design solutions to Eq. (3.11), i.e. the Pareto Frontier in Fig. 3.6, have the property of decreasing in one objective function when increasing another objective function. The trade-off between the objectives shows a typical Pareto Optimum.

Despite the advantages of simplicity and computational efficiency, this method suffers from several short-comings. The Weighted-sum method is only guaranteed to find unique solutions on the entire Pareto Frontier if the cost functions J_{FE}, J_{100kph} are convex in the objective space [51]. Thus, some of the potential candidates within the concave segment of the Pareto Frontier are missed and neglected by this method, as illustrated in Fig. 3.7. Also, uniformly distributed weighting factors do not guarantee uniformly distributed Pareto solutions. Multiple solutions may exist for a specific weighting factor that represent different designs in the Pareto Frontier, as illustrated in Fig. 3.6.

3.3.2 ϵ-Constraint Method

In order to address the short-comings of the Weighted-Sum method mentioned previously, the ϵ-Constraint method is another classical method that can be utilized to complement the Weighted-Sum method [49, 53]. In the ϵ-Constraint method, only one of the objective functions is optimized, while other objectives are converted into constraints. The multi-objective optimization problem is converted into:

$$\begin{aligned} & \min_{\mathbf{x}} J_j(\mathbf{x}) \\ \text{subjected to} \quad & J_i(\mathbf{x}) < \epsilon_i \quad \text{for all } i = 1, .., k, i \neq j \\ & \mathbf{x} \in S \end{aligned} \tag{3.12}$$

[4] Please note that direct search is only applied here to illustrate this example. Weighted-sum method does not require evaluating the entire design space.

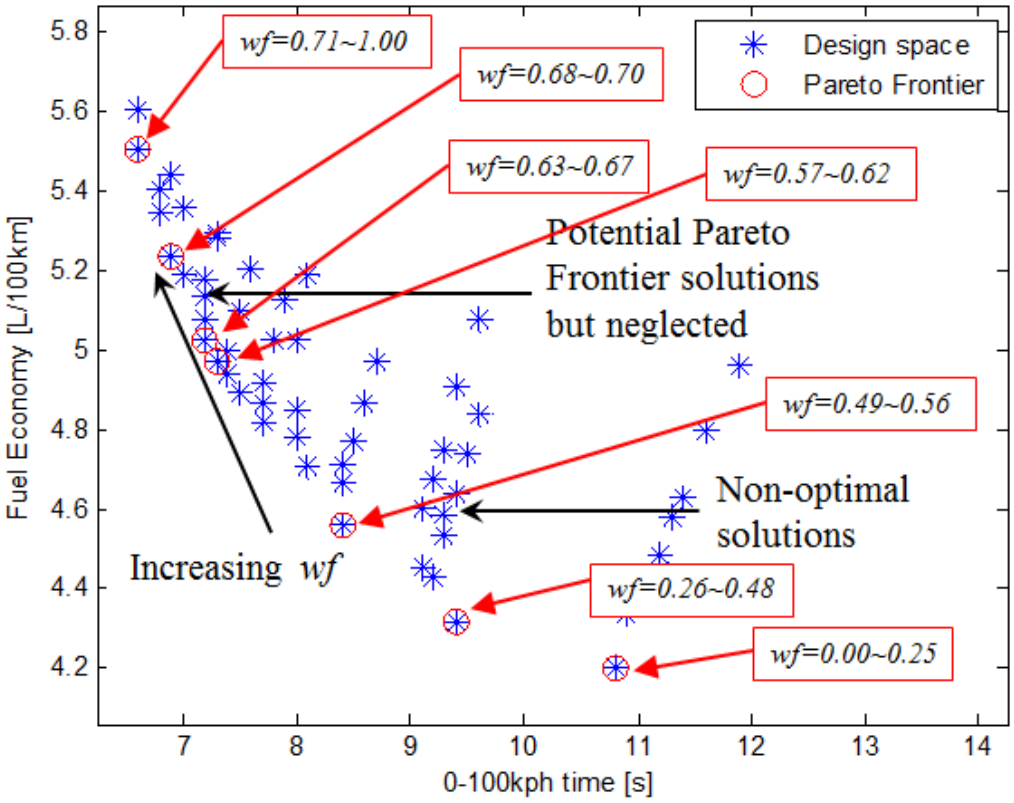

Figure 3.6: An example of generating Pareto frontier, solutions to Eq. (3.11), using weighted sum method from the pre-evaluated objective space ('o' points).

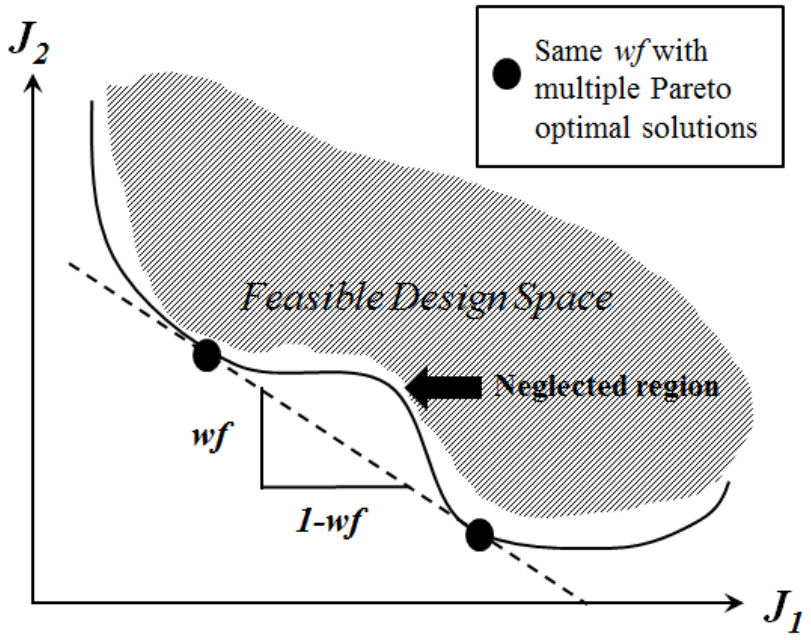

Figure 3.7: An illustration of the limitations on non-convex problems using weighted sum method.

where $j \in [1, ..., k]$ and ϵ_i is the upper bound for the objective $J_i (i \neq j)$. Again, a unique solution of Eq. (3.12) is proven to be Pareto optimal for any upper bounds [49, 53].

Theorem 3. *The solution* $\mathbf{x}^* \in \mathbf{S}$ *is Pareto optimal if and only if* $\mathbf{x}^*$ *solves the problem in Eq.* (3.12) *for every* $j = 1, ..., k$, *where* $\epsilon_i = J_i(\mathbf{x}^*)$ *for* $i = 1, .., k, i \neq j$.

Thus, it is required to solve k different problems to ensure Pareto optimality. The advantage of this method is that convexity of the objective space is not necessary to obtain a Pareto optimal solution. However in practice, it may be difficult to specify the upper bound ϵ_i such that $\epsilon_i = J_i(\mathbf{x}^*)$.

Since this transmission design problem is limited to only two objectives, it is proposed to modify the inequality objective constraints into equality constraints. The idea of this method is to optimize only one objective and restrict the rest of the objectives to some user-specified values ϵ. The multi-objective problem in Eq. (3.9) is then modified

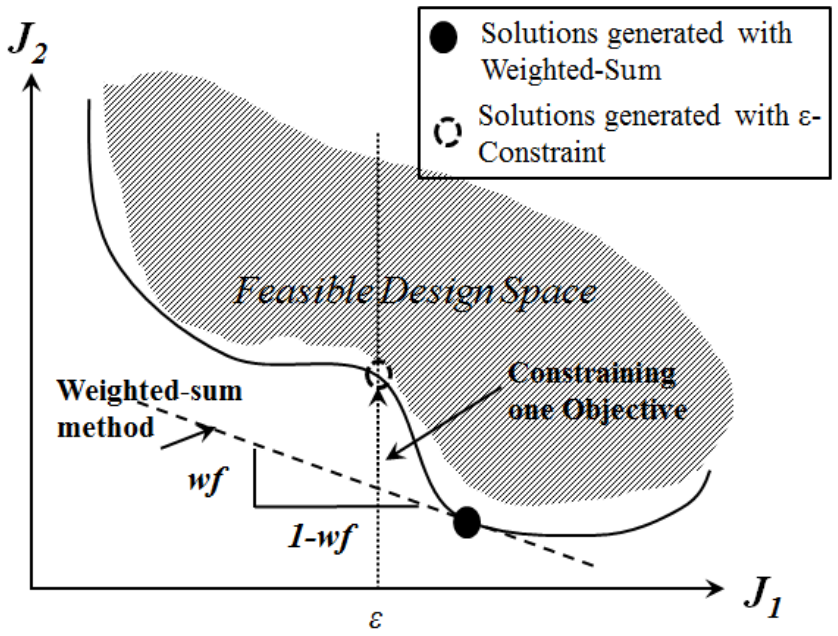

Figure 3.8: An illustration of using ϵ-Constraint method to complement the Weight-Sum method.

to the following:

$$\begin{aligned} & \min_{\nu} \left(-J_{FE}(\nu)\right) \\ \text{subjected to} \quad & J_{100kph}(\nu) - \epsilon = 0 \end{aligned} \tag{3.13}$$

where ϵ is the desired 0-100kph acceleration time for the transmission design. The ϵ-Constraint method optimizes one objective while constraining other objectives to a user-specified value. After using the Weighted-Sum method to generate the sketch of a Pareto Frontier, the ϵ-Constraint method can be utilized to generate the Pareto solutions at the concave section of the frontier, thus completing the Pareto-optimal solutions.

In order to solve Eq. (3.13), it is reformulated into:

$$\min_{\nu} J_{EC} = \min_{\nu} -J_{FE}(\nu) + \xi \cdot \left(J_{100kph}(\nu) - \epsilon\right)^2 \tag{3.14}$$

where J_{EC} is the augmented cost with the constraint function in Eq. (3.13), ξ is a

penalty coefficient set to a large value. Figure 3.8 depicts the use of the ϵ-Constraint method to complete the Pareto Frontier generation. By imposing the constraint ϵ, the optimization is performed only along the vertical line, searching for the Pareto optimum within the feasible design space.

In summary, the Weighted-Sum method is complemented by the ϵ-Constraint method in order to generate the Pareto optimal solutions, even if the multi-objective optimal problem in Eq. (3.9) is non-convex. The optimization process is summarized below:

1. Initialize transmission kinematics and pump/motor sizes (G, D_{max1}, D_{max2}).
2. Discretize the range of wf and determine the normalizing factors nf_i.
3. Solve the Weighted-Sum optimization in Eq. (3.11) for each wf to generate the Pareto Frontier.
4. Check if significant gaps are present between the solutions generated using the Weighted-Sum method.
5. Solve the ϵ-Constraint optimization in Eq. (3.14) for specific t_{100kph} if necessary to fill the gap of Weighted-Sum method solutions.
6. Select the transmission designs from the Pareto solutions that fulfills design specifications.

3.4 Case study: Generation I powertrain design

In this section, the methods of Sec. 3.3 are applied to optimize the HHPV transmission (including pump/motor sizes and gear ratios). In this case study, the transmission architecture is an input-coupled configuration, the design of the CCEFP Testbed 3 set-up. Instead of only optimizing the pump/motor sizes as illustrated in Sec. 3.3, all gear ratios and pump/motor sizes are considered in this study.

The multi-objective design optimization using Weighted-Sum method is formulated as:

$$\min_{\nu} J_{WS}(wf) = \min_{\nu} \left[-(1 - wf) \cdot \frac{J_{FE}(\nu)}{nf_1} + wf \cdot \frac{J_{100kph}(\nu)}{nf_2} \right] \tag{3.15}$$

where $\nu = (G, D_{max1}, D_{max2})$ is the tuple of design parameters mentioned in Sec. 2.5, where G is the upper diagonal transmission gear matrix and $D_{max1,2}$ is the maximum volumetric displacement of the pump/motors. $nf_1 = 75$ and $nf_2 = 19$ are the selected

normalizing factors for each objective[5] . As gear matrix G is optimized in this case, the normalizing factors differ from those in Sec. 3.3.1. $wf \in [0, 1]$ is the weighting factor. Fuel economy J_{FE} is evaluated using the Lagrange Multiplier method with constant system pressure assumed to be 15.2 MPa (2200 psi). Acceleration time from 0-100kph J_{100kph} is evaluated using the constant engine power strategy proposed in Sec. 3.2.3. In multi-objective optimization, different cost functions are treated as isolated problems, thus assumptions are made separately.

The multi-objective design optimization in Eq. (3.9) using ϵ-Constraint method is formulated as:

$$\min_{\nu} J_{EC} = \min_{\nu} \left[-J_{FE}(\nu) + \xi \cdot (J_{100kph}(\nu) - \epsilon)^2 \right] \tag{3.16}$$

where ϵ is the user specified t_{100kph} value, ξ is a penalty coefficient set to a large value, $\xi = 100$ in this case. Both Eqs. (3.15) and (3.16) are solved using the Matlab `fminsearch` function.

The result of the Weighted-Sum method ('+' points) is shown in Fig. 3.9. The Pareto Frontier resembles the trend shown in Fig. 3.6, with a fairly linear trade-off relationship between the two objectives. Also, even with uniformly distributed weighting factors, the Pareto optimums are not equally spaced. Even though the convexity of the transmission design problem cannot be guaranteed, the Pareto Frontier is approximately convex with a wide region of linearity between the two objectives. The plot shows the Pareto Frontier of the hydraulic hybrid powertrain design can be generated using the Weighted-Sum method even without using the complementary ϵ-Constraint method. The result of the ϵ-Constraint method ('o' points) shown in Fig. 3.9 coincides with the Pareto Frontier generated using the Weighted-Sum method.

As mentioned earlier in the Weighted-Sum method, a uniformly distributed set of weighting factors does not guarantee uniformly distributed optimal solutions. The uniformly distributed weighting factors map to two major clusters of Pareto-optimum at the extremum of both objectives. However, by refining the discretization of the weighting factors, a more complete outline of the Pareto Frontier is generated. Table 3.2 shows the optimum design parameters (ν) of the transmission with various weighting factors. $wf = 0.0$ shows the acceleration performance of the optimal design of input

[5] The normalizing factors are selected based on estimate of maximum values for each objective.

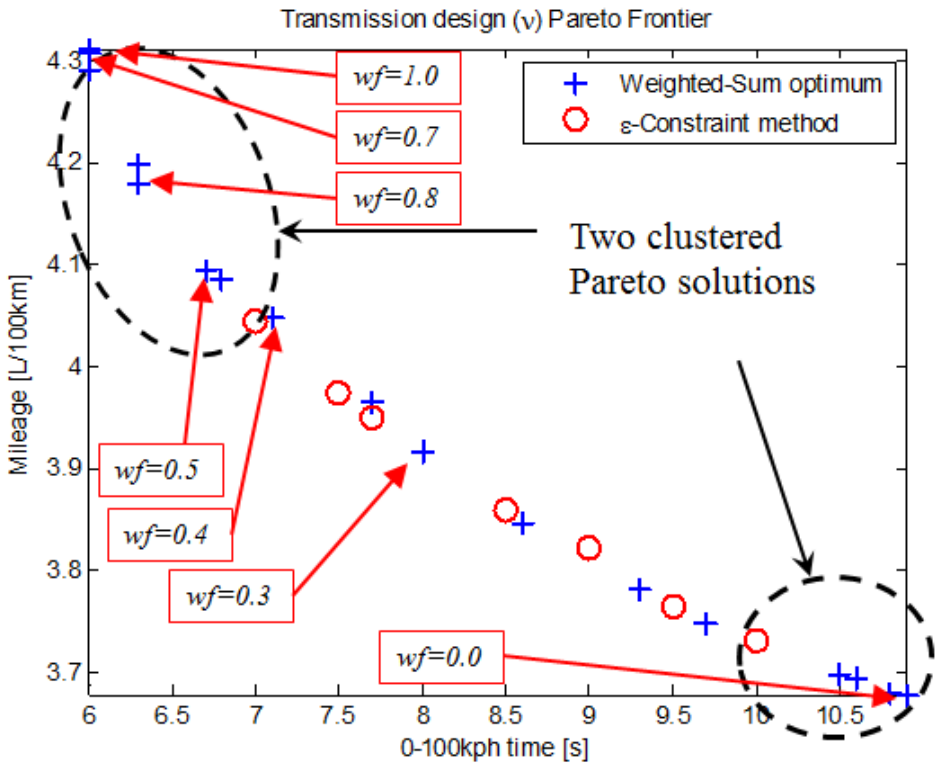

Figure 3.9: Multi-objective (Fuel economy and acceleration) Pareto frontier of the transmission design generated using the Weighted-sum and ϵ-Constraint methods.

wf	$FE[L/100km](mpg)$	$t_{100kph}[s]$	$G_{1,1}$	$G_{1,2}$	$G_{2,1}$	D_{maxT}	D_{maxS}
0.00	3.68 (64.0)	10.9	1.2051	2.3058	-9.5802	0.8072	0.8923
0.10	3.68 (63.9)	10.8	1.2659	2.2185	-9.2948	0.7613	0.9164
0.20	3.69 (63.7)	10.6	1.2652	2.2066	-9.4195	0.7615	0.9263
0.30	3.91 (60.1)	8.0	1.0734	1.8228	-10.3701	0.9300	1.1027
0.40	4.05 (58.1)	7.1	1.0558	1.6897	-11.0300	0.9623	1.2434
0.50	4.10 (57.4)	6.7	0.9659	1.5105	-10.5743	1.0492	1.3156
0.60	4.08 (57.6)	6.8	1.0227	1.6854	-11.2923	1.0089	1.2680
0.70	4.32 (54.5)	6.0	0.9980	1.3322	-10.3401	1.0624	1.7795
0.80	4.19 (56.2)	6.4	0.8914	1.2026	-8.9839	1.1586	1.7506
0.90	4.31 (54.6)	6.0	0.9300	1.1397	-8.7129	1.1003	1.7499
1.00	4.32 (54.5)	6.0	0.9980	1.3322	-10.3401	1.0624	1.7795

Table 3.2: Multi-objective optimization results with respect to various weighting factors ($wf \in [0, 1]$).

coupled architecture in Chap. 2. The result indicates that by sacrificing 15% of the fuel economy, the transmission design can reduce the 0-100kph acceleration time by 45%. This trade-off varies linearly throughout the range of wf. In order to achieve 45% faster acceleration time, P/M-T displacement is increased 32% and P/M-S displacement increased nearly 100%, substantially increasing the output torque capability.

In order to prove the ϵ-Constraint method is capable of complementing the Weighting-Sum method, several designs are optimized using the ϵ-Constraint method by constraining the acceleration performance to a specified value. Figure 3.9 and Tab. 3.3 shows that the Pareto-optimum generated using ϵ-Constraint method lies on top of the Pareto Frontier generated by Weighted-Sum method, confirming the effectiveness of this systematic procedure to optimize the design of the transmission with multiple objectives.

Discussions: Tables 3.2 shows a consistent trend of trade-off between the fuel economy and t_{100kph}. However, the variations for both objectives are not consistent with the monotonically increasing weighting factor, wf. At $wf = 0.70$ and $wf = 0.90$, both the fuel economy and t_{100kph} acceleration time are very similar, while the transmission design parameters for $wf = 0.70$ and $wf = 0.90$ are different (especially the matrix G). This suggests that the mapping of design space to the objective space is non-unique, yielding two non-unique designs that can achieve similar performance. This

Des. Param. ν	$FE[L/100km](mpg)$	$G_{1,1}$	$G_{1,2}$	$G_{2,1}$	D_{maxT}	D_{maxS}
$t_{100kph} = 7.0s$	4.04 (58.2)	1.0246	1.6278	-10.6992	0.9987	1.2449
$t_{100kph} = 7.5s$	3.97 (59.2)	0.9744	1.7452	-10.7369	1.0378	1.1262
$t_{100kph} = 7.7s$	3.95 (59.6)	0.9810	1.8449	-10.9015	1.0298	1.1043
$t_{100kph} = 8.5s$	3.86 (61.0)	0.9943	1.9399	-10.3541	1.0137	1.0008
$t_{100kph} = 9.0s$	3.82 (61.6)	1.2330	2.1150	-10.4200	0.8383	0.9341
$t_{100kph} = 9.5s$	3.76 (62.5)	1.0780	2.2774	-10.7864	0.9219	0.8466
$t_{100kph} = 10.0s$	3.79 (63.0)	1.0915	2.2872	-10.1969	0.9084	0.8813

Table 3.3: ϵ-Constraint method results with various t_{100kph}.

issue indicates the transmission optimization problem is non-convex.

Table 3.3 also shows a consistent trend of trade-off between the fuel economy and acceleration time. The gear ratios are fairly consistent throughout the range of t_{100kph}, indicating that the pump/motor sizes are dominating the design optimality. However, it is interesting to observe that the design solution for $t_{100kph} = 9.5sec$ has the smallest total pump/motor displacements.

As emphasized previously, the goal of multi-objective optimization is not to find a single best solution but a set of equally balanced solutions, called the Pareto Frontier. The Pareto Frontier helps narrowing the entire design space to a set of potential designs, and serves as a guideline to understand the consequences of how improving one objective function could affect the other objective function. For example in this case study, if the hybrid powertrain is desired to achieve better t_{100kph} acceleration time than $7.0sec$, transmission designs with $wf = [0.5, 0.6, 0.7, 0.8, 0.9, 1.0]$ are considered potential candidates, and the $wf = 0.6$-design may be the best choice due to its highest fuel economy and smaller pump/motor sizes.

Computational advantage: Using these classical methods of solving the multi-objective optimization, computational efficiency is not compromised and capable of accurately generating the Pareto Frontier. According to [54], the Weighted-Sum method is only computationally impractical when the number of objectives is above three. In our case, we are only interested in two objectives. For each weighting factor wf, the Weighted-Sum method requires approximately 3 mins to complete the design optimization, as opposed to the single objective optimization in Ch. 2 which takes approximately

2 mins. The ϵ-Constraint method is equally time-efficient: it requires approximately 3 mins to accomplish design optimization for each ϵ. This methodology to optimize the hydraulic hybrid powertrain for both fuel efficiency and acceleration performance is proven to be effective and time-efficient[6] . This method is not limited to the objectives studied in this chapter. It can easily be adapted to improve other performances such as vehicle top speed, towing capacity, etc.

3.5 Concluding Remarks

This chapter has presented a simplified 0-100kph acceleration time optimization and evaluation of a hydraulic hybrid powertrain, as the Dynamic Programming method would be approximately 120 times slower. Without using any advanced and complicated solver, such as Genetic Algorithm, the acceleration performance is integrated into the transmission design optimization. By formulating the design optimization problem into a multi-objective problem, and applying the classical Weighted-Sum method to generate the Pareto Frontier, a set of optimum designs with trade-offs between the objectives is produced.

The core of multi-objective optimization is that there is no single best solution, instead the Pareto Frontier is a set of equally optimal solutions. However, since the Weighted-sum method relies on the convexity of the problem to generate a complete Pareto-optimum set and the convexity of the transmission design problem cannot be guaranteed, another classical method of ϵ-Constraint can be utilized to complement the former method. A case study using the UMN-built transmission as a reference vehicle is investigated, and a complete set of Pareto Frontier solutions, considering the transmission kinematic relationship and pump/motor sizes, is successfully generated.

[6] Design optimization computation time depends on the initial design.

Chapter 4

Powertrain Uncertainties and Robust Optimal Design

From previous Ch. 2 and 3, the optimal design of the hybrid powertrain discussed so far is deterministic, meaning no uncertainty is considered, whether in manufacturing variation, operating condition variations or perhaps due to system modeling error. Generally, variation in manufacturing and environment affects the performance and quality of the designed system. Robust design is a mathematical approach to address the effect of these variations. This chapter will discuss the effect of torque loss uncertainty to the optimal control of the hydraulic hybrid powertrain, and robust optimal design of the hydraulic hybrid transmission.

This rest of this chapter is organized as follows: Section 4.1 presents a literature review of analyzing design uncertainties for mechanical systems. Section 4.2 presents the development of the uncertainty model for the hydraulic hybrid powertrain. Section 4.3 defines the transmission design feasibility under various uncertainties, and motivates the energy management strategy using worst-case variation to guarantee design feasibility. Section 4.4 presents the method and results of the robust optimal transmission design using worst-case variation. Section 4.5 defines the performance sensitivity of the design, and incorporates both objective functions using the Weighted-Sum method from previous chapter. Section 4.6 contains some concluding remarks for this robust design optimization chapter.

4.1 Review of Robust Optimal Design

For robust mechanical component design, several methods to account for design uncertainty to achieve robust reliability of the designed products are presented in [55, 56]. According to [55], the analysis of the reliability of a mechanical system should include three sections: (i) a physical model with mechanical properties of the system, (ii) feasibility condition for the particular system, where constraints of the system are not violated, and (iii) model of the uncertainties which can be incorporated in the system. This analysis process will be applied in this study to investigate the effect of uncertainties on the hydraulic hybrid powertrain system.

There are at least 7 methods for robust design mentioned in [56] that use engineering models to achieve robust design. The one approach discussed in most detail is the 'transmitted variation' method. This method estimates the transmitted variation using Taylor's series expansion and investigates the effect of the uncertainties to the nominal design. The nominal design can then be optimized based on the analysis to achieve either feasibility robustness or sensitivity robustness. For design parameters robustness, 'tolerance box' approach proves to be particularly useful and direct to obtain feasibility robustness, as the goal is to push the 'tolerance box' as close to the nominal optimal design without violating the constraints. This formulation is similar to [57], that is to evaluate the worst value of the function in the uncertainty set by searching for the worst case vertex of the 'tolerance box'. Similar worst-case approach will be applied in this chapter for robust optimal design.

For electromechanical devices, an approach of formulating multi-objective function that composed of mean and standard deviation to handle the manufacturing uncertainty is used in [58]. Gerald (2004) [57] minimized the worst case performance by converting the optimization problem into a min-max problem. Both studies utilized Sequential quadratic programming (SQP) to numerically solve the nonlinear robust optimal design problem, and this method proves to be useful for solving the robust optimization of the hybrid transmission in this chapter.

Apart from the manufacturing uncertainties, in hydraulic components, Yuan and Li (2007) [59] has presented a methodology to design a valve that makes use of the instability due to flow force, with respect to varying operating conditions. By converting the

mechanical valve design problem into controller design problem, one can apply the established robust control design technique, for instance H_∞ synthesis to solve the robust optimal design. In this study, uncertain properties of the unstable valve is captured by using Linear Fractional Transformation (LFT). The robust optimal valve design is formulated with upper and lower LFT. By synthesizing the optimal 'controller' as design parameters, specified robustness throughout various operating range is achieved. However, due to the nonlinearity of the hybrid powertrain system, this method will not be utilized in this study.

Kokkolaras et al. (2005) [60] presented the design of a medium truck with hydraulic hybrid powertrain and fuel cell auxiliary power unit under uncertainty. In this study, Monte Carlo simulation is used to analyze the propagation of uncertainty in the model and sensitivity of the design. Eventually, a series of reliability-based optimization is solved, that consist of an optimization loop and a reliability assessment loop nested in the formulation. An in depth investigation on engine uncertainty is conducted. It includes physical design (engine displacement, compression ratio, turbocharger, etc.) and thermodynamical variations (ambient temperature, heat transfer model, heat release correlation, etc.) that will essentially affect the efficiency of the engine operation. The uncertainty of frontal area, drag coefficient and other parameters of the vehicle are also being studied. However, there are no study of variation of the hydraulic transmission available which plays a crucial role in a passenger size hydraulic hybrid vehicle. This is considering that the engine loss will dominate the total loss of the hybrid powertrain. This study concluded that optimality of the design must be sacrificed to increase the reliability, and the relationship between optimality and reliability trade-off could be highly nonlinear. In this study, instead of modeling the uncertainties of the powertrain in details, the uncertainties of each component will be lumped into a single uncertainty, as multiplicative uncertainty to the powertrain loss model.

Developing an energy management strategy that considers model uncertainty has not been addressed in the literature. Uncertainties will affect the hybrid powertrain's overall performance and efficiency significantly, especially when operating under uncertainties. Energy management strategies synthesized to handle stochastic driver's demand are studied, including Stochastic Dynamic Programming [61], Model Predictive Control, etc. However, stochastic operating conditions are not accounted for, and the computational

effort for these strategies are extremely high.

The above literatures point to the gap between optimal transmission design and robust transmission design for a hydraulic hybrid passenger vehicle. This motivates the study in this chapter to connect the optimal and robust design, achieving the goal of devising a routine to systematically design a robustly optimal hydraulic hybrid power-split transmission.

4.2 Nominal Powertrain System and Powertrain Uncertainties

Each component of the powertrain may exhibit different uncertainties at various operating conditions that will affect the vehicle's performance and efficiency. Apart from designing the powertrain for its efficiency as described in Ch. 2, it is also crucial that the powertrain is robust against the uncertainties, and such that fuel efficiency is less sensitive to varying operating conditions. Characteristics of the powertrain uncertainties will be discussed in this section.

Before investigating the effect of the powertrain uncertainties, the nominal powertrain system will be discussed. Input coupled architecture design described in Ch. 2 will be used as the reference transmission in this chapter. Consider the input coupled power-split transmission kinematic relation:

$$\begin{pmatrix} \omega_{pmT} \\ \omega_{pmS} \end{pmatrix} = \begin{pmatrix} g_{11} & 0 \\ g_{21} & g_{22} \end{pmatrix} \begin{pmatrix} \omega_{eng} \\ \omega_{whl} \end{pmatrix} \tag{4.1}$$

$$\begin{pmatrix} T_{pmT} \\ T_{pmS} \end{pmatrix} = \begin{pmatrix} G_{T11} & G_{T12} \\ 0 & G_{T22} \end{pmatrix} \begin{pmatrix} T_{eng} \\ T_{whl} \end{pmatrix} \tag{4.2}$$

where $G_T = -g^{-\mathsf{T}}$.

The nominal torque model of the engine is expressed as:

$$T_{eng} = \frac{\dot{m}_f LHV(\omega_{eng}, T_{eng})}{\omega_{eng}} - Loss_{mech,eng}(\omega_{eng}, T_{eng}) \tag{4.3}$$

where T_{eng} is the nominal engine output torque, $\dot{m}_f$ is the fuel rate, LHV is the lower

heating value of the fuel, and $Loss_{mech,eng}$ is the engine torque loss. Thus, the nominal engine power loss $Loss_{eng}$ is defined as:

$$Loss_{eng}(\omega_{eng}, T_{eng}) = \omega_{eng} Loss_{mech,eng}(\omega_{eng}, T_{eng}) \tag{4.4}$$

And the nominal torque and flow model of the pump/motor are expressed as:

$$T_{pm\,i} = \frac{P_{sys} D_{max\,i}}{2\pi} x_{pm\,i} - sgn(\omega_{pm\,i}) Loss_{mech,pm\,i}(x_{pm\,i}, \omega_{pm\,i}, P_{sys}) \tag{4.5}$$

$$Q_{pm\,i} = \frac{\omega_{pm\,i} D_{max\,i}}{2\pi} x_{pm\,i} + Loss_{vol,pm*}(x_{pm\,i}, \omega_{pm\,i}, P_{sys}) \tag{4.6}$$

where $T_{pm\,i}$ is the nominal pump/motor torque, $Loss_{mech,pm\,i}$ is the pump/motor's torque loss, $Q_{pm\,i}$ is the nominal pump/motor flow, $Loss_{vol,pm\,i}$ is the pump/motor's volumetric loss. T_{eng}, T_{pmT}, T_{pmS} and T_{whl} have to satisfy the transmission torque relation in Eq. (4.1).

Similar to Ch. 2, the pump/motor's nominal power loss $Loss_{pm\,i}$ is defined as:

$$Loss_{pm\,i}(x_{pm\,i}, \omega_{pm\,i}, P_{sys}) = P_{sys} Loss_{vol,pm\,i} + sgn(\omega_{pm\,i}) \omega_{pm\,i} Loss_{mech,pm\,i} \tag{4.7}$$

where $Loss_{pm\,i} = \infty$ is defined for $|\omega_{pm\,i}(t)| > \omega_{pm,max}$ or $|x_{pm\,i}(t)| > 1$, such that the operation of components is constrained within its operating range. The high pressure accumulator as energy storage can be described as:

$$P_{hi}(t) = \frac{P_{pr} V_0}{V_0 - V_{acc}(t)} \tag{4.8}$$

$$\dot{V}_{acc}(t) =: Q_{acc}(t) = -\sum_{i=1}^{2} Q_{pm\,i}(t) \tag{4.9}$$

where P_{pr} is the pre-charge pressure of the accumulator, V_0 is the accumulator volume, V_{acc} is the hydraulic fluid volume in the accumulator, and Q_{acc} is the flow into the accumulator. With the low pressure P_{lo} assumed to be constant, the system pressure is defined as $P_{sys} =: P_{hi} - P_{lo}$.

Uncertainty in the powertrain systems may have several origins. Examples include: imperfections of the measurements when characterizing the engine and pump/motors,

unmodelled powertrain dynamics, inaccurate parameters of the powertrain model, variations in the operating conditions, etc. Discussion of the powertrain's loss variation in this study will include two major aspects:

1. **Variations of the powertrain's operating conditions throughout the duty cycle.** Pressure, temperature, viscosity, speed, load, etc. have direct influence on the performance and efficiency of the components, especially the engine and hydraulic pump/motors in this case. Unlike manufacturing uncertainties, uncertainty of the operating conditions is caused by uncontrollable variations outside of laboratory. For example, the ambient temperature fluctuates widely throughout the year and will affect the performance of the powertrain. Operating temperature is an important attribute that affects the efficiency of engine and hydraulic components. As hydraulic viscosity is highly dependent on temperature (viscosity decreases as temperature rises), the fluid viscosity will generally affect the component's leakage and friction. Thus, the variation of temperature will eventually cause variation in efficiency.

2. **Modeling error of the losses of the powertrain's components.** Despite that engine and hydraulic components' efficiencies are influenced by the operating conditions, the accuracy of the loss models obtained from laboratory test has its limitation. Even under stable controllable operating conditions, the measurements may not be perfectly accurate to construct the powertrain model. Moreover, the powertrain model presented considers no inertial dynamics and transient effects, which may have significant impact on instantaneous fuel consumption and emissions [62, 63].

Lumped uncertainty: In this chapter, uncertainties due to various causes mentioned previously are combined into one single lumped perturbation to the nominal system. Hybrid powertrain loss uncertainty will be quantified as a uniformly distributed multiplicative uncertainty for the engine, P/M-T, and P/M-S for a range of $\Delta = [\Delta_{eng}, \Delta_{pmT}, \Delta_{pmS}]$. $\Delta \in S$ is the multiplicative uncertainty, where S is the uncertainty set for $\Delta_{eng} \in [-\Delta_{eng,max}, +\Delta_{eng,max}]$, and $\Delta_{pm\,i} \in [-\Delta_{pm\,i,max}, +\Delta_{pm\,i,max}]$.

Unlike the study conducted in [60], the engine uncertainties in this study will not be modeled in details. Instead, it will focus on loss model variation, lumping all engine

parameters uncertainties that essentially mapped to efficiency variation. Thus, the engine loss variation is described as:

$$\Delta_{eng} \in [-\Delta_{eng,max}, +\Delta_{eng,max}]$$

Thus, the engine power variation due to the engine torque loss variation is modelled as:

$$\omega_{eng}(T_{eng} + \Delta T_{eng}) = \dot{m}_f LHV - \omega_{eng} Loss_{mech,eng}(\omega_{eng}, T_{eng})(1 + \Delta_{eng})$$

where ΔT_{eng} is the engine torque variation.

Similarly for the hydraulic components, different system pressure, temperature, and viscosity will affect the pump/motor efficiency. Gear mesh efficiency also vary at different speed and torque. For simplicity, gear mesh are considered lossless, and gear mesh losses are lumped into the losses of hydraulic units. Therefore, the pump/motors loss variation is described as:

$$\begin{aligned} \Delta_{pmT} &= \Delta_{pmS} \\ \Delta_{pm\,i} &\in [-\Delta_{pm\,i,max}, +\Delta_{pm\,i,max}] \end{aligned}$$

Thus, the pump/motor torque variation is modelled as:

$$T_{pm} + \Delta T_{pm} = \frac{P_{sys} D x_{pm}}{2\pi} - sgn(x_{pm}) Loss_{mech,pm}(x_{pm\,i}, \omega_{pm\,i}, P_{sys})(1 + \Delta_{pm})$$

The assumptions made in this chapter can be summarized as:

1. **Only torque loss uncertainty of components is considered.** The powertrain loss uncertainties affects only the torque characteristic of the engine and pump/motors for a specific (x_S, ω_S, P_{sys}). Flow characteristic of the pump/motor is neglected in this study.
2. **Input coupled architecture is assumed.** For simplicity, only input coupled architecture design described in Ch. 2 will be used as the reference transmission in this study.
3. **System pressure is assumed constant and accumulator capacity is unconstrained.** Similar to Ch. 2, it is assumed that the system pressure of the

transmission is constant and accumulator capacity is unconstrained in order to apply Lagrange Multiplier method for energy management.

4. **Inertial dynamics are neglected.** Similar to Ch. 2, the transmission design procedure neglects the inertial dynamics of the hybrid powertrain's components. As a result, the desired operating conditions of the engine and pump/motors are assumed to be achieved instantaneously.
5. **Operating modes of the hybrid powertrain assumed.** The four operating modes defined in Ch. 2, i.e. `HMT`, `Parallel`, `P/M-T only`, and `P/M-S only` modes, will be utilized in this study to restrict the engine operation.

4.2.1 Transmission Design Feasibility

Due to the uncertainties, a specific transmission design may not be able to fulfill designer's requirement, hence the design is infeasible. Feasibility of the transmission is defined as the powertrain must be able to fulfill the demanded vehicle output conditions. Demanded vehicle output conditions in this case is referred to as a specified drive cycle speed ω_{cyc}, and the vehicle output torque required to achieve the speed and acceleration T_{cyc}.

Definition 3. *The powertrain design is feasible if there exist control input over the range of* $t \in [t_0, t_f]$*, such that the output speed and torque match the desired drive cycle:*

$$(\omega_{whl}(t), T_{whl}(t)) = (\omega_{cyc}(t), T_{cyc}(t))$$

subjected to the hybrid powertrain model in Eqs. (4.1) $\sim$ (4.9)*.*

With transmission design feasibility defined, *the hybrid powertrain is said to be robustly feasible if there exist a feasible transmission design* $\nu = (G_\omega, D_{maxT}, D_{maxS})$ *under the range of uncertainty* $\Delta \in [-\Delta_{max}, +\Delta_{max}]$*.*

4.2.2 Perturbation of Hybrid Powertrain Losses

With the variation of engine and pump/motors torque modelled as multiplicative uncertainty, the loss and torque variations of each components can be determined. The

engine torque output variation can be expressed as:

$$\Delta T_{eng} = -\Delta_{eng}(t) Loss_{mech,eng}(\omega_{eng}, T_{eng}) \tag{4.10}$$

Similarly, the pump/motors torque variation can also be expressed as:

$$\Delta T_{pm} \quad = \quad -sgn(\omega_{pm}) \Delta_{pm} Loss_{mech,pm} \tag{4.11}$$

where ΔT_{pm} is the pump/motor torque variation, $\Delta_{pm} \in [-\Delta_{pm,max}, +\Delta_{pm,max}]$ is the pump/motor torque loss variation, and P_{sys} is the system pressure. The power loss variation of the pump/motor is expressed as:

$$\Delta Loss_{pm} = -sgn(\omega_{pm}) \omega_{pm} \Delta_{pm} Loss_{mech,pm} \tag{4.12}$$

Operating Mode Losses: The losses when operating at various operating modes defined in Sec. 2.4.1 can be modified to include the torque variation with respect to the multiplicative powertrain loss uncertainty, where total losses in the four operating modes are expressed as follows:

$$\hat{Loss}_{mode}(t, \texttt{HMT}, \Delta) = Loss_{eng}(\omega^*_{eng}, T^*_{eng})(1 + \Delta_{eng}) +$$
$$Loss_{pmT}(\omega^*_{eng}, T^*_{eng}, T_{whl}, P_{sys})(1 + \Delta_{pmT}) + Loss_{pmS}(\omega_{whl}, T_{whl}, P_{sys})(1 + \Delta_{pmS})$$

where $\hat{Loss}_{mode}(t, \texttt{HMT})$ is the perturbed powertrain loss for `HMT` mode.

$$\hat{Loss}_{mode}(t, \texttt{parallel}, \Delta) = Loss_{eng}(\omega_{eng}(\omega_{whl}(t)), T_{eng,max})(1 + \Delta_{eng})$$
$$+Loss_{pmT}(\omega_{eng}, T_{whl}, P_{sys})(1 + \Delta_{pmT})$$

where $\hat{Loss}_{mode}(t, \texttt{parallel}, \Delta)$ is the perturbed powertrain loss for `Parallel` mode.

$$\hat{Loss}_{mode}(t, \texttt{P/M} - \texttt{T}, \Delta) = Loss_{pmT}(\omega_{whl}, T_{whl}, P_{sys})(1 + \Delta_{pmT})$$

where $\hat{Loss}_{mode}(t, \texttt{P/M} - \texttt{T}, \Delta)$ is the perturbed powertrain loss for `P/M-T` mode.

$$\hat{Loss}_{mode}(t, \texttt{P/M} - \texttt{S}, \Delta) = Loss_{pmS}(\omega_{whl}, T_{whl}, P_{sys})(1 + \Delta_{pmS})$$

where $\hat{Loss}_{mode}(t, \mathtt{P/M-S}, \Delta)$ is the perturbed powertrain loss for `P/M-S` mode.

Accumulator flow of each operating mode can be expressed as:

$$Q_{acc}(t, \mathtt{mode}, \Delta) = -\sum_{i=1}^{2} Q_{pm\,i}(t, \mathtt{mode}, \Delta_{pm\,i})$$

Note that even though flow loss variation is not considered in this study, pump/motor's displacement $x_{pm\,i}$ will have to be adjusted in order to compensate for torque variations. As a result, pump/motor flow is indirectly affected by torque variation $\Delta_{pm\,i}$, hence the net flow into the accumulator $Q_{acc}(t, \mathtt{mode}, \Delta)$ is affected by the torque variation.

In this chapter, the main motivations to understand the uncertainties within the hybrid powertrain system are:

1. To ensure robust feasibility of the transmission design with respect to the specified uncertainty set.

2. To reduce the sensitivity of fuel efficiency of the hybrid powertrain with respect to the uncertainties.

4.3 Energy Management Synthesis

The uncertainties representation so far allows the analysis of the effect of uncertainty on the perturbed powertrain losses at each instantaneous time. However, throughout the specific drive cycle, the uncertainty Δ could vary within the specified range of $[-\Delta_{max}, +\Delta_{max}]$. Moreover, the hybrid powertrain offers extra degree of freedom, the transmission output conditions can be met with different combination of engine power and hydraulic power. This flexibility could potentially give the powertrain more robustness against uncertainties in achieving the output conditions. To address this ambiguity, it is desired to formulate the energy management to handle the uncertainties, thus making the specific design to be feasible by changing the controller.

Under such circumstances, the definition of *robust feasibility of the hybrid powertrain* is modified to

Definition 4. *For a specific transmission design $\nu = [G_\omega, D_{maxT}, D_{maxS}]$, and for every uncertainty $\Delta \in S$, there exist control inputs such that the hybrid powertrain*

design is able to fulfill the desired powertrain output conditions $(\omega_{whl}(t), T_{whl}(t)) = (\omega_{cyc}(t), T_{cyc}(t))$ *with respect to the uncertainty* $\Delta \in S$*, where* Δ *is unknown to the controller.*

Without considering the uncertainties in powertrain loss, the nominal optimal energy management strategy control law described in Ch. 2 is expressed as:

$$\begin{aligned} \lambda^*(\Delta = 0) &= \arg\max_{\lambda} \int_{t_0}^{t_f} \min_{\texttt{mode}(t)} [Loss_{mode}(t, \texttt{mode}(t), \Delta = 0) \\ &+ \lambda \cdot P_{sys} Q_{acc}(t, \texttt{mode}(t), \Delta = 0)] dt \end{aligned} \tag{4.13}$$

where λ^* is the optimal Lagrange Multiplier for the nominal design of the transmission, $Loss_{mode}(\texttt{mode}(t))$ is the nominal powertrain loss for a specific $\texttt{mode}$. And therefore

$$\texttt{mode}^*(t) = \arg\min_{\texttt{mode}(t)} [Loss_{mode}(t, \texttt{mode}(t), \Delta = 0) + \lambda \cdot P_{sys} Q_{acc}(t, \texttt{mode}(t), \Delta = 0)]$$

With the powertrain uncertainties modelled in Sec. 4.2, the perturbed powertrain loss under the nominal optimal energy management strategy is described as:

$$\begin{aligned} \texttt{mode}^*(t, \Delta) &= \min_{\texttt{mode}(\cdot)} [\hat{Loss}_{mode}(t, \texttt{mode}(t), \Delta) \\ &+ \lambda^*(\Delta = 0) \cdot P_{sys} Q_{acc}(t, \texttt{mode}(t), \Delta)] dt \end{aligned} \tag{4.14}$$

where Δ is the uncertainty in losses, and Δ is assumed known.

Recall from Ch. 2, the Lagrange Multiplier method is utilized to satisfy the terminal equality condition such that

$$\int_{t_0}^{t_f} P_{sys} Q_{acc}(t, \texttt{mode}^*(t), \Delta = 0) dt = 0$$

However, as mentioned previously, the net flow into the accumulator is indirectly affected by the torque variation $\Delta_{pm\,i}$. In a situation where the uncertainty is unknown, using the nominal energy management controller cannot guarantee the equality constraint to be fulfilled, i.e.

$$\int_{t_0}^{t_f} P_{sys} Q_{acc}(t, \texttt{mode}^*, \Delta) dt \neq 0 \tag{4.15}$$

Since the Lagrange Multiplier method does not take the variation into account, it is not guaranteed that the equality constraint of the perturbed system can be fulfilled. The powertrain output conditions are considered to be a strictly satisfied equality constraint (by feedback control in implementation).

Equality constraints for energy management: Equality constraints in robust design optimization are considered generally difficult to be handled as mentioned in [64, 65]. Under stochastic conditions of the parameter, equality constraints can generally be categorized into soft constraints and hard constraints.

According to [65, 66], *soft constraints* are defined as the constraints that are not necessarily satisfied due to stochastic conditions; while *hard constraints* are defined as the constraints that must be satisfied even under stochastic conditions. Soft constraints can be handled in two ways. One is constraint relaxation, i.e. the constraints are satisfied within a bounded value. Another way is satisfying mean condition, i.e. only the expected value of the states satisfy the constraints. Since hard constraints must be satisfied, other parameters will not be independent in order to fulfill the equality constraints, or remove the hard equality constraint through substitution [65].

The terminal constraint of the energy management strategy

$$\int_{t_0}^{t_f} P_{sys} Q_{acc}(t, \texttt{mode}^*(t), \Delta) dt = 0$$

and the powertrain output conditions constraint

$$(\omega_{whl}(t), T_{whl}(t)) = (\omega_{cyc}(t), T_{cyc}(t))$$

are considered as hard constraints. As the drive cycle must be followed by the powertrain, the variations in loss will be reflected in accumulator storage, as seen in Eq. (4.16).

$$\begin{aligned} &\int_{t_0}^{t_f} [Loss_{mode}(t, \texttt{mode}^*(t), \Delta = 0) + \Delta_{loss}(t) \\ &+ P_{sys} Q_{acc}(t, \texttt{mode}^*(t), \Delta = 0) + \Delta_{Pacc}(t)] dt = \int_{t_0}^{t_f} \omega_{cyc} T_{cyc} dt \end{aligned} \tag{4.16}$$

where $Loss_{mode}(t, \texttt{mode}^*(t), \Delta = 0)$ is the nominal powertrain loss, $P_{sys} Q_{acc}(t, \texttt{mode}^*(t), \Delta = 0)$ is the nominal accumulator power, $\Delta_{loss}(t, \texttt{mode}^*(t), \Delta) = \Delta Loss_{eng} + \Delta Loss_{pmT} +$

$\Delta Loss_{pmS}$ is the powertrain loss variation, and $\Delta_{Pacc}(t, \texttt{mode}^*(t), \Delta)$ is the accumulator power variation. At the same time, the equality constraint is to ensure a fair comparison of the best fuel efficiency of each design with optimal energy management. Without considering the variations in the energy management, the equality constraints will not be met and hence comparison would not be fair.

Prescribed uncertainty variations: Christopher (2003), Sirisha (2007) and Messac (2002) [65, 66, 67] mentioned the difference and importance of prescribed and non-prescribed variations in robust design optimization. For non-prescribed variations, the variation of uncertain parameters is optimized in order to further improve the efficiency or robustness of the design. However, the purpose of this study is to understand how the variations will impact the feasibility and efficiency of the hybrid powertrain. *Hence, the uncertainties of the powertrain losses and operating conditions are considered prescribed variations.* This means Δ is 'known' by the controller, allowing the equality constraints to be fulfilled. Therefore, in the presence of Δ, λ^* is computed as:

$$\lambda^* = \arg\max_{\lambda} \min_{\texttt{mode}(\cdot)} \int_{t_0}^{t_f} [\hat{Loss}_{mode}(\texttt{mode}(t), \Delta) + \lambda \cdot P_{sys} Q_{acc}(\texttt{mode}(t), \Delta)] dt$$

and the constraints are satisfied as

$$\int_{t_0}^{t_f} P_{sys} Q_{acc}(t, \texttt{mode}(t), \Delta) dt = 0$$
$$(\omega_{whl}(t), T_{whl}(t)) = (\omega_{cyc}(t), T_{cyc}(t))$$

4.3.1 Worst-Case Uncertainty Condition

It is crucial that the energy management controller can guarantee the feasibility of the transmission design within the range of prescribed uncertainties.

Proposition 2. *The feasibility of a specific hybrid transmission design is guaranteed if there exist an energy management controller for the worst-case set of uncertainties, where* $\Delta = \Delta_{max} = [|\Delta_{eng,max}|, |\Delta_{pmT,max}|, |\Delta_{pmS,max}|]$.

Proof: As described earlier, the uncertainties of the powertrain loss are translated into torque variation of the powertrain components, seen in Eq. (4.10) and (4.11).

From kinematic point of view, assuming measurements are available and feedback control on the engine speed and transmission output shaft speed, the pump/motors' speeds are assumed to be uncertainty-free, where Eq. (4.1) is exact. Uncertainty only enters in the torque relationship in Eq. (4.2):

$$\begin{pmatrix} \omega_{pmT} \\ \omega_{pmS} \end{pmatrix} = G_\omega \begin{pmatrix} \omega_{eng} \\ \omega_{whl} \end{pmatrix} \tag{4.17}$$

$$\begin{pmatrix} T_{pmT} + \Delta T_{pmT} \\ T_{pmS} + \Delta T_{pmS} \end{pmatrix} = G_T \begin{pmatrix} T_{eng} + \Delta T_{eng} \\ T_{whl} \end{pmatrix} \tag{4.18}$$

By analyzing each pump/motors individually, and recall drive cycle is hard constraint $(\omega_{whl}, T_{whl}) = (\omega_{cyc}, T_{cyc})$,

$$T_{pmT} + \Delta T_{pmT} = G_{T11}(T_{eng} + \Delta T_{eng}) + G_{T12} T_{cyc} \tag{4.19}$$

$$T_{pmS} + \Delta T_{pmS} = G_{T22} T_{cyc} \tag{4.20}$$

Substituting with Eqs. (4.10) and (4.11), the P/M-T torque and engine torque are related to T_{cyc} as

$$\begin{aligned} T_{cyc} &= (\frac{P_{sys} D x_{pmT}}{2\pi} - sgn(\omega_{pmT}) Loss_{mech,pmT}(1 + \Delta_{pmT}))/G_{T12} \\ &- (\frac{\dot{m}_f LHV}{\omega_{eng}} - Loss_{mech,eng}(1 + \Delta_{eng}))G_{T11}/G_{T12} \end{aligned} \tag{4.21}$$

and P/M-S torque is related to T_{cyc} as

$$T_{cyc} = (\frac{P_{sys} D x_{pmS}}{2\pi} - sgn(\omega_{pmS}) Loss_{mech,pmS}(1 + \Delta_{pmS}))/G_{T22} \tag{4.22}$$

Consider the maximum torque can be delivered by the engine and pump/motors, where $x_{pmT,S} = 1$ and $\dot{m}_f = \dot{m}_{f,max}$, the drive cycle torque (T_{cyc}) has to be smaller than the

maximum provided output torque,

$$
\begin{aligned}
|T_{cyc}| \;\leq\; & |(\frac{P_{sys}D}{2\pi} - sgn(\omega_{pmT})Loss_{meach,pmT}(1+\Delta_{pmT}))/G_{T12} \\
& -(\frac{\dot{m}_{f,max}LHV}{\omega_{eng}} - Loss_{mech,eng}(1+\Delta_{eng}))G_{T11}/G_{T12}| \qquad (4.23) \\
|T_{cyc}| \;\leq\; & |(\frac{P_{sys}D}{2\pi} - sgn(\omega_{pmS})Loss_{mech,pmS}(1+\Delta_{pmS}))/G_{T22}| \qquad (4.24)
\end{aligned}
$$

Therefore, *the transmission design is feasible only if the inequality condition in Eqs.* (4.23) *and* (4.24) *hold.* To guarantee the transmission is feasible for all defined loss uncertainty, the inequality condition in Eqs. (4.23) and (4.24) has to hold when losses variation are the worst, i.e. $\Delta_{eng} = \Delta_{eng,max}$, $\Delta_{pmT} = +\Delta_{pmT,max}$ or $\Delta_{pmT} = -\Delta_{pmT,max}$, and $\Delta_{pmS} = +\Delta_{pmS,max}$ or $\Delta_{pmS} = -\Delta_{pmS,max}$.

In another word, when vehicle is driving forward $T_{cyc} < 0$, $\Delta_{eng} = \Delta_{eng,max}$ and $\Delta_{pmT} = \Delta_{pmT,max}$. While $\Delta_{pmS} = +\Delta_{pmS,max}$ for $\omega_S < 0$, or $\Delta_{pmS} = -\Delta_{pmS,max}$ for $\omega_S > 0$. When vehicle is braking $T_{cyc} > 0$, $\Delta_{eng} = \Delta_{eng,max}$ and $\Delta_{pmT} = -\Delta_{pmT,max}$. While $\Delta_{pmS} = +\Delta_{pmS,max}$ for $\omega_S > 0$, or $\Delta_{pmS} = -\Delta_{pmS,max}$ for $\omega_S < 0$. $\diamond$

Figure 4.1 illustrates an example of the effect of varying Δ_{pmS} in Eq. (4.22), with $x_S = -1$ at system pressure of $P_{sys} = 13.8$MPa. This example explains the case when the vehicle is driving forward $T_{cyc} < 0$. For a specific output torque condition $G_{T22}T_{cyc} = -53.3Nm$, the torque variation of $\Delta_{pmS} > 0.03$ caused P/M-S to fail to fulfill the drive cycle torque T_{cyc} with $\omega_S < 0$. Thus, the transmission design is considered *infeasible with* $\Delta_{pmS} > 0.03$. Also, the transmission design is considered as *not robustly feasible.*

Meanwhile, as P/M-S is pumping when $\omega_S > 0$, the torque variation aids the transmission output torque as Δ_{pmS} increases positively. In other words, this indicates that increasing torque variation $\Delta_{pmS} \Rightarrow \Delta_{pmS,max}$ (increase in P/M-S torque losses) during pumping operation, the output torque capability increases.

Figure 4.2 illustrates another example of the effect of varying Δ_{pmT} in Eq. (4.21), with $x_T = 1$ at system pressure of $P_{sys} = 13.8$MPa. This example explains the case when the vehicle is driving forward $T_{cyc} < 0$, and engine operated at maximum torque $T_{eng} = 70Nm$. For a specific output torque condition $G_{T12}T_{cyc} = 104.5Nm$, the torque variation of $\Delta_{pmT} > 0.03$ caused P/M-T to fail to fulfill the drive cycle torque T_{cyc}.

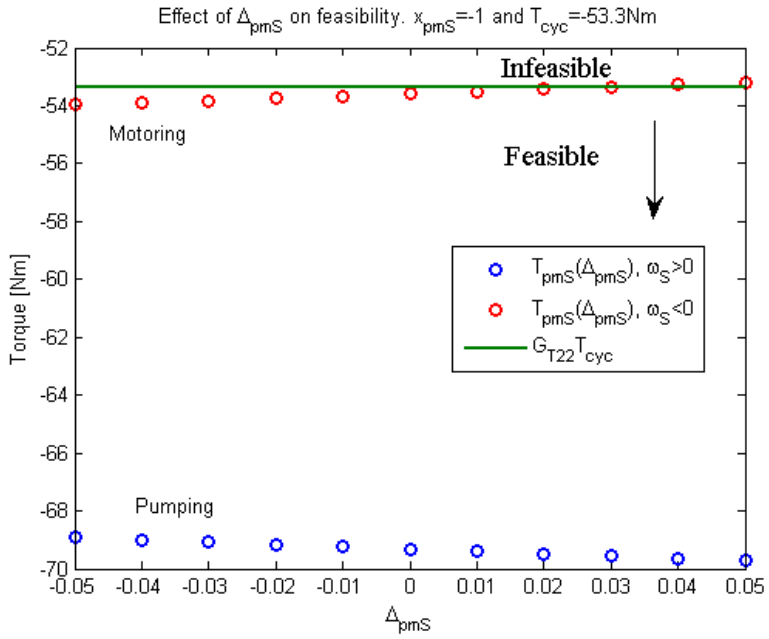

Figure 4.1: The effect of P/M-S torque variation on transmission feasibility at $13.8MPa$ $(2000psi)$, with $x_{pmS} = -1$, under specific output torque $G_{T22}T_{cyc} = -53.3Nm$.

Only $\omega_T > 0$ is considered in this case because the engine can only run in positive direction, and P/M-T is coupled to the engine. In this example, the transmission design is considered *infeasible with* $\Delta_{pmT} > 0.03$. Again, the transmission design is considered as *not robustly feasible.*

In summary, the transmission is robustly feasible if

$$\begin{aligned} |T_{cyc}| \quad \leq \quad & |(\frac{P_{sys}D}{2\pi} - sgn(\omega_{pmT})Loss_{mech,pmT}(1 \pm \Delta_{pmT,max}))/G_{T12} \\ & -(\frac{\dot{m}_{f,max}LHV}{\omega_{eng}} - Loss_{mech,eng}(1 + \Delta_{eng,max}))G_{T11}/G_{T12}| \qquad (4.25) \\ |T_{cyc}| \quad \leq \quad & |(\frac{P_{sys}D}{2\pi} - sgn(\omega_{pmS})Loss_{mech,pmS}(1 \pm \Delta_{pmS,max}))/G_{T12}| \qquad (4.26) \end{aligned}$$

In another word, *the feasibility of a specific hybrid transmission design is guaranteed if the energy management controller is feasible for the worst-case set of uncertainties.*

Accumulator power variation: According to Eq. (4.16), any loss variation from the powertrain will be reflected in the accumulator power. Equation (2.1) is modified

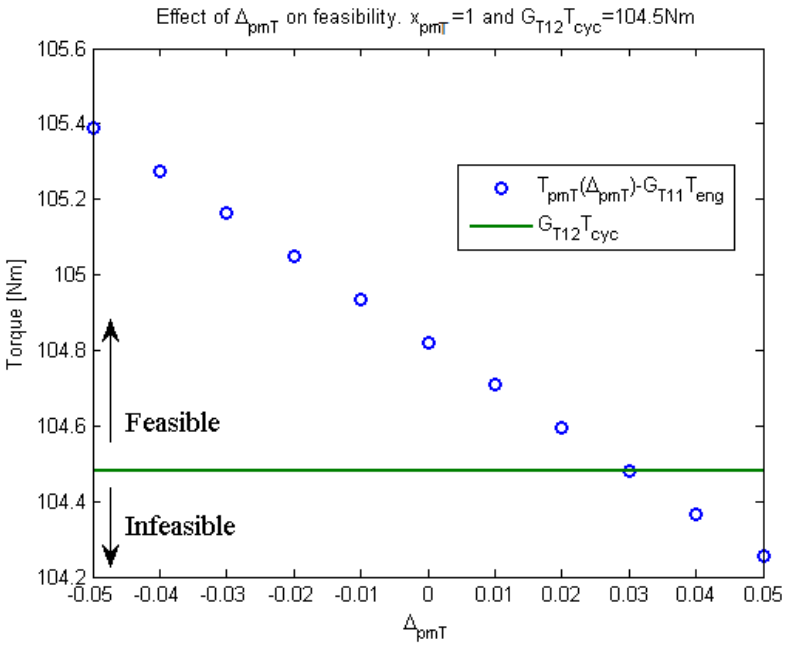

Figure 4.2: The effect of P/M-T torque variation on transmission feasibility at $13.8MPa$ ($2000psi$), with $x_{pmT} = 1$ and engine operating at maximum torque $T_{eng} = 70$Nm, under specific output torque $G_{T12}T_{cyc} = 104.5Nm$.

to include the torque variation of the engine and pump/motors, and expressed as:

$$\begin{aligned} \omega_{eng}(T_{eng}+\Delta T_{eng}) &+ \omega_{whl}T_{whl}+\omega_{pmT}(T_{pmT}+\Delta T_{pmT}) \\ &+ \omega_{pmS}(T_{pmS}+\Delta T_{pmS})=0 \qquad (4.27) \\ \omega_{eng}T_{eng}+\omega_{whl}T_{whl} &+ \omega_{pmT}T_{pmT}+\omega_{pmS}T_{pmS}+\omega_{eng}\Delta T_{eng} \\ &+ \omega_{pmT}\Delta T_{pmT}+\omega_{pmS}\Delta T_{pmS}=0 \qquad (4.28) \end{aligned}$$

where $\Delta T_{eng}, \Delta T_{pmT}, \Delta T_{pmS}$ are the torque variation of the engine and pump/motors. And Δ_{loss}, the power variation, is defined as:

$$\Delta_{loss}=\omega_{eng}\Delta T_{eng}+\omega_{pmT}\Delta T_{pmT}+\omega_{pmS}\Delta T_{pmS} \qquad (4.29)$$

As shown, the power variation is attributed to torque variations (from transmission output power point-of-view). And the power variation ΔPow is bounded by

$$\begin{aligned} -\omega_{eng}\Delta T_{eng,max} &- \omega_{pmT}\Delta T_{pmT,max}-\omega_{pmS}\Delta T_{pmS,max} \\ &< \Delta_{loss} < \\ \omega_{eng}\Delta T_{eng,max} &+ \omega_{pmT}\Delta T_{pmT,max}+\omega_{pmS}\Delta T_{pmS,max} \end{aligned}$$

where $\Delta T_{eng,min} < \Delta T_{eng} < \Delta T_{eng,max}$ is the range of engine torque variation, $\Delta T_{pmT,min} < \Delta T_{pmT} < \Delta T_{pmT,max}$ is the P/M-T torque variation, $\Delta T_{pmS,min} < \Delta T_{pmS} < \Delta T_{pmS,max}$ is the P/M-S torque variation, and $\omega_{eng}, \omega_{pmT} > 0$ since the engine can only run in positive direction, and P/M-T is coupled to the engine. Since any loss variation from the powertrain is reflected in the accumulator power, $\Delta_{Pacc}(t) = -\Delta_{loss}$.

4.3.2 Worst-case Optimal Energy Management Formulation

Previously, it is shown that the feasibility of a specific hybrid transmission design is guaranteed if the energy management controller is feasible for the worst-case set of uncertainties. Also as mentioned previously, the terminal constraint for the energy management is considered as a hard constraint for fair comparison. Combining these two definitions, a worst-case optimal energy management is proposed to handle the uncertainty in energy management.

The worst-case variation is assumed to be (i) prescribed uncertainty variation, where the uncertainty is 'known' by the energy management controller, and (ii) the worst-case uncertainty variation is time-invariant. Generically, the energy management is formulated as:

$$\begin{aligned} J^*_{WC} &= \max_{\Delta} \min_{mode(\cdot)} \int_{t_0}^{t_f} Loss_{mode}(t, \texttt{mode}, \Delta) \\ \text{subjected to} \quad & \int_{t_0}^{t_f} P_{sys} Q_{acc}(t, \texttt{mode}, \Delta) dt = 0 \\ & (\omega_{whl}(t), T_{whl}(t)) = (\omega_{cyc}(t), T_{cyc}(t)) \end{aligned} \tag{4.30}$$

where J^*_{WC} is the optimum worst-case cost function. This can be interpreted as *for a given design of the transmission, find the best achievable fuel economy at worst-case variation conditions.* By applying the Lagrange Multiplier method explained in Ch. 2, the worst-case optimal energy management is expressed as:

$$J^*_{WC} = \max_{\lambda} \min_{\texttt{mode}\cdot} \int_{t_0}^{t_f} Loss_{mode}(t, \texttt{mode}, |\Delta_{max}|) + \lambda \cdot P_{sys} Q_{acc}(t, \texttt{mode}, |\Delta_{max}|) dt \tag{4.31}$$

Worst-case variation simplification: In order to reduce the complexity of the uncertainty, the uncertainty torque variation $\Delta_{max} = [\Delta_{eng,max}, \Delta_{pmT,max}, \Delta_{pmS,max}]$ is reduced such that $\Delta_{max} = \Delta_{eng,max} = |\Delta_{pmT,max}| = |\Delta_{pmS,max}|$ in this study. This simplification allows the worst-case uncertainties to be represented by a single variable Δ_{max}. This may not be representative of the actual torque loss uncertainty since variation of engine is generally different from variation of pump/motors. However, this simplification provides insight of the worst-case uncertainty on transmission design.

Figure 4.3 shows the variation of optimum worst-case fuel economy J^*_{WC} with respect to the worst-case variation $\Delta = \Delta_{max}$. As seen, the best achievable fuel economy decreases monotonically as the worst-case uncertainty variation increases, using the energy management synthesized in Eq. (4.31). The assumption of constant $13.8MPa$ $(2000psi)$ pressure is increased to $20.7MPa$ $(3000psi)$ constant pressure in this case because the design is not feasible at $13.8MPa$ $(2000psi)$ with $\Delta_{max} = 0.05$ worst-case variation.

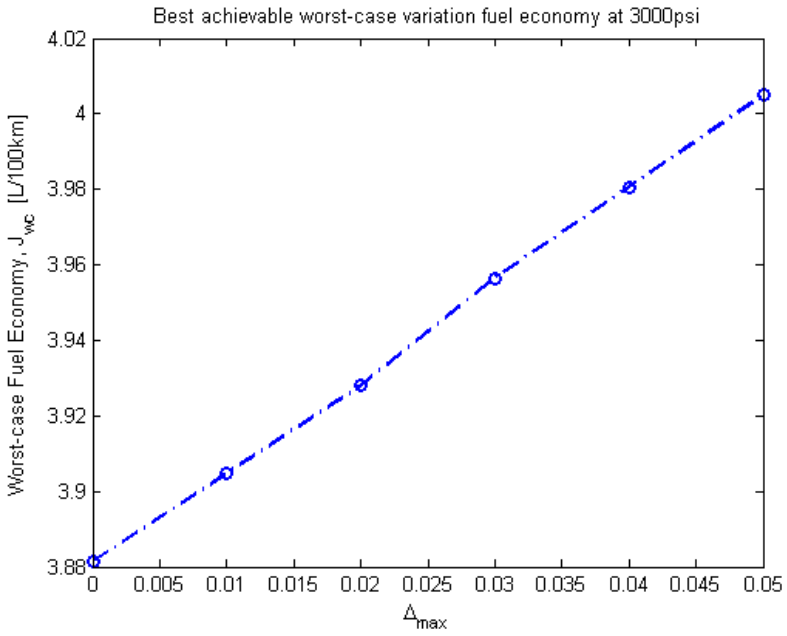

Figure 4.3: Best achievable fuel economy J^*_{WC} decreases as worst-case uncertainty variation increases at $20.7MPa$ $(3000psi)$, using Lagrange Multiplier method as energy management strategy.

4.4 Robust Transmission Design Optimization using Worst-Case Variation

With the energy management formulated in the previous section, the design of the transmission can proceed with considering uncertainties in power loss. Similar to the design process in Ch. 2, the design parameters of the transmission are $\nu = (G_\omega, D_{maxT}, D_{maxS})$, transmission gear kinematic matrix and pump/motor maximum displacements. Again, the uncertainty $\Delta_{max} = \Delta_{eng,max} = |\Delta_{pmT,max}| = |\Delta_{pmS,max}|$ is assumed in this study.

Using the worst-case optimal energy management strategy presented in Sec. 4.3.2, the specific transmission design is guaranteed to achieve its highest efficiency under worst-case condition. The focus is then shifted back towards optimizing the design of the transmission. The transmission robust optimal design can then be expressed as:

$$\min_{\upsilon} \max_{\lambda} \min_{\texttt{mode}(\cdot)} \int_{t_0}^{t_f} [Loss_{mode}(t, \texttt{mode}, |\Delta_{max}|, \nu) + \lambda \cdot P_{sys} Q_{acc}(t, \texttt{mode}, |\Delta_{max}|, \nu)] dt \tag{4.32}$$

4.4.1 Case 1: Worst-case Optimization of Pump/motor Sizes $\nu = (D_{maxT}, D_{maxS})$

To test if the transmission design method is effective, the optimization of the transmission design is limited to only the pump/motor sizes $\nu = (D_{maxT}, D_{maxS})$, while keeping the input coupled powersplit transmission kinematic to be the same as $(G_{1,1}, G_{1,2}, G_{2,1}, G_{2,2}) = (1.123, 2.276, -9.428, 0)$. Vehicle drag characteristics used are identical to the model presented in Sec. 2.6.1, and the constant system pressure of 20.7MPa (3000psi) is assumed. Again, simplified worst-case uncertainty is assumed, where $\Delta = \Delta_{max}$.

Table 4.1 shows the design optimization results at various worst-case conditions driving through the Combined drive cycle. In this study, D_{maxT} and D_{maxS} correspond to the reference P/M-T and P/M-S maximum displacements of 28cc. The result show the optimized P/M-S size does not change despite all various worst-case variation, while the optimized P/M-T size increases with increasing worst-case uncertainty variation Δ_{max}.

Figure 4.4 and 4.5 show the operating points of P/M-T and P/M-S under various worst-case variation Δ_{max}. As seen in Fig. 4.4, there are instants when P/M-T

Δ_{max}	FE $L/100km$ (mpg)	D_{maxT}	D_{maxS}
0.00	3.72 (63.3)	0.903	1.006
0.01	3.74 (62.9)	0.903	1.006
0.02	3.76 (62.5)	0.903	1.006
0.03	3.85 (61.1)	1.024	1.006
0.04	3.87 (60.7)	1.024	1.006
0.05	3.92 (60.0)	1.068	1.006

Table 4.1: Transmission pump/motor sizes optimization at various worst-case uncertainty Δ_{max} at constant system pressure of $20.7MPa$.

Table 4.2: Full transmission design optimization at various worst-case uncertainty at constant system pressure of 20.7MPa.

Δ_{max}	FE $L/100km$ (mpg)	$G_{1,1}$	$G_{1,2}$	$G_{2,1}$	D_{maxT}	D_{maxS}
0.00	3.72 (63.3)	1.123	2.276	-9.428	0.903	1.006
0.01	3.74 (62.9)	1.123	2.276	-9.428	0.903	1.006
0.02	3.76 (62.5)	1.123	2.276	-9.428	0.903	1.006
0.03	3.82 (61.6)	1.124	2.431	-9.519	1.024	0.996
0.04	3.84 (61.3)	1.124	2.410	-9.434	1.024	1.005
0.05	3.88 (60.6)	1.274	2.333	-10.285	0.810	0.914

is operating at near full displacement ($x_T \approx 0.98$). While in Fig. 4.5, P/M-S is operating approximately 0.86 ($x_S \approx 0.86$) under no-uncertainty condition ($\Delta_{max} = 0.00$). As worst-case uncertainty increases, pump/motors are required to operate at higher displacement to compensate for extra torque loss. Thus, intuitively P/M-T size is increased.

4.4.2 Case 2: Worst-case Optimization of Full Hybrid Transmission $\nu = (G_\omega, D_{maxT}, D_{maxS})$

For full transmission optimization with design parameters, $\nu = (G_\omega, D_{maxT}, D_{maxS})$, it is expected to further improve the fuel economy at the same worst-case variation, Δ_{max}. Table 4.2 shows the optimization results of the full transmission design with worst-case uncertainty.

Result shows that worst-case variations smaller than $\Delta_{max} \leq 0.02$ yield identical

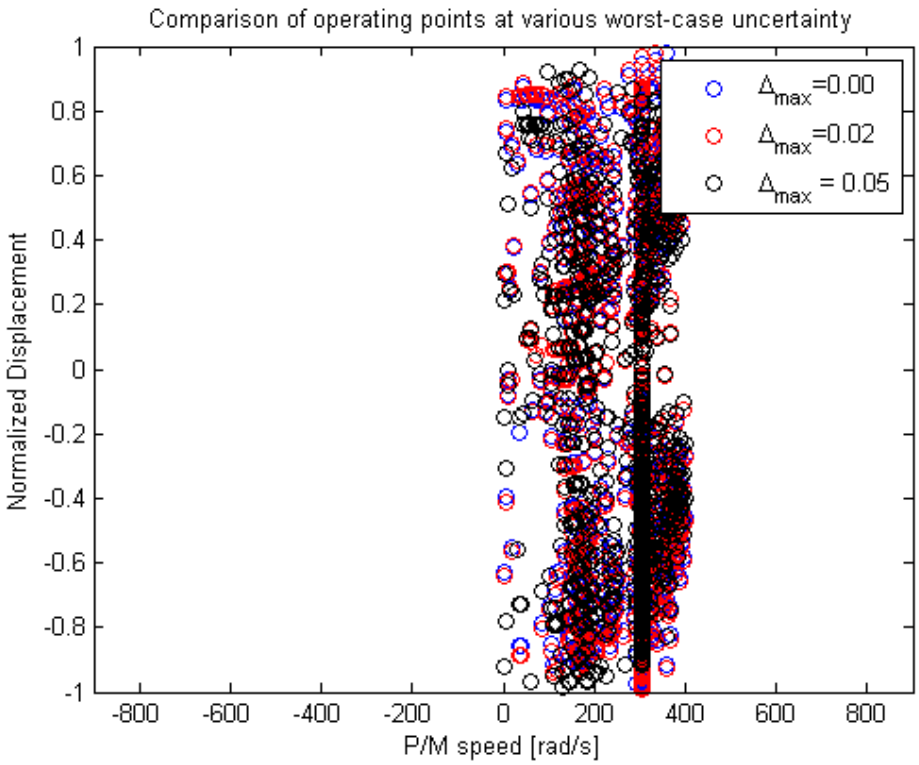

Figure 4.4: Comparison of P/M-T operating points at various worst-case uncertainty with optimized transmission design at constant system pressure of 20.7MPa.

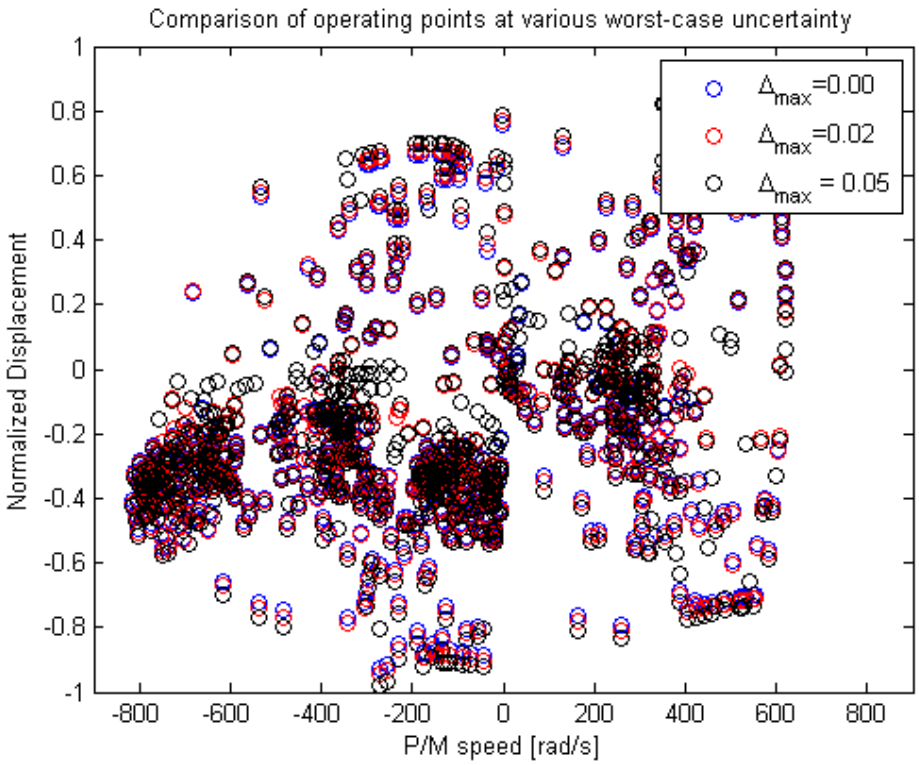

Figure 4.5: Comparison of P/M-S operating points at various worst-case uncertainty with optimized transmission design at constant system pressure of 20.7MPa.

design as in Tab. 4.1. With $\Delta_{max} = 0.03$ and 0.04, even though the pump/motor sizes are similar, the gear ratios are optimized to achieve higher fuel efficiency than in Tab. 4.1. Compared to results in Tab. 4.1, the fuel economy is further improved by reducing the pump/motor sizes for $\Delta_{max} = 0.05$.

4.5 Robust Design Optimization with Minimized Uncertainty Sensitivity

As discussed at the beginning of this chapter, robust optimality should consider both robust feasible design and design sensitivity to uncertainty. Robust feasibility is achieved using worst-case uncertainty for transmission design optimization as presented in Sec. 4.4. Design sensitivity with respect to uncertainty variation can be used to minimize the effect of powertrain loss and operating conditions uncertainty due to transmission design. In this section, the sensitivity function will be defined and it will be incorporated into the worst-case uncertainty robust design.

4.5.1 Uncertainty Sensitivity

Design sensitivity with respect to uncertainty variation can be defined as:

$$J_{sens}(\nu, \Delta_{max}) = \frac{\delta J^*_{WC}(\nu, \Delta_{max})}{\delta \Delta_{max}} \tag{4.33}$$

where J_{sens} is the sensitivity function with respect to worst-case uncertainty variation Δ_{max}. Again, simplified worst-case uncertainty $\Delta = \Delta_{max}$ is assumed. With the empirically derived losses, the sensitivity function J_{sens} cannot be easily evaluated analytically. Thus, the expression is discretized numerically into the following form:

$$J_{sens}(\nu, \Delta_{max}) = \frac{J^*_{WC}(\nu, \Delta_{max1}) - J^*_{WC}(\nu, \Delta_{max2})}{\Delta_{max1} - \Delta_{max2}} \tag{4.34}$$

4.5.2 Design optimization with Minimized Uncertainty Sensitivity

Similar to the method in Ch. 3.3, the design sensitivity is incorporated into the robust feasible design using *Weighted-Sum* multi-objective optimization approach. This multi-objective problem is originally formulated as:

$$\begin{cases} \max_{\nu} J^*_{WC}(\nu) & \text{in Sec. 4.4} \\ \min_{\nu} J_{sens}(\nu) & \text{in Eq. (4.34)} \end{cases} \tag{4.35}$$

where J^*_{wc} is the worst-case variation fuel economy, J_{sens} is the design sensitivity with respect to uncertainty variation. Using the *Weighted-Sum* method, the original problem is transformed into:

$$J_{WS} = \min_{\nu} \left[-(1-wf) \cdot \frac{J^*_{WC}(\nu)}{nf_3} + wf \cdot \frac{J_{sens}(\nu)}{nf_4} \right] \tag{4.36}$$

where J_{WS} is the Weighted-Sum cost, nf_3 and nf_4 are the normalizing factors for the worst-case variation fuel economy and design sensitivity objective functions, and wf is the weighting factor of the *Weighted-Sum* method. Figure 4.6 shows the generated Pareto Frontier using Weighted-Sum method, and the design parameters from the multi-objective optimization is summarized in Tab. 4.3.

As seen in the plot, the generated Pareto Frontier shows trade-off between the best achievable fuel economy for worst-case condition and design sensitivity. However, according to Tab. 4.3, the fuel economy did not decrease monotonically, as $wf = 0.6$ and $wf = 0.8$ is lower than previous wf. On the other hand, the optimized design parameters for all wf are fairly similar, with difference of 3% between largest and smallest D_{maxT}, and 7% between largest and smallest D_{maxS}. Moreover, the variation of both objective functions did not vary significantly for all wf, with fuel economy ranging only from $3.679 \sim 3.687 L/100km$ and sensitivity ranging from $3.066 \sim 3.043 \times 10^7 J$. This is mainly due to the similar parameters for all optimized design.

4.5.3 Discussions

In order to evaluate the effectiveness of the minimized sensitivity design, a series of Monte Carlo simulations using 1000 samples are conducted for each weighting factor

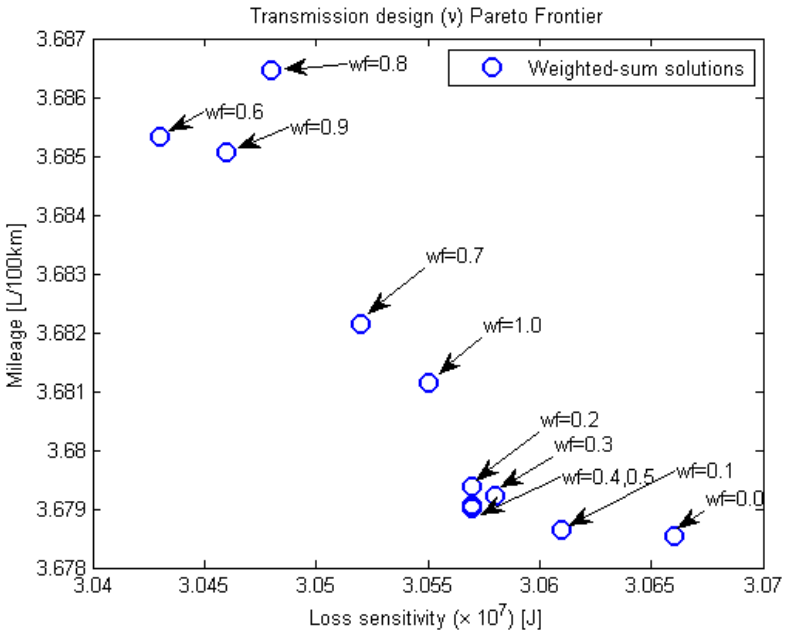

Figure 4.6: Pareto frontier for robust feasible design and design sensitivity.

wf. The torque loss variation $\Delta = [\Delta_{eng}, \Delta_{pmT}, \Delta_{pmS}]$ for the engine and pump/motors are assumed to behave as gaussian distribution individually, with zero mean and 0.05Nm standard deviation. The system pressure used in the simulation is 13.8MPa (2000psi).

The Monte Carlo simulation results are shown in Tab. 4.4. The trend of the mean fuel economy matched well with the worst-case fuel economy. However, the standard deviation of fuel economy did not follow the trend of the design sensitivity. This is potentially caused by discretization of the sensitivity function, leading to computational noise. On the other hand, since the standard deviations are very small, the Monte Carlo simulation may require significantly larger sample to accurately calculate the standard deviations.

The results shown have suggested that the transmission design has very low sensitivity with respect to 5% of the component loss variation. Thus, any design presented in this section is robust against 5% of worst-case powertrain loss variation, and fuel economy for each design is insensitive to the loss variations.

wf	J_{wc} $L/100km$ (mpg)	J_{sens} $\times 10^7 J$	$G_{1,1}$	$G_{1,2}$	$G_{2,1}$	D_{maxT}	D_{maxS}
0.0	3.679 (63.94)	3.066	1.094	2.247	-9.187	0.906	0.926
0.1	3.679 (63.94)	3.061	1.094	2.247	-9.188	0.906	0.927
0.2	3.679 (63.93)	3.057	1.095	2.250	-9.197	0.907	0.925
0.3	3.679 (63.93)	3.058	1.095	2.249	-9.193	0.907	0.927
0.4	3.679 (63.93)	3.057	1.094	2.252	-9.203	0.908	0.925
0.5	3.679 (63.92)	3.057	1.094	2.248	-9.188	0.908	0.929
0.6	3.685 (63.82)	3.043	1.107	2.247	-9.239	0.899	0.960
0.7	3.682 (63.88)	3.052	1.096	2.246	-9.216	0.907	0.928
0.8	3.687 (63.80)	3.048	1.125	2.241	-9.196	0.880	0.996
0.9	3.685 (63.83)	3.046	1.096	2.242	-9.225	0.908	0.945

Table 4.3: Transmission robust optimal design with minimized sensitivity using Weighted-sum method.

4.6 Conclusions

This chapter has briefly discussed and analyzed the effect of uncertainty in powertrain losses. To design a robust transmission, the powertrain must be feasible under certain range of uncertainties, and the efficiency is also insensitive to the variations. This study mainly focuses on powertrain's losses and operating condition uncertainties. However, it is shown that operating condition uncertainties eventually translated into powertrain loss uncertainty due to the defined objective function. Due to the stochastic nature of the uncertainties, it poses a equality constraint issue with the energy management strategy on whether the performance of the transmission can be compared fairly under stochastic uncertainty. Thus, a worst-case energy management strategy is synthesized assuming a prescribed variation.

In order to design the transmission robust against the operating conditions or model uncertainties, a worst-case variation design optimization approach is proposed to ensure the feasibility of the design. It is shown that the transmission design remains identical as long as the operating points are within feasible range. Apart from the robust transmission design, to incorporate the design sensitivity with the robust transmission design, the classical method of weighting-sum is applied again to solve this multi-objective problem. Monte Carlo simulation is conducted to evaluate the effectiveness of the designs.

wf	J_{wc} $L/100km$ (mpg)	J_{sens} $\times 10^7 J$	$mean_{mpg}$ $(L/100km)$	std_{mpg}
0.0	3.679 (63.94)	3.066	65.26 (3.604)	0.0765
0.1	3.679 (63.94)	3.061	65.26 (3.604)	0.0806
0.2	3.679 (63.93)	3.057	65.25 (3.605)	0.0768
0.3	3.679 (63.93)	3.058	65.25 (3.605)	0.0767
0.4	3.679 (63.93)	3.057	65.25 (3.605)	0.0782
0.5	3.679 (63.92)	3.057	65.25 (3.605)	0.0768
0.6	3.685 (63.82)	3.043	65.12 (3.612)	0.0795
0.7	3.682 (63.88)	3.052	65.19 (3.608)	0.0795
0.8	3.687 (63.80)	3.048	65.09 (3.614)	0.0763
0.9	3.685 (63.83)	3.046	65.13 (3.611)	0.0732

Table 4.4: Monte Carlo simulation results for various transmission designs.

Result shows low standard deviation for fuel economy, suggesting that the transmission design fuel efficiency is inherently insensitive to the loss variation.

Chapter 5

Modeling of the Generation I Hydraulic Hybrid Vehicle

Chapter 2, 3 and 4 developed a series of systematic optimization approaches to improve the fuel efficiency, acceleration performance, and robustness against a wide-range of operating conditions. In order to validate the effectiveness of the transmission optimal design procedures and the behaviour of the energy management, a hydraulic hybrid power-split powertrain is built as a proof-of-concept hardware, called the 'Generation I' vehicle.

The Generation I vehicle was built in-house using the platform of an off-road all terrain vehicle (a Polaris Ranger in Fig. 5.1). An input-coupled power-split architecture is utilized in this vehicle. The vehicle has been outfitted with a modular power train. This enables experimenting with different pump, motor and energy storage technologies, including those developed in complementary CCEFP projects.

The main goal of this chapter is to describe the Generation I hardware and to develop a control-oriented model for controller design and performance prediction for the Generation I powertrain. Components of the powertrain including the engine and pump/motors are experimentally characterized for efficiency, performance, and dynamical behaviors.

The rest of this chapter is organized as follow: Section 5.1 introduces the goals and the evolution of the Generation I test bed. Modeling and characterization of the

Figure 5.1: Hydraulic Hybrid Passenger Vehicle and hydrostatic dynamometer built by CCEFP at University of Minnesota.

diesel engine are described in Sec. 5.2, and the hydraulic pump/motors are presented in Sec. 5.3. Section 5.4 presents an ideally isothermal accumulator model. The dynamic modeling of the overall drivetrain is discussed in Sec. 5.5. Section 5.6 contains some concluding remarks for this chapter.

5.1 Introduction

The overall goal of this test bed is to realize a hydraulic hybrid power-train with drastic improvement in fuel economy and good performance to be competitive with other technologies such as electric hybrid, for the passenger vehicle segment. As a test bed of the Center for Compact and Efficient Fluid Power (CCEFP), it also drives and integrates associated projects by identifying the technological barriers to achieving that goal.

The in-house built powertrain is an input coupled power-split transmission (described in Ch. 2), coupled with a 1.5 liter diesel engine, and a pair of 38L (10 gal) composite bladder type accumulators. As described in Ch. 1, the transmission was

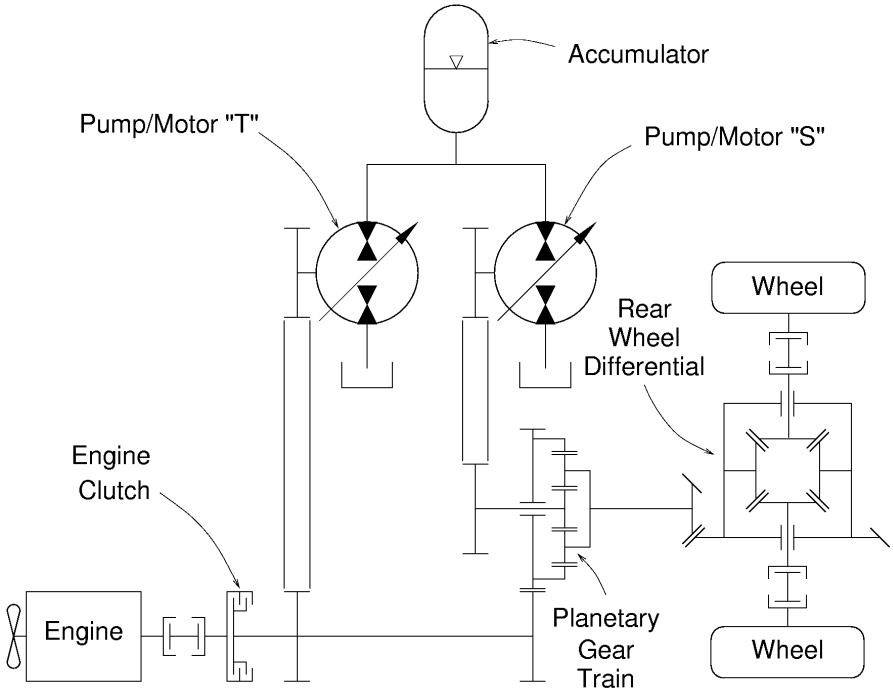

Figure 5.2: Schematic representation of redesigned Generation I HHPV powertrain (from Sedler (2012) [19]).

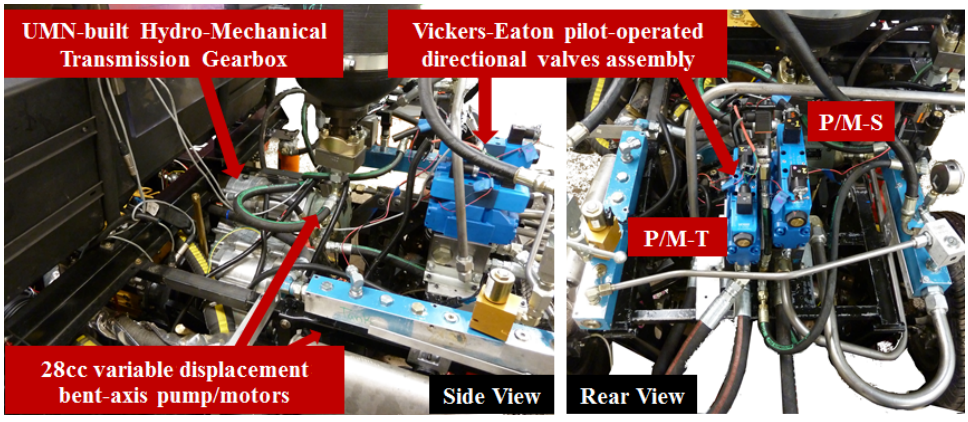

Figure 5.3: Generation I hybrid Hydro-Mechanical Transmission.

redesigned due to its over-sized components and the resulting inefficiencies. The detailed design of the redesigned transmission including component selection and CAD modeling are done in [19] and the schematic of the finalized design is shown in Fig. 5.2. As described in [19], the redesigned transmission is optimized using the methodology presented in Ch. 2. However, due to the limited selection of off-the-shelf gears that are available, the component sizes are different than the optimal design presented in Tab. 2.2. The selected components will be discussed in this chapter.

The transmission and the hydraulic components are assembled and installed onto the vehicle to power the rear wheels, as shown in Fig. 5.3. Due to the lack of over-center capability of the variable displacement pump/motors, pilot-operated directional valves are installed on each pump/motor to allow four-quadrant operation, which is a necessary feature for full hybrid operation and engine management. Meanwhile, the closed-center position of the directional valves provides the capability of locking-up the pump/motors to further reduce losses, as presented in Ch. 2. Appendix A presents the hydraulic circuit of this test bed.

The hybrid powertrain is equipped with encoders, speed sensors, a torque sensor and pressure transducers for control and verification purposes. The encoders are installed on the engine for engine speed and at the left rear wheel for wheel speed. The two transmission pump/motors have built-in Hall-effect speed sensors. A TECAT WISER-200 (Ann Arbor, MI) wireless telemetry strain gauge torque sensor is installed between the engine flywheel and transmission to measure the engine output torque. Pressure transducers measure the pressures in the high and low pressure accumulators.

On the other hand, this vehicle cannot be driven at speeds higher than about 40 kph due to concerns about chassis stability. Thus, a hydrostatic dynamometer has been designed and built to overcome this limitation, as shown in Fig. 5.1 [68]. The in-house built hydrostatic dynamometer also allows experiments to be conducted consistently on the Generation I test bed.

In-house Hydrostatic Dynamometer: The detail design of the dynamometer hardware can be found in [68], and the control of the dynamometer can be found in [69]. Figure 5.4 shows the architecture of the in-house built hydrostatic dynamometer.

This dynamometer allows in-door hybrid powertrain testing and repeatable testing

under a controlled environment. Moreover, this dynamometer design is capable of motoring (instead of exclusively absorbing as is the case with the majority of electrical dynamometers) the test vehicle, simulating various vehicle attributes and load conditions. More importantly, it provides a platform for rapid control algorithm evaluation and fine-tuning.

5.2 Engine Modeling and System Identification

The prime mover of the powertrain is a 1.5 litre diesel engine (Fig. 5.5). In this section, the engine is modeled as a quasi-static system, with a combination of static map and dynamic equations. The inertia, viscous friction and fuel solenoid actuation are considered in the dynamic model, whereas the engine's efficiency in converting fuel to output power is treated as a static mapping between the engine speed/torque to fuel consumption. This was obtained from dynamometer testing of the engine. In this section, the details of system modeling and parameters identification will be discussed.

The diesel engine is originally controlled by a mechanical governor that determines the fuel rack position[1] within the fuel injection pump. The fuel injection pump is driven by the engine's crankshaft, hence pumping speed is proportional to engine speed. Since the engine has been modified by replacing the original fuel cut-off solenoid with a linear solenoid, the solenoid directly controls the position of the fuel rack and hence the engine's power output.

The fuel rack position u^* determines the fuel injection rate $\dot{m}_f$ for a specific engine speed (ω_{eng}), hence the fuel mass flow rate and fuel rack position are related by:

$$\dot{m}_f(t) = K_\omega \omega_{eng} u^*(t) \tag{5.1}$$

where $\dot{m}_f$ is the mass flow rate of the fuel injection, and K_ω represents the fuel pump's volumetric displacement. To determine K_ω, the fuel consumptions $\dot{m}_f$ at different engine speeds ω_{eng} with $u^* = 1$[2] are plotted in Fig. 5.6. From the slope of the fitted line, K_ω is identified to be $0.0056 g/rad$. The parameter K_ω translates to the net engine fuel pump capacity of 0.0336g/rev, which represents the net capacity of fuel consumed

[1] Fuel rack acts as a fuel distribution valve.

[2] $u^* = 1$ represents engine's maximum engine torque condition.

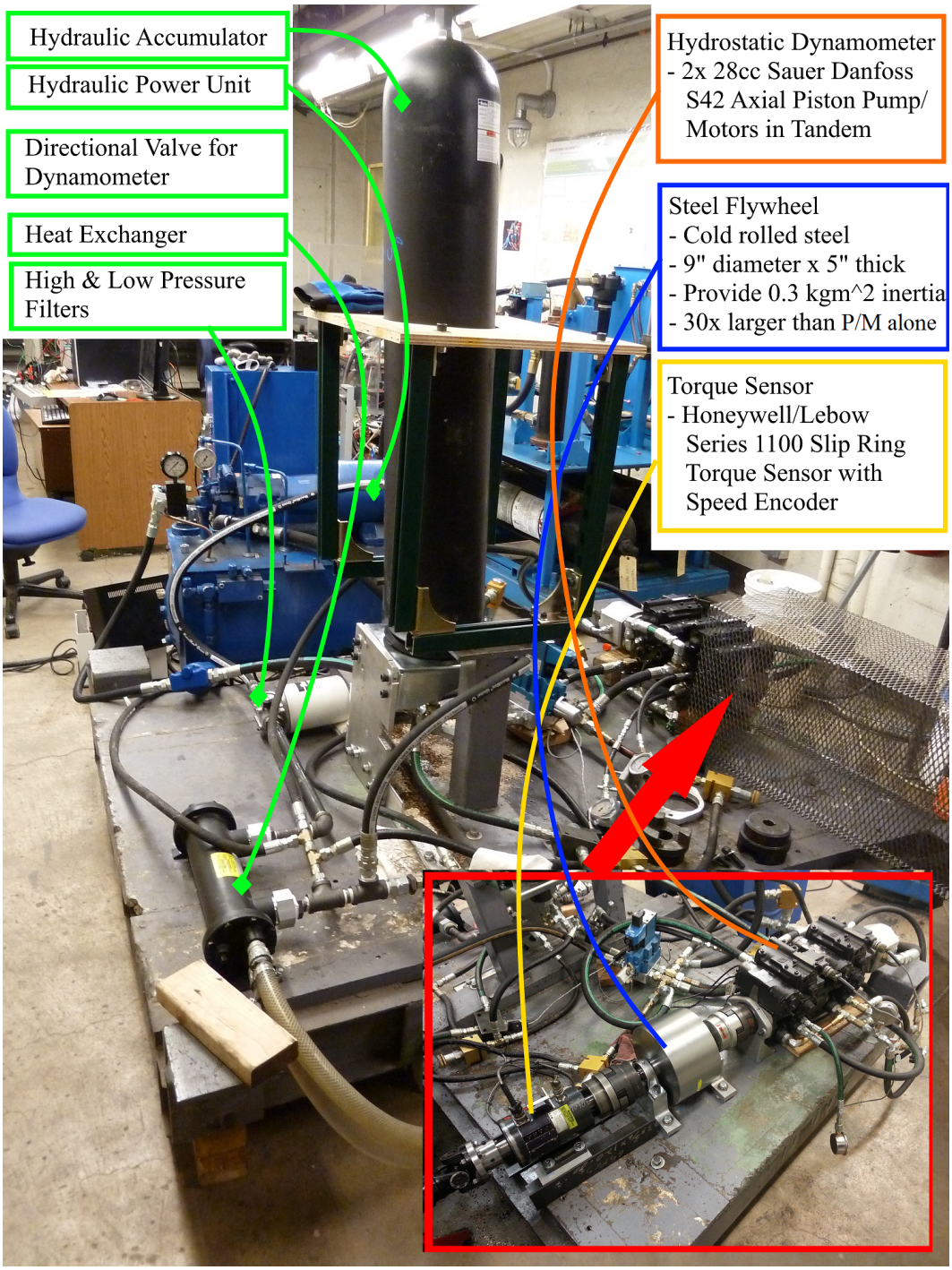

Figure 5.4: In-house built hydrostatic dynamometer to evaluate powertrain performance.

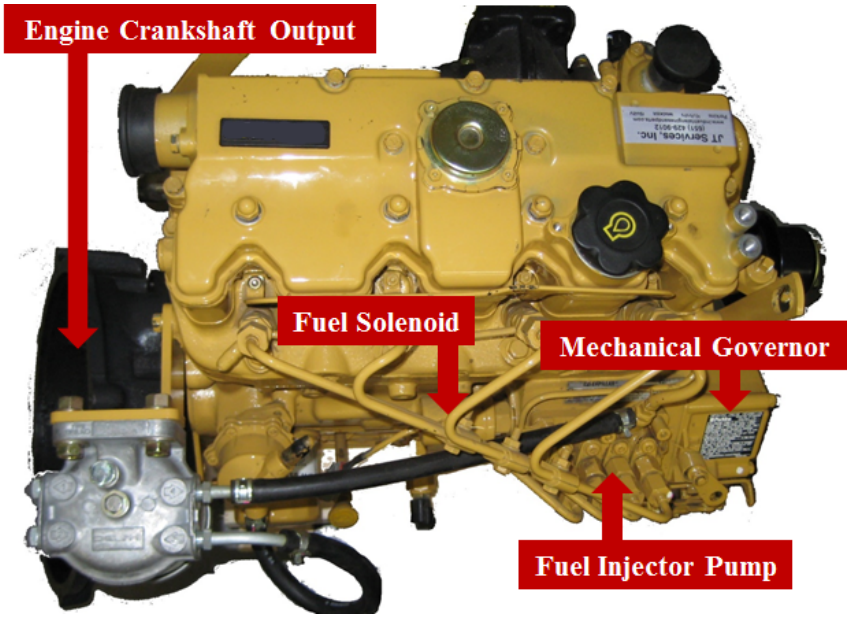

Figure 5.5: Hybrid powertrain's 1.5 litre 4-cylinder diesel engine.

by the engine.

According to [37, 70], fuel mass flow rate dictates engine indicated power $Pow_{eng,IP}$, which does not include mechanical losses. Hence, $Pow_{eng,IP}$ is assumed to be proportional to fuel rate $\dot{m}_f$, as expressed by:

$$Pow_{eng,IP} = K_{eng}\dot{m}_f \tag{5.2}$$

$$= K_{eng}K_{\omega}\omega_{eng}u^*(t) \tag{5.3}$$

where K_{eng} is the engine gain between the fuel injection rate and the indicated engine power. K_{eng} assumes constant indicated efficiency. Similarly, the engine indicated torque ($T_{eng,IP}$) is defined as the engine output torque without considering friction loss T_{frict}. By assuming the friction loss is only speed dependent, $T_{eng,IP}$ can be related to the friction loss by:

$$T_{eng,IP} = T_{eng} + T_{frict}(\omega_{eng}) \tag{5.4}$$

where $T_{frict}(\omega_{eng})$ is the speed dependent friction.

In order to identify the parameters K_{eng}, steady-state fuel consumption at various

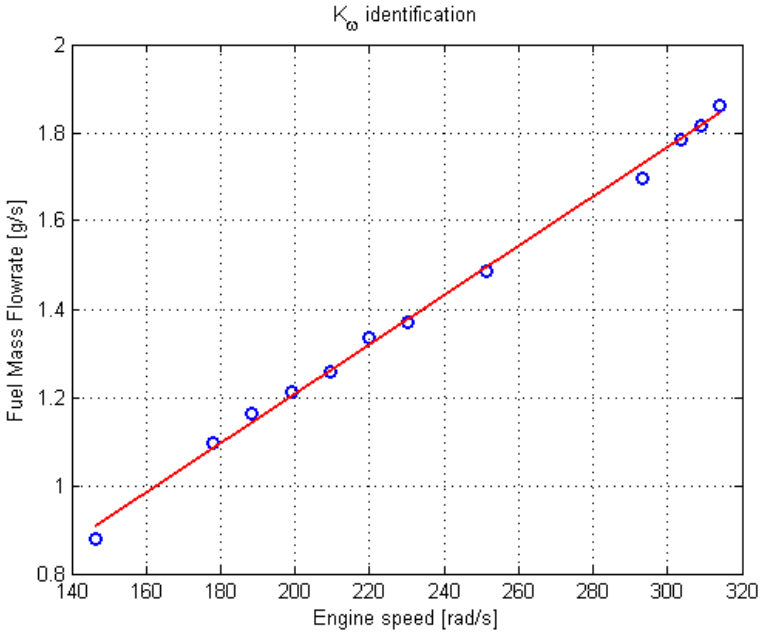

Figure 5.6: Identification of parameter K_ω using engine's full load ($u^* = 1$) fuel consumption.

conditions is required. Fuel consumption at full load operation is provided by the manufacturer, while the intermediate load conditions are obtained from engine dynamometer tests using the in-house built hydrostatic dynamometer.

A method for estimating the friction loss $T_{frict}(\omega_{eng})$ of compression ignition engines is the Willan's line [37, 70]. This method assumes that T_{frict} is constant for a specific engine speed. Combining Eqs. (5.3) and (5.4), the friction loss is related to T_{eng} and $\dot{m}_f$ by:

$$T_{eng} = \frac{K_{eng}}{\omega_{eng}} \dot{m}_f - T_{frict} \tag{5.5}$$

To determine $T_{frict}(\omega_{eng})$ for each speed, engine torques T_{eng} is plotted with various $\dot{m}_f$ for the specific speed. The fitted line is extrapolated to zero fuel flow rate, where the y-axis intercept (when $\dot{m}_f = 0$) is the friction loss $T_{frict}(\omega_{eng})$. $T_{frict}(\omega_{eng})$ for various engine speeds is illustrated in Fig. 5.7 and the calculated friction is summarized in Tab. 5.1.

With the estimated T_{frict}, indicated engine torque ($T_{eng,IP}$) is calculated using

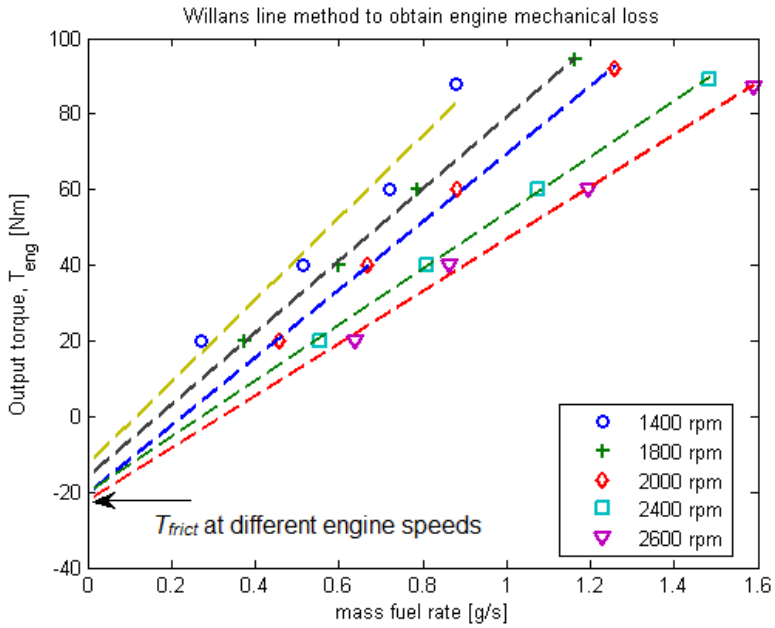

Figure 5.7: Willan's line method to estimate engine friction loss for various engine speeds.

Eq. (5.4). Since $Pow_{eng,IP} = \omega_{eng} T_{eng,IP}$, K_{eng} can be determined using the $T_{eng,IP}$ and $\dot{m}_f$ according to Eq. (5.2). $K_{eng} = 19142$J/g can be identified from the slope of the plot in Fig. 5.8. According to [70], $K_{eng} = \eta_v \eta_c LHV$ is heavily dependent on lower heating value (LHV) of the fuel and cycle efficiency (η_c), and weakly dependent on air intake volumetric efficiency ($\eta_v \approx 1$). By assuming the lower heating value of diesel fuel to be 45.9MJ/kg [70], the engine's cylinder cycle efficiency is approximately 41.7%, a reasonable efficiency for a mid-range diesel engine.

From Eqs. (5.3) and (5.4), the engine mechanical output torque is expressed as:

$$T_{eng} = K_{eng} K_\omega u^*(t) - T_{frict}(\omega_{eng}) \tag{5.6}$$

Figure 5.9 shows the efficiency map and the best Brake Specific Fuel Consumption (BSCF) operating curve, the engine efficiency is calculated using:

$$\eta_{eng} = \frac{\omega_{eng} \cdot T_{eng}}{\dot{m}_f \cdot LHV}$$

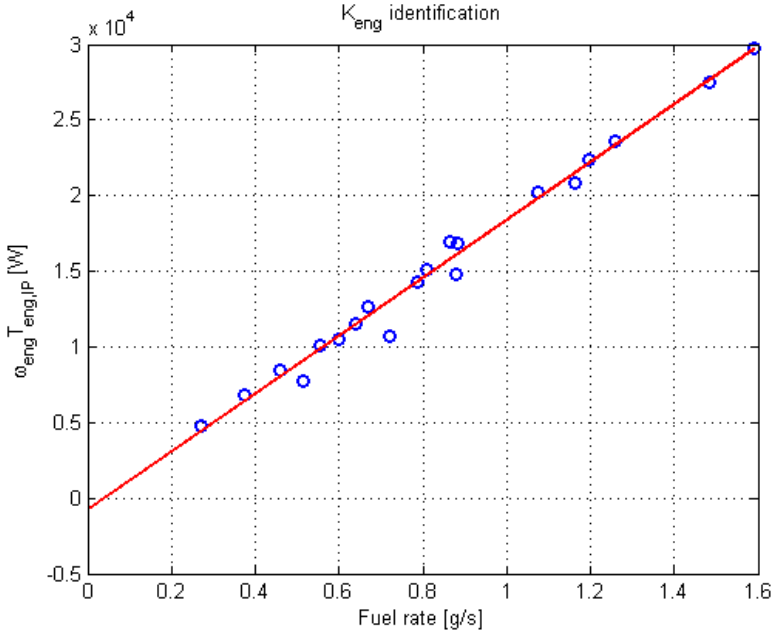

Figure 5.8: Identification of parameter K_{eng} using indicated engine power and fuel consumptions.

where LHV is the lower heating value of the diesel fuel. Figure 5.10 shows the engine static power loss, where the engine power loss is computed according to:

$$Loss_{eng} = \dot{m}_f \cdot LHV - \omega_{eng} \cdot T_{eng}$$

Please note that the experimentally generated engine map in this chapter is different from the reference engine map used in Ch. 2 $\sim$ 4 that uses 1.1L diesel engine[3] .

The engine inertial dynamics are modeled as a first order system:

$$J_{eng}\dot{\omega}_{eng}(t) = \underbrace{K_{eng}K_{\omega}u^*(t) - T_{frict}(\omega_{eng})}_{T_{eng}} - T_{eng,L} \tag{5.7}$$

where J_{eng} is the engine's inertia, and $T_{eng,L}$ is the load acting on the engine crankshaft.

For the fuel delivery system, the fuel solenoid controlling the fuel rack position is

[3] The 1.1L diesel engine is replaced with the 1.5L diesel engine in 2013 due to an accident that damaged the engine.

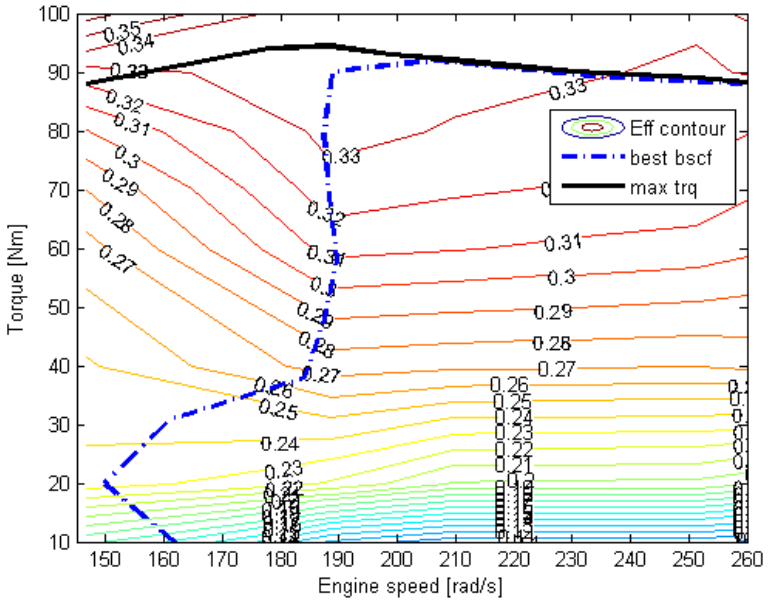

Figure 5.9: Engine static efficiency map.

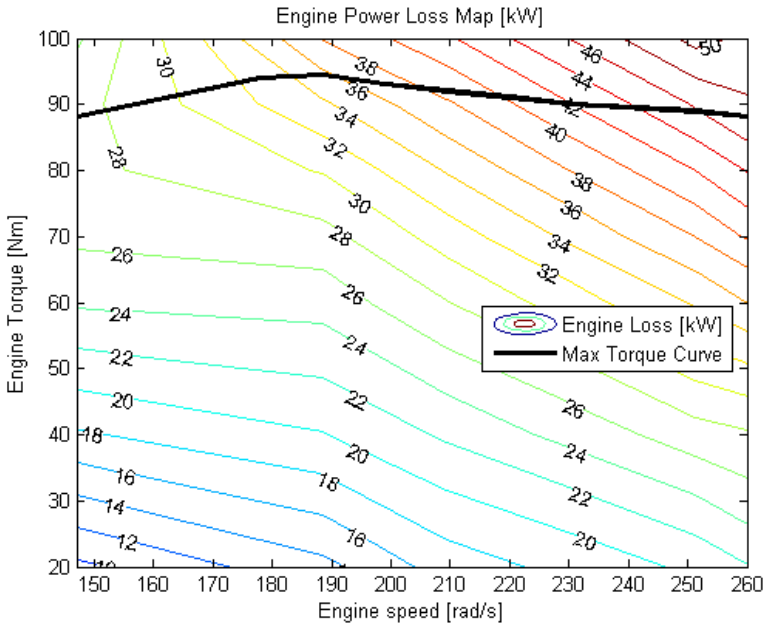

Figure 5.10: Engine static power loss map.

Engine speed ω_{eng}	Friction loss $T_{frict}(\omega_{eng})$
146.6rad/s (1400rpm)	12.7 Nm
188.5rad/s (1800rpm)	15.9 Nm
209.4rad/s (2000rpm)	20.5 Nm
251.3rad/s (2400rpm)	20.3 Nm
272.3rad/s (2600rpm)	22.3 Nm

Table 5.1: Estimated engine friction loss from Willan's lines.

modeled as a first order system:

$$\dot{u^*}(t) = -\lambda_{sol} u^*(t) + \lambda_{sol} u(t) \tag{5.8}$$

where $u^* \in [0, 1]$ is the normalized fuel rack position, $1/\lambda_{sol}$ is fuel solenoid's time constant, and u is the normalized fuel rack position command.

Engine inertia is dominated by the flywheel and therefore estimated to be $J_{eng} = 0.0975 kgm^2$ based on the geometry of the engine flywheel. System identification experiments[4] were also conducted to obtain $\lambda_{sol} = 10.18 rad/s$, and the system identification process and the least-squares identification method can be found in [71]. Figure 5.11 shows a comparison of the transient experimental and simulated engine speed responses.

The overall engine model is summarized as:

$$\begin{aligned} J_{eng}\dot{\omega}_{eng}(t) &= K_{eng} K_\omega u^*(t) - T_{frict}(\omega_{eng}) - T_{eng,L} \\ \dot{u^*}(t) &= -\lambda_{sol} u^*(t) + \lambda_{sol} u(t) \\ \dot{m}_f(t) &= K_\omega \omega_{eng} u^*(t) \end{aligned}$$

where $K_{eng} = 19142$J/g, $K_\omega = 0.0056$g/rad, and $\lambda_{sol} = 10.18$.

[4] The system identification experiment consists of conducting step changes of reference engine speed to obtain the engine's step responses.

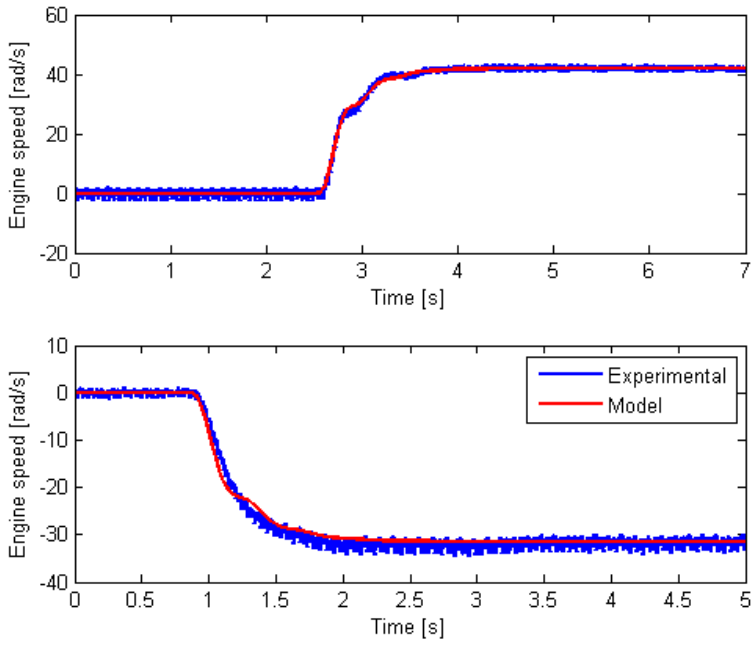

Figure 5.11: Experimental and simulated (proportional) closed loop engine speed responses due to step changes in reference speed. The speeds shown are offset such that the initial speed is at zero.

5.3 Hydraulic Pump/Motor Characterization

Another critical component of the powertrain is the hydraulic pump/motor units. A pair of 28.1cc variable displacement bent-axis pump/motors are used for the 'torquer' and the 'speeder'. The displacement actuation has bandwidth of approximately $3rad/s$ (from experiment) so that the displacement set points $x_S(t)$ and $x_T(t)$ are used as control inputs. They are related to the high pressure line flows and torques by:

$$T_*(t) = \frac{P_{sys}(t)D_{max}}{2\pi}x_*(t) - sgn(\omega_*)\cdot Loss_{mech,pm*}(x_*, \omega_*, P_{sys}) \tag{5.9}$$

$$Q_*(t) = \frac{\omega_* D_{max}}{2\pi}x_*(t) + Loss_{vol,pm*}(x_*, \omega_*, P_{sys}) \tag{5.10}$$

where subscript $* = S$ or T, $Loss_{vol,pm*}$ and $Loss_{mech,pm*}$ are the experimentally obtained volumetric and mechanical loss maps of the pump/motors, $P_{sys} = P_{hi} - P_{lo}$ is the system pressure, $x_* \in [-1, 1]$ is the normalized pump/motor displacement, and D_{max} is the maximum volumetric displacement. $Loss_{vol,pm*}$ and $Loss_{mech,pm*}$ are always positive. $Q_* > 0$ defines the pump/motor in motoring mode, where fluid flows into the hydraulic unit. $T_* \cdot \omega_* > 0$ means the pump/motor is motoring.

The transmission pump/motor units lack the capability of operating over-center, thus they rely on reversing the high pressure and low pressure port by using a directional valve to achieve four-quadrant operation. The sign convention for (T_*, Q_*) of the pump/motors on the transmission is defined in Fig. 5.12, where $T_* > 0$ when torque is exerted counter-clockwise from the front view of the shaft, and $Q_* > 0$ when high pressure fluid flows into the unit. When (x_*, ω_*, P_{sys}) are all positive, the hydraulic unit is motoring. As the stroke piston position measurement is not available, the volumetric displacement is estimated from the commanded displacement based on calibrated electrical current through the control solenoid.

Figure 5.13 illustrates the sign convention defined for the pump/motor loss model for a given pressure. The sign convention for the pump map is defined with respect to speed, pressure and normalized torque. The sign of the speed of the test pump is defined as positive when spinning in the counter-clockwise (CCW) direction, and negative when spinning in clockwise (CW) direction. Hence, Quadrant 1 and 3 are motoring mode, and Quadrant 2 and 4 are pumping mode. The hydraulic unit is defined to be *motoring*

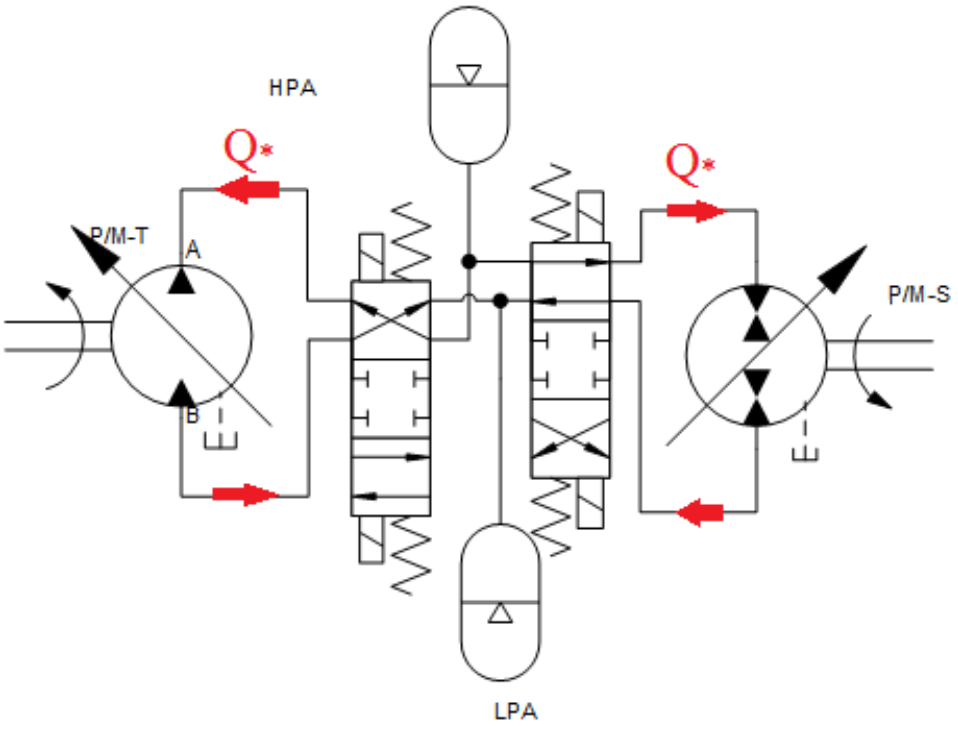

Figure 5.12: Simplified schematic of the pump/motors and directional valve configuration, and sign convention for (T_*, Q_*) (Arrows define positive directions).

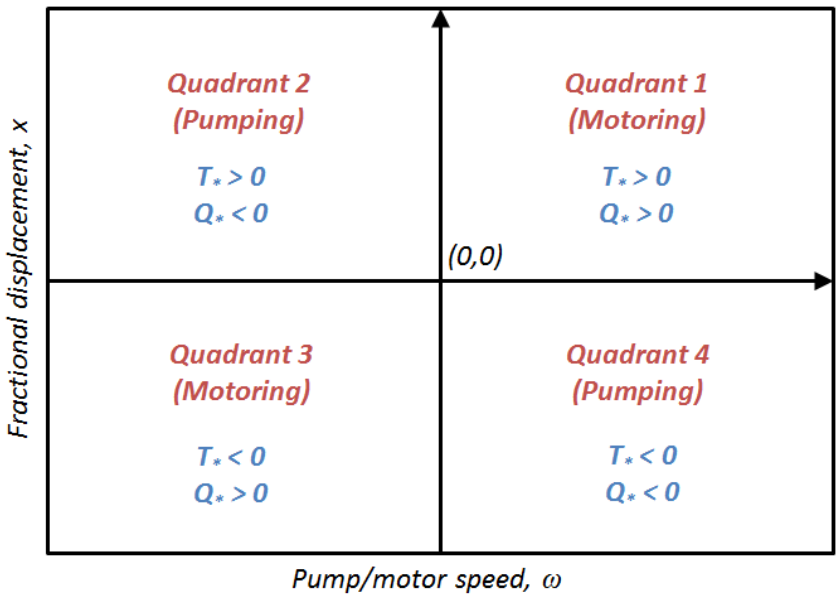

Figure 5.13: Sign conventions for pump/motor loss model.

when $x_* \cdot \omega_*$ is positive, and *pumping* when $x_* \cdot \omega_*$ is negative. Note that due to lack of the capability of the operating over-center, $x^* < 0$ of the pump/motor displacement indicates the the directional valve is switched.

This section describes the procedures to experimentally obtain the actual performance map of a test pump[5] . An experimental pump test-stand (Fig. 5.14) is designed and setup for the purpose of evaluating the efficiency and performance of the variable displacement bent-axis hydraulic pump/motor unit[6] .

The test bench is a regenerative hydraulic test-stand, similar to the set-up described in [72]. The test pump is directly coupled to a driving hydraulic pump/motor unit. 'Regenerative' means that, depending on whether the test pump is pumping or motoring, the driving pump will be operating in the opposite mode. Thus, the shop hydraulic supply only compensates for flow losses in the circuit, as seen in Fig. 5.15. The role of the driving pump is to maintain the shaft speed. A slip ring type torque sensor is installed in between the driving pump and the test pump. This torque sensor provides torque

[5] The test stand pump/motor is different from the pump/motors used in the vehicle but the basic model and displacement are the same.

[6] The flush pressure valve is removed from the test pump in order to reduce leakage.

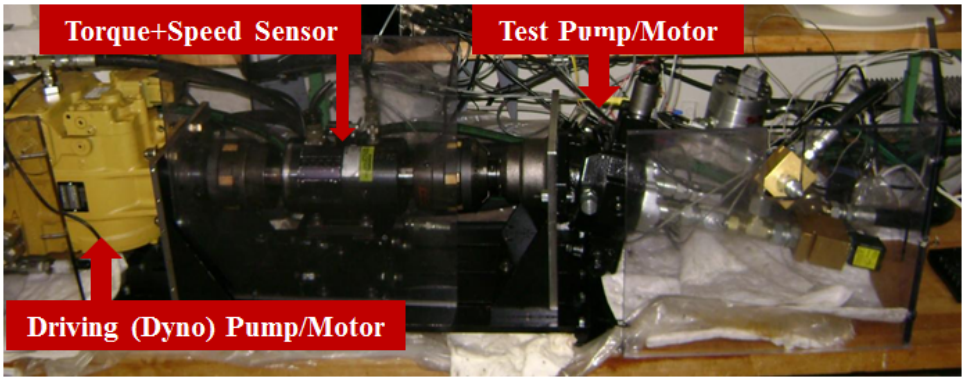

Figure 5.14: Regenerative pump test-stand setup.

measurement and it includes a digital sensor. A Kalman filter is used to convert the speed count to the output pump's filtered speed measurement. The filtered speed is used for feedback control of the pump speed. The experiment is conducted by maintaining the pump/motor speed, and varying the pressure and displacement to measure performance and efficiency at the specific condition.

5.3.1 Pump/Motor Performance Model

Based on the work done in [73], a linear model with constant coefficients is modified to model the characteristics of a hydrostatic pump/motor. Similarly, a linear torque and flow model with respect to pressure and speed for the pump/motor is hypothesized here to describe the loss characteristics of the hydraulic unit. It is assumed that the demanded volumetric displacement $D_* = D_{max}x_*$, where D_{max} is the maximum volumetric displacement of the hydraulic pump/motor unit.

Torque Model:

$$T_*(x_*, P_{sys}, \omega_*) = C_v(x_*, Q_d)P_{sys} + C_w(x_*, Q_d)\omega_* + C_f(x_*, Q_d) \tag{5.11}$$

where T_* is the unit's torque in Nm, P_{sys} is the system pressure in Pa[7] , ω_* is the unit's rotational speed in rad/s, $x_* \in [0, 1]$ is the normalized displacement, and $Q_d \in [1, 2, 3, 4]$ is the quadrant.

[7] The system pressure here is which is the pressure difference between the high and low pressure accumulator, and constrained to be non-negative.

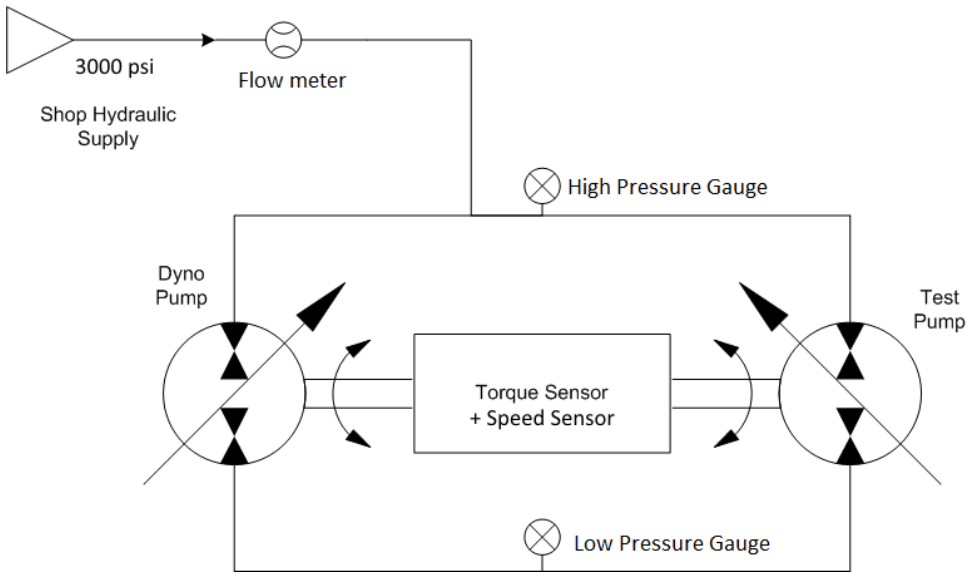

Figure 5.15: Simplified schematic of the pump test-stand setup.

$C_v(x_*, Q_d), C_w(x_*, Q_d), C_f(x_*, Q_d)$ are the coefficients for the torque model that are related to pressure, speed and intercept respectively. By applying linear least squares to fit T_*, with (P_{sys}, ω_*) obtained experimentally, the coefficients C_v, C_w, C_f can be determined in Eq. (5.11) for each (x_*, Q_d).

The coefficients for the torque model $C_v(x_*, Q_d), C_w(x_*, Q_d), C_f(x_*, Q_d)$ are also parameterized into 3rd order polynomials,

$$C_* = a_3 x_*^3 + a_2 x_*^2 + a_1 x_* + a_0$$

where (a_3, a_2, a_1, a_0) are the polynomial coefficients, and obtained similarly through the least squares method. The variation of the coefficients for different displacements and quadrants are plotted in Fig. 5.16 $\sim$ 5.19, and summarized in Tab. 5.2. The coefficient C_v varies fairly linearly with respect to pressure. The coefficient C_w matches the 3rd order polynomial trend with respect to speed. Even though the coefficient C_f does not show a clear trend, C_f is approximately 5 orders-of-magnitude smaller than the operating torque.

A torque/flow prediction example can be seen in Fig. 5.20. The predicted data points overlapped the experimentally obtained data points.

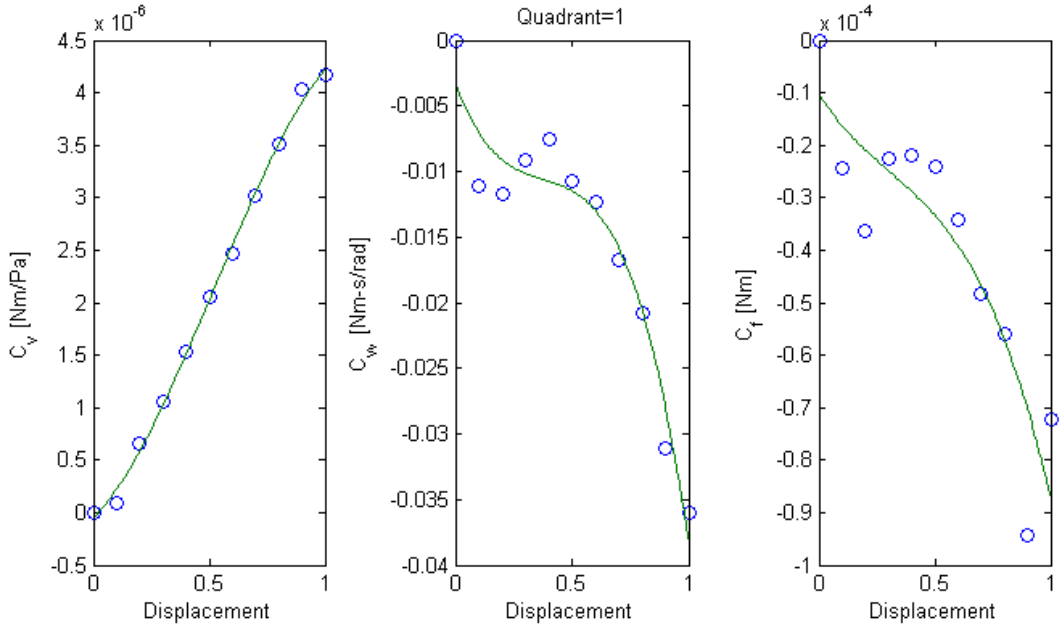

Figure 5.16: Torque model parameters variation in Quadrant 1.

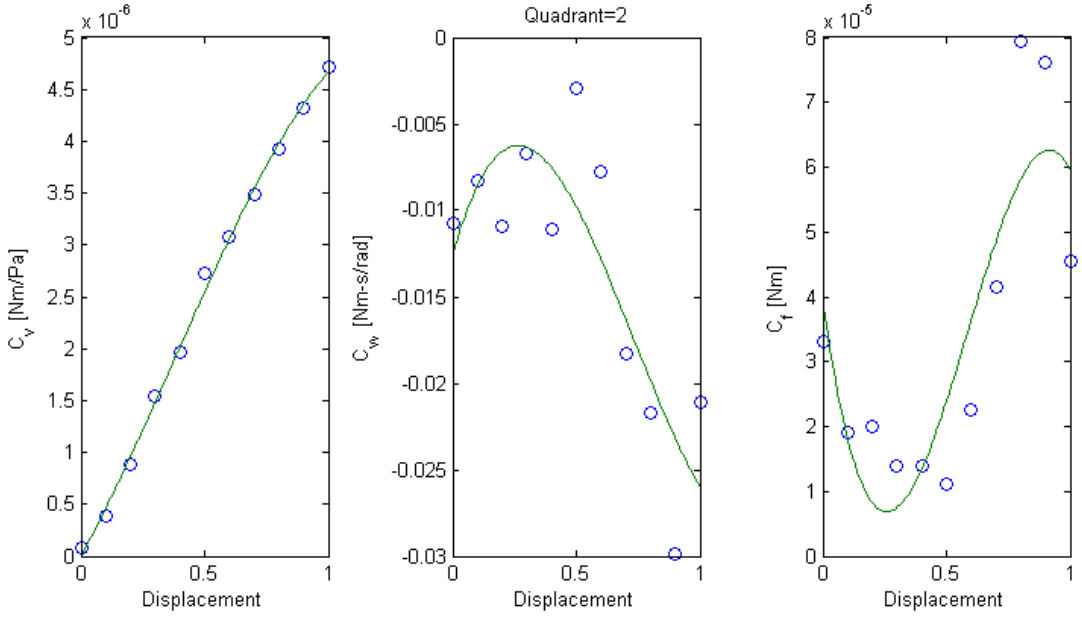

Figure 5.17: Torque model parameters variation in Quadrant 2.

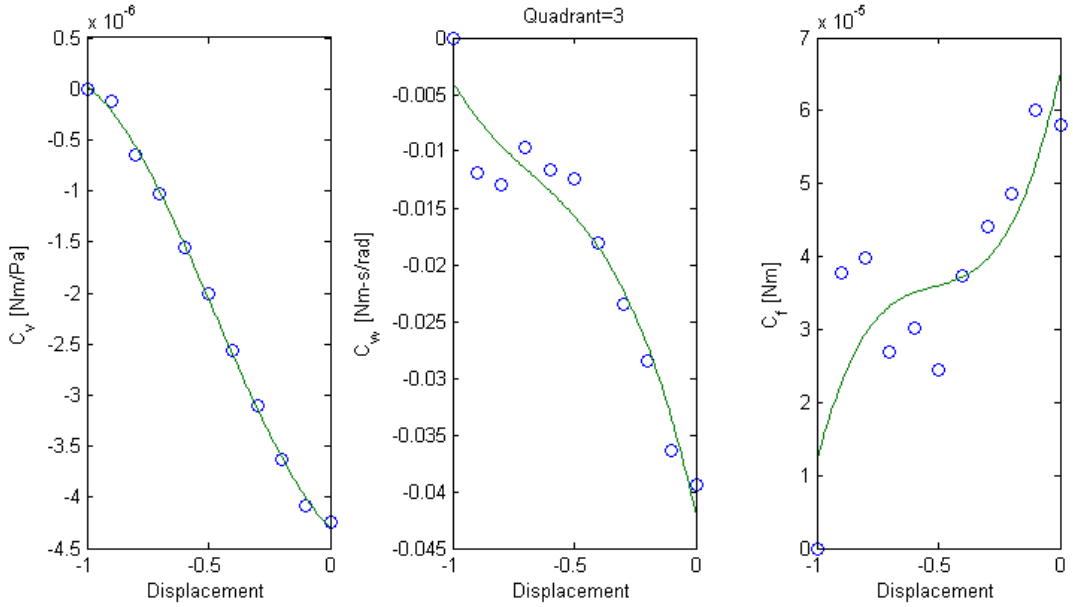

Figure 5.18: Torque model parameters variation in Quadrant 3.

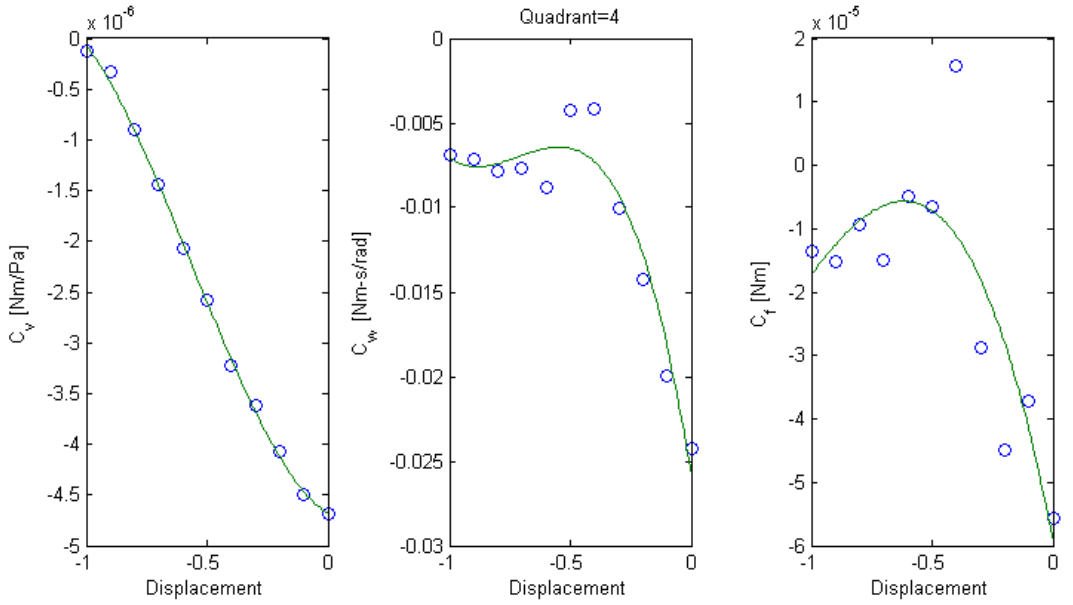

Figure 5.19: Torque model parameters variation in Quadrant 4.

Quadrant	Coeff.	a_3	a_2	a_1	a_0
Q1	$C_v \times 10^{-5}$	-0.3764	0.5891	0.2149	-0.0047
	C_w	-0.1006	0.1138	-0.0483	-0.0032
	$C_f \times 10^{-3}$	-0.1081	0.1004	-0.0693	-0.0102
Q2	$C_v \times 10^{-5}$	-0.2288	0.2568	0.4379	-0.0006
	C_w	0.0539	-0.1187	0.0514	-0.0126
	$C_f \times 10^{-3}$	-0.3944	0.6943	-0.2799	0.0396
Q3	$C_v \times 10^{-5}$	0.4635	0.6621	-0.2335	-0.4299
	C_w	-0.0557	-0.1123	-0.0948	-0.0420
	$C_f \times 10^{-3}$	0.1772	0.2760	0.1522	0.0653
Q4	$C_v \times 10^{-5}$	0.4667	0.7865	-0.1418	-0.4683
	C_w	-0.0614	-0.1319	-0.0893	-0.0258
	$C_f \times 10^{-3}$	-0.0617	-0.2169	-0.1970	-0.0592

Table 5.2: Pump/motor torque model 3rd order model coefficients (C_v, C_w, C_f), where $C_* = a_3 x_*^3 + a_2 x_*^2 + a_1 x_* + a_0$.

Flow Model:

$$Q_*(x_*, \omega_*, P_{sys}) = C_s(x_*, Q_d)\omega_* + C_p(x_*, Q_d)P_{sys} + C_r(x_*, Q_d) \tag{5.12}$$

where Q_* is the unit's flow rate in m^3/s, P_{sys} is the system pressure in Pa, ω_* is the unit's rotational speed in rad/s, and $x_* \in [-1, 1]$ is the normalized displacement.

$C_s(x_*, Q_d), C_p(x_*, Q_d), C_r(x_*, Q_d)$ are the coefficients for the flow model related to speed, pressure and intercept respectively. Similar to the torque model, the coefficients are determined using linear least squares, fitting the experimental data Q_* with (ω_*, P_{sys}) in Eq. (5.12).

Similarly, the coefficients of the flow model $C_s(x_*, Q_d), C_p(x_*, Q_d), C_r(x_*, Q_d)$ are parameterized into 3rd order polynomials:

$$C_* = b_3 x_*^3 + b_2 x_*^2 + b_1 x_* + b_0$$

where (b_3, b_2, b_1, b_0) are the polynomial coefficients obtained using the least squares method. The variation of the coefficients for different displacements and quadrants are plotted in Fig. 5.21 $\sim$ 5.24 and summarized in Tab. 5.3. The coefficient C_s varies fairly linearly with respect to speed. The coefficient C_p does not show clear trends with

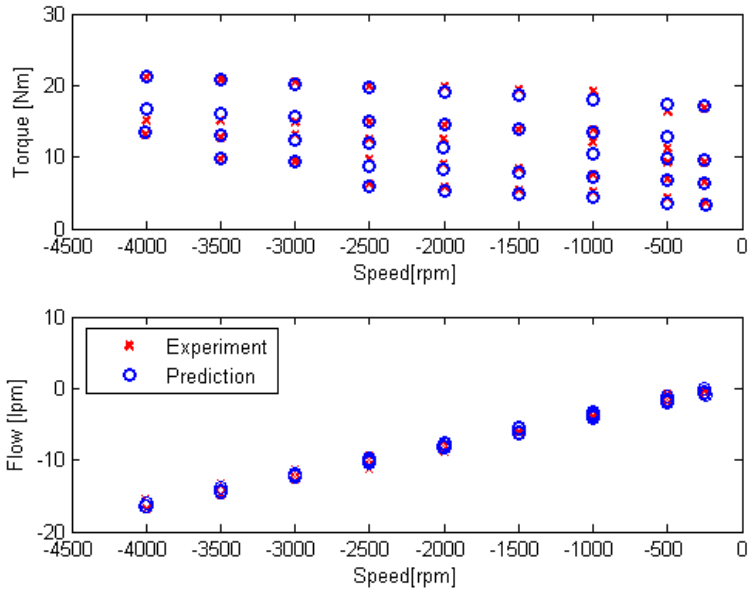

Figure 5.20: Example of torque and flow predictions, for $x = 0.3$ at various system pressures.

pressure, and C_r is approximately 6 orders-of-magnitude smaller than maximum flow of the pump/motor.

The main difference compared to the model originally proposed by [73] is that each coefficient $C_{v,w,f,s,p,r}(x_*, Q_d)$ is defined as a function of the command normalized displacement $x_* \in [0, 1]$ and operating quadrant $Q_d \in [1, 2, 3, 4]$, as illustrated in Fig. 5.13, instead of constant coefficients in [73].

Pump/Motor Efficiencies: From the above empirically fitted torque and flow models of the pump/motors, the mechanical efficiency and loss of the hydraulic pump/motors in **motoring mode** (Quadrants 1 and 3) are calculated as:

$$\eta_{mech}(x_*, P_{sys}, \omega_*) = \frac{T_*(x_*, P_{sys}, \omega_*)}{P_{sys} D_{max} x_* / 2\pi} \tag{5.13}$$

$$Loss_{mech}(x_*, P_{sys}, \omega_*) = sgn(\omega_*) \cdot \left[\frac{P_{sys} D_{max} x_*}{2\pi} - T_*(x_*, P_{sys}, \omega_*) \right] \tag{5.14}$$

The volumetric efficiency and loss of the hydraulic pump/motor in **motoring mode**

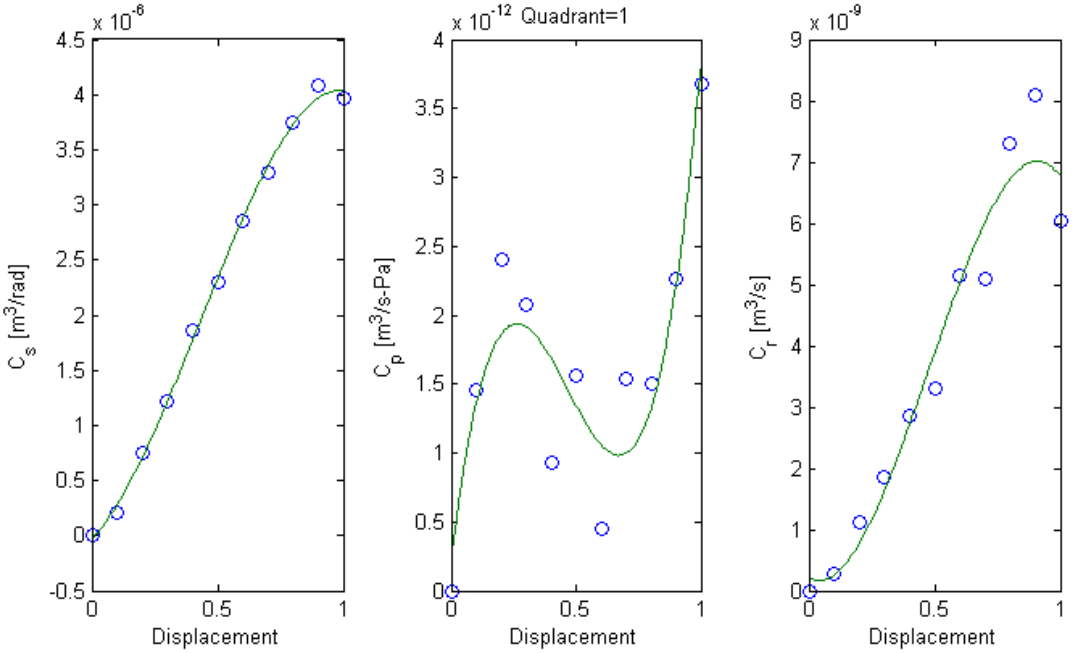

Figure 5.21: Flow model parameters variation in Quadrant 1.

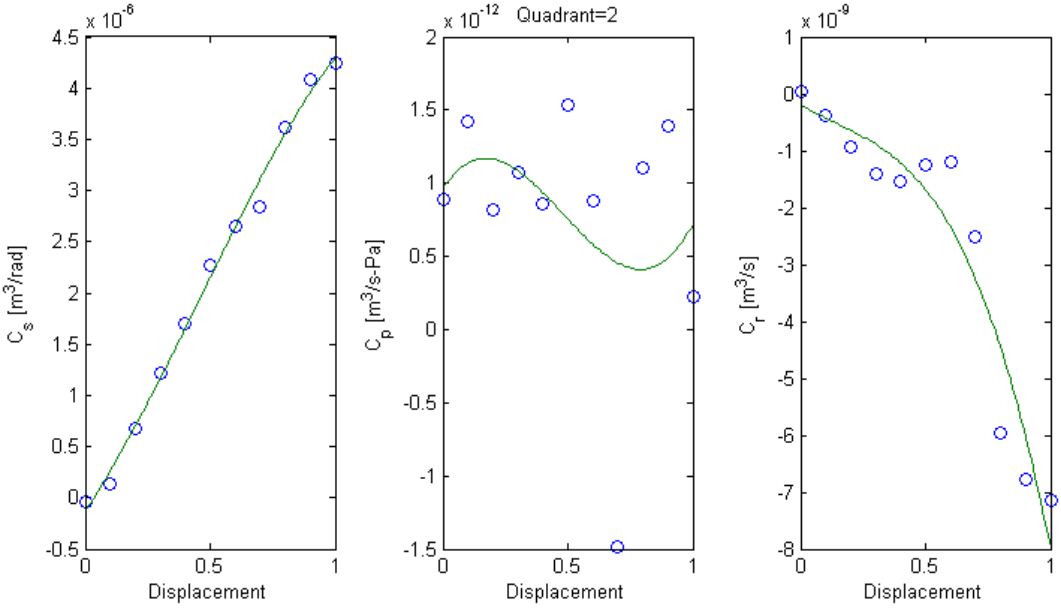

Figure 5.22: Flow model parameters variation in Quadrant 2.

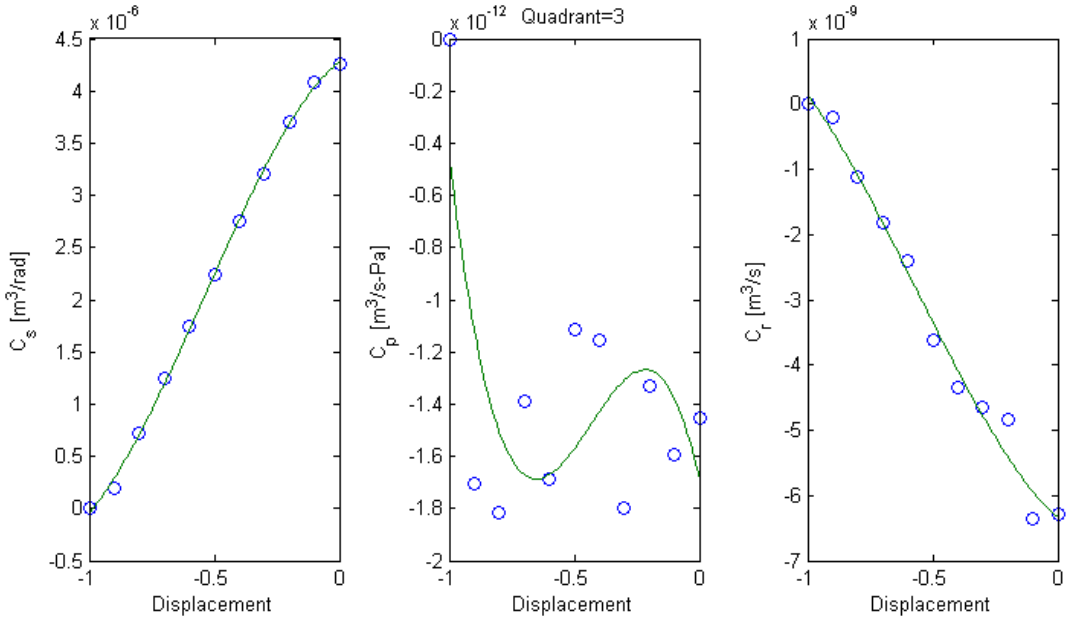

Figure 5.23: Flow model parameters variation in Quadrant 3.

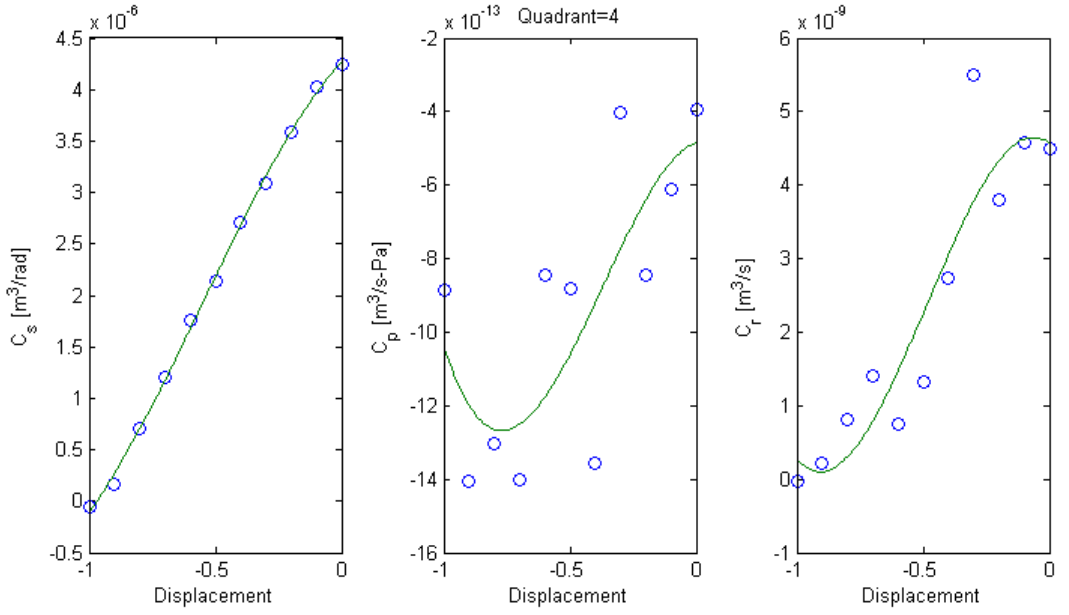

Figure 5.24: Flow model parameters variation in Quadrant 4.

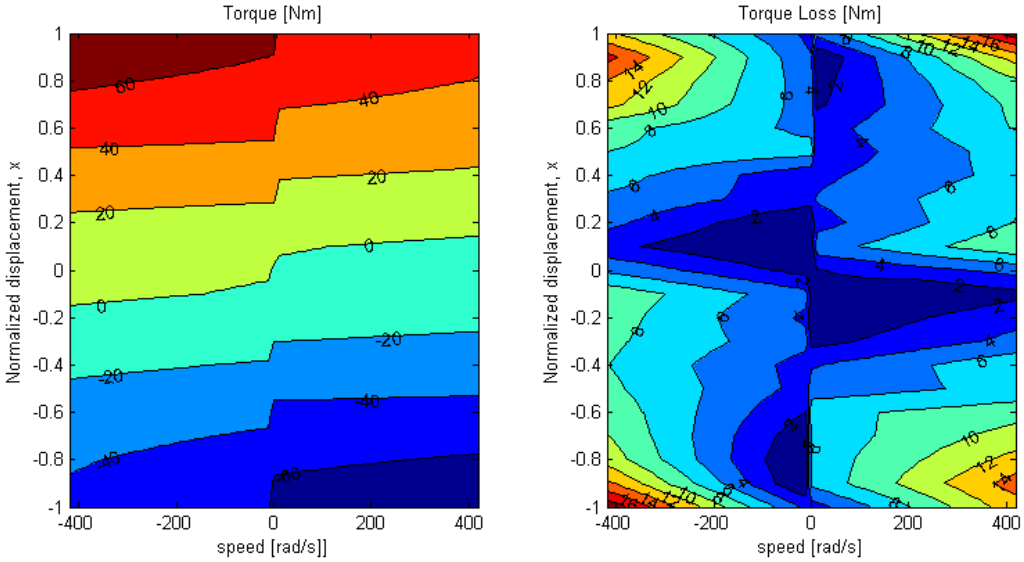

Figure 5.25: Torque and torque loss model at 13.8MPa (2000psi).

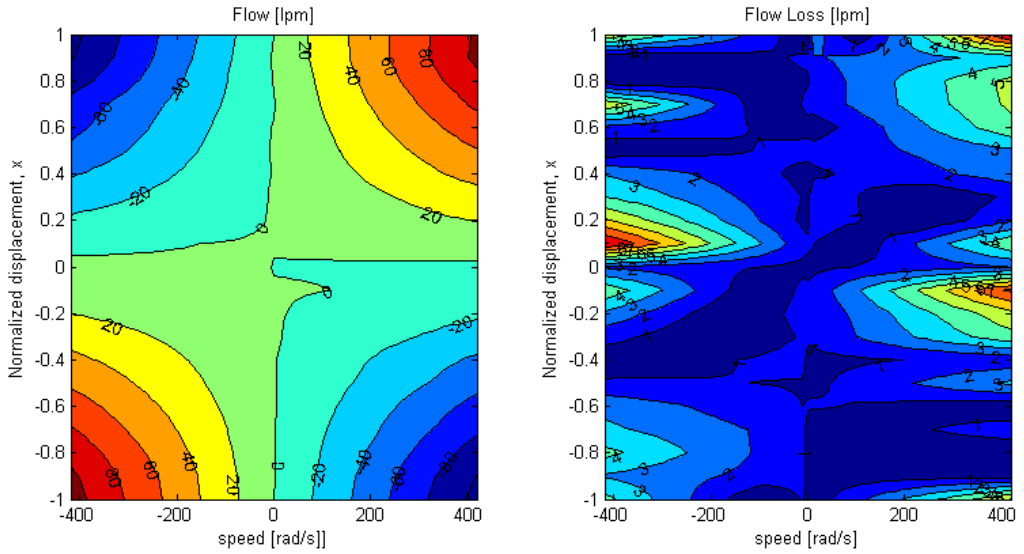

Figure 5.26: Flow and flow loss model at 13.8MPa (2000psi).

Quadrant	Coeff.	b_3	b_2	b_1	b_0
Q1	$C_s \times 10^{-5}$	-0.6110	0.7810	0.2360	-0.0027
	$C_p \times 10^{-10}$	0.2809	-0.3935	0.1486	0.0024
	$C_r \times 10^{-7}$	-0.2091	0.2972	-0.0225	0.0021
Q2	$C_s \times 10^{-5}$	-0.2052	0.2811	0.3663	-0.0125
	$C_p \times 10^{-10}$	0.0631	-0.0910	0.0254	0.0097
	$C_r \times 10^{-7}$	-0.0906	0.0400	-0.0272	-0.0019
Q3	$C_s \times 10^{-5}$	-0.3989	-0.6506	0.1803	0.4277
	$C_p \times 10^{-10}$	-0.1028	-0.1340	-0.0436	-0.0169
	$C_r \times 10^{-7}$	0.0442	0.0759	-0.0331	-0.0634
Q4	$C_s \times 10^{-5}$	-0.2803	-0.4637	0.2534	0.4263
	$C_p \times 10^{-10}$	-0.0309	-0.0344	0.0020	-0.0049
	$C_r \times 10^{-7}$	-0.1512	-0.2206	-0.0265	0.0457

Table 5.3: Pump/motor flow model 3rd order model coefficients (C_s, C_p, C_r), where $C_* = b_3 x_*^3 + b_2 x_*^2 + b_1 x_* + b_0$.

(Quadrants 1 and 3) are computed as:

$$\eta_{vol}(x_*, P_{sys}, \omega_*) = \frac{\omega_* D_{max} x_* / 2\pi}{Q_*(x_*, P_{sys}, \omega_*)} \tag{5.15}$$

$$Loss_{vol}(x_*, P_{sys}, \omega_*) = Q_*(x_*, P_{sys}, \omega_*) - \frac{\omega_* D_{max} x_*}{2\pi} \tag{5.16}$$

The mechanical efficiency and loss of the hydraulic pump/motor in **pumping mode** (Quadrants 2 and 4) are calculated as:

$$\eta_{mech}(x_*, P_{sys}, \omega_*) = \frac{P_{sys} D_{max} x_* / 2\pi}{T_*(x_*, P_{sys}, \omega_*)} \tag{5.17}$$

$$Loss_{mech}(x_*, P_{sys}, \omega_*) = sgn(\omega_*) \cdot \left[\frac{P_{sys} D_{max} x_*}{2\pi} - T_*(x_*, P_{sys}, \omega_*) \right] \tag{5.18}$$

The volumetric efficiency and loss of the hydraulic pump/motor in **pumping mode** (Quadrants 2 and 4) are computed as:

$$\eta_{vol}(x_*, P_{sys}, \omega_*) = \frac{Q_*(x_*, P_{sys}, \omega_*)}{\omega_* D_{max} x_* / 2\pi} \tag{5.19}$$

$$Loss_{vol}(x_*, P_{sys}, \omega_*) = Q_*(x_*, P_{sys}, \omega_*) - \frac{\omega_* D_{max} x_*}{2\pi} \tag{5.20}$$

The mechanical and volumetric losses are defined such that in each quadrant, the losses are positive. Figure 5.25 depicts the torque and torque loss, and Fig. 5.26 depicts the flow and flow loss of the pump/motor at 13.8MPa. The overall power loss model of the pump/motor at 13.8MPa is shown in Fig. 5.27.

Individual torque and flow losses information is used in the low level controller to achieve engine control and vehicle output torque control. With the torque loss information, displacement x_* to achieve the desired pump/motor torque can be evaluated as a function of desired torque, system pressure, and speed (T_*, P_{sys}, ω_*) by:

$$x_*(T_*, P_{sys}, \omega_*) = \frac{2\pi}{P_{sys} D_{max}} \left(T_* + sgn(\omega_*) \cdot Loss_{mech,pm*}(x_*, P_{sys}, \omega_*)\right) \tag{5.21}$$

Similarly, with the flow loss information, displacement x_* to achieve the desired pump/motor flow can be evaluated as a function of desired flow, system pressure, and speed (Q_*, P_{sys}, ω_*) by:

$$x_*(Q_*, P_{sys}, \omega_*) = \frac{2\pi}{\omega_* D_{max}} \left(Q_* - Loss_{vol,pm*}(x_*, P_{sys}, \omega_*)\right) \tag{5.22}$$

However, as seen in Eqs. (5.21) and (5.22), the loss maps are also dependent on P/M displacements, making the evaluation of x_* to achieve a desired torque or flow to be implicit. Thus, this function is evaluated beforehand and saved as numerical maps.

5.4 Hydraulic Accumulators

The hydraulic accumulators are utilized for energy storage in hydraulic hybrid transmissions, an important component that offers an extra control degree-of-freedom for engine management. A high pressure and a low pressure accumulator, each 38 liter (10 gallons) in capacity, are connected to the high and low pressure lines respectively. The accumulators are modeled as isothermal gas-charged accumulators. By applying the ideal gas law, the high pressure accumulator is modeled as:

$$P_{high}(t) = \frac{P_{pr,hi} V_{0,hi}}{V_{0,hi} - V_{HPA}(t)} \tag{5.23}$$

$$\dot{V}_{HPA} := Q_{HPA} = -(Q_T + Q_S) \tag{5.24}$$

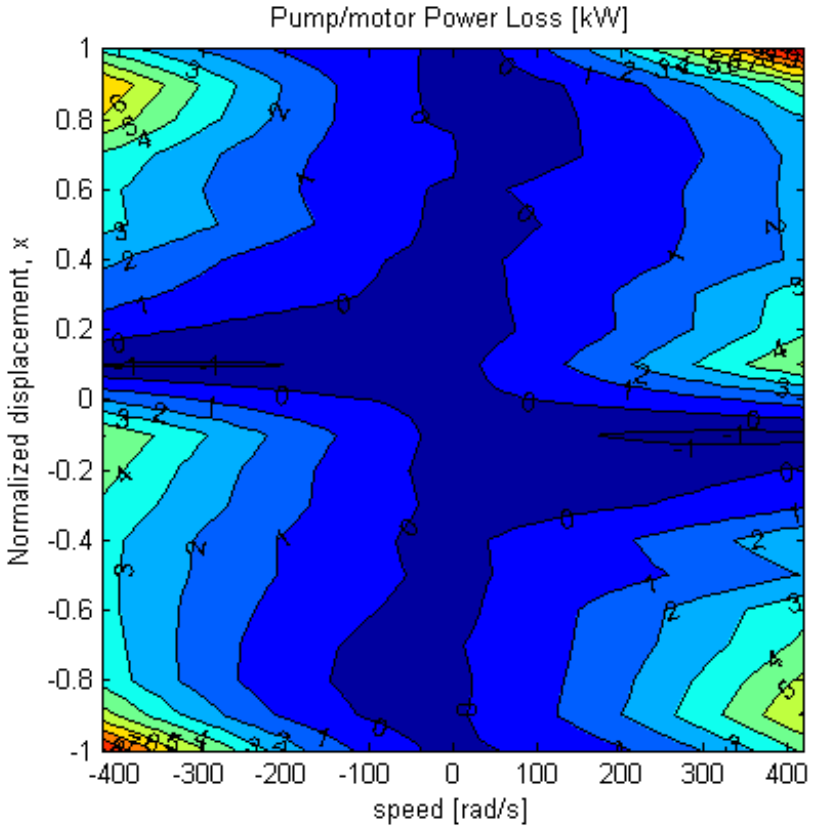

Figure 5.27: Power loss model of the pump/motor unit at 13.8MPa (2000psi).

P_{pr} is the gas pre-charged pressure, V_0 is the total accumulator volume, and V_{HPA} is the stored volume of hydraulic fluid, Q_{HPA} is the liquid accumulator input flow rate which is also the sum of the pump/motor flows to the high pressure line in Eq. (5.24). The low pressure accumulator pressure P_{low} is modeled similarly except that a charge pump (Q_{cp}) for replenishing leakage is present.

$$P_{low}(t) = \frac{P_{pr,lo}V_{0,lo}}{V_{0,lo} - V_{LPA}(t)} \tag{5.25}$$

$$\dot{V}_{LPA} := Q_{LPA} = (Q_T - Loss_{vol,T}) + (Q_S - Loss_{vol,S}) + Q_{cp} \tag{5.26}$$

where Q_{cp} is the volumetric output flow of the charge pump, and it only runs intermittently at a fixed speed[8] . $Q_i - Loss_{vol,i}$ is the ideal pump/motor flow. The system pressure is defined as $P_{sys} := P_{high} - P_{low}$.

5.5 Overall Powertrain Dynamic Model

With the components' models described in Sec. 5.2 through 5.4, an overall powertrain model can be assembled. To further expand the modeling work in Ch. 2 to understand the physical system and design the powertrain controller, the transmission's kinematic model and dynamic model will be derived in this section. Moreover, components' characteristics will be discussed and identified. The rest of this section will be organized as follows: Section 5.5.1 applies the kinematic modeling approach in Ch. 2 on the vehicle. Section 5.5.2 presents the overall vehicle dynamics of Generation I vehicle.

5.5.1 Transmission's Kinematic Relations

According to the discussions in Ch. 2, the power-split transmission can be modeled as a four-port system. By assuming a lossless geartrain, the kinematic relationship between

[8] Charge pump is on when the sum of fluid volume of both accumulators is smaller than $34.2L$ ($9gal$), and is off when sum of fluid volume is larger than $41.8L$ ($11gal$).

the engine, wheel, and both pump/motors can be derived as:

$$\begin{pmatrix}\omega_T\\ \omega_S\end{pmatrix} = \begin{pmatrix}R_T & 0\\ \frac{1}{\rho R_S} & -\frac{(1+1/\rho)}{R_S}\end{pmatrix}\begin{pmatrix}\omega_{eng}\\ \omega_{out}\end{pmatrix} \tag{5.27}$$

$$\omega_{out} = R_f\omega_{whl} \tag{5.28}$$

$$\begin{pmatrix}T_T\\ T_S\end{pmatrix} = \begin{pmatrix}-\frac{1}{R_T} & -\frac{1}{R_T(1+\rho)}\\ 0 & \frac{R_S}{1+1/\rho}\end{pmatrix}\begin{pmatrix}T_{eng}\\ T_{out}\end{pmatrix} \tag{5.29}$$

$$T_{out} = \frac{1}{R_f}T_{whl} \tag{5.30}$$

where ω_T and ω_S are the P/M-T and P/M-S speed, T_T and T_S are the P/M-T and P/M-S torque respectively. ω_{eng} and T_{eng} are the engine speed and torque. ω_{out} and T_{out} are the transmission output speed and torque. ω_{whl} and T_{whl} are the wheel speed and torque. $\rho = 0.25$ is the radius-ratio of the sun and ring of the planetary gear, $R_T = 1.3$ is the fixed gear ratio on P/M-T, $R_S = 2$ is the fixed gear ratio on P/M-S, and $R_f = 3.45$ is the ratio of the differential geartrain at the rear wheels.

Frictionless gear mesh is assumed during the development of the transmission gearbox model. However, as discussed in Ch.7, the experiments show transmission friction loss is significant.

5.5.2 Vehicle Dynamic Model

Torque relationships associated with the planetary gearset is shown in Fig. 5.28. Based on Newton's 2nd Law and inertial dynamics of each mesh of the planetary gearset, and assuming zero gears' inertia, the dynamic equations can be summarized as:

$$(J_{eng} + R_T^2 J_T)\dot{\omega}_{eng} = T_{eng} + R_T T_T - T_{ring} \tag{5.31}$$

$$J_S\dot{\omega}_S = T_{sun}\cdot R_S + T_S \tag{5.32}$$

$$J_{veh}\dot{\omega}_{out} = T_{carrier} - T_{load} \tag{5.33}$$

where $J_{eng} = 0.0975 kgm^2$ is the engine rotational inertia, $J_{veh} = MR_{tire}^2 = 65.36 kgm^2$ is the equivalent vehicle rotational inertia, $M = 1000kg$ is the vehicle mass, $R_{tire} = 0.31m$ is the tire's effective radius, and $J_T = J_S = 0.0018 kgm^2$ is the pump/motor's

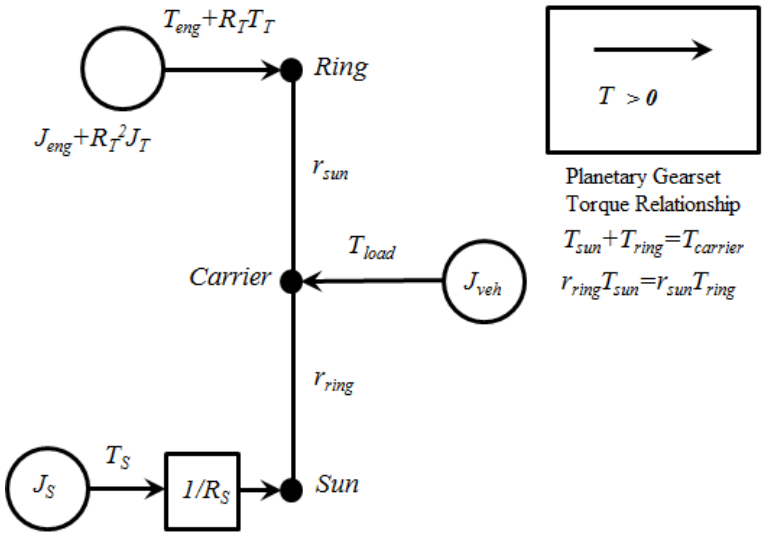

Figure 5.28: Torque relationships associated with the planetary gearset.

rotational inertia individually. $T_{sun}, T_{ring}, T_{carrier}$ represent the internal torques of the planetary gear, r_{sun}, r_{ring} represent the sun and ring radii of the planetary gearset. By applying the kinematic constraints, $\omega_S = \frac{1}{\rho R_S}\omega_{eng} - \frac{(1+1/\rho)}{R_S}\omega_{out}$ in Sec. 5.5.1 and eliminating $T_{sun}, T_{ring}, T_{carrier}$ from Eqs. (5.32)$\sim$ (5.33), the dynamic equations above can be reduced to a two degree-of-freedom system:

$$\begin{pmatrix} (J_{eng} + R_T^2 J_T + \frac{1}{\rho^2 R_S^2} J_S) & -\frac{(1+\rho)}{\rho^2 R_S^2} J_S \\ -\frac{(1+\rho)}{\rho^2 R_S^2} J_S & (J_{veh} + \frac{(1+1/\rho)^2}{R_S^2} J_S) \end{pmatrix} \begin{pmatrix} \dot{\omega}_{eng} \\ \dot{\omega}_{out} \end{pmatrix} = \begin{pmatrix} T_{eng} + R_T T_T + \frac{1}{\rho R_S} T_S \\ -\frac{(1+1/\rho)}{R_S} T_S - T_{load} \end{pmatrix} \tag{5.34}$$

where $T_{eng} = K_{eng} K_\omega u^*(t) - T_{frict}(\omega_{eng})$ as defined in Eq. (5.6), and T_* is defined in Eq. (5.9)

Table 5.4 summarizes the parameters used and experimentally obtained for the development of the Generation I vehicle model.

Parameter	Value	Parameters	Value
ρ	0.25	K_ω	0.0056 g/rad
R_T	1.3	K_{eng}	19142 J/g
R_S	2	λ_{sol}	10.18 rad/s
R_f	3.45	D_{max}	28.1 cc
J_{eng}	0.0975 kgm^2	$P_{pr,hi}$	11.0 MPa
J_T	0.0018 kgm^2	$P_{pr,lo}$	1.0 MPa
J_S	0.0018 kgm^2	$V_{0,hi,lo}$	38 L
J_{veh}	65.36 kgm^2		

Table 5.4: Parameters for the Generation I vehicle.

5.6 Concluding Remarks

The modeling of the Generation I input-coupled powersplit hydraulic hybrid vehicle has been presented in this chapter. The engine is modeled as a quasi-static system, where the fuel conversion efficiency is a static map, with the fuel delivery and inertia modeled as the engine dynamics. The fuel consumption map of the engine is obtained using the in-house built dynamometer. The dynamics of the engine has been validated through experiments. The hydraulic pump/motor's efficiency and performance maps are obtained using a regenerative hydraulic test-stand. A hypothesized pump/motor model as a function of the system pressure, rotating speed and normalized displacement is proposed to match the experimental data. The overall vehicle dynamics is reduced to a two-state coupled linear system. The system has been simplified by assuming an ideal gear mesh within the transmission and lumping the gearbox friction effects into torque losses of the engine and pump/motors.

The importance of this chapter is to lay out the baseline performance and control oriented model of each component, such that the basic performance of the hybrid powertrain can be predicted and basic controllers can be designed and implemented. In the following chapter, several cases of energy management strategies will be implemented, and controller implementation issues will be analyzed and discussed.

Chapter 6

Control Design for the Generation I Vehicle

Hybrid vehicles exploit the extra degrees-of-freedom to use the engine power for propulsion or to store energy into energy storage devices, enabling the powertrain to operate the engine at higher efficiency and to regenerate the braking energy, hence reducing fuel consumption and emission. However, this extra flexibility also increases the complexity of controlling the hybrid powertrain. There are two main challenges in controlling a hydraulic hybrid powertrain system, (i) determining the instantaneous optimal usage of the stored accumulator energy, and (ii) achieving the driver's demanded vehicle power.

In this dissertation, several energy management strategies, including a continuously variable transmission (CVT) strategy (as a baseline for comparison), a Dynamic Programming (DP) strategy (as best fuel economy for upper bound comparison), a Lagrange Multiplier strategy, a Modified Lagrange Multiplier (MLM) Strategy, and a rule based hybrid energy management strategy to manage the stored energy will be presented.

In this chapter, the design and simulation of the three-level hierarchical control approach for Generation I vehicle with a redesigned hardware will be presented. The rest of this chapter will be organized as follows: Section 6.1 presents a review of hybrid powertrain controller design, including energy management strategy synthesis. Section 6.2

explains the control structure proposed to control the vehicle's powertrain system. Section 6.3 discusses several energy management strategies to be implemented on the Generation I test bed. Section 6.4 presents the simulation results and discussions on the controllers performance and behavior. Section 6.5 contains some concluding remarks.

6.1 Review of Hybrid Powertrain Control Design

To address the optimal energy management issue, efforts are being made to improve the fuel efficiency by considering the equivalent fuel usage of the storage energy [74, 75], statistically estimating the driver's future demands, or even predicting vehicle's trajectories via GPS technologies [76]. The effort in [76] studies the fuel economy improvements for an electric parallel hybrid vehicle by predicting vehicle's trajectories. However, due to the substantial computational burden of this method, this approach will not be adopted in this dissertation.

There are numerous research works that focus solely on developing energy management strategies for hybrid vehicles such as Dynamic Programming (DP) in [77], Stochastic Dynamic Programming (SDP) in [61], Equivalent Consumption Minimization Strategy (ECMS) in [74, 75] and Pontryagin's Minimization in [78], and they are mainly for electric hybrid vehicles. Dynamic Programming will be utilized to benchmark the best fuel economy performance of the Generation I vehicle in this chapter. Due to the high computation requirement for SDP, this approach will not be considered in this chapter. The ECMS approach synthesizes the strategy by converting stored energy into equivalent fuel consumption. This chapter utilizes the Lagrange Multiplier method which is similar to the ECMS approach, and a modified version of Lagrange Multiplier method designed for real-time implementation.

Filipi and Kim (2010) [79] reported on the control of a series hydraulic hybrid vehicle using a thermostatic energy management (engine fully on/off strategy) approach. The thermostatic strategy is simple and easily implementable in experiments. Kumar (2010) [80] investigated energy management strategies for an output coupled power-split hydraulic hybrid transmission. However, in their experiments, a hardware-in-the-loop simulation is conducted where the engine is simulated using an electric dynamometer. This chapter will present the development of various energy management strategies and

evaluate the performance of the strategies. Experimental results of implementing the strategies will be presented in Ch. 7.

The three-level hierarchical control approach originally proposed in [11, 81] is used to control the HMT hydraulic hybrid vehicle test bed in this research. This control strategy segregates the tasks of the drive-train into three layers that respectively 1) manages the accumulator energy storage *(high level)*; 2) performs vehicle level optimization *(mid-level)*; and 3) attains the desired vehicle operating condition *(low level)*, as seen in Fig. 6.1. This approach allows controller modularity and the redundancy afforded by the additional degree of freedom in power-split architectures is resolved by the mid-level in an optimal fashion. Various 'high level' energy management strategies can be substituted while retaining the same mid and low level control implementations, which will be demonstrated in this chapter.

In Ch. 2, the low level controller is assumed to be ideal during the vehicle design. However, implementation of the low level controller is needed for actual driving. While there are many works on hybrid vehicle control reported in the literature earlier, most focus on electric hybrids. Also, the majority focus on the 'high level' energy management control aspect to improve fuel economy. Literature of overall control implementation on vehicle hardware, including energy management strategy and individual component actuation, are scarce. The low level controller should (i) satisfy the desired torque command by the driver demand and (ii) ensure that the engine operates at the desired efficient operating point as determined by the higher level controls. A rudimentary control approach is presented in [12], and initial control design for power-split hydraulic hybrid vehicles and implementation of optimal control strategy can be found in [81, 82]. This chapter will discuss the details of low level controller design and the effects of energy management strategy on low level controller performance.

6.2 Three-Level Control Hierarchy

Hybrid power-split transmissions allow arbitrary operation of the engine in order to improve the fuel efficiency. The hydraulic powertrain model presented in Ch. 5 shows that the accumulator flow Q_{acc} and transmission output torque T_{out} are directly controlled by u, x_T, and x_S (engine fuel rack position, P/M-T and S displacement). Consequently,

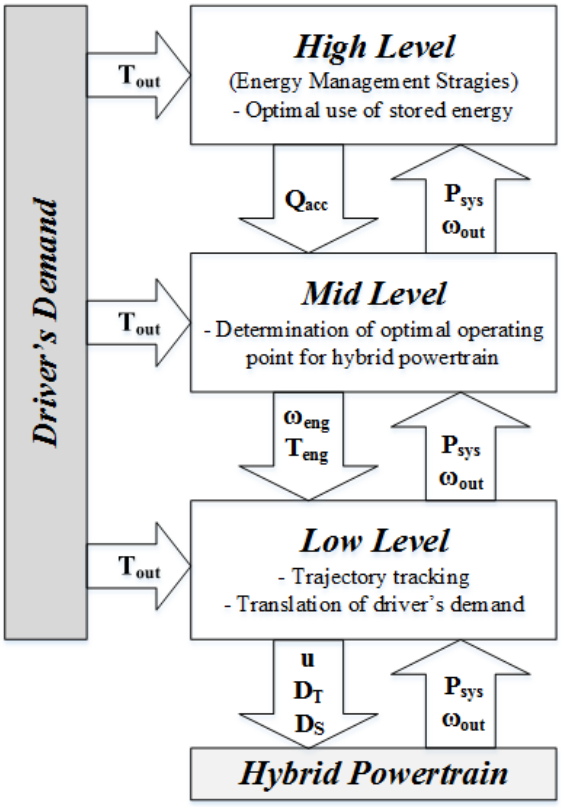

Figure 6.1: The proposed three-level hierarchical control for hybrid powertrain control.

powertrain control is needed to ensure the following:

1. The powertrain is operating optimally, minimizing the powertrain losses (from engine and pump/motors) by choosing when to store or consume accumulator flow.
2. The driver's demand is fulfilled.

In view of these requirements, a three-level hierarchical control architecture can be defined to simplify the powertrain control problem, as described in [11]. This method also has the advantage of implementing different layers at different sampling rates, usually a slower rate for high and mid level and higher rate for low level controls, hence significantly reducing computational burden.

The purpose of the hybrid powertrain controller is to determine the operating speed and torque for the engine and transmission that minimize fuel consumption while satisfying the driver's torque demand. The mid-level resolves one of the two degrees of freedom afforded by the power-split architecture by performing a vehicle level loss minimization that does not depend on drive cycles. The high level control manages accumulator energy which typically involves a computationally expensive, drive cycle dependent, dynamic optimization. With the use of the mid-level control, the high level control has only **one** dynamic state (accumulator pressure P_{sys} or stored energy), and **one** decision variable (accumulator flow Q_{acc} in Eq. (5.24)) which improves computational efficiency.

6.2.1 High-level

The high level control represents the energy management strategy that determines the optimal accumulator power flow ($Pow_{acc} = P_{sys}Q_{acc}$) to ensure the overall system efficiency is maximized throughout a drive cycle:

$$Q_{acc}(P_{sys}) = HighLevel(\omega_{out}, T_{out}, P_{sys}) \tag{6.1}$$

where $HighLevel$ is a generic representation of the high-level control function, Q_{acc} is the desired accumulator flow, P_{sys} is the current system pressure, ω_{out} is the vehicle speed, and T_{out} is the demanded vehicle torque. In order to synthesize the high level controller, an optimized vehicle level loss function (created by the mid level in Sec. 6.2.2)

which captures the total engine and transmission losses for a given accumulator flow is used. A variety of strategies can be employed, e.g. Rule-based strategy [77], Stochastic Dynamic Programming (SDP) [61], Equivalent Consumption Minimization Strategy (ECMS) [24, 75], Pontryagin's Minimization [78], and Lagrange Multipliers [22, 32]. If Q_{acc} is set to be 0, the high level control reduces to non-hybrid CVT operation.

6.2.2 Static Optimization of Powertrain Loss (Mid-level)

For a given system pressure P_{sys} and vehicle (ω_{out}, T_{out}), the selection of engine operating conditions (ω_{eng}, T_{eng}) will have two significant effects, (i) total powertrain loss in Eq. (6.2), and (ii) change in accumulator power flow in Eq. (5.24). Therefore it is necessary to solve the instantaneous loss minimization problem for each possible vehicle output operating point (ω_{out}, T_{out}), system pressure (P_{sys}), and desired accumulator flow (Q_{acc}). The powertrain's total loss is satisfied by a specific Q_{acc} given by Eq. (5.24), and the pump/motors' operation $(\omega_T, T_T, \omega_S, T_S)$ is constrained to fulfill the kinematic relation Eqs. (5.27) $\sim$ (5.29).

Maximizing the system efficiency is equivalent to minimizing the total powertrain system losses. The instantaneous losses of the drivetrain is given by:

$$\begin{aligned} &Loss_{tot}(\omega_{eng}, T_{eng}, \omega_{out}, T_{out}, P_{sys}, Q_{acc}) = \\ &Loss_{eng}(\omega_{eng}, T_{eng}) + Loss_{pmT}(x_T, \omega_T, P_{sys}) + Loss_{pmS}(x_S, \omega_S, P_{sys}) \end{aligned} \tag{6.2}$$

where $Loss_{eng}$ and $Loss_{pmT,S}$ are the loss maps shown in Fig. 5.10 and 5.27 evaluated in Ch. 5. The transmission gearbox and accumulators are assumed to be ideal in Eq. (6.2). $Loss_{tot}$ in Eq. (6.2) is the total power losses in the engine and transmission pump/motors which includes fuel energy conversion losses and all losses due to friction and leakage. x_S and x_T are set to satisfy the kinematic relations Eqs. (5.27) $\sim$ (5.30), the torque and flow relations of the pump/motors in Eqs. (5.9)$\sim$ (5.10) and Eqs. (5.21)$\sim$ (5.22), the accumulator in Eqs. (5.23)$\sim$ (5.26) for the engine operating point (ω_{eng}, T_{eng}), vehicle operating point (ω_{out}, T_{out})), and accumulator flow Q_{acc}.

The mid-level controller translates statically the high-level's decision Q_{acc} and demand vehicle torque T_{out} into optimal operating points for the engine and hydraulics. For the given accumulator flow Q_{acc} (from high level), and desired vehicle torque T_{out}

(from driver), and the current vehicle speed ω_{out} and system pressure P_{sys}, the mid-level controller determines the optimal engine speed/torque $(\omega^*_{eng}, T^*_{eng})$ that is the minimizer for:

$$(\omega^*_{eng}, T^*_{eng}) = \arg \min_{(\omega_{eng}, T_{eng})} Loss_{tot}(\omega_{eng}, T_{eng}, \omega_{out}, T_{out}, P_{sys}, Q_{acc}) \tag{6.3}$$

This optimization does not involve the drive cycle and therefore needs only be computed once off-line as a four-dimension map $(\omega_{out}, T_{out}, P_{sys}, Q_{acc})$. It produces an optimized vehicle loss function $Loss^*(\omega_{out}, T_{out}, P_{sys}, Q_{acc})$ that can be used as an abstraction of the vehicle in computing the high level control.

$$Loss^*(\omega_{out}, T_{out}, P_{sys}, Q_{acc}) = \min_{(\omega_{eng}, T_{eng})} Loss_{tot}(\omega_{eng}, T_{eng}, \omega_{out}, T_{out}, P_{sys}, Q_{acc}) \tag{6.4}$$

This static map is powertrain-specific and energy management strategy independent. This feature provides the modularity for the three-level hierarchy control strategy. Controller modularity means high or low level control can be replaced without modifying the mid-level while resolving the degree-of-freedom afforded by the power-split architecture. $Q_{acc} = -(Q_T + Q_S)$ in Eq. (5.24) is defined to be satisfied with $(x_T, \omega_T, x_S, \omega_S)$. $Q_{acc} > 0$ is defined as flow into accumulator (charging).

Figure 6.2 illustrates the minimization process of the Mid-level for a specific demanded vehicle output condition (ω_{out}, T_{out}), and system pressure (P_{sys}). The left plot shows the contour map of accumulator power $Pow_{acc} = P_{sys}Q_{acc}$ as functions of engine speed and torque, and the right plot shows the contour map of powertrain total loss map $Loss_{tot}$ as functions of engine speed and torque. For instance, if the accumulator power, $Pow_{acc} = 6kW$, is desired, the red curve on the contour represents all possible engine operating points that can achieve the specified Pow_{acc}. It is then mapped to the total loss of the powertrain contour, and the optimal engine operating point $(\omega^*_{eng} = 188.5rad/s, T^*_{eng} = 50Nm)$ results in minimum total loss $Loss^*$ (yellow star) of 25kW.

Mid-Level Controller Simplification: The optimal engine operating points determined by this method requires high computational memory (large data maps) for implementation. Also, due to numerical optimization, mid-level generates non-smooth

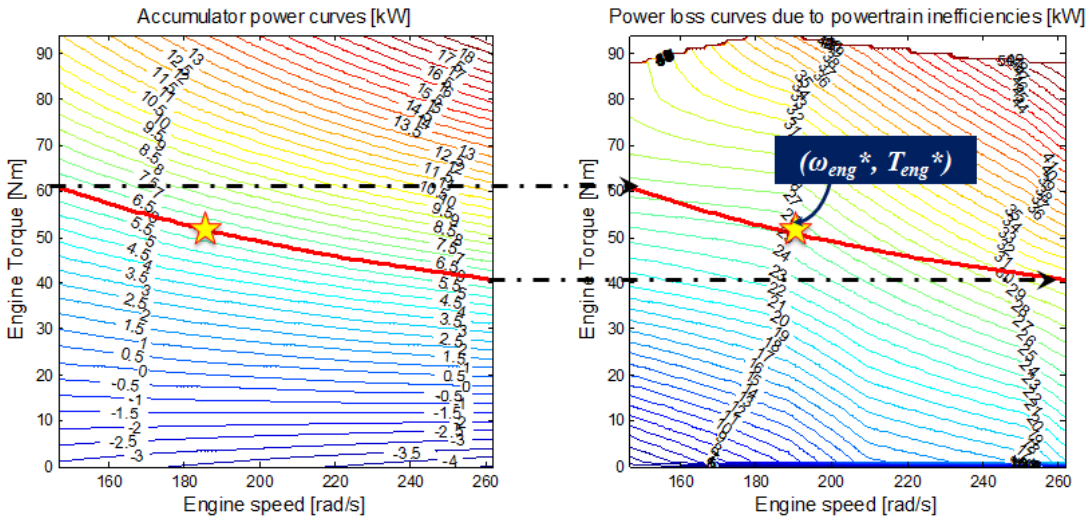

Figure 6.2: Illustration of powertrain loss static optimization for a specific accumulator power ($Pow_{acc} = 6kW$). Mid-level controller maps optimal engine operating points (stars) from accumulator power (left) to powertrain total loss (right).

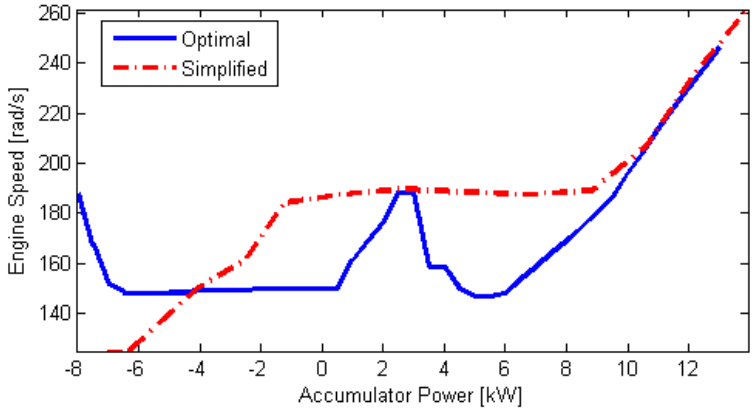

Figure 6.3: An example of non-smooth desired engine speed generated by the mid-level controller, for vehicle condition at $\omega_{whl} = 25$ rad/s, $T_{whl} = 190$ Nm

desired engine speed with respect to accumulator power Pow_{acc} (see Fig. 6.3). These issues are avoided by constraining the engine operating points onto the best Brake Specific Fuel Consumption (BSFC) curve of the engine, shown in Fig. 5.9. This simplification significantly reduces the computational memory and smoothen the desired engine speed as long as the high level command is continuous. The simplification of the mid-level controller can be summarized as:

$$\begin{aligned} Pow_{eng} &= \frac{1}{\eta_{trans}} \cdot (\omega_{out} \cdot T_{out} + P_{sys} Q_{acc}) && (6.5) \\ (\omega^*_{eng}, T^*_{eng}) &= BSFC(Pow_{eng}) && (6.6) \\ Loss^*(\omega_{out}, T_{out}, P_{sys}, Q_{acc}) &= \\ Loss_{eng}(\omega^*_{eng}, T^*_{eng}) &+ (1 - \eta_{trans}) \cdot \omega^*_{eng} T^*_{eng} && (6.7) \end{aligned}$$

where η_{trans} is the transmission efficiency assumed to be a constant value of 85%, as engine loss dominates the total powertrain loss. Since the best BSFC engine speed monotonically increases with transmission output power, the desired engine speed is guaranteed to be smooth with respect to accumulator power Pow_{acc}, reducing the risk of erratic engine speed tracking performance.

Figure 6.4 illustrates the difference of loss between the optimal and simplified mid-level controllers at various accumulator powers. The illustrated conditions occur frequently throughout the Urban and Highway drive cycles. The simplified mid-level behaves similarly to the optimal mid-level. The maximum difference between the optimal and simplified mid-level loss is approximately $5kW$ (excluding the high engine power region).

The simplified mid-level controller substantially reduces the memory requirement compared to the optimal pre-computed map, by using a simplified mid-level that is sub-optimal. Moreover, the monotonic increase of engine speed with engine power could reduce the risk of stalling the engine, improving the engine speed control performance.

6.2.3 Low-level

The low level controller determines the actuation commands, i.e. the engine fuel solenoid and pump/motor displacement inputs (u, x_T, x_S) to achieve the operating conditions specified by the high and mid levels control.

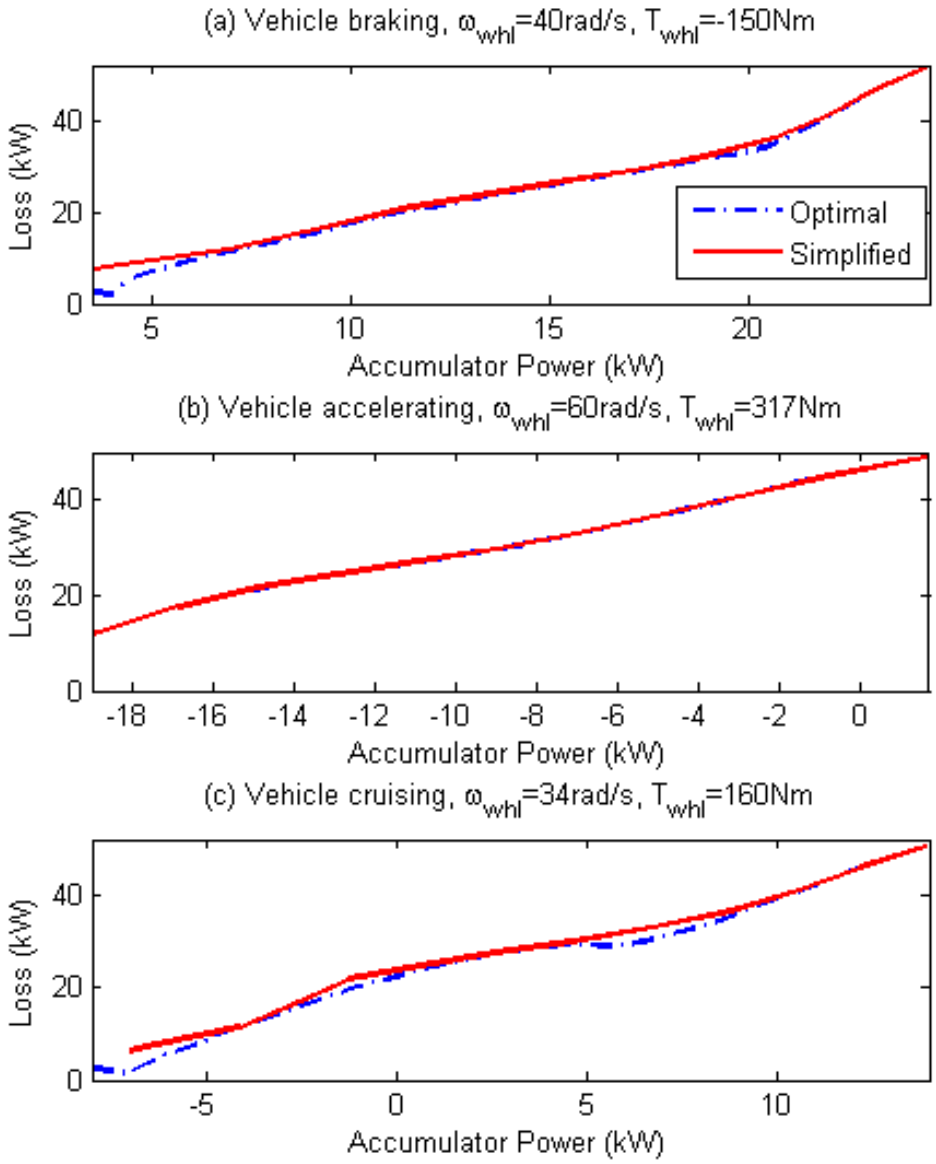

Figure 6.4: Comparison of powertrain loss between the optimal and simplified mid-level controllers at various vehicle conditions.

Dynamic Decomposition: According to Ch. 5, the overall powertrain dynamics in Eq. (5.34) is a coupled two-state system due to the planetary gearset. With the engine speed and transmission output speed coupled, the analysis and controller design becomes cumbersome and less intuitive. In order to decouple the two speeds, a previously developed passive decomposition approach proposed by Lee (2007) [83] is applied to transform the original system into new coordinates (similarly in Li (2010) [11]).

The original system in Eq. (5.34) is represented as

$$\underbrace{\begin{pmatrix} \hat{J}_{eng} & -\hat{J}_{coup} \\ -\hat{J}_{coup} & \hat{J}_{out} \end{pmatrix}}_{J} \begin{pmatrix} \dot{\omega}_{eng} \\ \dot{\omega}_{out} \end{pmatrix} = \underbrace{\begin{pmatrix} T_{eng} + R_T T_T - \frac{1}{\rho R_S} T_S \\ T_{load} + \frac{(1+1/\rho)}{R_S} T_S \end{pmatrix}}_{T} \tag{6.8}$$

where $\hat{J}_{eng} = J_{eng} + R_T^2 J_T + \frac{1}{\rho^2 R_S^2} J_S$ is the equivalent engine inertia including the effect of the pump/motors through the planetary geartrain, $\hat{J}_{out} = J_{veh} + \frac{(1+1/\rho)^2}{R_S^2} J_S$ is the equivalent vehicle inertia, $\hat{J}_{coup} = \frac{(1+\rho)}{\rho^2 R_S^2} J_S$ is the coupling term of the engine and output shaft dynamics, ω_{eng} is the engine speed, and ω_{out} is the transmission output speed. The main idea is to eliminate the diagonal terms in J. Assume a transformation matrix to separate the dynamics between engine and vehicle,

$$S = \begin{pmatrix} 1 & 0 \\ a & 1 \end{pmatrix} \tag{6.9}$$

Also, the old $(\omega_{eng}, \omega_{out})$ and new $(\omega_{int}, \omega_{ext})$ coordinates are related by,

$$\begin{pmatrix} \omega_{eng} \\ \omega_{out} \end{pmatrix} = \begin{pmatrix} 1 & 0 \\ a & 1 \end{pmatrix} \begin{pmatrix} \omega_{int} \\ \omega_{ext} \end{pmatrix} \tag{6.10}$$

Then, define this coordinate transformation with new variables,

$$S^\intercal JS = \begin{pmatrix} 1 & a \\ 0 & 1 \end{pmatrix} \begin{pmatrix} \hat{J}_{eng} & -\hat{J}_{coup} \\ -\hat{J}_{coup} & \hat{J}_{out} \end{pmatrix} \begin{pmatrix} 1 & 0 \\ a & 1 \end{pmatrix} \tag{6.11}$$

$$= \begin{pmatrix} \overbrace{\hat{J}_{eng} + 2a\hat{J}_{coup} + a^2\hat{J}_{out}}^{J_{int}} & -\hat{J}_{coup} + a\hat{J}_{out} \\ -\hat{J}_{coup} + a\hat{J}_{out} & \underbrace{\hat{J}_{out}}_{J_{ext}} \end{pmatrix} \tag{6.12}$$

By setting the dynamic decomposition coefficient from passive decomposition [11, 83], $a = \hat{J}_{coup}/\hat{J}_{out}$, the system in Eq. (6.8) is then dynamically decomposed into a system described as:

$$S^\intercal JS \begin{pmatrix} \dot{\omega}_{int} \\ \dot{\omega}_{ext} \end{pmatrix} = S^\intercal T \tag{6.13}$$

$$\begin{pmatrix} J_{int} & 0 \\ 0 & J_{ext} \end{pmatrix} \begin{pmatrix} \dot{\omega}_{int} \\ \dot{\omega}_{ext} \end{pmatrix} = \begin{pmatrix} \overbrace{T_{eng} + R_T T_T - \frac{1}{\rho R_S} T_S + a(T_{out} + \frac{(1+1/\rho)}{R_S} T_S)}^{T_{int,load}} \\ T_{out} + \frac{(1+1/\rho)}{R_S} T_S \end{pmatrix} \tag{6.14}$$

where the internal speed, $\omega_{int} = \omega_{eng}$ and external speed, $\omega_{ext} = \omega_{out} - a \cdot \omega_{int}$. The diagonal matrix in Eq. (6.14) represents the passively decomposed system, where ω_{int} and ω_{ext} are decoupled and treated as two SISO systems, with the external dynamics $J_{ext}\dot{\omega}_{ext}$ coupled to the internal dynamics $J_{int}\dot{\omega}_{int}$ with only the term a. Analysis and controller design can be conducted independently by specifying the engine torque and pump/motors displacements. Figure 6.5 depicts the overview scheme of the low-level controller.

Engine Speed Control: The objectives for the engine controller are to regulate the engine speed at the desired speed specified by the mid-level controller and reject load disturbances from the hydraulics. Based on the analysis from dynamic decomposition, the internal speed, ω_{int}, can be regulated using a feedforward controller to decouple the effect of vehicle load $T_{int,load}$ from ω_{int}. A feedback controller is needed to account for the model uncertainties. In this case, a Proportional-Integral (P-I) with feedforward controller for specifying the engine solenoid displacement in Eq. (5.7) is utilized to

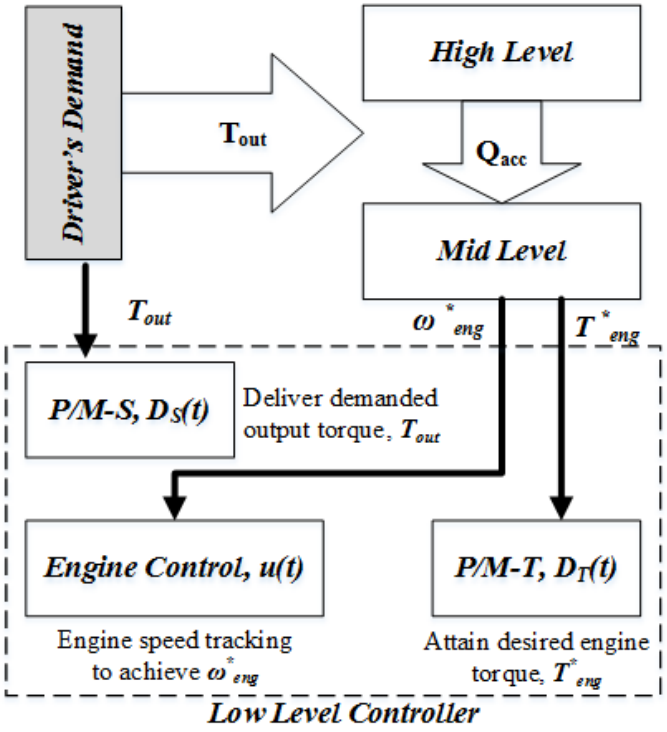

Figure 6.5: Low level transmission control scheme.

achieve the objective:

$$u(t) = \underbrace{K_p(\omega^*_{eng} - \omega_{eng}) + K_I \int (\omega^*_{eng} - \omega_{eng})dt}_{\text{feedback}} - \underbrace{\frac{T_{int,load}}{K_{eng}K_\omega}}_{\text{feedforward}} \tag{6.15}$$

where $K_p = 0.00323$ and $K_I = 0.00646$ are chosen to achieve closed-loop poles of $[-2, -4.5 \pm 60i]rad/s$. The P-I feedback controller is designed such that the engine speed remains stable, and to account for the nonlinearly speed dependent engine friction T_{frict} [84]. The feedforward terms are to decouple the dynamics of the transmission from the engine. Note that the feedforward term uses the DC gain of the engine transfer function ($K_{eng}K_\omega$) in Eq. (5.7). The engine fuel solenoid dynamic inversion is not considered as the solenoid dynamic is considerably faster than the controller ($-10.18rad/s$ as opposed to $-2rad/s$).

Transmission Control: The transmission is required to deliver the torque demanded by the driver and to achieve the desired engine torque (T^*_{eng}) specified by mid-level controller by controlling the displacements of the two pump/motor displacements (x_T, x_S).

From Eqs. (5.29), and (6.14), to achieve the commanded vehicle torque T_{out}, the desired P/M-S torque is determined as:

$$T_S(t) = \frac{R_S}{(1 + 1/\rho)} T_{out}(t) \tag{6.16}$$

Since P/M-S is utilized to achieve the commanded vehicle torque, P/M-T is used to achieve the accumulator flow Q_{acc} determined by the high level controller according to Eq. (5.24), where the desired P/M-T flow is evaluated as:

$$Q_T(t) = -Q_{acc}(t) - Q_S(x_S(t), \omega_S(t), P_{sys}(t)) \tag{6.17}$$

To attain the desired torque and flow in Eqs. (6.16) and (6.17), the implicit mappings from T_* to x_* (from Eq. (5.21)) and Q_* to x_* (from Eq. (5.22)) previously evaluated in Sec. 5.3 is used[1] . Once the pump/motors are actuated to the correct shaft torque,

[1] Note that while the simplified mid-level controller does not utilize the pump/motor maps developed in Sec. 5.3, the low level controller does.

assuming the engine speed trajectory is tracked, the engine will be loaded at the desired torque, T^*_{eng}.

Virtual Driver for Dynamometer Driving: A speed-tracking controller is designed in dynamometer testing to enable the powertrain output speed to follow the prescribed drive cycle $\omega_{cyc}(t)$. The virtual driver controller will determine the transmission output torque necessary to achieve the desired speed. In this case, a P-I feedback with feedforward controller is utilized to be the virtual driver, shown as follows:

$$T_{out}(t) = \underbrace{K_{p,cyc}(\omega_{cyc} - \omega_{out}) + K_{i,cyc}\int(\omega_{cyc} - \omega_{out})dt}_{\text{P-I feedback}} + \underbrace{\hat{J}_{veh}\dot{\omega}_{cyc} + f(\omega_{cyc})}_{\text{feedforward}} \quad (6.18)$$

where $K_{p,cyc} = 4.2$ and $K_{i,cyc} = 200$ are chosen to produce closed-loop poles of $-2rad/s$. $\hat{J}_{veh} = 47.9kgm^2$ is the equivalent vehicle inertia and $f(\omega_{cyc})$ is the vehicle road and aero-dynamic drag term defined as:

$$f(\omega_{cyc}) = MgR_{tire}\left(f_0 + (3.24 \cdot f_s\frac{2.237}{100}R_{tire}\omega_{cyc})^{2.5}\right) + \frac{1}{2}C_D A_f \rho_{air} R^3_{tire}\omega^2_{cyc} \quad (6.19)$$

where $M = 500$kg is the vehicle weight[2] , $g = 9.81\ m/s^2$ is the gravitational constant, $\rho_{air} = 1.29\ kg/m^3$ is the air density, and $R_{tire} = 0.306m$ is the effective tire radius. The rolling resistance coefficients assumed are $f_0 = 0.0095, f_s = 0.0035$. An aerodynamic drag coefficient (C_D) of 0.5 and a frontal area (A_f) of 1.784 m^2 were assumed.

6.3 High level energy management case studies

As mentioned earlier in this chapter, one advantage of this hierarchical control structure is the modularity of different layers, where each control level can be modified independently of others (in Sec. 6.2.1). These case studies will demonstrate this control structure's advantages and disadvantages. This section will explain various high level energy management strategies to be implemented on the Generation I test bed.

[2] A vehicle mass of 500kg is assumed instead of the originally assumed vehicle mass 1000kg used in Ch. 2 due to dynamometer power limitations of the experimental platform that existed when the experiments described in this thesis were run, which will be discussed in Ch. 7.

6.3.1 Continuously Variable Transmission (CVT) as Baseline

In this case study, the energy management strategy is restricted to the non-hybrid continuously variable transmission (CVT) operation. Simplified Mid-level controller described by Eq. (6.7) is utilized for the CVT strategy. Here, without utilizing energy storage, flow from pump/motor T results in the same flow into pump/motor S and vice versa. As a result from Eq. (5.24), this mode requires zero accumulator flow: $Q_{acc} = 0$. In a conventional CVT, the two pump/motors are connected only by a pipe, and the pressure is determined by the compressibility of the fluid within the pipe and torque transmitted. In this case, we do not shut off the accumulators even when $Q_{acc} = 0$, and the pressure is determined by the accumulator, although ideally $Q_{acc} = 0$ constrains the pressure to be constant. The hydraulic capacitance added by the accumulator provides the benefit of reducing transmission speed oscillation. By setting the accumulator pressure appropriately, component losses can also be minimized. On the other hand, the added capacitance attributable to the hydraulic accumulator slows the pressure dynamics. As a result, the transmission's output torque bandwidth is highly dependent on the pump/motor's actuation bandwidth instead of the engine in a non-hybrid case.

Zero Q_{acc} cannot be exactly achieved unless the loss models of the pump/motors are exact and the low level control is perfect. Biases in the achieved Q_{acc} can lead to depletion or saturation of hydraulic oil, or significant variation in accumulator pressure. Thus, instead of directly demanding $Q_{acc} = 0$ from the high level control layer, CVT mode is defined as regulating the high accumulator pressure[3] at P^*_{high} instead (in the test, $P^*_{high} = 13.8MPa(2000psi)$). Since the accumulator pressure dynamics are given by:

$$\dot{P}_{high} = \frac{P^2_{high}}{P_0 V_g} Q_{acc} \tag{6.20}$$

for simplicity, Q_{acc} is specified as a proportional controller

$$Q_{acc} = \gamma_P \cdot \left(P^*_{high} - P_{high}(t)\right) \tag{6.21}$$

[3] Low pressure accumulator is assumed to be regulated at $1.38MPa$ $(200psi)$ by a charge pump.

where $\gamma_P = K_{cvt}\frac{P_0 V_g}{P_{high}^2}$, and K_{cvt} is an adjustable gain for the pressure regulating controller. Clearly, this stabilizes P_{high} at P_{high}^*. K_{cvt} is set to 2 in this study to achieve 2 rad/s bandwidth[4] . Simplified mid-level controller in Eq. (6.7) is used in this strategy.

The transmission is not capable of reducing the transmission speed without recovering energy into the accumulator, or using mechanical brakes as in a conventional vehicle. As a result, the powertrain requires regenerative braking to reduce speed, something that is not done in a non-hybrid HMT. With this control strategy, engine power will decrease and energy recovered from braking will automatically be utilized to compensate for transmission losses. If the pressure is regulated as intended by the controller, then all recovered braking energy is dissipated as losses.

6.3.2 Dynamic Programming (DP) hybrid operation

With CVT strategy as baseline control strategy for the Generation I hybrid powertrain, hybrid control strategy is required to further improve the fuel economy of the powertrain. In contrast with the CVT strategy, the Dynamic Programming (DP) approach is utilized to evaluate the maximum fuel economy achievable by the Generation I hybrid powertrain, including the pressure dynamics and accumulator capacity. By utilizing the optimized mid-level controller Eq. (6.4), the DP control strategy is expressed as:

$$\begin{aligned} Q_{acc}^*(t) = \arg\min_{Q_{acc}(\cdot)} & \int_{t_0}^{t_f} Loss^*(\omega_{out}, T_{out}, P_{sys}, Q_{acc}, t)dt \\ \text{subject to } & \int_{t_0}^{t_f} P_{sys}(t)Q_{acc}(t)dt = 0 \\ & P_{sys}(t_0) = P_{sys,0} \\ & \underline{V_{acc}} \leq V_{acc}(t) \leq \overline{V_{acc}} \end{aligned} \tag{6.22}$$

where $Loss^*$ is the full optimized mid-level in Eq. (6.4), P_{sys} is the system pressure, $P_{sys,0}$ is the initial pressure of the accumulator, Q_{acc} is the accumulator volumetric net flow, and V_{acc} is the accumulator liquid volume. The precharge pressure of the accumulator is 11.0MPa (1600psi), the maximum pressure is 34.5MPa (5000psi), and the accumulator capacity is 38L. This energy management strategy guarantees a global

[4] A P-I controller should be designed to handle disturbances such as error in estimating flow losses.

optimal solution of Eq. (6.22).

The control law $Q^*_{acc}(t)$ is computed off-line due to the high computational load and backward time-facing calculation nature of DP. $Q^*_{acc}(t)$ is then directly applied as the high level control output in the dynamic simulation in a feed-forward (forward time-facing) manner. The initial condition of the accumulator is not optimized. The initial condition of the accumulator is chosen such that the initial state is equal to the final state of the accumulator.

6.3.3 Lagrange Multiplier (LM) hybrid operation

The basic Lagrange Multiplier (LM) strategy is developed similarly to the energy management strategy in Ch. 2, without restricting the engine operation in operating modes. The optimized mid-level controller in Eq. (6.4) is utilized for the LM strategy. Assuming constant system pressure and unconstrained accumulator capacity, the Lagrange Multiplier method is expressed as:

$$\lambda^* = \arg\max_{\lambda} \int_{t_0}^{t_f} \min_{Q_{acc}} [Loss^*(\omega_{out}, T_{out}, P_{sys}, Q_{acc}, t) + \lambda \cdot P_{sys} Q_{acc}] dt \tag{6.23}$$

Using the Lagrange Multiplier method, the control law can be expressed as:

$$Q^*_{acc}(t) = \arg\min_{Q_{acc}} [Loss^*(\omega_{out}, T_{out}, P_{sys}, Q_{acc}, t) + \lambda^* \cdot P_{sys} Q_{acc}] \tag{6.24}$$

where λ^* is the optimal Lagrange Multiplier for a specific drive cycle. Full mid-level controller in Eq. (6.4) is used in this strategy. The optimized $\lambda^* = -2.01$ for the urban cycle, and $\lambda^* = -2.03$ for the highway drive cycle. This optimal control strategy will fulfill the terminal constraint under constant pressure but does not guarantee the accumulator volume lies within bounds. When accumulator pressure dynamics are considered, both pressure and volume bounds will be violated. Thus, this motivates modification to the basic Lagrange Multiplier approach to allow for real-time implementation.

6.3.4 Modified Lagrange Multiplier (MLM) hybrid operation

The basic Lagrange Multiplier method in Sec. 6.3.3 uses a constant multiplier λ^* in the energy management strategy. However, the basic Lagrange Multiplier approach does

not consider the variation of system pressure nor accumulator capacity. Moreover, the computation of the optimized multiplier λ^* requires the prescribed drive cycle information. In order to enable the real-time implementation of the Lagrange Multiplier method, varying the multiplier λ as a function of the system pressure is proposed to handle the accumulator capacity constraint.

The $\lambda(P_{sys})$ function is expressed as a 12-point linear piece-wise function. Given $\lambda(P_{sys})$, the function will generate the instantaneous control strategy as:

$$Q^*_{acc}(t) = \arg \min_{Q_{acc}(t)} (Loss^*(\omega_{out}, T_{out}, P_{sys}, Q_{acc}, t) + \lambda(P_{sys}(t)) \cdot (P_{sys} Q_{acc})) \quad (6.25)$$

where $Loss^*$ is the full optimized mid-level controller in Eq. (6.4). The 12-point piece-wise function is optimized off-line to maximize fuel efficiency using the `fminsearch` function in Matlab. The optimized $\lambda(P_{sys})$ is illustrated in Fig. 6.6.

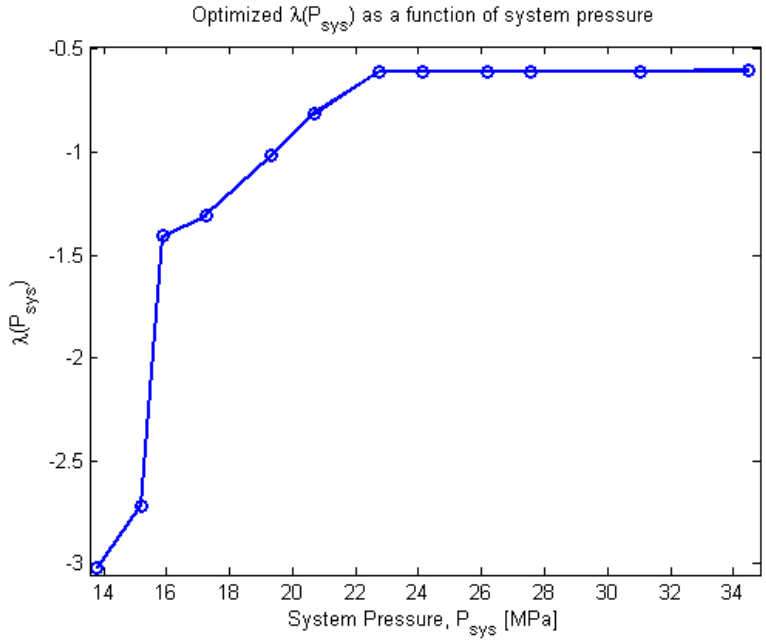

Figure 6.6: Optimized Modified Lagrange Multiplier function $\lambda(P_{sys})$.

This $\lambda(P_{sys})$ function is optimized under the combined drive cycle, and ensuring the system pressure lies within bounds of 13.8- 34.5MPa (2000-5000psi). Using the optimized $\lambda(P_{sys})$ into Eq. (6.25) creates the optimized control strategy.

As seen in Fig. 6.6, $\lambda(P_{sys})$ is more negative at low pressure to encourage accumulator charging, and $\lambda(P_{sys})$ is less negative at high pressure to encourage accumulator discharging. As a result, the system pressure will be bounded. This controller allows instantaneous energy management to compute the desired accumulator power $Q^*_{acc}(t)$. Results from Sec. 6.3.3 show that the optimized $\lambda^* \approx -2.0$, hence the pressure is expected to remain near 16MPa.

6.3.5 Rule based hybrid operation

The Rule-based strategy is one of several high level energy management strategies developed by CCEFP Project 1A.1 (J. Meyer, 2014) [85]. These rules are extracted from regular Dynamic Programming optimal control (with known trajectory) results (see [85] for details). Please note that the rules are obtained based on the vehicle mass of 1000kg, instead of the 500kg assumed in this chapter. On the other hand, the original Urban and Highway combined drive cycle is used for extracting the rules, unlike the reduced Combined drive cycle used in this chapter. Consequently, results from this strategy are not representative of the expected performance and behavior. The study of this strategy is solely to investigate the modularity of the three-level control structure.

Engine idle logic is set to reduce the engine power to zero when high accumulator pressure is higher than 22.8MPa (3300psi) or demanded transmission output torque is lower than $-5Nm$ (regenerative braking), and return to rule-based when pressure is lower than 15.2MPa (2200psi). Since [85] did not make use of the mid-level abstraction but used the full powertrain model directly, the rule is expressed in terms of engine power, which is a function of the demanded output torque T_{out} and the current output speed ω_{out}:

$$\begin{aligned} Pow_{eng} = {} & 137870 + 848\omega_{out} + 27.3T_{out} - 37.4\omega_{out}^2 \\ & -2.336T_{out}\omega_{out} + 0.3608\omega_{out}^3 + 0.0686\omega_{out}^2 T_{out} \end{aligned} \tag{6.26}$$

Again, since this rule-based strategy is not optimized for the vehicle mass and drive cycles to be simulated in this chapter, Fig. 6.7 is not a representative strategy to achieve improved fuel efficiency. Hence, the fuel economy of this strategy will not be compared to other energy management strategies.

While Eq. (6.26) is given in terms of engine power, it can be translated into accumulator flow Q_{acc} by decomposing it into the mid-level map. In this way, the mid and low level control layers would be identical to the CVT case, where the simplified mid-level controller in Eq. (6.7) is used. As seen in Fig. 6.7, the engine power is higher than $11kW$ even with negative wheel torque, thus this rule-based strategy is expected to behave as on/off (thermostatic) control, dominated by the engine idle logic and pressure bound.

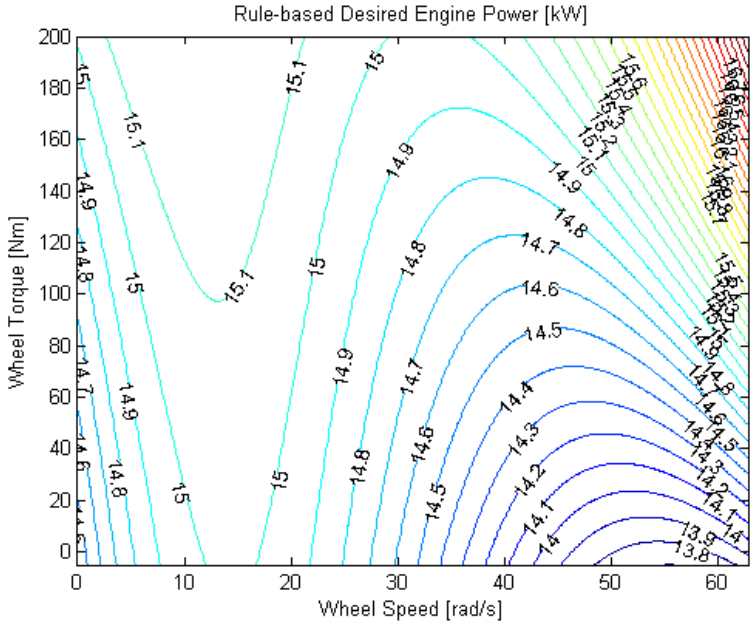

Figure 6.7: Rule-based strategy mapping from desired wheel speed and torque to engine power.

6.4 Simulation Results and Discussions

Using the hybrid powertrain model and controller developed, the Generation I vehicle, with reduced mass, is simulated through the drive cycles using the energy management strategies mentioned, i.e. Continuously Variable Transmission (CVT) strategy (Sec. 6.3.1), Dynamic Programming (DP) Strategy (Sec. 6.3.2), Lagrange Multiplier (LM) Strategy (Sec. 6.3.3), Modified Lagrange Multiplier (MLM) Strategy (Sec. 6.3.4), and Rule-based Strategy (Sec. 6.3.5). The low level controller described in Sec. 6.2.3 is

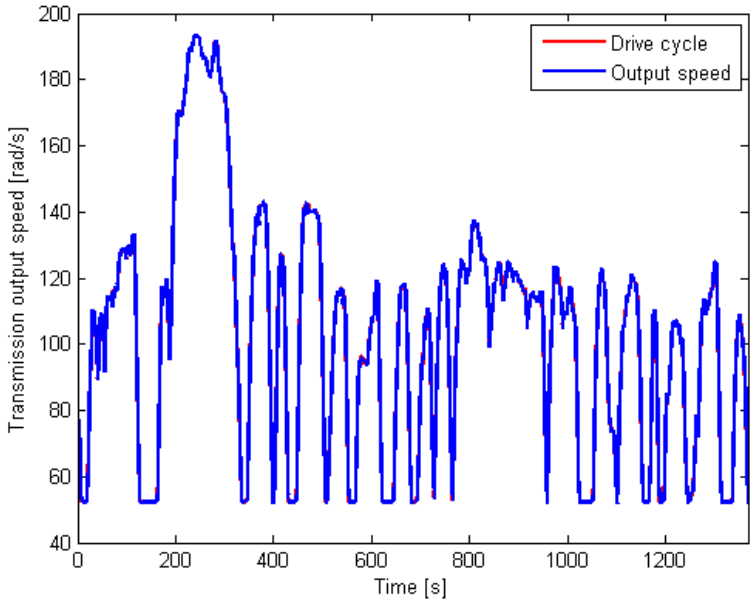

Figure 6.8: Simulated 'Virtual Driver control' for the Urban drive cycle.

used. Full mid-level controller in Eq. (6.4) is used for DP, LM, and MLM strategies in order to evaluate the best possible fuel economies achievable.

The vehicle is assumed to weigh 500kg (instead of 1000kg in Ch. 2). The vehicle's drag attributes are described in Eq. (6.19). The duty cycles used in this chapter are modified from the standard EPA Urban and Highway drive cycles, where the lowest speed of $0m/s$ is increased to $4.7m/s$ (or wheel speed of $(15rad/s)$. This is limited by the lowest operating speed that the hydrostatic dynamometer in the experimental platform could achieve when the tests described here were run.

The simulation results will be used to assess and predict the performance of the powertrain controller. Figure 6.8 shows the 'Virtual Driver' successfully following the modified drive cycle speed by controlling the vehicle output torque.

6.4.1 Predicted Fuel Economy

This predicted fuel economies of the energy management strategies are summarized in Tab. 6.1. For CVT strategy, it is expected that the predicted fuel economy for Highway

Ctrl. Stgy.	Urban $L/100km$ (mpg)	Highway $L/100km$ (mpg)
CVT	4.19 (56.2)	3.83 (61.4)
DP	2.41 (97.6)	2.30 (102.3)
LM (@ 13.8MPa)	2.40 (98.2)	2.24 (105.2)
MLM	2.57 (91.6)	2.40 (98.0)
Rule-based	4.28 (55.0)	3.92 (60.0)
Ideal Trans.	0.90 (260.0)	1.51 (155.5)

Table 6.1: Predicted fuel economy results based on different energy management strategies.

drive cycle will be higher than Urban drive cycle (approximately 9% higher). Since the regenerative braking does not benefit the CVT strategy, the transmission is operating more efficiently by transmitting most engine power through the mechanical path.

The ideal transmission assumes lossless transmission and the engine is operating at maximum efficiency of 33%, setting the highest efficiency achievable by the selected engine. Ideal transmission achieves fuel consumptions of 0.90L/100km on the Urban drive cycle and 1.51L/100km on the Highway drive cycle. For ideal transmission, all braking energy is recovered, and thus only losses due to road and aerodynamic drags will affect the fuel economy. DP strategy achieves only 38% of ideal transmission fuel efficiency on Urban drive cycle, and 66% of ideal transmission fuel efficiency on Highway drive cycle.

The Dynamic Programming strategy predicts 74% better fuel economy than the baseline CVT mode for the Urban drive cycle and 67% higher for the Highway drive cycle. Considering pressure dynamics and accumulator capacity constraint, this strategy achieves the highest fuel economy (globally optimal). The basic Lagrange Multiplier strategy achieves 0.6% and 2.8% higher fuel economy than the DP strategy for the Urban and Highway drive cycles. The difference is mainly due to the constant pressure and unconstrained accumulator capacity assumptions. The Modified Lagrange Multiplier strategy is predicted to achieve 63% and 59.6% fuel economy increments from CVT mode for the Urban and Highway drive cycles.

Note that the predicted fuel economy results shown in Tab. 6.1 are significantly different from the fuel economies predicted in Ch. 2. The discrepancy is due to several

factors, i.e. (i) the vehicle mass in this chapter assumes 500kg while Ch. 2 assumes vehicle mass of 1000kg, (ii) the engine in this chapter is more efficient (33% peak efficiency) than the reference engine (28% peak efficiency) used in Ch. 2, (iii) the engine operation in Ch. 2 is constrained but pump/motors can be locked up to reduce losses, (iv) the transmission kinematic relation matrix G is slightly different from the optimal design in Ch. 2, and (v) the duty cycles used in Ch. 2 are standard Federal Drive Cycles, while the duty cycles used in this chapter are modified due to dynamometer's limitations mentioned earlier. If the differences were to be made equal to conditions in Ch. 2, the fuel economy is expected to be lower than reported in Tab. 2.2 due to the transient of the powertrain dynamics and zero pump/motors' loss when locked-up in Ch. 2.

6.4.2 Continuously Variable Transmission (CVT) mode

Figure 6.9 shows the engine speed controller is capable of tracking the desired engine speed, and the pressure regulation controller stabilized the high pressure at 13.8MPa (2000psi) with maximum error of 1.50MPa (217psi). The pressure tracking error is due to the high flow requirement during high acceleration events. The CVT strategy achieves 4.19L/100km (56.2mpg) for the Urban drive cycle and 3.83L/100km (61.4mpg) for the Highway drive cycle. Figure 6.10 illustrates that the engine controller is capable of tracking the desired engine speed specified by the mid-level controller.

According to the accumulator characteristics described in Sec. 5.4, the energy required in order to recover the high pressure accumulator pressure from 13.1MPa (1900pis) to the set pressure 13.8MPa (2000psi) is approximately 11kJ. This suggests that if the transmission were to recover the accumulator pressure from 13.1MPa to 13.8MPa within one second, the pump/motors need to supply 11kW into the accumulator.

Figure 6.11 shows the engine operations for the CVT strategy throughout the Urban and Highway drive cycle. Since the simplified mid-level controller (see Eq. (6.7)) is used, the engine operated along the best BSFC curve expectedly and at lower engine power region. Even though operating the engine at low power causes the efficiency to be lower, the maximum operated efficiency of the engine is still approximately 31%. Due to engine speed tracking transients, the engine operating points are not perfectly constrained along the best BSFC curve.

Figure 6.12 and 6.13 show the engine power, and accumulator power throughout the

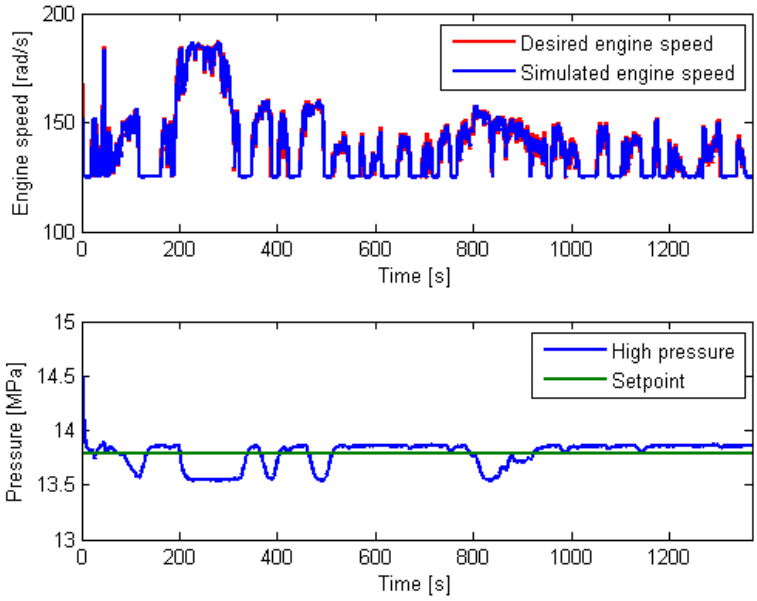

Figure 6.9: Simulated engine speed tracking and pressure regulation control under CVT strategy.

Urban and Highway drive cycles. As seen in the figure, the accumulator power is kept at low power only to compensate for flow losses. Figure 6.14 illustrates the braking condition under CVT strategy. During braking events, the engine is operating at low power while the accumulator power is near zero. This indicates the recovered braking power is utilized to compensate for transmission losses.

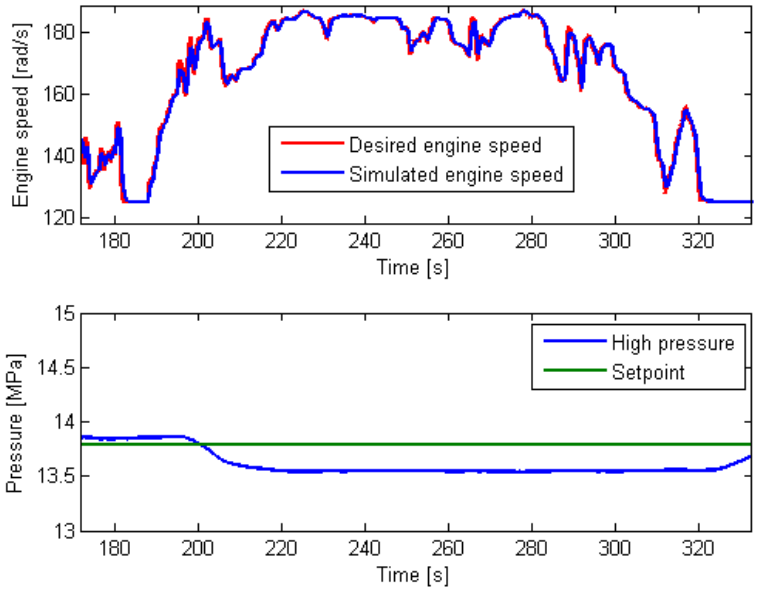

Figure 6.10: Engine controller tracking performance for the Urban drive cycle under CVT strategy (zoomed in).

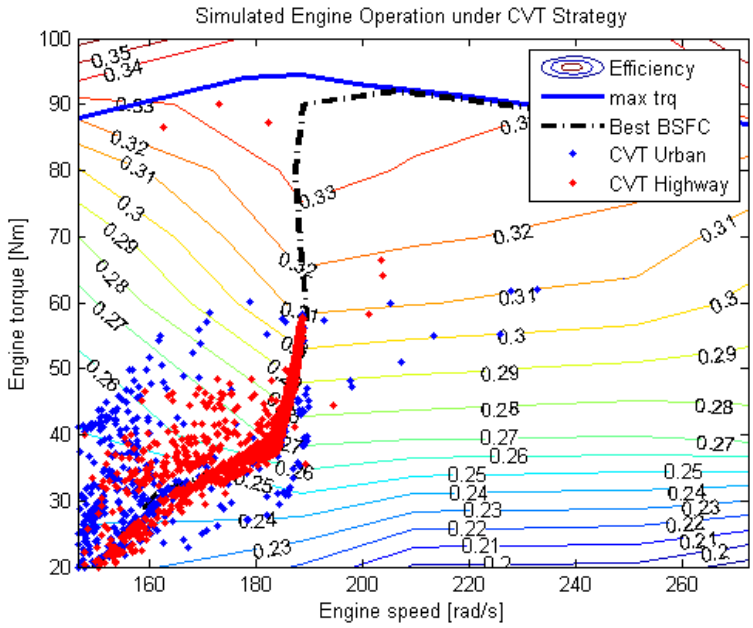

Figure 6.11: Simulated engine operation for the Urban and Highway drive cycle under CVT strategy.

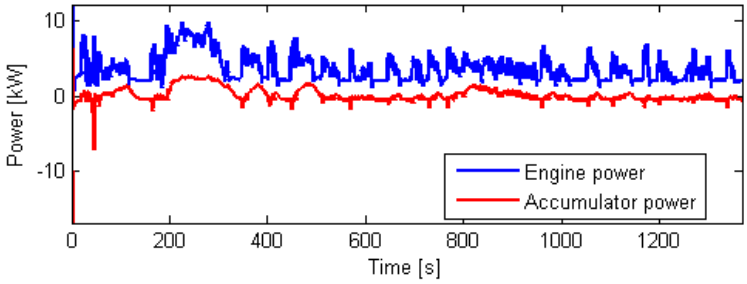

Figure 6.12: Simulated power usage for the Urban drive cycle under CVT strategy.

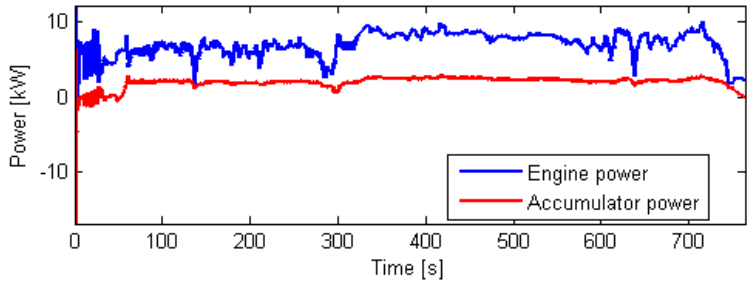

Figure 6.13: Simulated power usage for the Highway drive cycle under CVT strategy.

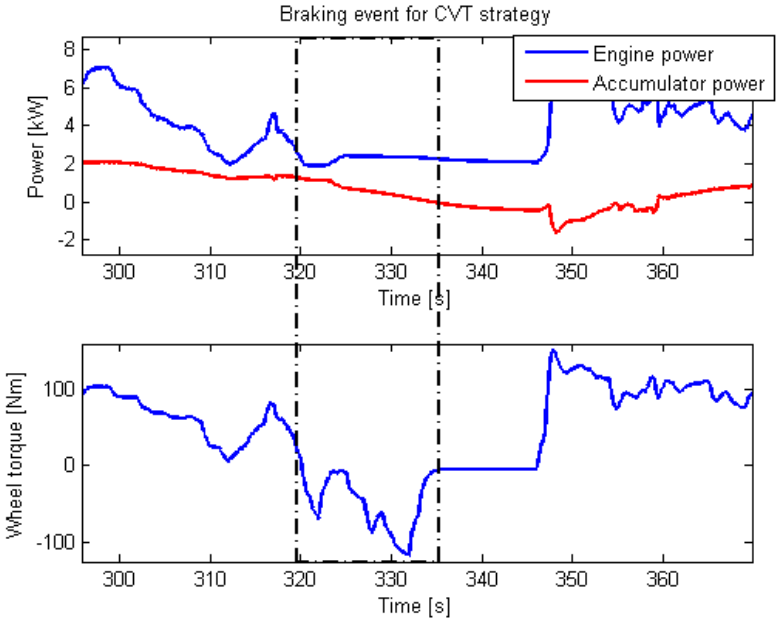

Figure 6.14: Braking behavior of the hybrid powertrain under CVT strategy.

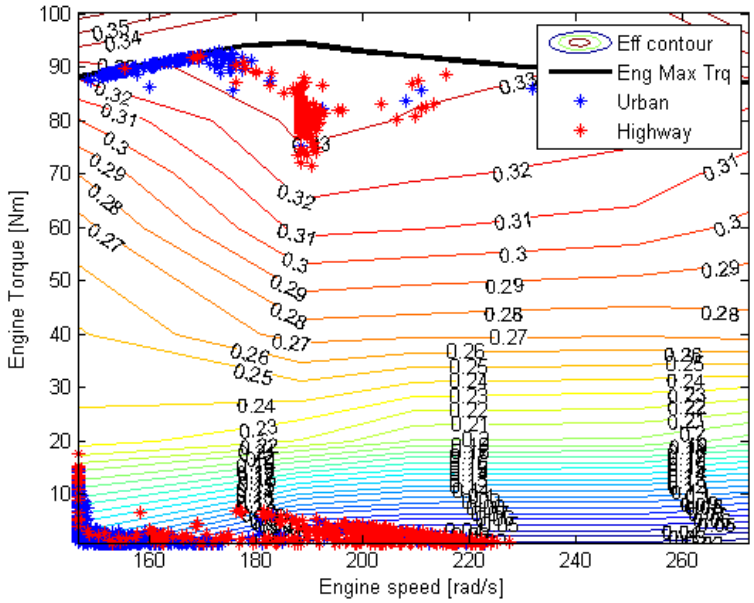

Figure 6.15: Simulated engine operation for the Urban and Highway drive cycle under DP strategy.

6.4.3 Dynamic Programming (DP) Strategy Operating Mode

Figure 6.15 shows the engine operations for the DP strategy throughout the Urban and Highway drive cycle. Recall, the optimized mid-level controller in Eq. (6.4) is used for this strategy, the engine operating points do not lie on the best BSFC curve. As the engine operation is not restricted to the best BSFC curve, the engine appears to be running using thermostatic control. During the Urban drive cycle, the engine operates at low speed and maximum torque. The engine generally operates at peak engine efficiency during the Highway drive cycle. The DP strategy achieves 2.41L/100km (97.6mpg) for the Urban drive cycle and 2.30L/100km (102.3mpg) for the Highway drive cycle.

Figure 6.16 shows the engine speed tracking and accumulator pressure variation under DP strategy for Urban drive cycle, and Fig. 6.17 shows the engine speed tracking and accumulator pressure variation under DP strategy for Highway drive cycle. Even though the desired engine speed is fluctuating at high frequency, the engine speed controller is shown to be capable of tracking the desired engine speed.

On the other hand, the DP strategy tends to maintain the system pressure at

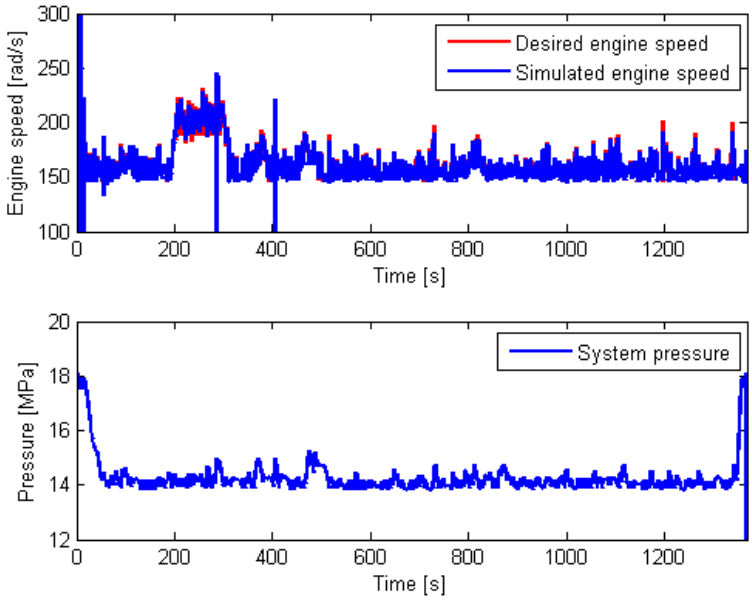

Figure 6.16: Simulated system pressure for the Urban drive cycle under DP strategy.

13.8MPa (2000psi), as seen in Fig. 6.16 and 6.17. By maintaining low system pressure, the transmission efficiency is improved due to higher pump/motor displacements, which contributes to the significant fuel economy gain. Figure 6.18 shows the zoomed in plot of Fig. 6.16. It depicts that the engine controller is capable of tracking the desired engine speed with slight oscillation at near 150rad/s.

Figure 6.19 and 6.20 show the engine power, and accumulator power throughout the Urban and Highway drive cycles under DP strategy. The DP strategy operates the engine in a thermostatic manner, frequently switching between high and low power. This strategy exhibits similar behavior for both drive cycles. Regenerative braking and accumulator usage reduce the overall engine energy required, thus yielding higher fuel economy.

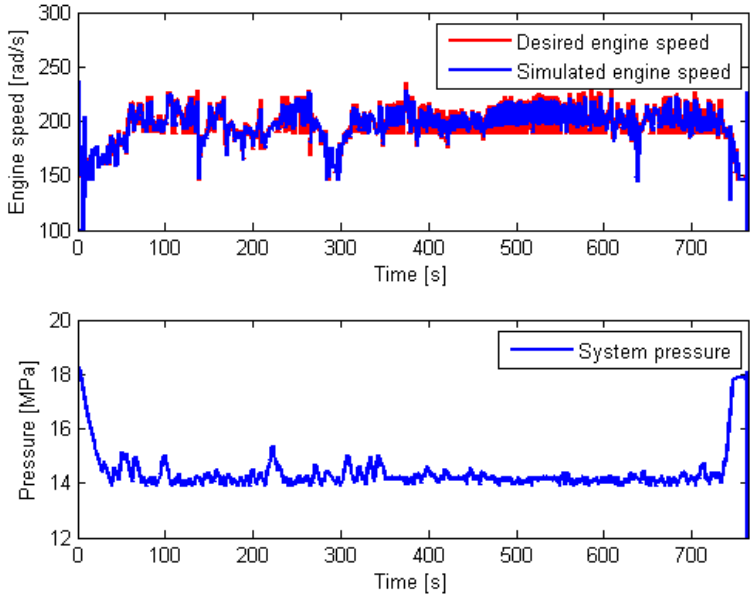

Figure 6.17: Simulated system pressure for the Highway drive cycle under DP strategy.

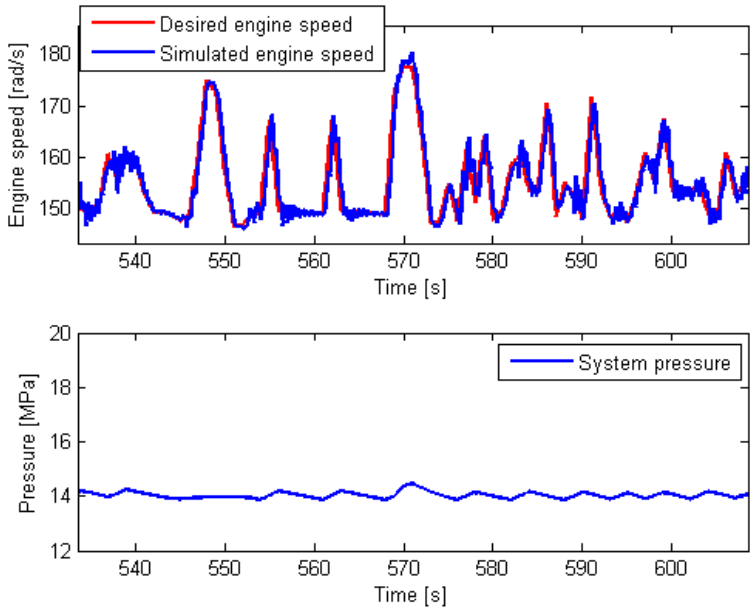

Figure 6.18: Engine controller tracking performance for the Urban drive cycle under DP strategy.

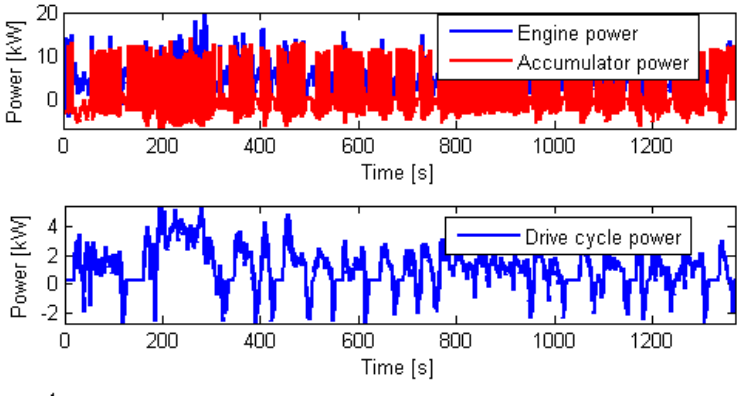

Figure 6.19: Simulated power usage for the Urban drive cycle under DP strategy.

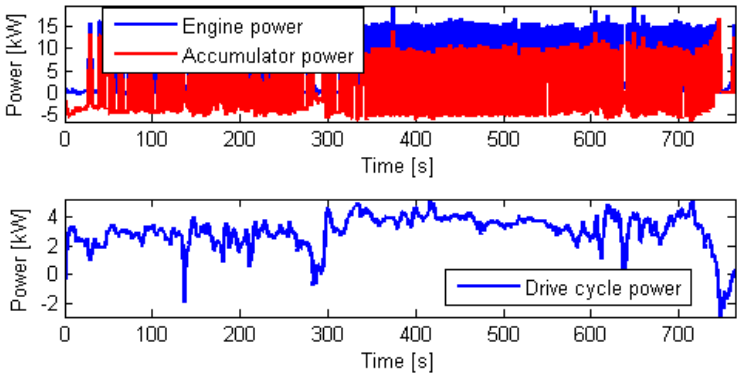

Figure 6.20: Simulated power usage for the Highway drive cycle under DP strategy.

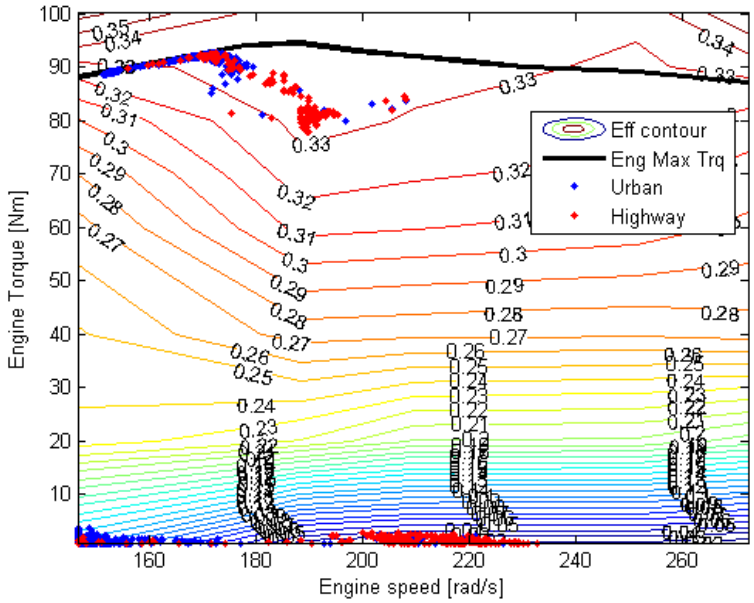

Figure 6.21: Simulated engine operation for the Urban and Highway drive cycle under LM strategy.

6.4.4 Lagrange Multiplier (LM) Strategy Operating Mode

Due to the nature of this control strategy, the powertrain is simulated without the accumulator pressure dynamics, i.e. assuming constant system pressure and unconstrained accumulator capacity. Without considering pressure dynamics, only energy variation is considered as the state-of-charge of the accumulator. The optimized mid-level controller in Eq. (6.4) is used for this strategy, the engine operating points do not lie on the best BSFC curve.

Figure 6.21 shows the engine operation for the Lagrange Multiplier (LM) method throughout the Urban and Highway drive cycles. The LM strategy behaves very similarly to the DP strategy, where the engine operates at maximum torque or maximum efficiency. Assuming a constant pressure of 13.8MPa (2000psi), the Lagrange Multiplier method achieves 2.40L/100km (98.2mpg) for the Urban drive cycle and 2.24L/100km (105.2mpg) for the Highway drive cycle. Figure 6.22 shows the state-of-charge (SOC) variation of the LM strategy. The SOC discharges continuously earlier and then charges back to its initial state for the Urban drive cycle. During the Highway drive cycle, the

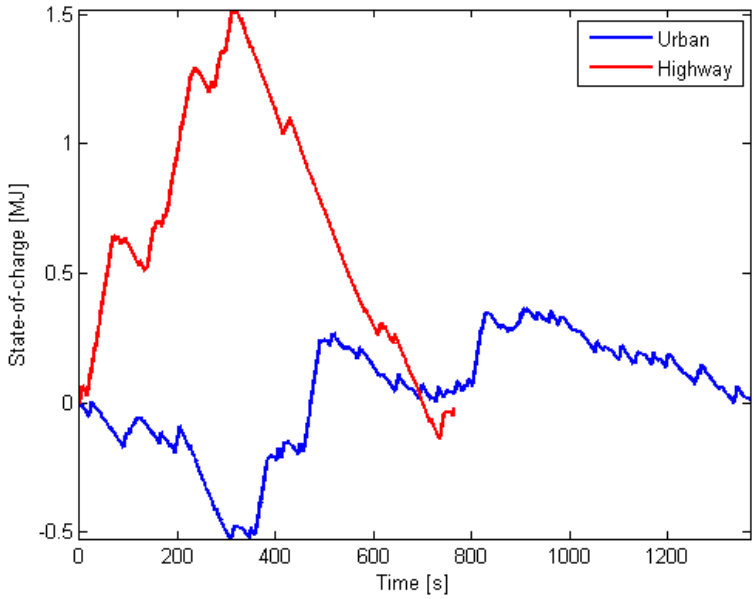

Figure 6.22: Simulated accumulator State-of-Charge (SOC) for the Urban and Highway drive cycle under LM strategy.

SOC charges continuously earlier and discharges back to its initial state. This operating behavior will violate the accumulator maximum capacity as $1.7MJ$ of energy capacity is required.

Figure 6.23 and 6.24 show the engine power and accumulator power throughout the Urban and Highway drive cycles under LM strategy. The engine also exhibits thermostatic behavior, similar to DP.

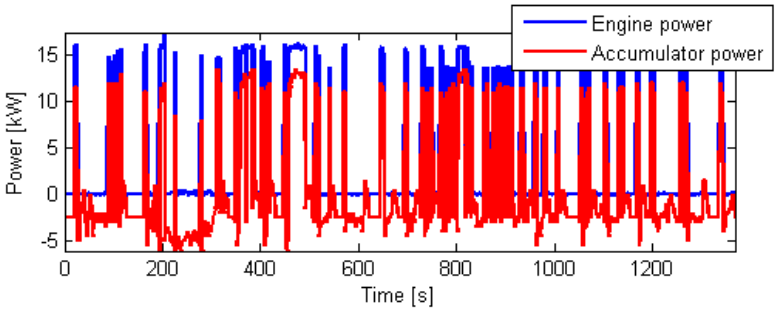

Figure 6.23: Simulated power usage for the Urban drive cycle under LM strategy.

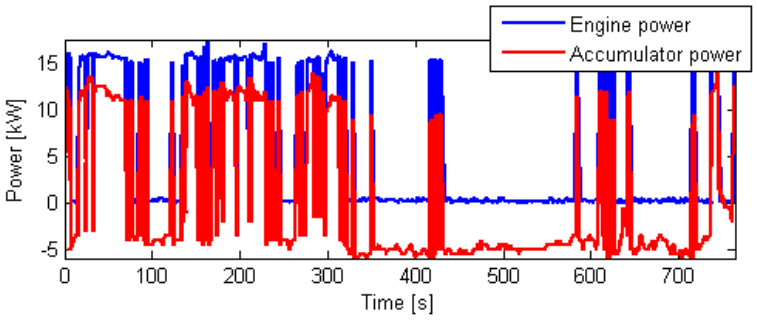

Figure 6.24: Simulated power usage for the Highway drive cycle under LM strategy.

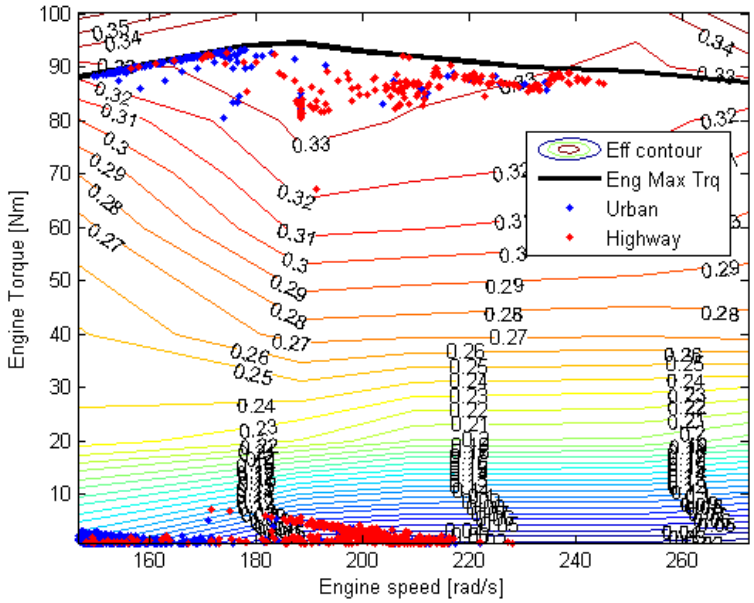

Figure 6.25: Simulated engine operation for the Urban and Highway drive cycle under MLM strategy.

6.4.5 Modified Lagrange Multiplier (MLM) Strategy Operating Mode

Figure 6.25 shows the engine operation under the Modified Lagrange Multiplier (MLM) strategy throughout the Urban and Highway drive cycles. Again, the optimized mid-level controller is used for this strategy, thus the engine operating points do not lie on the best BSFC curve. Similar to the basic Lagrange Multiplier strategy, the engine operates near maximum torque. For the Highway drive cycle, the engine operates at higher speed compared to the LM strategy, leading to lower fuel economy. The MLM strategy achieves 2.57L/100km (91.6mpg) for the Urban drive cycle and 2.40L/100km (98.0mpg) for the Highway drive cycle.

Figure 6.26 shows the engine speed tracking and accumulator pressure variation under the MLM strategy for the Urban drive cycle, and fig. 6.27 shows the engine speed tracking and accumulator pressure variation under the MLM strategy for the Highway drive cycle. The engine controller shows good tracking performance in both Urban and Highway drive cycles. The desired engine speed mainly fluctuates between 130rad/s and 250rad/s for the Urban drive cycle. However, the desired engine speed fluctuates

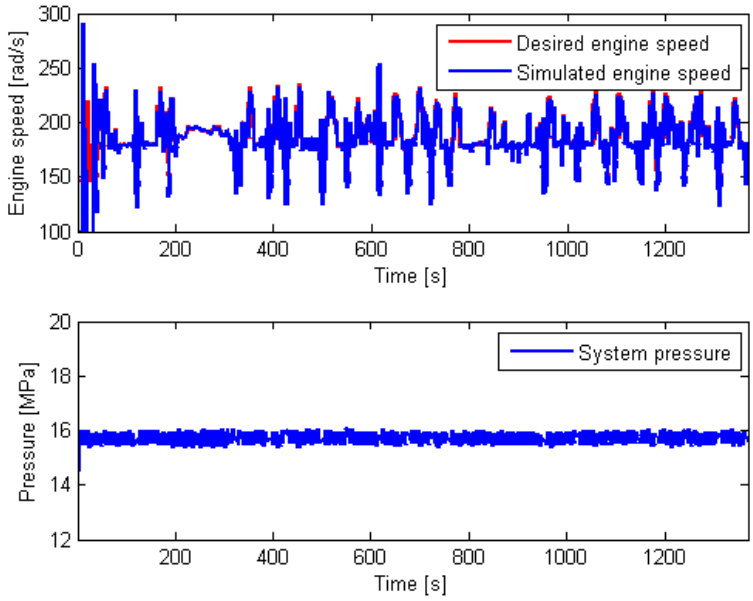

Figure 6.26: Simulated engine speed and system pressure for the Urban drive cycle under MLM strategy.

between 150rad/s and 200rad/s at high frequency ($\approx 0.25Hz$) for the Highway drive cycle. This is not desirable in real engine operation due to poor emissions even though the engine is capable of tracking the desired speed.

Figure 6.26 and 6.27 depicts the system pressure under the MLM strategy. This strategy maintains the system pressure at 15.7MPa (2300psi) as expected, which is 2.1MPa (300psi) higher than the DP strategy. Among the energy management strategies, the MLM strategy behavior is the most similar to the DP strategy. Moreover, DP, Rule-based, LM, and MLM strategies exhibit similar engine thermostatic control behavior, where the engine frequently switches between high and low power operating points. Based on system pressure variation of various strategies, significant fuel efficiency gain can be achieved by maintaining lower system pressure. Figure 6.28 illustrates a closed-up of a portion of Fig. 6.26 around 600 sec. This figure illustrates that the engine controller is generally capable of tracking the desired engine speed, except oscillations occur when the desired engine speed returns from high speeds to near 150rad/s. However, the system pressure remained steady.

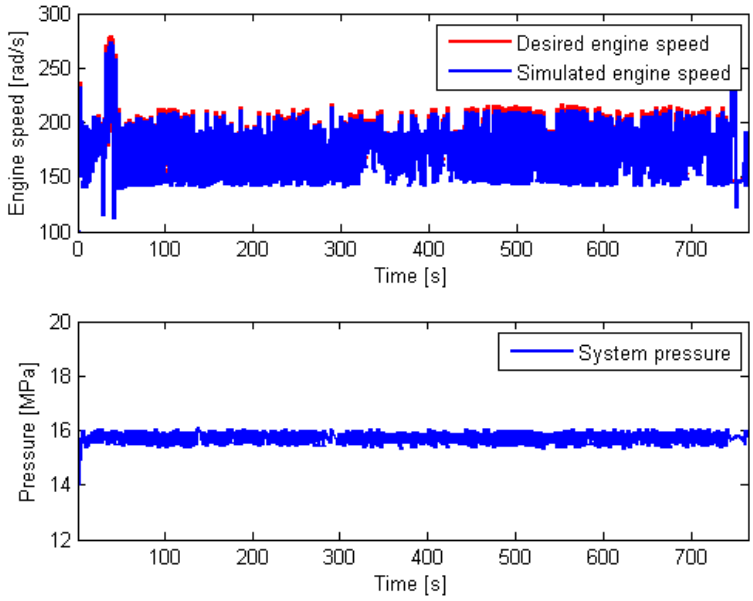

Figure 6.27: Simulated engine speed and system pressure for the Highway drive cycle under MLM strategy.

Figure 6.29 and 6.30 show the engine power, and accumulator power throughout the Urban and Highway drive cycles under the MLM strategy. This real-time implementable strategy behavior most resembles the DP strategy for both the engine power and split ratio, thus achieving only 7% less fuel efficiently than DP.

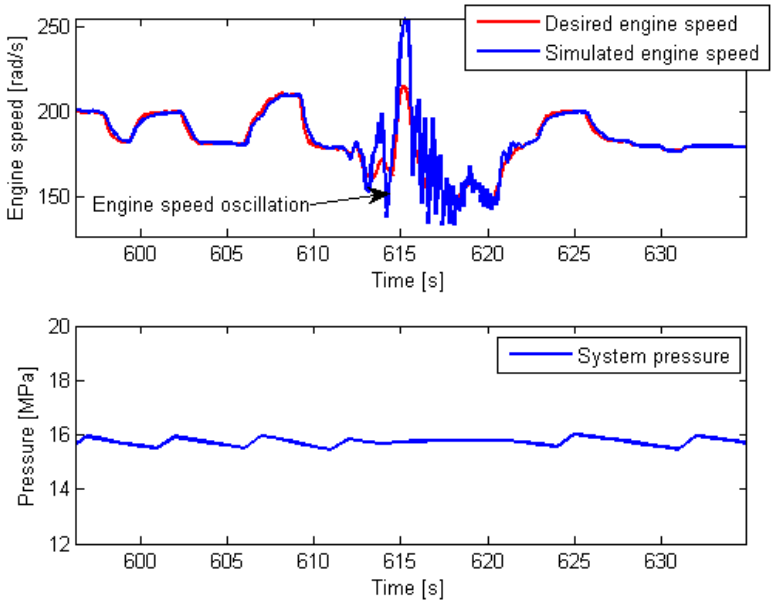

Figure 6.28: Engine controller tracking performance for the Urban drive cycle under MLM strategy.

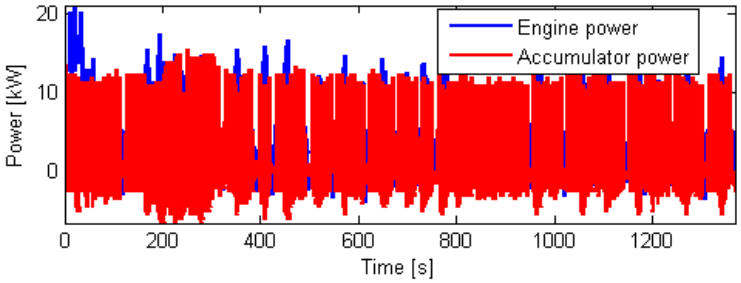

Figure 6.29: Simulated power usage for the Urban drive cycle under MLM strategy.

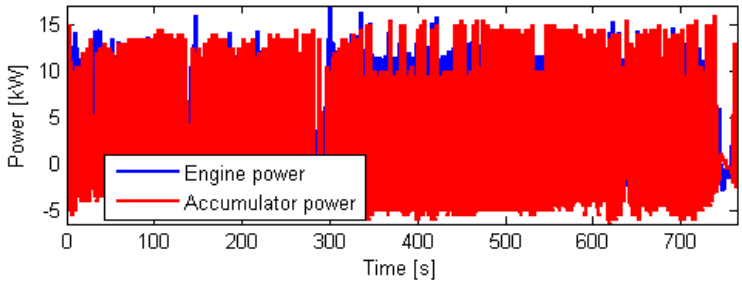

Figure 6.30: Simulated power usage for the Highway drive cycle under MLM strategy.

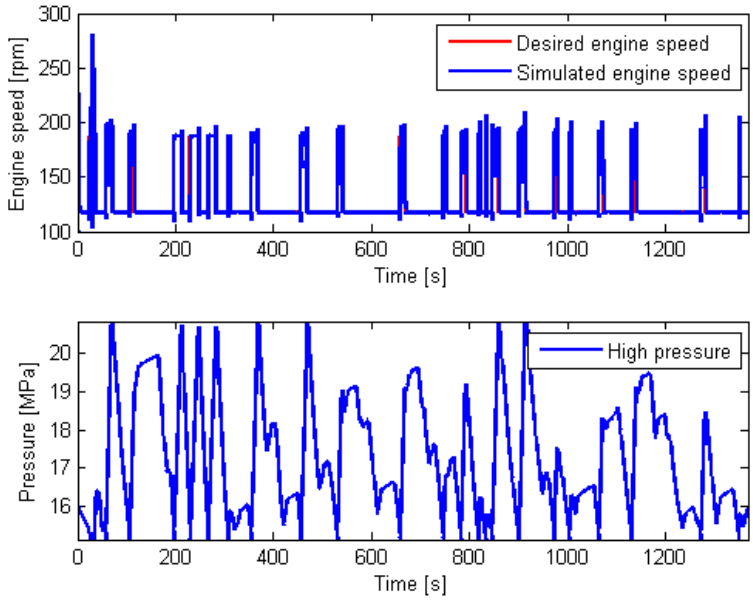

Figure 6.31: Simulated engine speed and pressure under Rule-based strategy for the Urban drive cycle.

6.4.6 Hybrid Rule-based Strategy Operating Mode

Figure 6.31 shows the engine speed tracking and accumulator pressure variation under Rule-based strategy for Urban drive cycle. The engine behaved as thermostatic (engine on/off) control as expected, and the pressure fluctuated between $15 - 21MPa$. The Rule-based strategy achieves 4.28L/100km (55.0mpg) for the Urban drive cycle and 3.92L/100km (60.0mpg) for the Highway drive cycle. Again, as mentioned previously in Sec. 6.3.5, the results of the rule-based strategy are not representative, and they are only to demonstrate the modularity of the three-level hierarchical control structure.

Figure 6.32 shows the engine speed tracking and accumulator pressure variation under Rule-based strategy for Highway drive cycle. Again, the engine behaved as thermostatic control, and the pressure fluctuated between $15-21MPa$. However, the controller behavior is more repetitive in the Highway drive cycle than in the Urban drive cycle. This is due to fewer start-stop cycles in the Highway drive cycle.

Figure 6.33 shows the engine operations for the Rule-based strategy throughout the Urban and Highway drive cycle. Recall the simplified mid-level controller in Eq. (6.7)

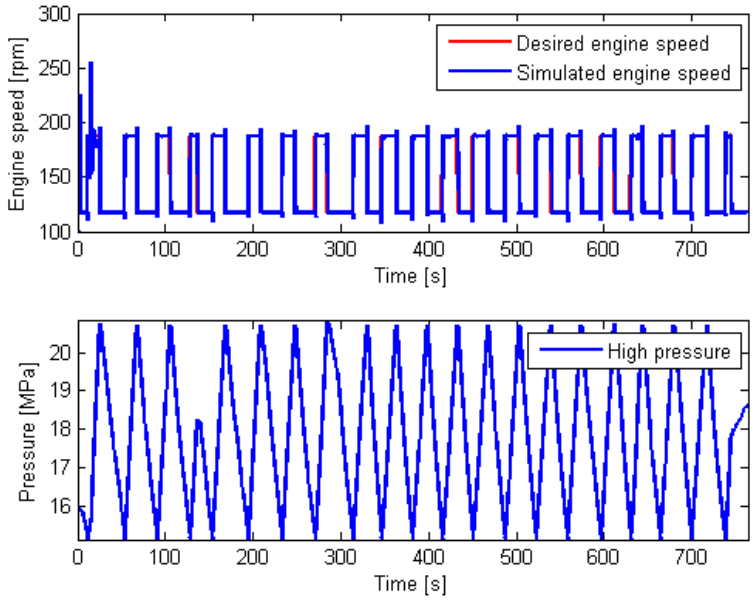

Figure 6.32: Simulated engine speed and pressure under Rule-based strategy for the Highway drive cycle.

is used for the Rule based strategy. However, unlike the CVT strategy, the Rule-based strategy operated the engine close to the highest efficiency, behaving like a thermostat. However, also because of this rapid on/off behavior, the engine operating points are scattered throughout high and low engine speed due to engine speed tracking transients. Figure 6.34 and 6.35 show the engine power, and accumulator power throughout the Urban and Highway drive cycles under Rule-based strategy.

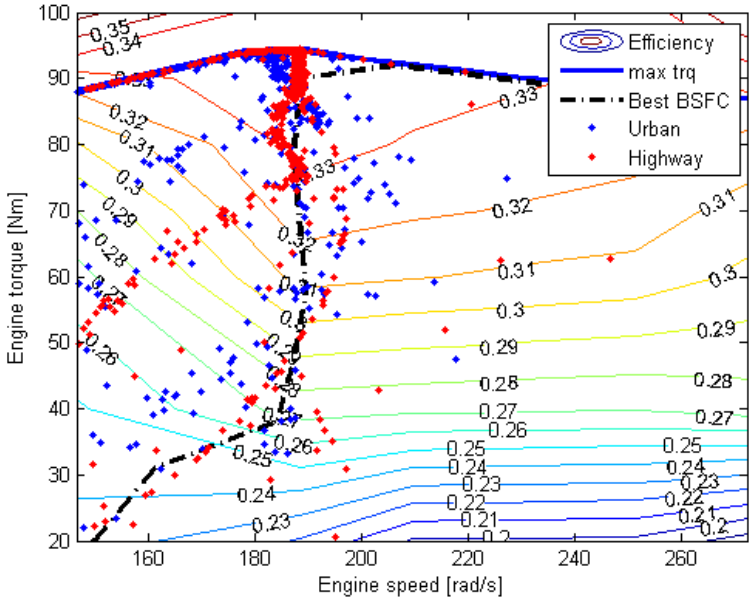

Figure 6.33: Simulated engine operation for the Urban and Highway drive cycle under Rule-based strategy.

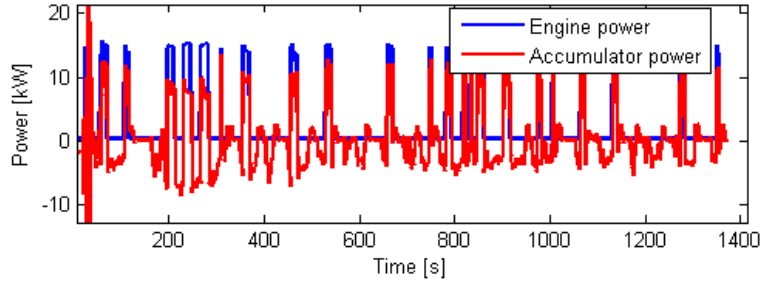

Figure 6.34: Simulated power usage for the Urban drive cycle under Rule-based strategy.

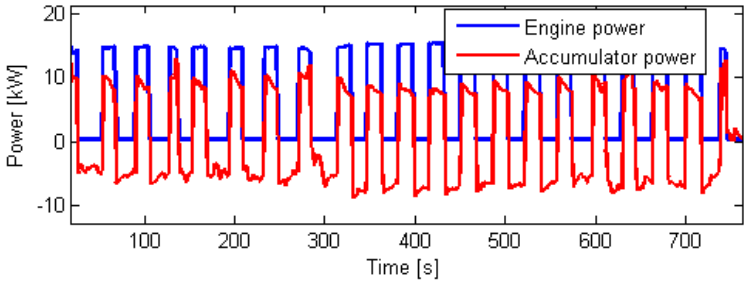

Figure 6.35: Simulated power usage for the Highway drive cycle under Rule-based strategy.

6.5 Concluding Remarks

This chapter has presented a three-level hierarchical control strategy to divide the hybrid powertrain controller into simpler segmented controllers. This strategy segregated the tasks of the drive-train into three layers that respectively 1) manages the accumulator energy storage *(high level)*; 2) performs vehicle level optimization *(mid-level)*; and 3) attains the desired vehicle operating condition *(low level)*. This approach allows controller modularity and simplifies the redundancy afforded by the additional degree of freedom in power-split architectures. The mid-level controller is also simplified to significantly reduce the computational memory and smoothen the desired engine speed.

Several energy management strategies, a continuously variable transmission (CVT) strategy (as a baseline for comparison), a Dynamic Programming (DP) strategy (as best fuel economy for upper bound comparison), a Lagrange Multiplier strategy, a Modified Lagrange Multiplier (MLM) Strategy, and a rule based hybrid energy management strategy to manage the stored energy were discussed. The Mid-level controller resolves the extra degree of freedom in power-split architectures into desired engine operations. The low level controller utilized the dynamic decomposition approach to simplify the engine speed tracking control. A 'Virtual Driver' controller is also designed to follow the drive cycle speed.

Simulation showed the powertrain controller is behaving as expected, where the engine speed control and pressure regulation control for CVT strategy is stable and tracks the desired conditions. The MLM strategy is a real-time implementable control law developed from the basic Lagrange Multiplier method to account for limited accumulator capacity. This strategy performs similar to the DP strategy, with more than 60% gain in fuel economy compared to the CVT strategy. The fuel economy with the Rule-based strategy is not representative due to the vehicle mass and drive cycle used to optimize the rules are not the same of the ones used in this chapter.

Chapter 7

Experimental Results of the Generation I Transmission

Chapter 5 developed the Generation I powertrain model. The three-level hierarchical control structure is utilized in Ch. 6, where mid and low level controllers are designed based on the developed powertrain model. Several energy management strategies are developed to predict the performance of Generation I vehicle. In this chapter, the Generation I test vehicle is experimentally tested on an in-house built hydrostatic dynamometer described in [68], as mentioned in Ch. 5.

The experiments to be summarized in this chapter demonstrate that the hardware is operational and the hierarchical powertrain control structure is effective. Due to limited hardware availability, this chapter is limited to two high level controllers: (i) Continuously Variable Transmission (CVT) strategy, and (ii) a Hybrid Rule-based Strategy developed by Meyer [85].

The rest of this chapter will be organized as follows: Section 7.1 presents the implementation results driving through the EPA urban and highway drive cycles, and Sec. 7.2 discusses the challenges, implementation issues, and fuel efficiencies achieved with current hardware and controls. Section 7.3 contains some concluding remarks.

7.1 Implementation Results of the high level energy management strategies

The instrumentation of the experimental set-up is as described in Sec. 5.1. The engine speed is measured by the encoder installed on the engine crank-shaft. The measured engine torque is obtained using a wireless telemetry strain gauge[1] installed between the engine flywheel and transmission. The torque sensor is calibrated and digitally filtered[2] . The pump/motor speed is measured with built-in hall-effect speed sensor. Pressure transducers measure the pressures in the high and low pressure accumulators. The transmission output torque is measure by the dynamometer slip-ring type torque sensor. The transmission output shaft speed is measured by the hall-effect speed sensor built-in with the dynamometer torque sensor. Fuel consumption throughout a drive cycle is determined by measuring weight of the fuel tank at the beginning and end of the drive cycle.

The simplified mid level controller described in Sec. 6.2.2 is used, where the engine operation is constrained to the best BSFC curve, and assuming a constant transmission efficiency of 85%. The low level controller used is as described in Sec. 6.2.3, where P/M-S displacement is set based on vehicle torque demand in Eqs. (5.21) and (6.16), and P/M-T displacement is set based on desired accumulator flow Q_{acc} in Eqs. (5.22) and (6.17).

The dynamometer control emulates [69], based on the torque exerted by the vehicle on the driveshaft, the load due to the acceleration/braking of any desired vehicle inertia and any desired aerodynamic and road drag characteristics. In this case, the vehicle weight is set as 500kg, instead of 1000kg in Ch. 2, due to limitations on dynamometer power at the time the experiments described here were run. The vehicle road and aero-dynamic drag term is as defined in Eq. (6.19):

$$f(\omega_{cyc}) = MgR_{tire}\left(f_0 + (3.24 \cdot f_s \frac{2.237}{100} R_{tire}\omega_{cyc})^{2.5}\right) + \frac{1}{2} C_D A_f \rho_{air} R_{tire}^3 \omega_{cyc}^2$$

where the vehicle weight $M = 500$kg, the gravitational constant $g = 9.81\ m/s^2$, the air

[1] TECAT WISER-200 (Ann Arbor, MI) wireless telemetry strain gauge torque sensor.

[2] The torque measurement is filtered using a first-order filter with cut-off frequency of 2rad/s.

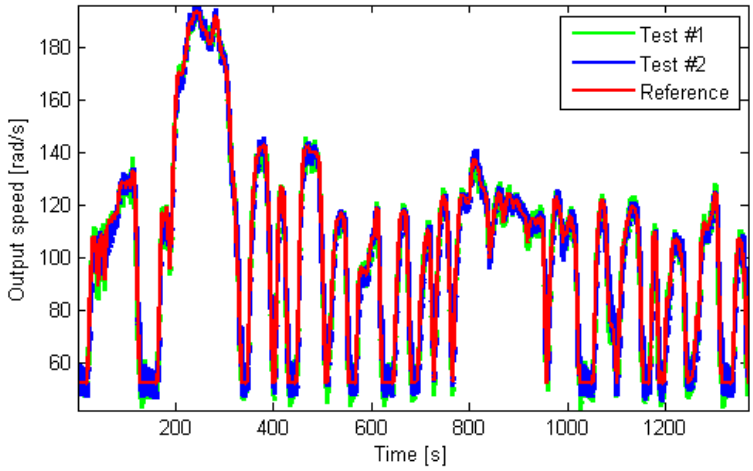

Figure 7.1: Repeatability of output speed tracking using 'Virtual driver' controller.

density $\rho_{air} = 1.29\ kg/m^3$, and the effective tire radius $R_{tire} = 0.306m$. The rolling resistance coefficients are $f_0 = 0.0095$, $f_s = 0.0035$, and the aerodynamic drag coefficient (C_D) of 0.5 and a frontal area (A_f) of 1.784 m^2 are used.

As described previously in Sec. 6.4, the vehicle is to follow a speed trajectory which is modified from the standard EPA Urban and Highway cycle where the lowest speed of 0m/s is increased to 4.7m/s (15 rad/s). This was due to a speed limitation of the charge pump of the dynamometer at the time that the experiments were run: the dynamometer speed (ω_{dyno}) was lower bounded to 52.4 rad/s (500rpm) in order for the dynamometer to remain operational. The vehicle is tested without the differential, where the transmission output shaft is connected directly to the dynamometer, hence $\omega_{dyno} = 3.45\omega_{whl}$.

The engine and transmission is warmed up for the first 400 seconds of each test. This is to allow the experimental set-up to approach steady-state (including fluids temperature, pressure and controllers) before commencing the drive cycle tests. Hence, the plots presented in this chapter mostly begin at $t = 400s$ instead of $t = 0$.

In this section, the results from implementing each energy management strategy is analyzed from three perspectives; e.g. (i) engine operation, (ii) accumulator state-of-charge (SOC) (or system pressure) variation, and (iii) driver's demand output torque

translation. Since the engine is the primary power source but also dominates the majority of the powertrain loss, the engine operation dictates the powertrain system overall efficiency. The accumulator SOC variation will provide insight on the energy management strategy in a hybrid powertrain, and potentially improving the fuel efficiency. Lastly, investigating output torque translation is to ensure the powertrain controller achieves the driver's demanded vehicle output torque.

7.1.1 Continuously Variable Transmission (CVT) Strategy

Fuel economy achieved by the CVT strategy is 4.73L/100km (49.7mpg) for the Urban drive cycle, and 4.12L/100km (57.1mpg) for the Highway drive cycle. Compared to the prediction in Tab. 6.1, the CVT strategy performs 11.6% less efficient (simulation predicts 4.19L/100km (56.2mpg)) for the Urban drive cycle, and 7.0% lower for the Highway drive cycle (simulation predicts 3.83L/100km (61.4mpg)).

Transmission output speed tracking: Figure 7.1 illustrates the repeatability of the test using the virtual driver throughout a drive cycle, where trajectories of the speed of the transmission output shaft from several tests are superimposed over each other, tracking urban drive cycle with accuracy of approximately 0.44 m/s (1 mph) standard deviation. Highway drive cycle in Fig. 7.2 also shows the tracking performance with accuracy of approximately 0.44 m/s (1 mph) standard deviation.

Engine speed tracking: Figure 7.3 shows that the engine speed controller is able to track the desired engine speed trajectory specified by the mid-level controller in this mode while rejecting the load disturbances from the hydraulic units. The maximum tracking error for the engine speed is approximately 3 rad/s (28.6 rpm) for both CVT and Rule-based operating modes.

The tracking error is most prominent when the engine is idling, as shown in Fig. 7.4(a). Torque pulses from the diesel engine are especially severe at low engine speed, due to less power strokes per second [37]. This causes the engine speed fluctuation magnitude to be higher, therefore leading to worse tracking performance. From Fig. 7.4(a), at lower engine speed of 128rad/s, the peak-to peak fluctuation is approximately 5rad/s with a frequency of 255rad/s. At higher speed (e.g. 188.5 rad/s in Fig. 7.4(b)), the peak-to-peak fluctuation is approximately 2 rad/s due to less severe torque pulses, at a frequency of 379rad/s. As shown, the torque pulse frequencies correlate with the engine

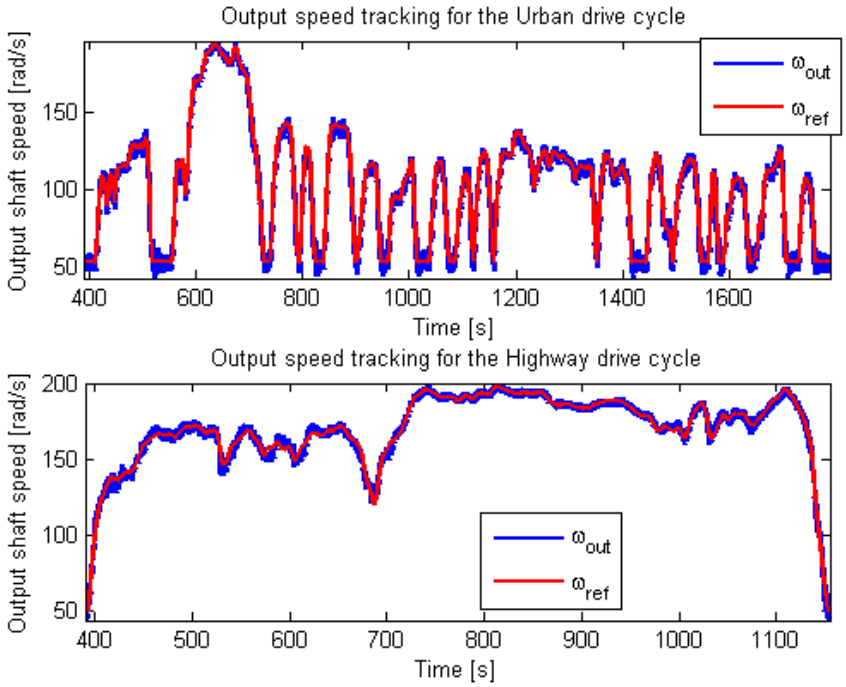

Figure 7.2: Desired and achieved speeds on the Urban and Highway drive cycles under CVT strategy.

speed, where pulse frequency is twice the engine speed frequency[3] .

Engine output torque: As described in Sec. 6.2, the engine speed is controlled actively by the engine throttle but the engine torque depends on P/M-T to achieve the desired engine torque. Hence, it is important to compare the commanded torque that the powertrain controller estimates to the actual measured engine output torque. While engine speed is measured, the commanded engine torque is only approximated from Eq. (5.29) using the demanded output torque, P/M displacements, system pressure and gear ratios, neglecting transmission friction.[4] .

Figure 7.5 depicts the difference between commanded and measured engine output torque in urban and highway drive cycles. The commanded engine torque is consistently higher than the measured engine torque, ranging from 45% to 240% higher especially

[3] This is due to 4-stroke 4 cylinder engines having 2 power stroke every engine cycle.

[4] Note that the measured engine torque is not used for powertrain control, but it is used for engine operating points verification.

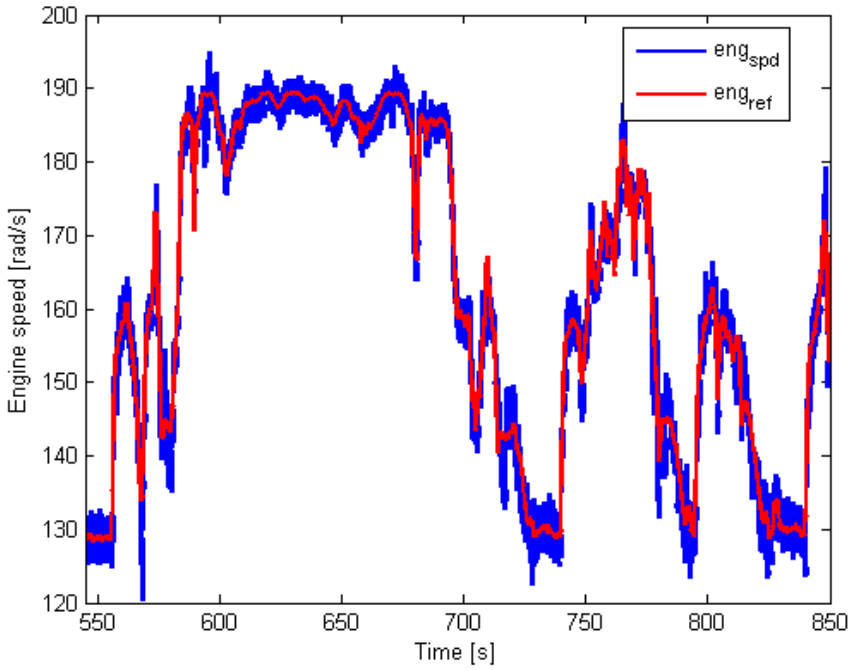

Figure 7.3: Engine speed controller tracking performance.

at higher desired engine output torque situations. As will be discussed later in Sec. 7.2, this is potentially caused by the over-estimation of the transmission output torque.

Assuming that the engine torque measurement is correct, the engine operating points have been shifted to a lower efficiency region of the engine map (generally lower efficiency at lower torque for the same speed), as seen in Fig. 7.6 and 7.7. Thus, lower fuel economy is expected for both urban and highway drive cycles than predicted by the simulations. The causes of this engine torque issue will be investigated in Sec. 7.2.

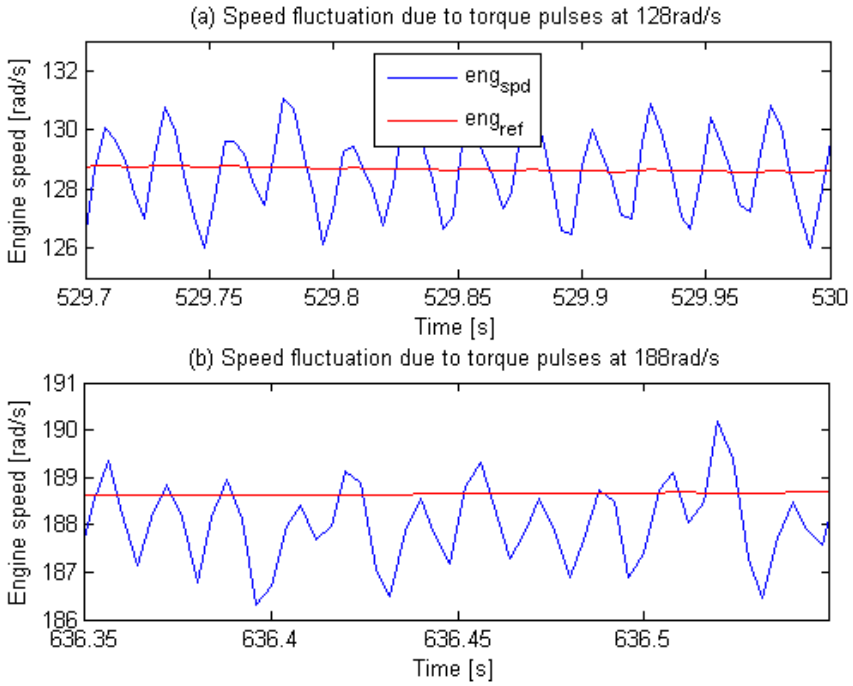

Figure 7.4: (a) Effect of torque pulses at low engine speeds. (b) Effect of torque pulses at high engine speed.

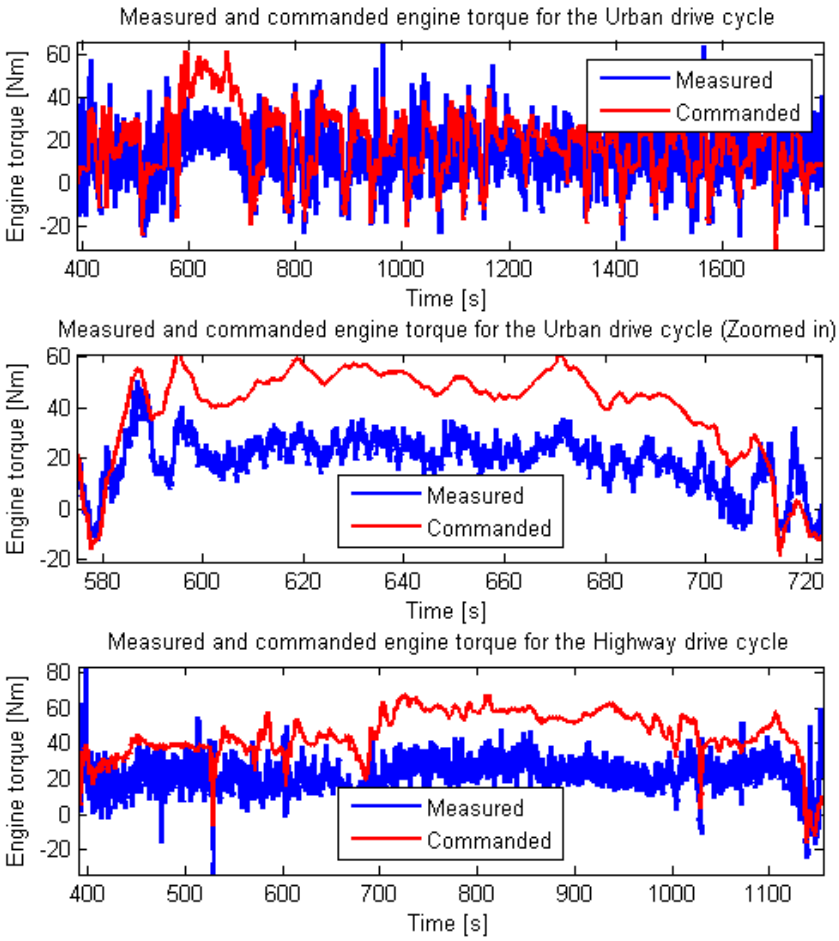

Figure 7.5: Comparison of commanded and measured engine output torque on Urban and Highway drive cycle for CVT mode.

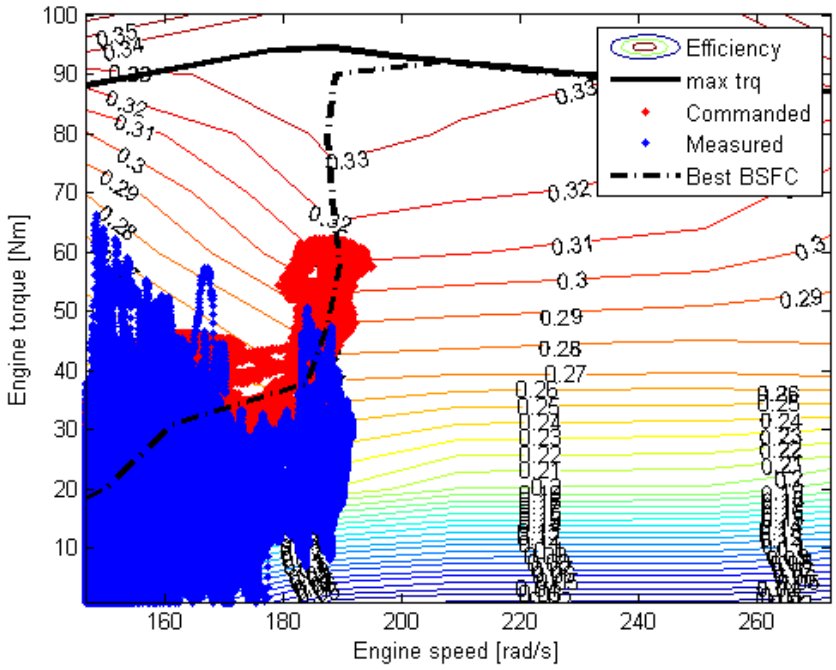

Figure 7.6: Comparison of commanded and measured engine operating points on Urban drive cycle for CVT mode.

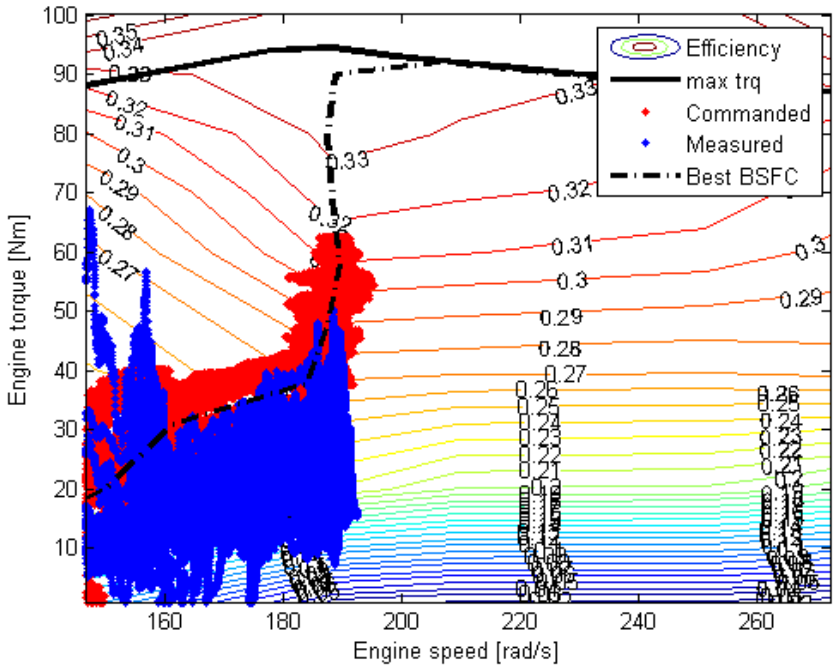

Figure 7.7: Comparison of commanded and measured engine operating points on Highway drive cycle for CVT mode.

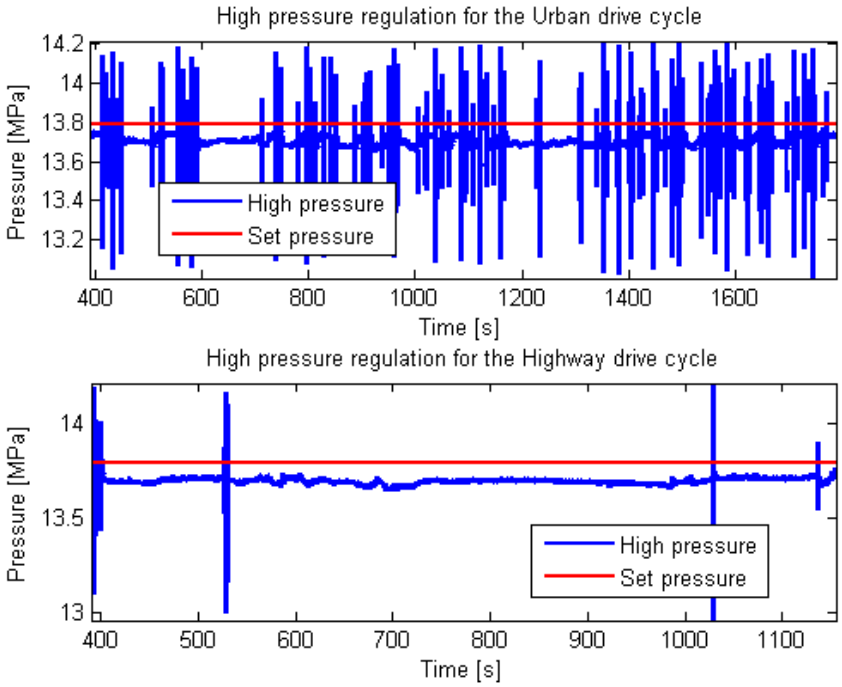

Figure 7.8: Achieved and target pressure in the high pressure accumulator under CVT strategy throughout the Urban and Highway drive cycles.

Pressure regulation: Figure 7.8 shows that high pressure regulation controller for the CVT mode is capable of stabilizing the high pressure at 13.8MPa (2000 psi)[5] within 0.14MPa (20 psi) error for both Urban and Highway drive cycles, except during directional valve switching events. Switching can affect the accumulator pressure up to 0.7MPa (100 psi) (pressure spikes). However, the pressure regulation performance is better than predicted, where the maximum error predicted is 1.50MPa (217psi).

The pressure regulating proportional controller gain is $\gamma_P = 4.4 \times 10^{-9}$, which will set the expected closed-loop pole at $-2rad/s$. The controlled high pressure is biased below the desired pressure. This is due to the under-estimation of the pump/motors' leakage or other hydraulic valves' leakage (relief valves and safety valves), that are not compensated by the proportional controller. A P-I controller for the pressure regulation will be able to compensate the steady-state error.

[5] with 11.0MPa (1600 psi) pre-charge pressure and 34.5MPa (5000psi) maximum pressure.

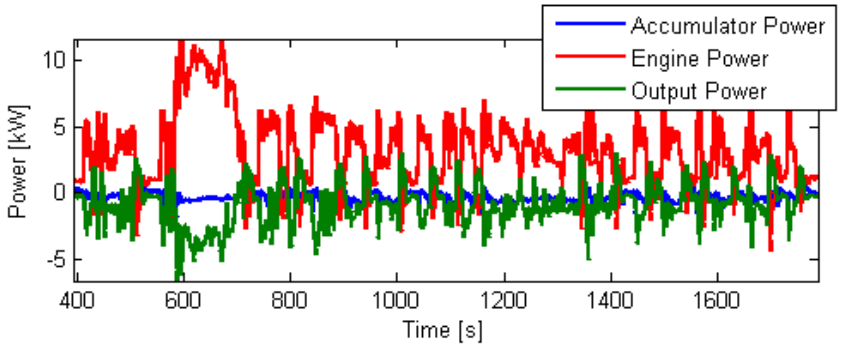

Figure 7.9: Power flow and power-split ratio for the CVT operation on Urban drive cycle.

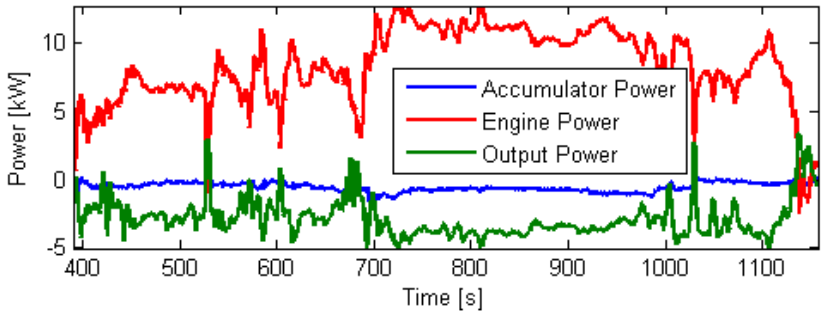

Figure 7.10: Power flow and power-split ratio for the CVT operation on Highway drive cycle.

Figure 7.9 and 7.10 show the engine and accumulator power when the vehicle is operated under CVT mode on the Urban and Highway drive cycles. Figure 7.11 illustrates the braking condition of the hybrid powertrain under the CVT strategy. Recall that the dynamometer is not capable of friction braking. During braking events, the engine is operating at low power[6] while the accumulator power is near zero. This indicates the recovered braking power is utilized to compensate for transmission losses, as predicted in Sec. 6.4.

[6] The negative engine power is due to the erroneous engine torque estimation.

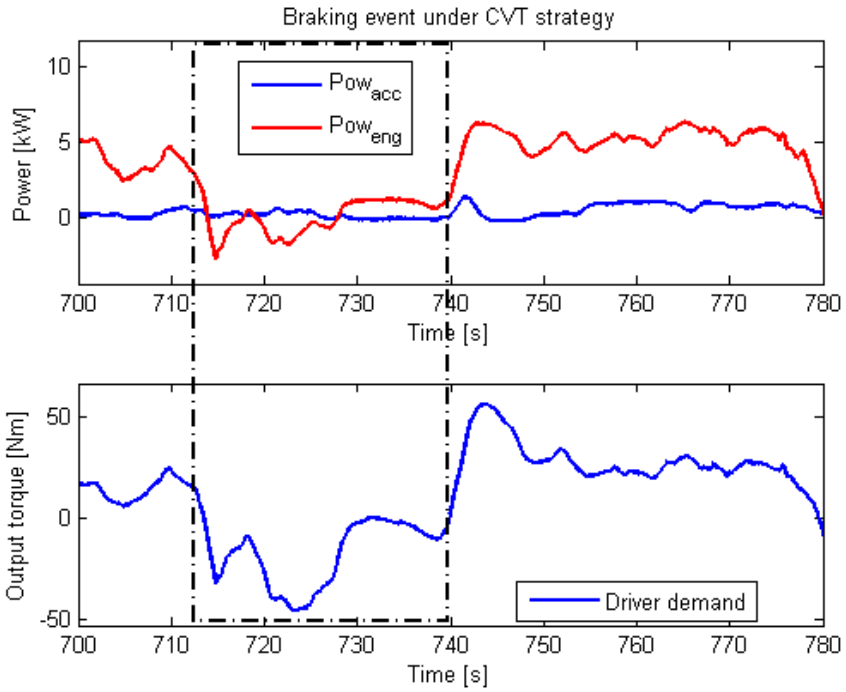

Figure 7.11: Braking behavior of the hybrid powertrain under CVT strategy.

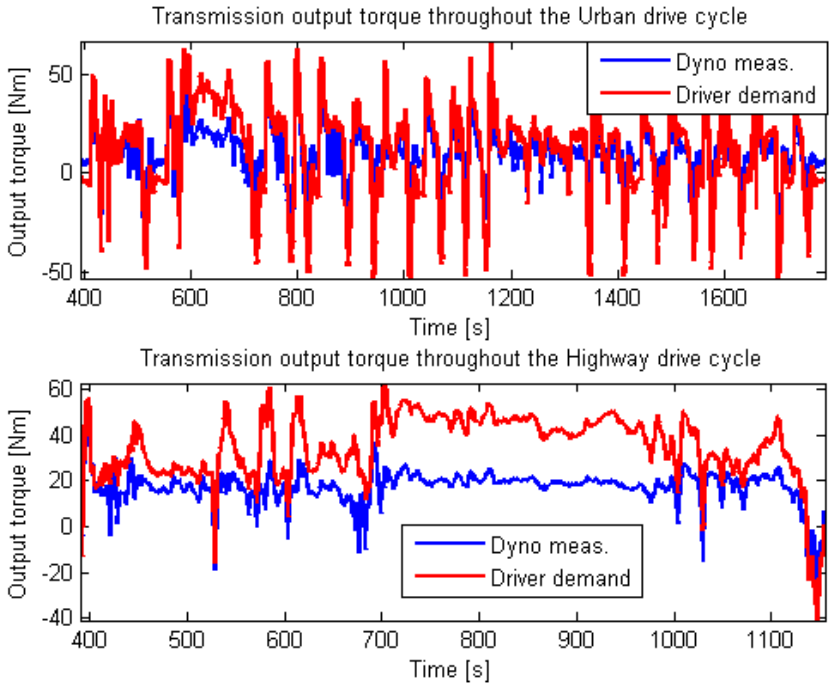

Figure 7.12: Achieved transmission output torque on Urban and Highway drive cycles for CVT mode.

Driver's demand translation: Figure 7.12 shows that the torque demanded by the driver varies widely from the measured output torque. The measured torque is 27% of the demanded torque at the worst case. This is mainly due to the lack of a friction model for the transmission, especially at high transmission output speed and torque.

Recall, the vehicle load is controlled by the dynamometer and the vehicle speed is controlled by the powertrain. Note that even though the measured torque is lower than the demanded torque, the vehicle output torque is correct as the dynamometer controller will exert the correct load if the output speed tracks [69].

7.1.2 Meyer Hybrid Rule-based Strategy

The implementation of the Rule-based strategy developed by Meyer [85]. Recall that this strategy is developed for vehicle mass of 1000kg and the original Combined drive cycle as described in Ch. 6. This strategy achieves 5.03L/100km (46.7mpg) on the Urban Cycle and 4.64L/100km (50.7mpg) on the Highway drive cycle. Compared to the fuel economy predicted in Tab. 6.1, the Rule-based strategy achieves 15.1% lower than predicted (simulation predicts 4.28L/100km (55.0mpg)) for the Urban drive cycle, and 15.5% lower than predicted (simulation predicts 3.92L/100km (60.0mpg)) for the Highway drive cycle. The Meyer Rule-based strategy is not optimized for this particular vehicle, where the rules are developed based on the full size vehicle weight and original EPA drive cycles. Therefore, the fuel efficiency and energy management behavior are not representative of this strategy. The results presented in this section is only used to demonstrate the modularity of the three-level control structure, and analyze the fidelity of the vehicle model.

Figure 7.13 shows the output shaft speed tracking for the Urban and Highway drive cycles, Fig. 7.14 shows the engine speed tracking, Fig. 7.15$\sim$ 7.17 compares commanded and measured engine operating points, and Fig. 7.18 show the system pressure in this energy management strategy. Note that the engine speed is well regulated and the desired drive cycle speed is tracked. Pressure fluctuates between 17.2MPa (2500psi) and 22.1MPa (3200psi). However, due to the thermostatic-behavior control (engine on/off strategy) and low speed torque pulses of the engine, the tracking performance of the vehicle speed has deteriorated to an accuracy of approximately 1 m/s standard deviation.

Engine speed tracking: For this hybrid rule-based operation, the strategy of switching between two-speeds in Fig. 7.14 is apparent, the engine speed behaved as a thermostatic control switching between 125.7 rad/s (1200rpm) and 188.5 rad/s (1800rpm). Apart from the engine torque pulses and valve switching issues mentioned in Sec. 7.1.1, the engine speed controller faces two other challenges in this hybrid strategy; i.e. engine overloading and engine motoring. As seen in Fig. 7.14(b), due to sudden overloading from the transmission pump/motors, the engine control input is saturated, causing the controller to recover from an engine speed transient effect. On the other hand, the inaccurate pump/motors' torque, due to estimating the torque by way of pressure and

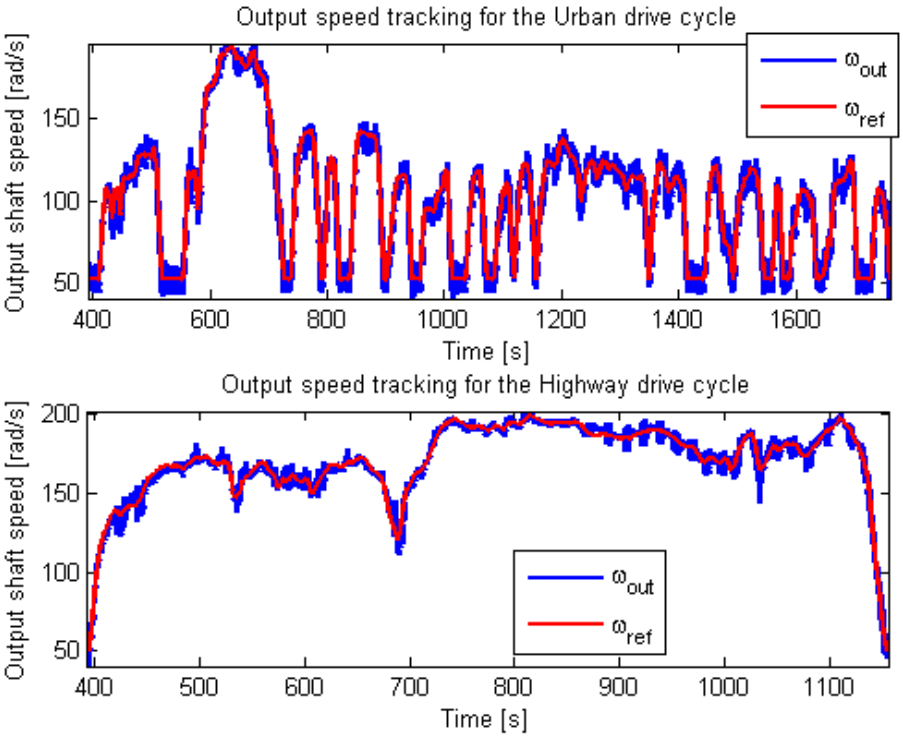

Figure 7.13: Output speed tracking performance under Rule-Based Strategy throughout the Urban and Highway drive cycles.

commanded displacement, could cause the controller to not be able to precisely achieve the desired engine torque. This issue is especially prominent when the engine is required to idle and provide zero torque, which causes the engine to be motored, and thus lowering engine speed tracking performance.

Engine output torque: Similar to the CVT strategy case, Fig. 7.15 depicts the difference between estimated and measured engine output torque in urban and highway drive cycles. Interestingly, the engine torque estimation matches the measured engine torque fairly closely in the Urban drive cycle. Whilst in the Highway drive cycle, the estimated engine torque is much higher than the measured engine torque at high output shaft speed. The cause of the discrepancy will be explained in Sec. 7.2.

The engine operating points are then shifted to a lower efficiency region (see Fig. 7.16 and 7.17), causing lower fuel economy. The actual engine operating points for the Urban Cycle only differs slightly from the commanded operating points, while the Highway Cycle differs significantly due to the over-estimation of the transmission output torque. Moreover for the highway drive cycle, both estimated and measured engine operating points are clustered at 188.5rad/s and 240.8rad/s with measured engine operating points at a lower torque level.

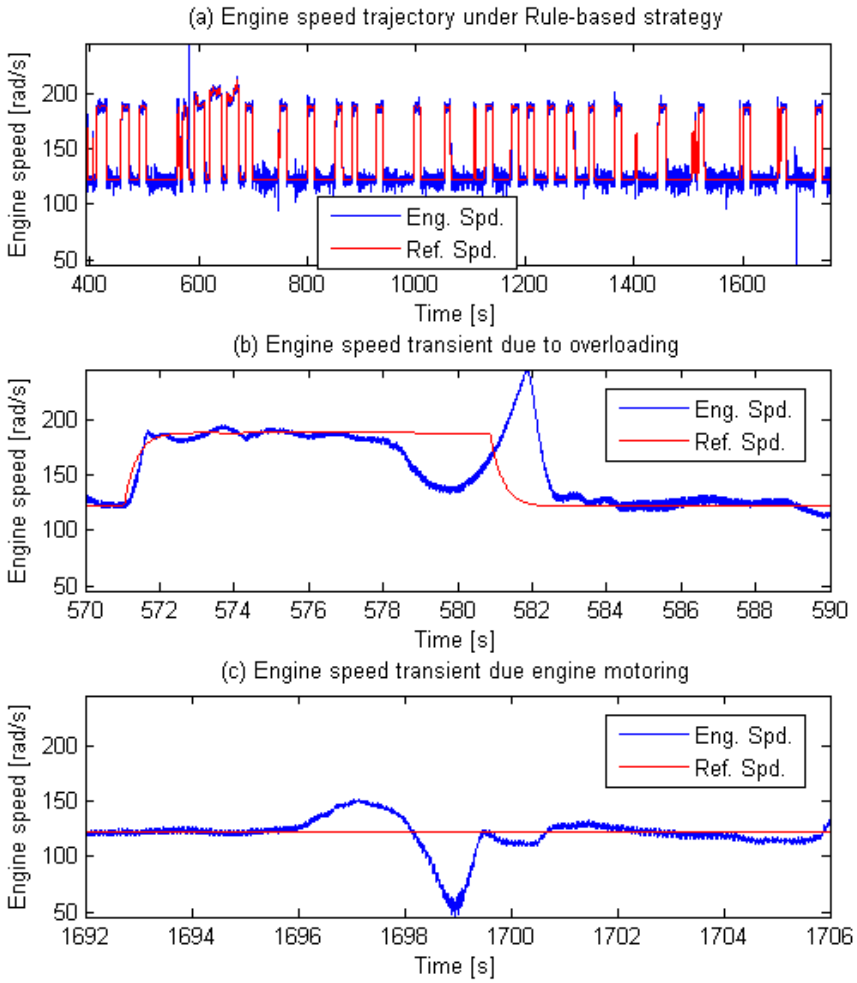

Figure 7.14: (a) Engine speed tracking under Rule-Based Strategy in the Urban cycle. (b) Engine speed tracking transient due to overloading. (c) Engine speed tracking transient due to engine being motored.

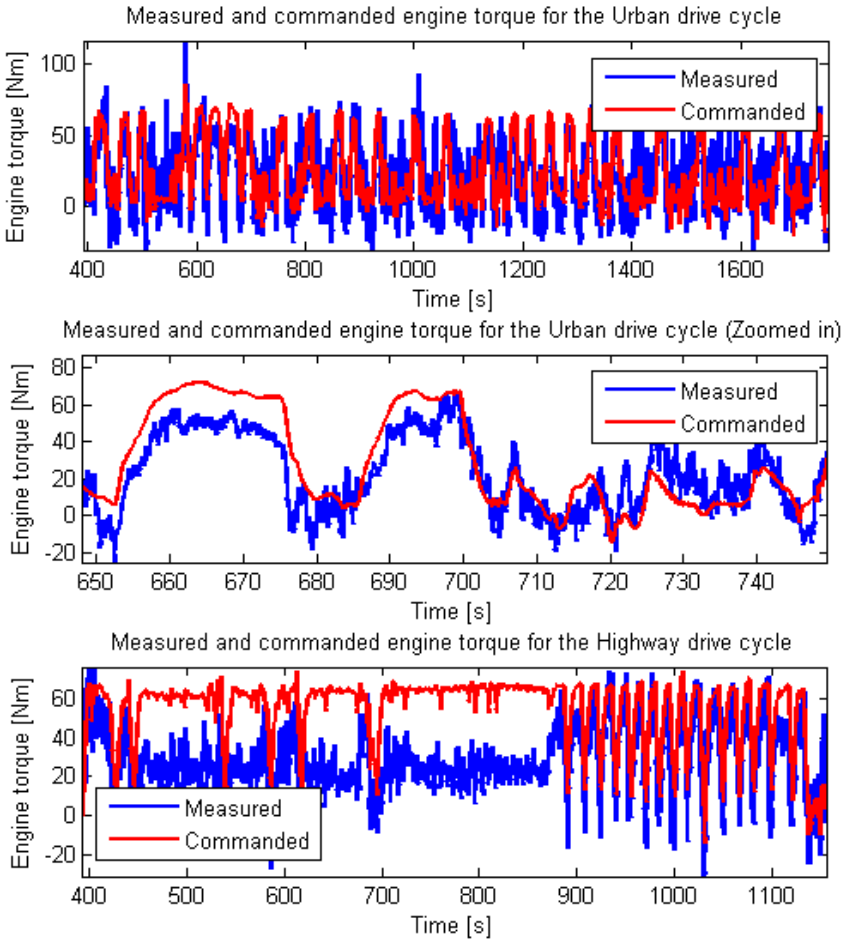

Figure 7.15: Comparison of estimated and measured engine torque on the Urban and Highway drive cycles under Rule-based strategy.

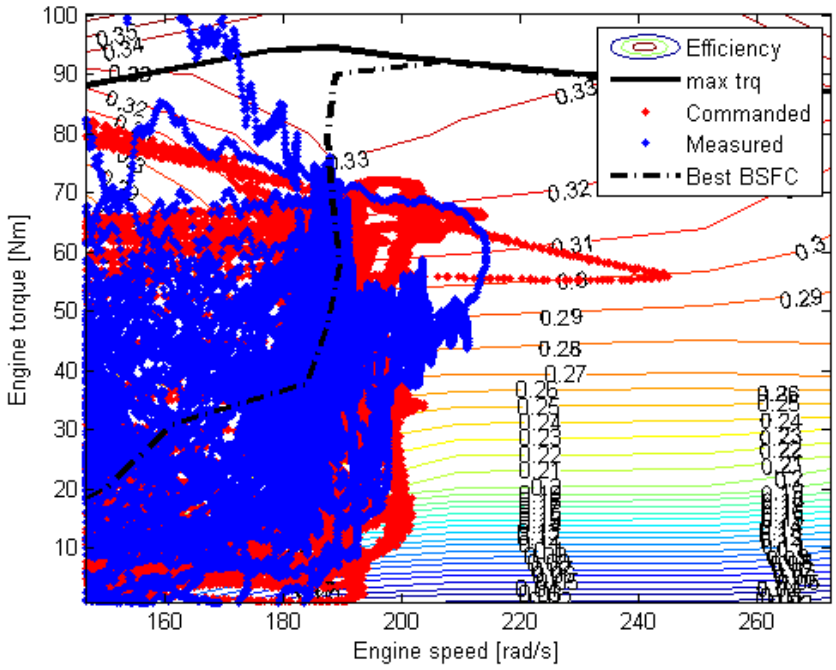

Figure 7.16: Comparison of estimated and measured engine operating points on Urban drive cycle for Rule-based control.

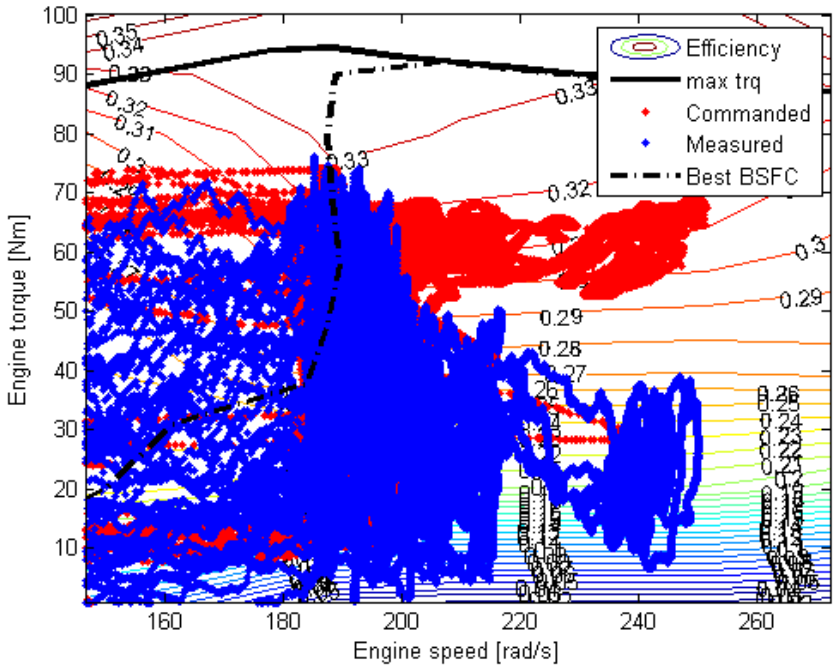

Figure 7.17: Comparison of estimated and measured engine operating points on Highway drive cycle for Rule-based control.

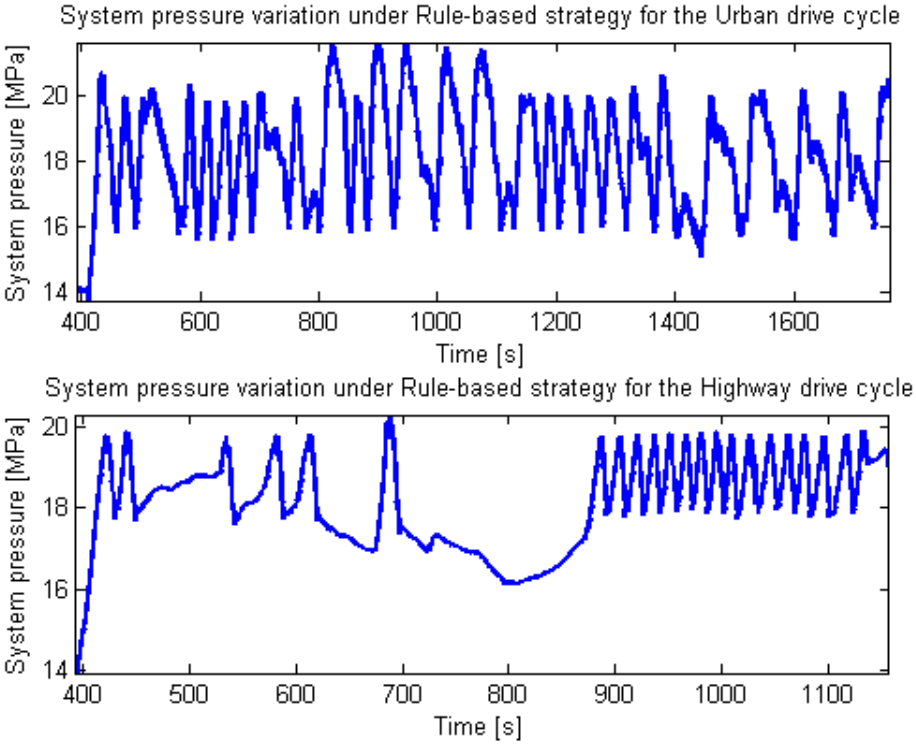

Figure 7.18: System pressure variation under Rule-Based Strategy.

System pressure variation: Unlike the CVT strategy to maintain the system pressure at a constant value, this hybrid strategy is required to vary the accumulator charge and system pressure. Figure 7.18 shows the system pressure variation throughout Urban and Highway cycles. Based on the thermostatic-behavior of the engine speed control, it is predictable that the system pressure will fluctuate between its high and low bounds (15.2-22.8MPa) (2200-3300psi). However, while the system pressure fluctuates between 15.9MPa (2300psi) and 20.7MPa (3000psi) in Urban drive cycle, the system pressure fluctuates between 17.2MPa (2500psi) and 22.1MPa (3200psi) for Highway drive cycle instead. Figure 7.19 and 7.20 show the engine and accumulator power when the vehicle is operated under the Rule-based strategy on the Urban and Highway drive cycles.

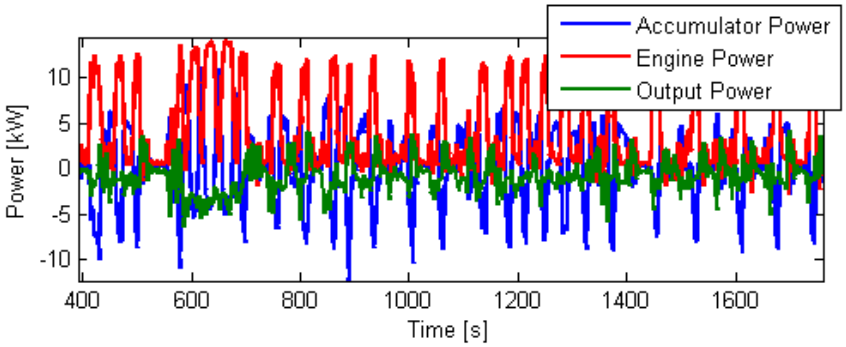

Figure 7.19: Power flow for the Rule-based strategy on Urban drive cycle.

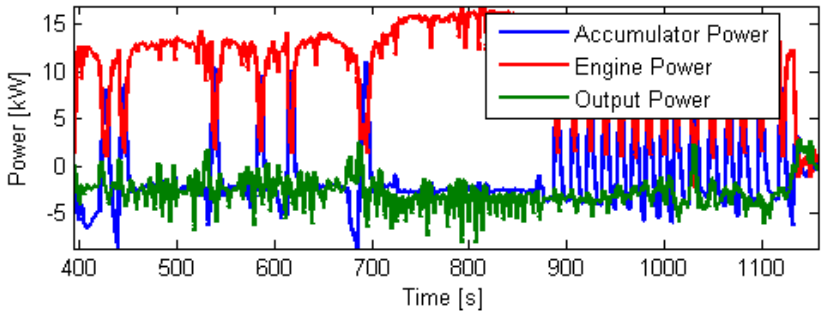

Figure 7.20: Power flow for the Rule-based strategy on Highway drive cycle.

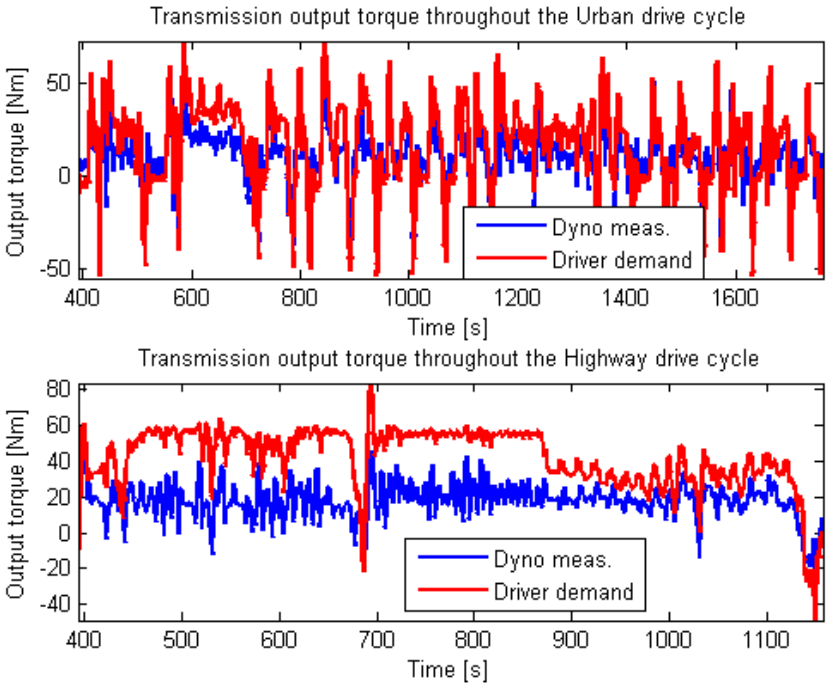

Figure 7.21: Achieved transmission output torque under Rule-based strategy on the Urban and Highway drive cycles.

Driver's demand translation: Expectedly, Fig. 7.21 shows the torque demanded by driver varies widely from the measured output torque. The estimated transmission output torque is generally higher than the actual output torque measured by dynamometer. The discrepancy ranges from 20% to 300% higher, especially at higher transmission speed.

7.2 Discussions

The results have revealed three major challenges; (i) discrepancy between simulated engine operating point and experimental data, (ii) discrepancy between controller commanded engine torque and measured engine torque, and (iii) significant over-estimation of the transmission output torque.

The discussions have important implications on the developed powertrain model and implementation of the controllers. The discrepancies between the simulated engine operation and measured engine operation indicates that the assumptions of neglecting transmission gear friction may not be valid. The transmission output torque is substantially lower than expected, and it caused the engine to operate in the incorrect region, effectively lowering the efficiency of the powertrain throughout the drive cycle. It is vital to refine the loss model of the powertrain in order to operate the engine accurately and efficiently.

Once the issues described are addressed, other energy management strategies presented in Ch. 6, including the Dynamic Programming (DP) strategy and the Modified Lagrange Multiplier (MLM) strategy can be implemented. According to simulation results in Ch. 6, the DP and MLM strategies will perform more efficiently than CVT and Meyer Rule-based strategies.

7.2.1 Comparison with simulated engine operating points

The purpose of this comparison is to ensure the Mid and Low level controllers are performing as expected. The simulated engine operation used for comparison is presented in Sec. 6.4, using the powertrain model presented in Ch. 5. Recall, the commanded engine operation is the desired engine operating point specified by the simplified Mid-level controller in Sec. 6.2.2, which constrains the engine operation to the best BSFC curve. The measured engine operation is determined from the real-time engine speed and torque measurement. As for the low level controller, the P/M-S displacement x_S is determined by the vehicle torque demand T_{out}, and P/M-T displacement x_T is determined by the desired accumulator flow Q_{acc}.

Figure 7.22 and 7.23 show the comparison between the simulated engine operation

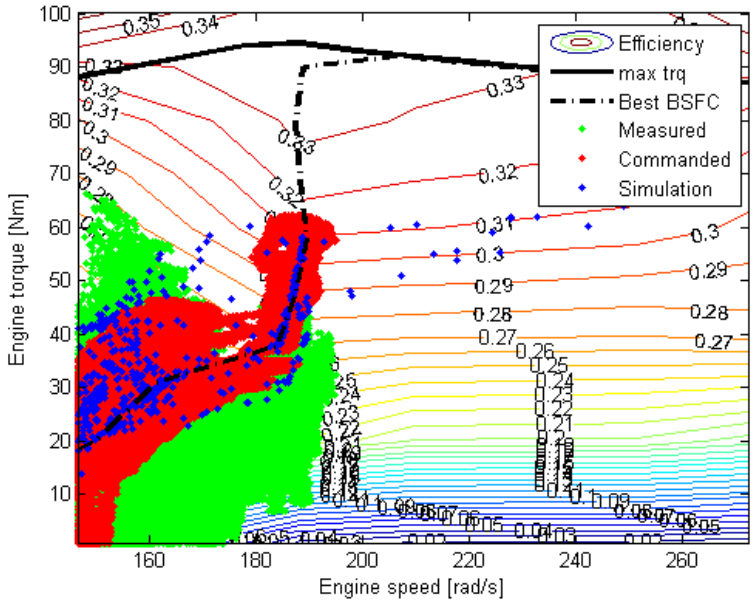

Figure 7.22: Comparison between simulated, commanded and measured engine operating points under CVT strategy on the Urban drive cycle.

(CVT results from Sec. 6.4), the real-time commanded engine operation (desired engine operation determined by the mid-level controller during the experiment), and the achieved engine operation (measured engine speed and torque during the experiment). For both drive cycles, the commanded engine operation is close to the best BSFC curve according to the simplified Mid-level controller designed. The commanded engine operation also behaves similarly to the simulated engine operation, showing the powertrain controller is behaving expectedly. The simulated engine operation tends to be at slightly lower power than the commanded engine operation. This is due to higher demanded output torque in the experiment than in simulation.

In contrast, the measured engine operation is generally at lower torque than the commanded engine torque, despite the large amplitude engine torque fluctuation[7] . The commanded engine speed is the same as the measured engine speed because the engine speed controller performs as expected. Recall in the low level controller in Sec. 6.2.3, the desired engine torque is achieved by setting x_T, x_S according to T_{out} and Q_{acc}. The

[7] Please note that the engine torque measurement is filtered by a low pass filter.

discrepancy between commanded and measured engine torque indicates the portion of the low level controller fails to achieve the desired engine torque. This issue will be further discussed in the following section.

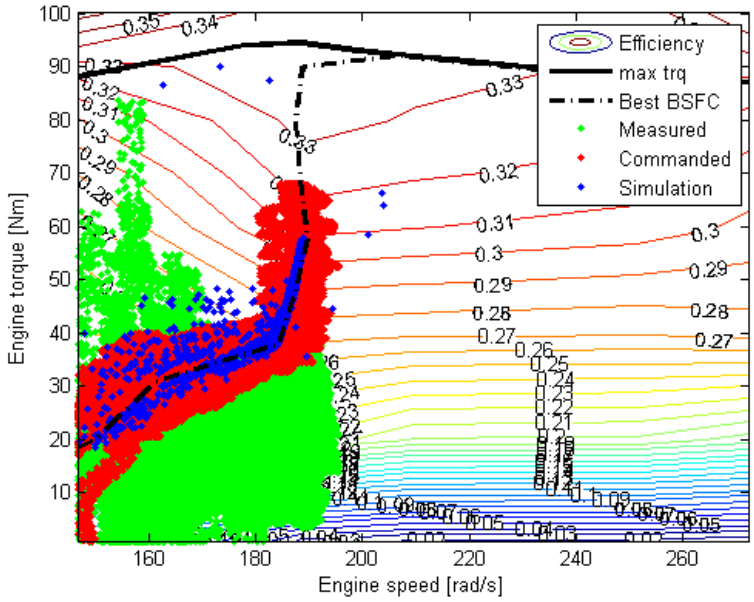

Figure 7.23: Comparison between simulated, commanded and measured engine operating points under CVT strategy on the Highway drive cycle.

Another possible cause for the discrepancy between commanded and measured engine operation is the erroneous engine torque measurement. Recall that the diesel engine generates high torque pulses, where the torque sensor may not perform as expected under such highly dynamic situation. The engine torque sensor measurement needs to be verified to ensure the measured engine operation is correct.

Figure 7.24 shows the comparison between the measured engine power and measured wheel power under the CVT strategy on the Urban drive cycle. The overall transmission efficiency throughout the drive cycle is 43%. The lowest transmission efficiency occurred during low vehicle speed, where the wheel power is near zero. On the other hand, the transmission operated between 62% $\sim$ 93% when wheel power is higher than 5kW. This also indicates that the engine torque measurement is within reasonable accuracy.

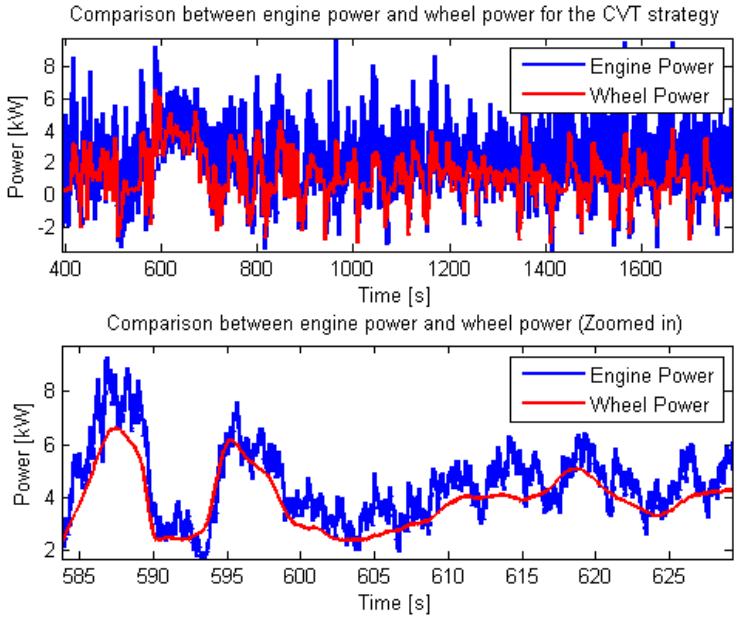

Figure 7.24: Comparison between measured engine power and measured wheel power under the CVT strategy on the Urban drive cycle.

7.2.2 Discrepancy of engine operation due to lower transmission output torque

The experimental data presented shows the measured engine operating torque tends to be lower than the commanded engine operating torque. As mentioned earlier, one possible explanation that causes the engine to produce lower than expected torque is due to the lower level controller failing to achieve the correct torque. From Eq. (5.29), the engine torque at steady-state can be expressed as:

$$T_{eng} = -R_T T_T(x_T, \omega_T, P_{sys}) - \frac{1}{\rho(1+1/\rho)} T_{meas} \tag{7.1}$$

$$\hat{T}_{eng} = -R_T T_T(x_T, \omega_T, P_{sys}) - \frac{1}{\rho R_S} T_S(x_S, \omega_S, P_{sys}) \tag{7.2}$$

where T_{eng} is the actual engine torque as a function of measured output torque, $\hat{T}_{eng}$ is the desired engine torque based on commanded P/M-S torque, T_T, T_S are the P/M-T and P/M-S torque, and T_{out} is the vehicle torque demand. The low level controller in Sec. 6.2.3 assumes that the desired engine torque is achieved if the desired T_T, T_S determined by T_{out} and Q_{acc} is achieved. Here, T_T and T_S are the only two sources of error to achieve T_{eng}.

Recall the simplified mid-level controller that constrains the engine to operate along the best BSFC curve is expressed as:

$$Pow_{eng} = \frac{1}{\eta_{trans}} \cdot (\omega_{out} \cdot T_{out} + Pow_{acc})$$
$$(\omega^*_{eng}, T^*_{eng}) = BSFC(Pow_{eng})$$

where η_{trans} is the transmission efficiency assumed to be a constant value of 85%, and the best BSFC engine speed ω^*_{eng} is monotonically increasing with transmission output power for a specific Pow_{acc}. $(\omega^*_{eng}, T^*_{eng})$ is the desired engine operation. Here, T_{out} is the vehicle torque demand of the hybrid powertrain controller, and T_{meas} is the measured output torque from the dynamometer. Both torques are acting on the same transmission shaft, which is the point before the differential.

Note that $T_{out} > T_{meas}$ does not invalidate the fuel economy results as the hydrostatic dynamometer is controlled to load the powertrain at the correct torque, while the

vehicle speed tracks the drive cycle speed. The dynamometer exerts the correct load for corresponding output shaft speed [69]. Since T_{meas} is the actual measured load exerted on the output shaft, T_{meas} defines the 'true' load for the vehicle and also the 'true' output torque of the transmission. T_{out} is the desired output torque condition specified by the powertrain controller, which may not be perfectly attainable. The 'virtual driver' feedback controller allows the output speed tracking despite T_{out} not being identical to T_{meas}.

Consider the case when the vehicle torque demand T_{out} (based on P/M-S torque in Eq. (7.2)) is greater than the actual measured output torque T_{meas}, i.e. $T_{out} > T_{meas}$ for a specific Pow_{acc}. Also, consider the case where $T^*_{eng}(T_{out}) > T^*_{eng}(T_{meas})$[8] , and T_T is exact (achieved accurately). The desired engine speed for T_{out} and T_{meas} becomes $\omega^*_{eng}(T_{out}) > \omega^*_{eng}(T_{meas})$ since the engine is constrained to operate along the best BSFC curve. As a result, the measured (achieved) engine torque $T_{eng}(T_{meas})$ is lower than the commanded engine torque $T^*_{eng}(T_{out})$, i.e. $T_{eng}(T_{meas}) < T^*_{eng}(T_{out})$. Graphically, it can be shown in Fig. 7.25.

Figure 7.25 illustrates the cause of the measured engine torque being lower than the commanded engine torque. Point (1) represents the fictitious commanded engine operating point of $(\omega^*_{eng}(T_{meas}), T^*_{eng}(T_{meas}))$ if measured torque were used, according to Eq. (7.1). This assumes T_{meas} is utilized to determine $(\omega^*_{eng}, T^*_{eng})$. Point (2) represents the commanded engine operating point of $(\omega^*_{eng}(T_{out}), \hat{T}^*_{eng}(T_{out}))$ based on vehicle torque demand provided by the controller, according to Eq. (7.2). Point (3) represents the measured engine operating point of $(\omega^*_{eng}(T_{out}), T^*_{eng}(T_{meas}))$ where $T_{out} > T_{meas}$, with lower engine torque at higher engine speed, causing lower engine efficiency.

This explains the discrepancy between the commanded engine torque and measured (achieved) engine torque caused by the measured output torque being lower than expected. This leads to another issue presented in Sec. 7.1.1, i.e. the measured output torque T_{meas} is significantly lower than the vehicle torque demand T_{out}. The following section will discuss this issue.

[8] This is valid for engine speed below 209rad/s from Fig. 5.9.

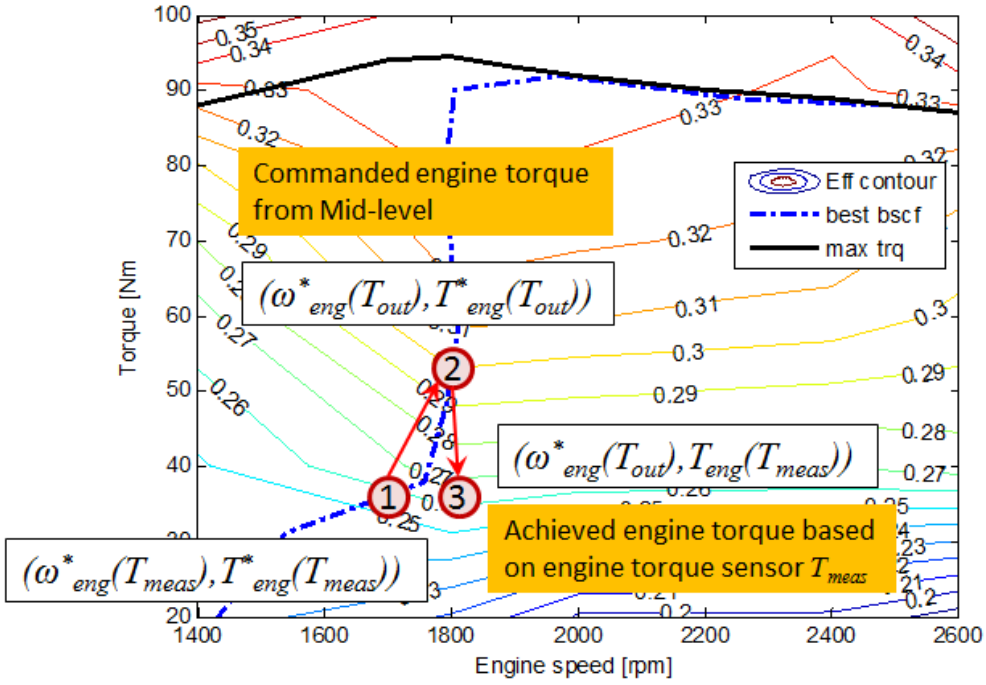

Figure 7.25: Illustration of the engine torque discrepancy. Point (1) represents the commanded engine operating point of $(\omega^*_{eng}(T_{meas}), T^*_{eng}(T_{meas}))$. Point (2) represents the commanded engine operating point of $(\omega^*_{eng}(T_{out}), T^*_{eng}(T_{out}))$. Point (3) represents the achieved engine operating point of $(\omega^*_{eng}(T_{out}), T^*_{eng}(T_{meas}))$, assuming $T_{out} > T_{meas}$.

7.2.3 Discrepancy between vehicle torque demand and measured output torque

As discussed previously, the discrepancy between vehicle torque demand and measured output torque may caused the failure of the low-level controller to achieve the desired engine torque. Experimental data from both energy management strategies shows discrepancy between demanded torque and measured output torque.

The model and controls developed from Ch. 5 and 6 have been assuming a frictionless transmission geartrain. By assuming all torque difference, $T_{out} - T_{meas}$, is attributed to the transmission gearbox friction, a friction model can be used to describe the discrepancy. By further assuming the friction between the gear mesh of the transmission is dominated by viscous friction[9] , the transmission's viscous friction model is expressed as:

$$T_{frict} = T_{out} - T_{meas} = a_1\omega_{out} + a_2\omega_S + a_3\omega_T \tag{7.3}$$

where T_{frict} is the overall transmission viscous friction translated at the transmission output shaft. The engine speed ω_{eng} is omitted since $\omega_{eng} = \omega_T/R_T$. The coefficients a_1, a_2, a_3 are determined using the least-squares method in Eq. (7.3) using the experimental data $T_{out}, T_{meas}, \omega_{out}, \omega_S, \omega_T$.

The viscous friction model coefficients are $a_1 = 0.1839$, $a_2 = -0.8141$, and $a_3 = 1.1117$. Note that the coefficient a_2 is negative, meaning that the friction from P/M-S is adding torque to the output shaft for $\omega_S > 0$. According to Eq. (5.29) for vehicle driving forward case, P/M-S is pumping when $\omega_S > 0$ and is motoring when $\omega_S < 0$. Recall the sign convention for $T_{out} < 0$ is driving forward, and $T_{out} > 0$ is braking.

From Eq. (5.27), P/M-S speed can be directly determined from ω_{eng} and ω_{out}, where $\omega_S = \frac{1}{\rho R_S}\omega_{eng} - \frac{(1+1/\rho)}{R_S}\omega_{out}$. The viscous friction model can therefore be simplified to:

$$T_{frict} = (R_T a_3 + \frac{1}{\rho R_S}a_2)\omega_{eng} + (a_1 - \frac{1+1/\rho}{R_S}a_2)\omega_{out} \tag{7.4}$$

The compensated demand torque $T_{comp} = T_{out} - (a_1\omega_{out} + a_2\omega_S + a_3\omega_T)$ is compared to the measured output torque T_{meas}. This is to ensure the viscous friction model is

[9] There are several sources of possible gearbox losses, including viscous friction, shaft seal friction, and oil churning losses.

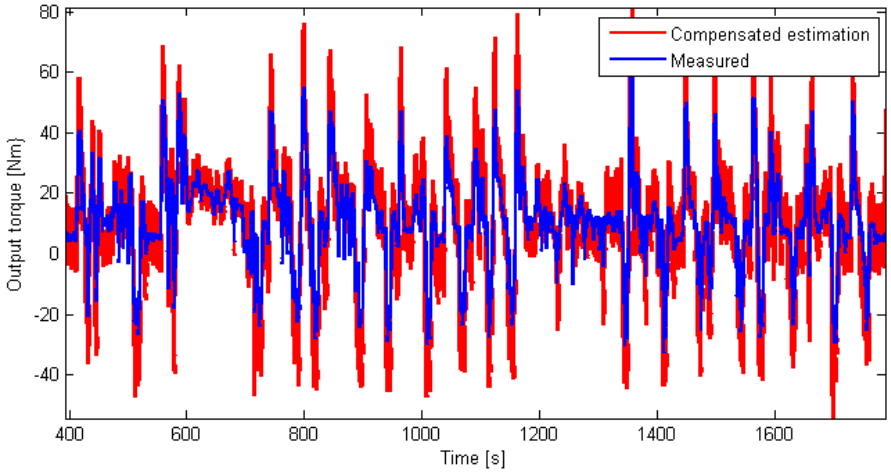

Figure 7.26: Friction compensated transmission output torque on Urban drive cycle

capable of predicting the transmission torque loss.

CVT mode: The friction compensated transmission output torque has significantly improved the match between the commanded and actual output torque for the Urban drive cycle, as seen in Fig. 7.26. Applying the viscous friction coefficients for the Highway drive cycle, the friction model has significantly improved the transmission output torque estimation. However, this friction model still generally over-estimates the output torque, especially at high output torque (see Fig. 7.27).

Meyer Rule-based Strategy: Applying identical viscous friction coefficients to the friction model to compensate for the transmission output torque, the results for the Urban drive cycle are promising but only improve the estimation slightly for Highway cycle. Results can be seen in Fig. 7.28 and 7.29.

The hypothesized friction model has explained the discrepancy of the demanded output torque and measured transmission torque, especially for the Urban drive cycle. The model only reduces the maximum discrepancy to 63% for the Highway drive cycle under CVT strategy, and to 101% for the Highway drive cycle under the Meyer Rule-based strategy. This friction model can be easily incorporated into the Mid-level controller to compensate for the geartrain friction loss.

The transmission dynamics in Eq. (5.34) can be modified to include the friction

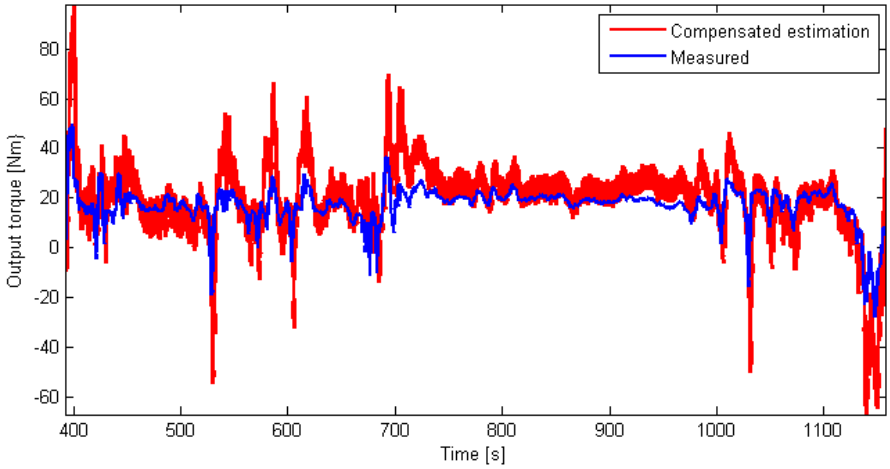

Figure 7.27: Friction compensated transmission output torque on Highway drive cycle for CVT mode.

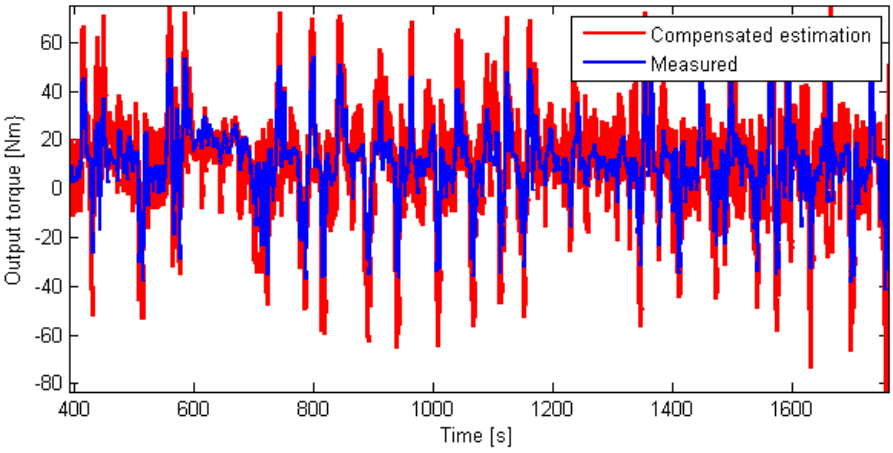

Figure 7.28: Compensated transmission output torque under Rule-based strategy on Urban drive cycle.

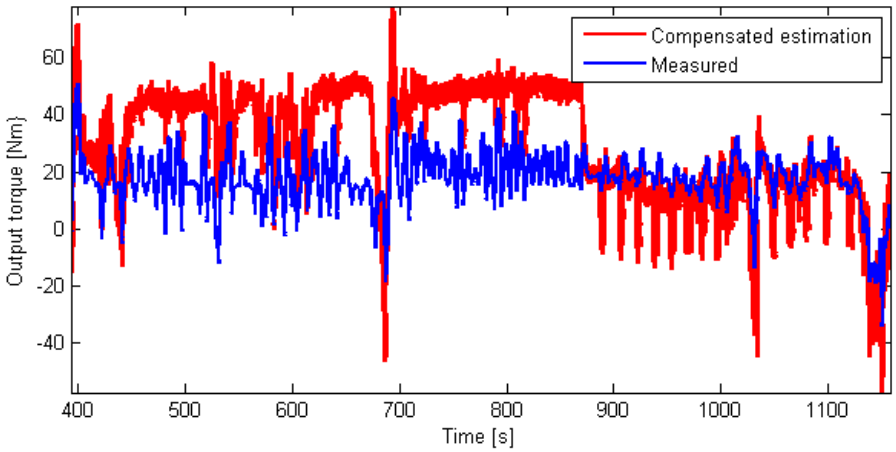

Figure 7.29: Compensated transmission output torque under Rule-based strategy on Highway drive cycle.

model:

$$\begin{aligned}
&\begin{pmatrix} (J_{eng} + R_T^2 J_T + \frac{1}{\rho^2 R_S^2} J_S) & -\frac{(1+\rho)}{\rho^2 R_S^2} J_S \\ -\frac{(1+\rho)}{\rho^2 R_S^2} J_S & (J_{veh} + \frac{(1+1/\rho)^2}{R_S^2} J_S) \end{pmatrix} \begin{pmatrix} \dot{\omega}_{eng} \\ \dot{\omega}_{out} \end{pmatrix} \\
&= -\begin{pmatrix} \frac{1}{\rho(1+1/\rho)}(R_T a_3 + \frac{1}{\rho R_S} a_2) & \frac{1}{\rho(1+1/\rho)}(a_1 - \frac{1+1/\rho}{R_S} a_2) \\ (R_T a_3 + \frac{1}{\rho R_S} a_2) & (a_1 - \frac{1+1/\rho}{R_S} a_2) \end{pmatrix} \begin{pmatrix} \omega_{eng} \\ \omega_{out} \end{pmatrix} \\
&\qquad + \begin{pmatrix} T_{eng} + R_T T_T + \frac{1}{\rho R_S} T_S \\ -\frac{(1+1/\rho)}{R_S} T_S - T_{load} \end{pmatrix}
\end{aligned} \tag{7.5}$$

The difference between the demanded and measured output torque has so far been assumed to be attributed to the friction previously mentioned. Another possibility that could cause this difference is under-calibrated P/M-S displacement actuation. As presented previously in Ch. 5, P/M-S torque determines the transmission output torque. Thus, if the actual P/M-S torque is lower than expected, the measured transmission output torque will be lower than the desired output torque. Another possible cause of the torque difference is neglected load-dependent friction loss in the friction model, even though it is generally estimated to be significantly lower than speed-dependent (viscous) friction loss [86, 87].

Ctrl. Stgy.	Exp. FE $L/100km$ (mpg)	Std. Dev. (mpg)	Sim. $L/100km$ (mpg)
CVT	Urban: 4.73 (49.7)	1.96	4.19 (56.2)
	Highway: 4.12 (57.1)	2.26	3.83 (61.4)
Rule-based	Urban: 5.04 (46.7)	n/a	4.28 (55.0)
	Highway: 4.64 (50.7)	n/a	3.92 (60.0)

Table 7.1: Fuel economy (FE) results based on two energy management strategies.

7.2.4 Fuel Economy Variation

Fuel economy for the CVT mode is 4.73L/100km (49.7mpg)[10] with standard deviation of 1.96mpg on the Urban Cycle, and 4.12L/100km (57.1mpg) with standard deviation of 2.26mpg on the Highway Cycle over five tests each. The Meyer rule-based hybrid strategy achieved lower fuel economy than the CVT mode, 46.7mpg on the Urban Cycle and 4.64L/100km (50.7mpg) on the Highway Cycle. The rule-based strategy was only tested once. The variation on the Urban drive cycle (*approx* 12.4km) is lower than the Highway drive cycle (*approx* 11.7km) mainly due to the longer distance travelled, thus it is less sensitive to fuel weight measurement error. Fuel consumption weight measurement accuracy is $\pm 10g$[11] . The measurement accuracy provides up to $\pm 1.0mpg$ for Urban drive cycle, and $\pm 1.6mpg$ for Highway drive cycle.

Estimated and simulated fuel consumptions are summarized in Table 7.1. Intuitively, the hybrid strategy is expected to increase the fuel economy significantly on the Urban cycle due to frequent starts and stops, while the benefit would be less substantial on the Highway cycle since CVT mode is fairly efficient transferring power through mechanical path. However, the simulation and experimental results show the Meyer Rule-based strategy is consistently less efficient than CVT strategy. This indicates that the Meyer Rule-based strategy is not optimized for this particular vehicle, where the rules are developed based on the full size vehicle weight and original EPA drive cycles.

The Meyer Rule-based hybrid strategy is expected to perform slightly less fuel efficient (4 mpg less) than CVT strategy on the Urban cycle from simulation. In experiment, the result is 8.3 mpg less efficient than expected. It is hypothesized that

[10] Recall that the test parameter corresponds to a fictional vehicle with mass of 500kg.

[11] The fuel consumptions are typically $\approx 500g$ for the Urban cycle, and $\approx 400g$ for the Highway drive cycle.

the difference is mainly due to the erroneous engine operating points described earlier. Another possible cause would be the unmodelled engine transient efficiency effect [60], where frequent fluctuation of engine operating speed is reducing the efficiency and increasing emissions of the engine.

Similarly on the Highway cycle, the CVT mode is fairly efficient already because most power is transferred through the mechanical path (see power-split ratio results in Sec. 7.1.1). The Rule-based hybrid strategy frequent pressure fluctuation causing the powertrain to be less efficient in simulation is therefore not too surprising. Once again in reality, the Rule-based strategy is 6.4 mpg less efficient than CVT mode, and 9.3mpg less than simulated mileage. This is again contributed by the wrongly estimated engine operating condition.

7.2.5 Directional Valve Switching

As mentioned in Sec. 5.3, the pump/motors are not capable of operating over-center, and both pump/motors on the transmission are required to operate over-center despite the selection of energy management strategy. Thus directional valves are switched to achieve such operation, causing disturbances to the engine controller as illustrated in Fig. 7.30. This particular negative effect is proportional to the system pressure: higher pressure causes stronger disturbances.

7.3 Concluding Remarks

The experiments presented in this chapter demonstrated that the hardware is operational and the hierarchical powertrain control structure is effective. A three-level hierarchical control strategy has been implemented on a hydraulic hybrid passenger vehicle test bed with the high level being a baseline CVT mode and a rule based hybrid energy management strategy. Both control strategies are tested through Urban and Highway drive cycles. The high level strategies are tested without modifying the mid and low level controllers, validating the modularity feature of the three level hierarchical control structure. The engine speed controller is shown to perform expectedly. However, due to torque pulses of the diesel engine, the engine tracking performance is worst at low engine speed.

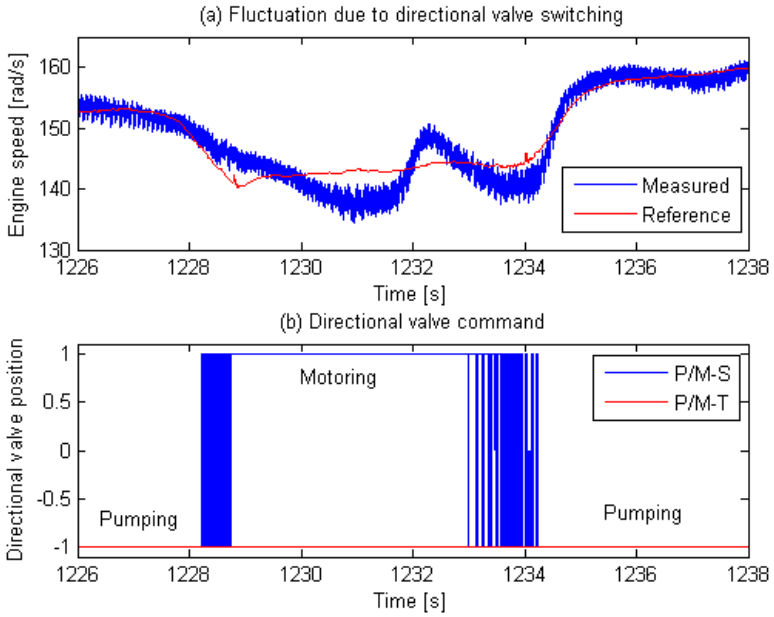

Figure 7.30: Effect of directional valve switching on engine speed regulation. Illustration shows P/M-T directional valve switching from pumping to motoring, and then from motoring to pumping.

The CVT strategy is a relatively simple energy management controller and it is used as a baseline strategy. For the CVT strategy, pressure regulation controller manages to maintain the high pressure at desired pressure level within 0.14MPa (20psi) accuracy. A P-I controller should be used to improve accuracy. The mid-level controller is capable of operating the engine efficiently. However, the measured output torque is substantially lower than the vehicle torque demand.

The hybrid strategy utilizes the accumulator energy and is supposed to improve the overall powertrain efficiency. However, according to results in Ch. 6, the rule-based strategy developed in Meyer [85] predicted to achieve lower fuel economy than the CVT strategy. Experimental results also shows lower fuel economy with the hybrid rule based strategy compared to the CVT strategy. This is due to the rules were developed based on the full size vehicle weight and original EPA drive cycles.

Comparison between experiments and simulation of the engine operating points shows the mid-level is behaving expectedly. However, the measured engine torque is

lower than the commanded engine operation. This issue is speculated to be caused by the measured output torque being lower than the vehicle torque demand. The vehicle torque demand discrepancy leads to engine operating points shifted to lower efficiency region, contributing to lower fuel efficiency.

The vehicle torque demand discrepancy suggests that there is significant transmission friction that has not been taken into account. The transmission friction is modelled as viscous friction, as a function of output shaft speed, engine speed and P/M-S speed. By making the assumption that the discrepancy between vehicle torque demand and measured torque is due to friction, the friction model is able to improve the output torque command especially for Urban drive cycle. However, the powertrain loss model still requires further tuning in order for the demanded vehicle torque to match the measured output torque.

The engine torque sensor measurement should be verified to ensure the engine operation is correct. Further fine tuning on the powertrain loss model, by including the friction model into the mid and low level controller, is required to operate the engine at higher efficiency region more accurately. Other energy management strategies including the DP and MLM strategies should be tested once the discrepancies of torques are addressed.

Chapter 8

Modeling and Optimization of the Generation II Hydraulic Hybrid Vehicle

The 'Generation II' project is a collaboration between Folsom Technologies International (FTI) and Center for Compact and Efficient Fluid Power (CCEFP) at the University of Minnesota. The vehicle donated by Ford Motor Company to the University of Minnesota is a Ford F-150 full-size pickup truck as seen in Fig. 8.1. The vehicle is reconfigured from the conventional drivetrain using a FTI Hydro-Mechanical Transmission (HMT). By adding directional control valves, and a low and a high pressure accumulator, it will be further developed into a hydraulic hybrid vehicle.

As a stand-alone transmission, the hydro-mechanical transmission can be used to operate the engine at its most efficient operating point for a specific power curve that satisfies the power demand at the wheel. As a hydraulic hybrid transmission, energy storage makes the engine management more flexible. By using power from the energy storage the engine can operate at a more optimal spot independent of the power output demand. Lost energy through friction braking can also be recovered into the high pressure accumulator and used for vehicle launch and engine management.

The main power source of the conventional, commercial F-150 truck is a typical 4.6 litre 24 valves V8 naturally aspirated gasoline engine. The differential at the rear splits

Figure 8.1: Ford F-150 Pickup Truck

the power between the two wheels with a final drive ratio of 3.31. The conventional F-150 truck achieves a fuel economy of 17.9mpg in the city and 26.0mpg over the highway drive cycle (provided by Ford Motor Company). The main goal of this test bed is to investigate the potential and benefits of converting a conventional powertrain to a hydraulic hybrid powertrain for a pick-up truck sized vehicle, and to understand the differences between an input coupled architecture (Generation I vehicle) and an output coupled architecture (Generation II vehicle).

Simulations are conducted to predict the fuel economy improvement that can be achieved by using the Folsom HMT. An increase of 61% in fuel economy is predicted by replacing the conventional 6-speed transmission with the hydraulic transmission operating in hybrid mode. Simulation results show fuel efficiency of the powertrain is improved by optimizing the engine management, even though the transmission efficiency is lower than that of a conventional transmission.

The rest of the chapter will be organized as follows: Section 8.1 introduces the design of the FTI hydro-mechanical transmission. Section 8.2 and 8.3 describe the engine and pump/motor model, which is similar to the Generation I vehicle. Section 8.4 presents the dynamic model of the hybrid powertrain. Section 8.5 discusses the basic operation of

the HMT as a stand-alone transmission. Section 8.6 presents the potential fuel economy improvement achieved by using the Folsom HMT and hybridizing the transmission with accumulators. Section 8.7 discusses the potential fuel economy improvement with the Folsom HMT optimized using the methodology presented in Ch. 2. Section 8.8 contains some concluding remarks on the Generation II powertrain and system identification method used to characterize the transmission.

8.1 Folsom Hydro-Mechanical Transmission

The Folsom Hydro-Mechanical Transmission (HMT) is configured as an output coupled power-split transmission. The transmission consists of two 222cc variable displacement axial piston bent-axis pump/motors, three planetary gear sets, a clutch, two morse chains, and a charge pump (see Fig. 8.2).

The charge pump is a variable displacement vane pump, located on the drive shaft on the input side, regulating the transmission's low pressure side between 0.69 MPa (100 psi) to 1.39 MPa (200 psi). The input shaft is connected to planetary gearset 1 (PG1) at the carrier. The power from the engine is split between the sun gear and ring gear. The sun is connected to planetary gearset 2 (PG2) and a Morse chain to one of the 222cc hydraulic units (P/M-S). The carrier of PG2 is grounded and therefore works as a simple gear ratio. The ring of PG1 transmits power to the output through a mechanical drive shaft. PG3 is also mechanically linked to the output at its carrier. A clutch on the sun gear can enable or disable the transmission of torque through this gear set. PG3 combines the power from the second hydraulic unit and the mechanical carrier. A hydraulic pump/motor (P/M-T) is connected through a Morse chain to the ring gear of this gear set. This configuration allows the transmission to adjust the portion of engine power to be transmitted through the mechanical path.

When operating the HMT as a stand-alone Continuously Variable Transmission (CVT), the pump/motor at the engine is mainly operated as a pump and the hydraulic unit at the wheels is used as a hydraulic motor. In order to hybridize the vehicle, the transmission has two hydraulic ports built-in, one in the high pressure line and one in the low pressure one. These ports can be used to connect the hydraulic pump/motors to a high and low pressure accumulator. A directional valve is implemented such that

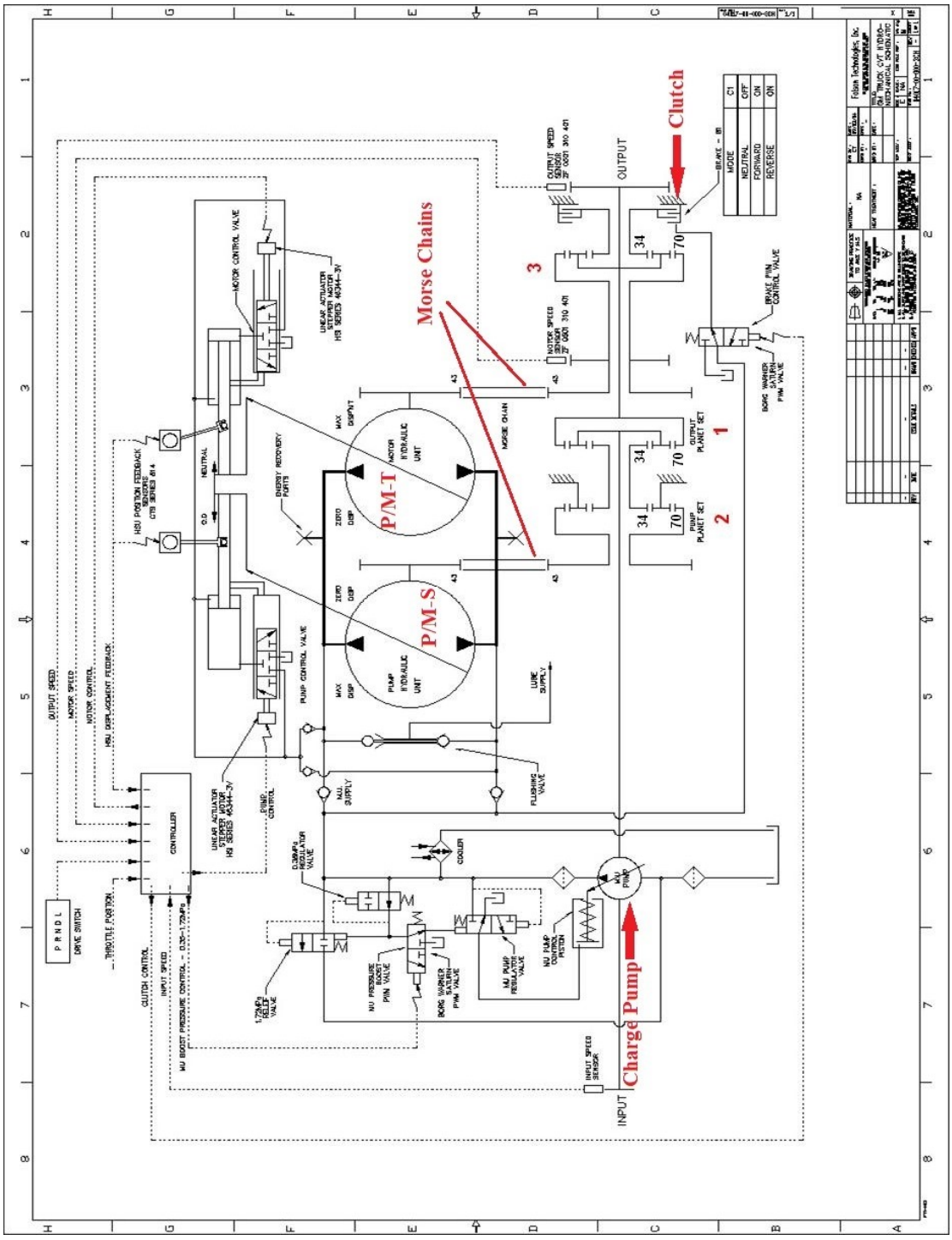

Figure 8.2: Schematic of FTI Hydro-Mechanical Transmission (provided by FTI).

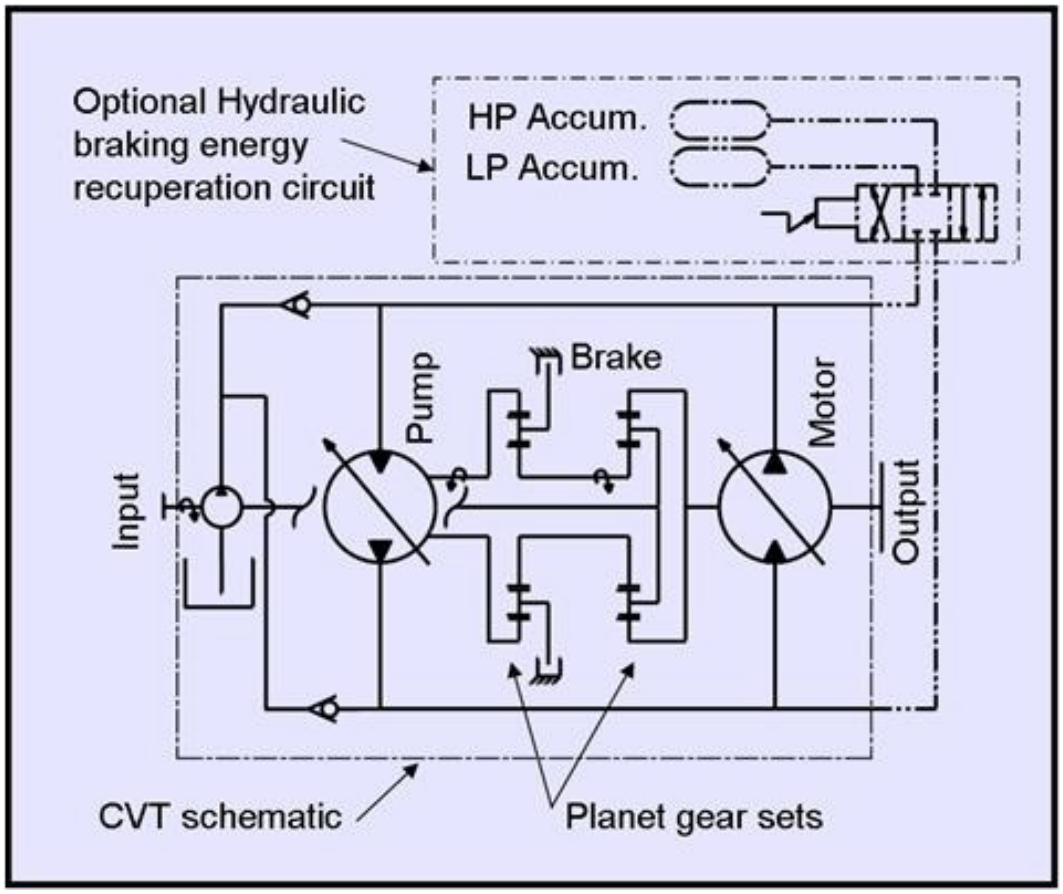

Figure 8.3: Simplified schematic of Folsom hybrid HMT

the high and low pressure sides of the pump/motors can be exchanged (see Fig. 8.3). When operating the transmission in hybrid mode both pump/motors can operate as pumps or as motors at any time, moving the engine operating point to higher efficiency operating regions. As an output coupled power-split transmission, the hydraulic unit at the engine (P/M-S) achieves a change in engine speed; it is therefore often called the 'speeder' and will here be denoted 'S'. The pump/motor closer to the output shaft (P/M-T) is often referred to as the 'torquer', as it shifts the engine operation in torque, denoted as 'T'.

This transmission is equipped with rotary sensors, speed sensors, and pressure transducers for control purposes. Non-contact rotary position sensors are installed on the pump/motors bent-axis angle to measure the actual displacements. The hall-effect speed sensors are installed on the P/M-T and transmission output shaft[1] . Engine speed measurement is obtained from the Engine Control Unit (ECU). Pressure transducers measure the high and low pressure accumulators.

8.2 Engine Characterization

The prime mover of this vehicle is a 4.6 liters V8 gasoline engine, with peak power of 218kW (292hp) at 597 rad/s (5700 rpm) and peak torque of 430Nm at 419 rad/s (4000 rpm). The peak efficiency is 35.7%. The engine is controlled by an Engine Control Unit (ECU) where the engine torque is controlled by the acceleration pedal. The powertrain controls implementation details will be discussed in Ch. 9.

Similar to the Generation I vehicle in Ch. 5, the engine is represented as a quasi-static model, where the engine inertial dynamics are modelled as a first order system and the fuel efficiency is modelled with a static map.

$$J_{eng}\dot{\omega}_{eng} = T_{eng} - T_{eng,load} \tag{8.1}$$

$$\dot{T}_{eng}(t) = -\lambda_{eng}T_{eng}(t) + \lambda_{eng}T^{*}_{eng}(t) \tag{8.2}$$

where J_{eng} is the engine inertia, T_{eng} is the engine output torque at the crankshaft, $T_{eng,load}$ is the load acting on the engine crankshaft, T^{*}_{eng} is the desired engine torque,

[1] The speed sensor is installed on P/M-T to enable ensuring that the clutch is fully engaged.

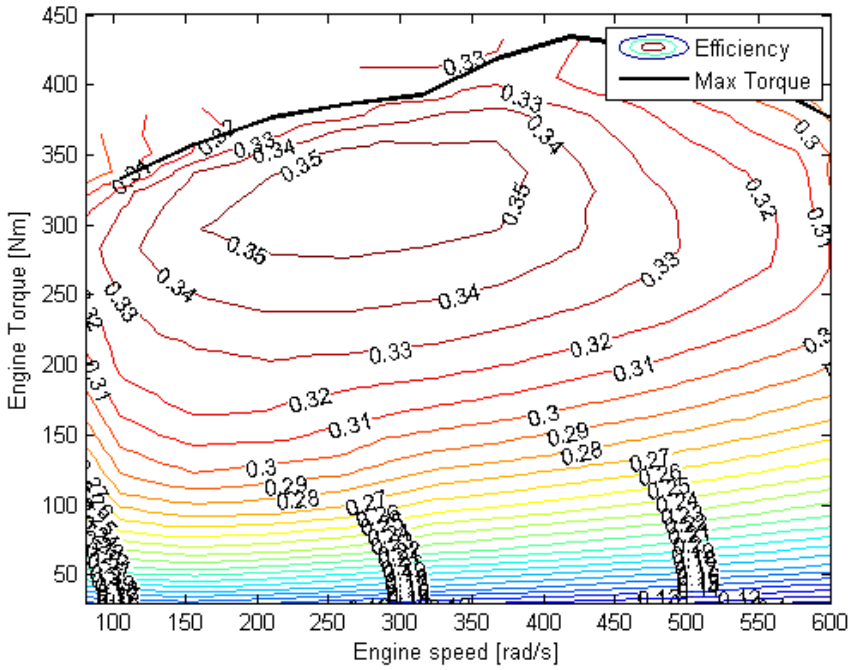

Figure 8.4: A typical 4.6L naturally aspirated gasoline engine efficiency map for Generation II vehicle.

and λ_{eng} is the first-order engine time constant to translate the command to actual output torque. Unlike the Generation I engine model, the desired engine torque (T^*_{eng}) is the direct control input to the engine (instead of a fuel solenoid) as the ECU is included in the engine grey box model. The fuel efficiency map of the engine can be represented as $\eta_{eng}(\omega_{eng}, T_{eng})$, as seen in Fig. 8.4.

8.3 Hydraulic Pump/Motors

The Folsom HMT consists of two 222cc bent-axis axial piston variable displacement pump/motors. The efficiency model of the pump/motor is provided by FTI, as shown in Fig. 8.5. Both P/M-S and P/M-T are assumed to exhibit identical performance and efficiency. The efficiency remains above 90% over a broad range, with peak efficiency of 95%.

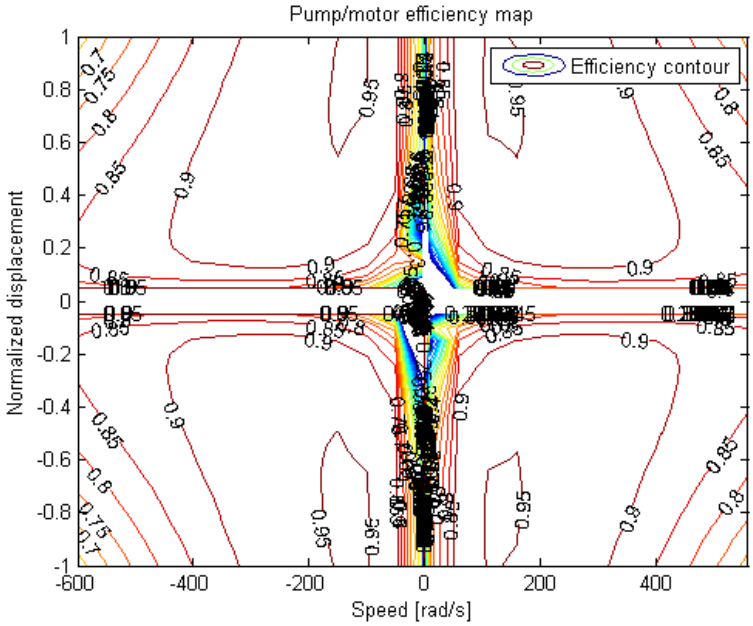

Figure 8.5: Folsom HMT pump/motor efficiency model at 13.8MPa provided by FTI.

The pump/motor displacement is related to the flows and torques by:

$$Q_*(t) = \frac{\omega_* D_{max}}{2\pi} x_*(t) + Loss_{vol,pm*}(x_*, \omega_*, P_{sys}) \tag{8.3}$$

$$T_*(t) = \frac{P_{sys}(t) D_{max}}{2\pi} x_*(t) - sgn(\omega_*) \cdot Loss_{mech,pm*}(x_*, \omega_*, P_{sys}) \tag{8.4}$$

where subscript $* = S$ or T, $D_{max} = 222cc/rev$ is the maximum volumetric displacement of the pump/motor, $Loss_{vol,pm*}$ and $Loss_{mech,pm*}$ are the volumetric and torque loss maps of the pump/motors, and P_{sys} is the system pressure. The volumetric and torque loss model of the pump/motor are provided by FTI, as shown in Fig. 8.6. These performance maps are obtained from the transmission model developed by FTI.

P/M-S of the Folsom HMT has limited and P/M-T has none over-center capability. In order to recover braking energy, only one directional valve is added to enable the high and low pressure lines to interchange, as seen in Fig. 8.3. For valve position 1 ($u_{DCV} = 1$), P/M-S on the transmission has a range in displacement from -0.1 to 1 ($x_S \in [-0.1, 1]$), while P/M-T can only operate at positive displacement ($x_T \in [0, 1]$).

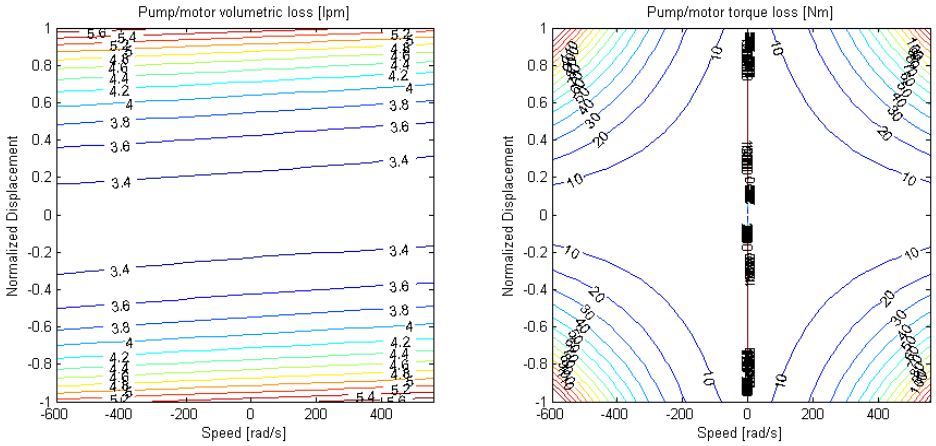

Figure 8.6: Folsom HMT pump/motor torque and volumetric loss model at 13.8MPa provided by FTI.

However, with only one directional control valve, the pump/motor's operation is restricted. Switching the valve to position 2 ($u_{DCV} = -1$) changes x_S to the range of $x_S \in [-1, 0.1]$, and $x_T \in [-1, 0]$.

Note that the restriction on pump/motor's operation potentially poses limitations on engine management. For instance, with $u_{DCV} = -1$, only 10% of P/M-S torque ($x_S > 0$) is available to load the engine as $x_S \in [-1, 0.1]$. However, it is shown in the simulation in Sec. 8.6 that the engine management restriction did not occur.

8.4 Drivetrain Dynamic Modeling

As discussed in Ch. 2, the power-split transmission can be modeled as a four-port system, similar to the Generation I transmission. By assuming a lossless geartrain, using the notation seen in Fig. 8.7, the kinematic relationship of the Folsom transmission between

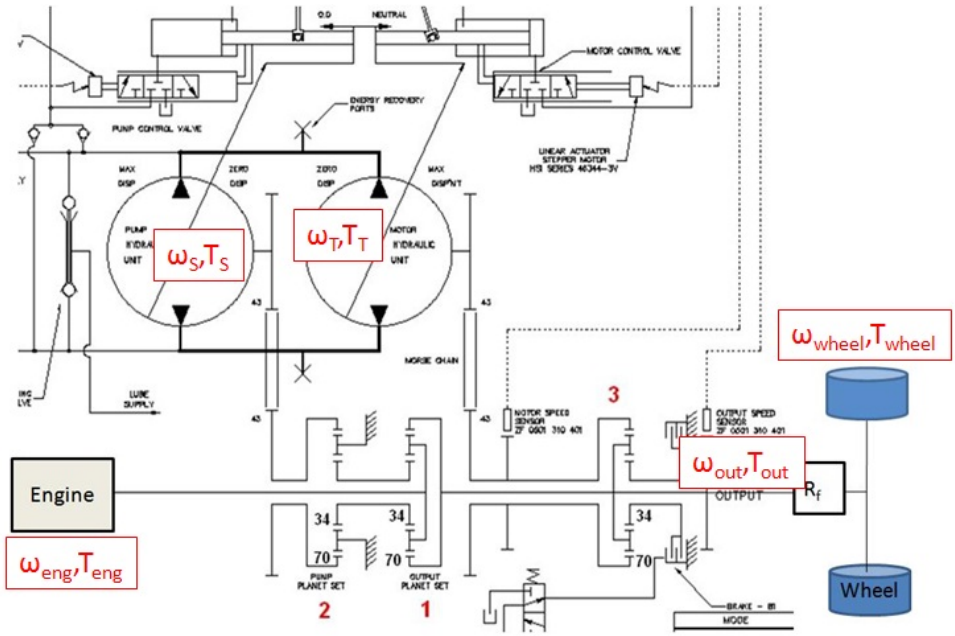

Figure 8.7: Notation used in the Folsom transmission.

the engine, transmission output, and both pump/motors can be derived as:

$$\begin{pmatrix} \omega_S \\ \omega_T \end{pmatrix} = \underbrace{\begin{pmatrix} -(1+\rho) & 1 \\ 0 & 1 \end{pmatrix}}_{G_w} \begin{pmatrix} \omega_{eng} \\ \omega_{out} \end{pmatrix} \tag{8.5}$$

$$\begin{pmatrix} T_S \\ T_T \end{pmatrix} = \underbrace{\begin{pmatrix} \frac{1}{1+\rho} & 0 \\ -\frac{1}{1+\rho} & -1 \end{pmatrix}}_{-G_w^{-T}} \begin{pmatrix} T_{eng} \\ T_{out} \end{pmatrix} \tag{8.6}$$

where $T_{out} = \frac{T_{wheel}}{R_f}$ and $\omega_{out} = R_f \omega_{wheel}$ are the transmission output torque and speed before the final drive ratio of $R_f = 3.31$. Each of the planetary sets in the hydraulic transmission has a ring gear of 70 teeth and a sun gear of 34 teeth. The parameter $\rho = r_{sun}/r_{ring} = 34/70$ is the sun-ring radii ratio of the planetary gearset. $T_{out} < 0$ is driving forward, while $T_{out} > 0$ is regenerative braking.

Similar to the Generation I drivetrain modeling approach, the drivetrain of the Generation II hydro-mechanical transmission can be described using the planetary gearset

kinematic relationship and torque balance at the power-split device:

$$\begin{aligned} J_S\dot{\omega}_S &= F \cdot S - T_S && (8.7)\\ J_{eng}\dot{\omega}_{eng} &= T_{eng} - F \cdot R - F \cdot S && (8.8)\\ (J_{veh} + J_T)\dot{\omega}_{out} &= T_T + F \cdot R - T_{load} && (8.9) \end{aligned}$$

where J_{eng} is the engine rotational inertia, J_{veh} is the equivalent vehicle rotational inertia and J_S, J_T are the pump/motors' rotational inertia. T_{load} is the vehicle drag load translated to the transmission output. F represents the internal force acting on the planetary gear mesh, and S, R represent the effective radii of the sun and ring of the planetary gearsets.

Additionally, combining the kinematic relationship Eqs. (8.5),(8.6) with Eqs. (8.8)-(8.9):

$$\begin{aligned} \omega_S &= (\frac{1}{\rho} + 1)\omega_{eng} - \frac{1}{\rho}\omega_{out} \\ F \cdot R &= (F \cdot S)\frac{1}{\rho} \\ &= (\dot{\omega}_S J_S + T_S)\frac{1}{\rho} \\ &= \dot{\omega}_{eng} J_S \frac{1}{\rho}(\frac{1}{\rho} + 1) - \dot{\omega}_{out} J_S (\frac{1}{\rho})^2 + T_S \frac{1}{\rho} \qquad (8.10) \end{aligned}$$

With the above expressions, the dynamic model can be reduced to a two degree-of-freedom system:

$$\begin{pmatrix} J_{eng} + (\rho+1)^2 J_S & -(\rho+1)J_S \\ -(\rho+1)J_S & J_{veh} + (\rho+1)^2 J_T + J_S \end{pmatrix} \begin{pmatrix} \dot{\omega}_{eng} \\ \dot{\omega}_{out} \end{pmatrix} = \begin{pmatrix} T_{eng} - (\rho+1)T_S \\ T_T + T_S - T_{load} \end{pmatrix} \qquad (8.11)$$

The values of inertia and parameters are summarized in Tab. 8.1[2] . As expected, the structure of the dynamic model in Eq. (8.11) is similar to Generation I transmission

[2] The inertias of the rotating parts in the transmission were estimated using the mass property calculation tools of Pro/Engineer software solid modeler.

model in Eq. (5.34), with symmetrical coupling terms. In contrast with the input coupled configuration, the transmission output torque is the sum of T_T and T_S.

Parameters	Values	Parameters	Values
J_S	$0.0696 kgm^2$	J_{veh}	$355 kgm^2$
J_T	$0.0671 kgm^2$	ρ	34/70
J_{eng}	$0.3536 kgm^2$	D_{max}	$222 cc/rev$

Table 8.1: Inertia values for the powertrain model (the engine inertia is provided by Ford Motor Co.).

The vehicle drag characteristics can be expressed as:

$$f(\omega_{cyc}) = MgC_r R_{tire}^2 \omega_{cyc} + \frac{1}{2} C_D A_f \rho_{air} R_{tire}^3 \omega_{cyc}^2 \tag{8.12}$$

where $M = 2612kg$ is the vehicle weight, $g = 9.81 m/s^2$ is the gravitational constant, $C_r = 0.015$ is the tire drag coefficient, $R_{tire} = 0.369m$ is the tire's effective radius, $C_D = 0.4030$ is the drag coefficient, $A_f = 3.36m^2$ is the frontal area, and $\rho_{air} = 1.1774 kg/m^3$ is the air density.

8.5 Basic FTI HMT Stand-alone Operation

As mentioned earlier, the FTI HMT is originally designed as a non-hybrid continuously variable transmission (CVT). It is important to understand the operation of the transmission as a CVT before hybridizing the powertrain. Non-hybrid transmission implies zero net flow to the accumulators. To illustrate the transmission operation, the net flow can be expressed as:

$$\begin{aligned} Q_S + Q_T &= 0 \\ \omega_S D_{max} x_S &+ Loss_{vol,pmS} + \omega_T D_{max} x_T + Loss_{vol,pmT} = 0 \qquad (8.13) \\ \frac{\omega_S}{\omega_T} &= -\frac{x_T}{x_S} - \frac{Loss_{vol,pmS} + Loss_{vol,pmT}}{\omega_T D_{max} x_S} \qquad (8.14) \end{aligned}$$

where $\omega_S < 0$ in normal driving situations, and $\omega_T > 0$ for driving forward. Define the transmission ratio as $\gamma = \frac{\omega_{eng}}{\omega_{out}}$. By combining Eq. (8.14) with Eq. (8.6),

$$\begin{aligned} \omega_S &= -(1+\rho)\omega_{eng} + \omega_{out} \\ \frac{\omega_S}{\omega_T} &= -(1+\rho)\frac{\omega_{eng}}{\omega_{out}} + 1 \qquad (8.15) \\ \frac{x_T}{x_S} &= (1+\rho)\gamma - 1 - \frac{Loss_{vol,pmS} + Loss_{vol,pmT}}{\omega_T D_{max} x_S} \qquad (8.16) \end{aligned}$$

Equation 8.16 indicates that the transmission ratio γ is achieved by setting the ratio of the pump/motors' displacement, instead of individual displacements.

In a conventional automatic transmission, the gear shift lever includes five basic positions; i.e. Park (P), Reverse (R), Neutral (N), and Drive (D), 'PRND' in short. When operating the hydraulic transmission as a stand-alone CVT, it is vital for the transmission to achieve similar functionality. This basic function is tested in a preliminary free-wheeling test, and will be discussed in Sec. 9.2.

Park, 'P' – In an automatic transmission, 'Park' mode is achieved by using a stopping pin to stop the transmission output shaft from spinning. In this Folsom HMT design, since the stopping pin is not available, a mechanical handbrake is required, which is applied manually.

Reverse, 'R' – In conventional vehicles the transmission gears are operated such that a reverse mode is available. In this mode the wheel speed is opposite of the engine speed, thus $\gamma < 0$ is desired. According to Eq. (8.14), this can be achieved by operating P/M-S at $x_S = -0.1$. This reverses the flow of the hydraulic fluid in the lines. The P/M-T is at $x_T = 1$ and spinning in the opposite direction as a result of the reversed flow.

Neutral, 'N' – In neutral operating mode, the speed of the engine is independent of the speed of the wheel, while no torque is transferred through the transmission. Since there is no clutch separating the engine from the input shaft, $\gamma = \infty$ is desired. Neutral is achieved by setting P/M-S to zero displacement ($x_S = 0$), according to Eq. (8.14). Thus, no engine torque is transmitted through the planetary gearset. The clutch on P/M-T is disengaged in neutral mode such that no P/M-T torque is added to the transmission output.

Drive, 'D' – During normal driving mode, the transmission is operated such that

CVT Operation	Clutch State
Neutral	Off
Forward Ratios	On
Overdrive	Off
Reverse Ratios	On

Table 8.2: Clutch Engagement Logic

a specific transmission ratio ($\gamma = \frac{\omega_{eng}}{\omega out}$) is achieved. Based on dynamometer efficiency tests, a specific combination of displacements is used to operate the transmission at its best efficiency [88].

Overdrive Mode – The transmission of power through the mechanical shaft is efficient. As part of the 'Drive' operating mode, it is desired to transmit the power from the engine through the mechanical path once the vehicle is at cruising speed. The engine efficiency is very low at low speeds but once higher speeds are reached the engine can be operated in a more efficient region. This operation is called 'overdrive' (also known as 'mechanical point') and implies that the hydraulic path of the transmission is not utilized at these speeds. Overdrive is achieved when $\omega_S = 0$, thus yielding a transmission ratio of $\gamma = \frac{\omega_{eng}}{\omega_{out}} = \frac{1}{1+\rho}$. P/M-S is set to maximum displacement, and P/M-T is set to zero displacement. As a result, the input power is not split and 100% of the engine power is transmitted through the mechanical shaft. There is no flow in the hydraulic lines. The clutch on P/M-T is disengaged in this mode to eliminate the free-spinning viscous drag friction from P/M-T.

Table 8.2 shows the clutching logic for the transmission. The clutch on P/M-T will need to be modulated during transition from neutral to forward/reverse to ensure smooth vehicle launch.

8.6 Potential Fuel Efficiency Improvements

To demonstrate the efficiency gain by replacing the 6-speed automatic transmission with the Folsom HMT, static simulation is conducted, i.e. without the dynamics of the components, to investigate the powertrain operation. The simulations assumed an ideal low level controller, i.e. desired operating conditions are achieved instantaneously.

Moreover, a mid-level controller similar to Ch. 6 is used for CVT strategy and DP strategy.

The upper bound fuel economies assumes lossless transmission and the engine is operating at maximum efficiency of 35.7%, setting the highest efficiency achievable by the selected engine. Upper bound CVT achieves fuel consumptions of 7.81L/100km on the Urban drive cycle and 7.59L/100km on the Highway drive cycle. For upper bound CVT, no braking energy is recovered throughout the drive cycles. Upper bound hybrid achieves fuel consumptions of 4.61L/100km on the Urban drive cycle and 6.03L/100km on the Highway drive cycle. For Upper bound hybrid, all braking energy is recovered, and thus only losses due to road and aerodynamic drags will affect the fuel economy.

The 6-speed automatic transmission uses a constant efficiency model of 85%[3] , with gear ratios of (4.171, 2.34, 1.521, 1.143, 0.867, 0.673)[4] . The 6-speed automatic transmission achieves 13.07 L/100km (18mpg) for the Urban and 9.05L/100km (26mpg) for the Highway drive cycle[5] . The gear selection for each time instant is chosen to minimize the engine loss. Figure 8.8 depicts the engine operation for the Urban and Highway drive cycles. The engine operating points are scattered due to the discrete gear ratio.

The CVT strategy is simulated with accumulators shut off, where the pump/motor displacement is determined to ensure net flow to the accumulators is zero. This is achieved by setting $Q_{acc} = 0$ as input to the full mid-level controller (Eq. (6.4)), while optimizing the system pressure that yields minimum loss for every time instant. The non-hybrid Folsom HMT achieves 11.76 L/100km (20mpg) for the Urban and 9.05L/100km (26mpg) for the Highway drive cycle. Figure 8.9 shows the engine operation using the non-hybrid Folsom HMT for Urban and Highway drive cycle under CVT mode. Compared to the 6-speed transmission, the engine operating points clustered along the best BSFC region, increasing the average engine operating efficiency. Since this CVT strategy optimizes the system pressure for minimum losses, CVT strategy with constant pressure is expected to be less efficient.

[3] This average efficiency considers the gear mesh efficiency and torque converter efficiency [89].

[4] Gear ratios provided by Ford Motor Co.

[5] The simulated fuel economies for 6-speed automatic transmission matches the fuel economies provided by Ford Motor, i.e. 17.9mpg for the Urban drive cycle and 26.0mpg for the Highway drive cycle.

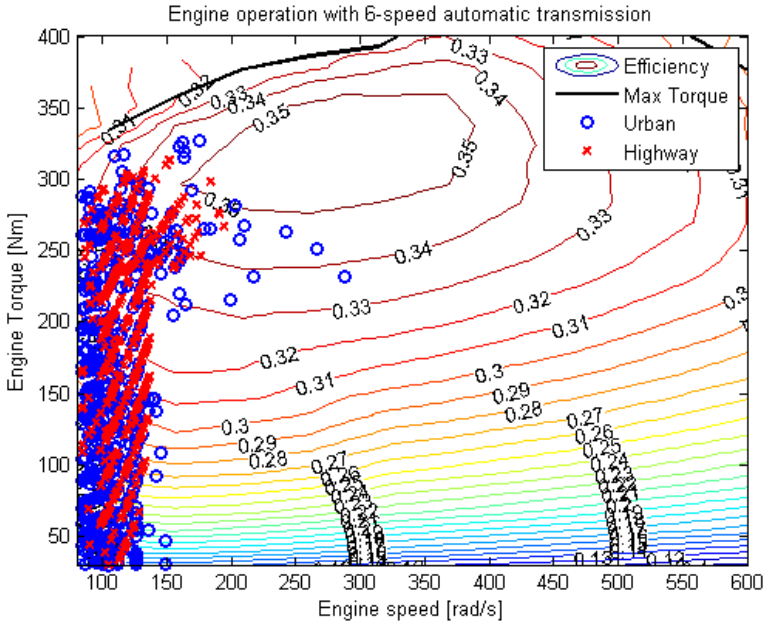

Figure 8.8: Engine operation with 6-speed automatic transmission throughout the Urban and Highway drive cycles.

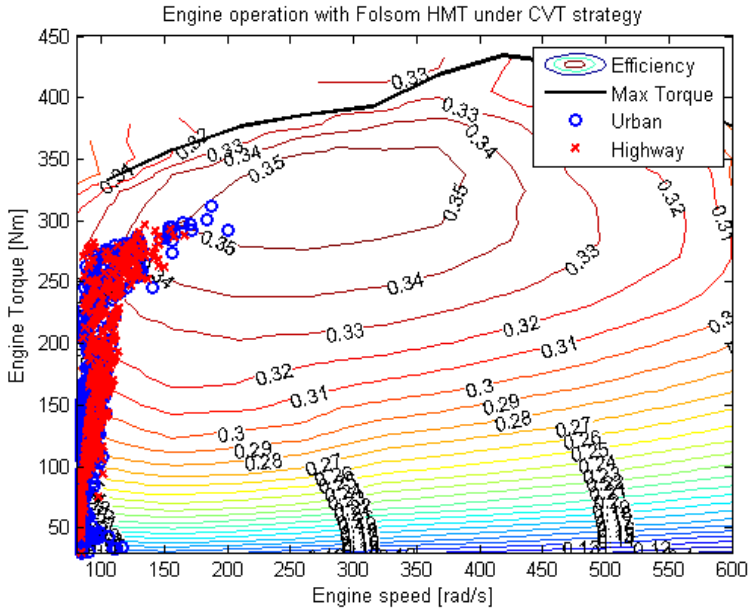

Figure 8.9: Engine operation with Folsom HMT under CVT strategy throughout the Urban and Highway drive cycles.

Dynamic programming (DP) is utilized to evaluate the optimal energy management for the hybridized Folsom HMT. The hybrid powertrain is paired with a set of accumulators of $38L$ $(10gal)$. For simplicity, the low pressure accumulator is assumed to have constant pressure of 1.38MPa (200psi), while the high pressure accumulator has a pre-charge pressure of 11.7MPa (1700psi) and maximum pressure of 34.5MPa (5000psi). Similar to Ch. 6, the DP strategy decides the optimal Q_{acc} while the full mid-level controller (Eq. (6.4)) determines the optimal engine operation. The Foslom HMT under DP strategy achieves 8.40 L/100km (29mpg) for the Urban and 6.53L/100km (36mpg) for the Highway drive cycle.

Figure 8.10 shows the engine operation using the Folsom HMT under hybrid mode strategy. Overall, the engine operates at lower power than in the 6-speed transmission and CVT strategy because the output torque is supplemented by the accumulator power, reducing the loss from the engine. In contrast with the result for Generation I, the engine is operated near the best BSFC curve instead of near the high efficiency region. This is mainly due to the high engine power at maximum efficiency will cause the accumulator to be charged to high pressure.

Figure 8.11 shows the system pressure throughout the Urban and Highway drive cycles under DP strategy. As seen, the DP strategy generally maintains the system pressure at low pressure whenever possible. The increase in system pressure is mainly due to the energy recovered during braking. Figure 8.12 depicts an example of the pump/motor displacements during regenerative braking in the Urban drive cycle. The transmission is operated such that during regenerative braking, P/M-T is pumping with $x_T < 0$ while P/M-S is near zero displacement $x_S \approx 0$[6] . Throughout the drive cycles, P/M-T operates in pumping mode only to achieve regenerative braking. This behavior is consistent throughout the Urban and Highway drive cycles. This implies that the restriction on pump/motor's operation that limits the engine management as mentioned in Sec. 8.3 did not occur, therefore the pump/motor's operation restriction will not affect the fuel economy.

The fuel efficiencies of different cases are summarized in Tab. 8.3. From Table 8.3[7] , it can be seen that using the hydraulic transmission to implement CVT mode in

[6] x_S is not exactly zero due to the interpolation error to achieve zero P/M-S torque $T_S = 0$.

[7] Model includes engine losses, hydraulic leakage and torque losses and charge pump losses. No auxiliary losses and no gear mesh efficiencies are included.

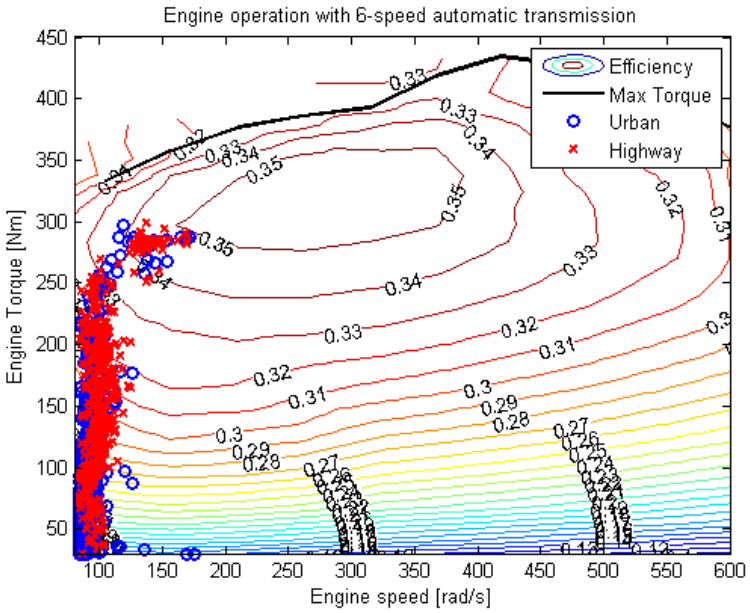

Figure 8.10: Engine operation with Folsom HMT under Dynamic Programming hybrid strategy throughout the Urban and Highway drive cycles.

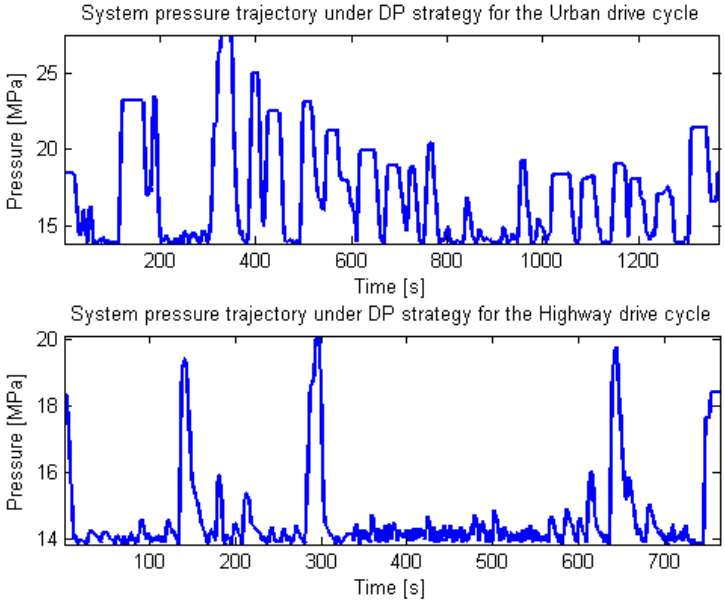

Figure 8.11: System pressure with Folsom HMT under DP strategy throughout the Urban and Highway drive cycles.

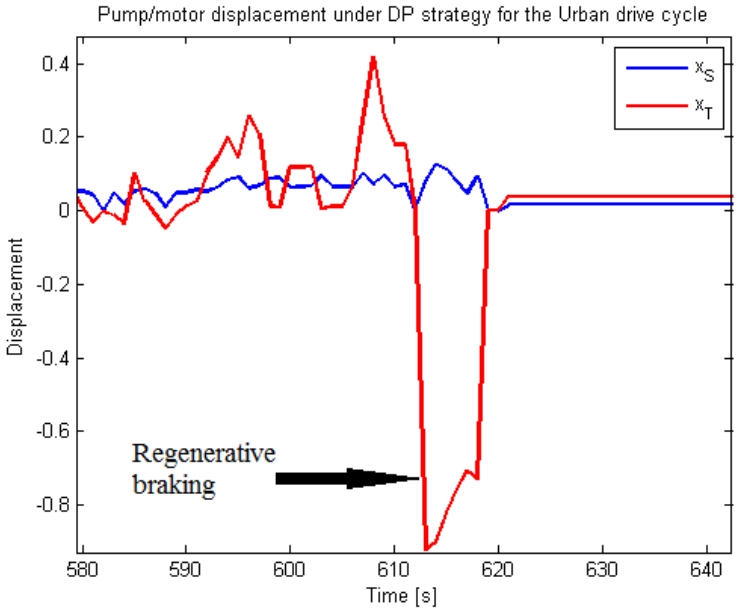

Figure 8.12: Pump/motor displacements under DP strategy in the Urban drive cycle during regenerative braking.

the F-150 truck has potential to increase fuel economy up by 11% from conventional 6-speed automatic transmission to stand-alone HMT, and drastic improvement of 61% from conventional 6-speed transmission to hybrid HMT in the Urban Drive cycle. The upper bound of fuel economies are calculated assuming optimal management with only engine losses in the system, where the transmission is considered lossless.

On the Urban drive cycle under CVT mode, the transmission is operating at an average 81% efficiency, while the mean engine efficiency is approximately 26%. In hybrid operating mode, the engine average efficiency is increased to 28.4% but the average transmission efficiency is reduced to 68.7%.

On the highway drive cycle, the improvement by converting the conventional transmission to non-hybrid Folsom HMT is approximately 8%. By operating the powertrain in hybrid mode, the fuel economy improves 38% over a conventional transmission. The results show that the average engine efficiency is increased compared to the 6-speed transmission, hence overall powertrain efficiency is increased. In another word, the hydraulic transmission offers better fuel efficiency by improving the engine management.

Transmission	F.E. $L/100km$ (mpg)	Mean η_{eng}	Mean η_{trans}	Improvement
6-speed auto	Urban: 13.07 (18)	22.8%	85%	-
	Highway: 9.05(26)	24.8%	85%	-
	Combined: 10.45 (22)	28.3%	85%	-
CVT	Urban: 11.76 (20)	25.9%	81.3%	11%
	Highway: 9.05 (26)	30.7%	68.6%	0%
	Combined: 9.71 (24)	28.3%	71.8%	9%
Upper bound CVT	$\overline{Urban}$: 7.84 (30)	35.7%	100%	66%
	$\overline{Highway}$: 7.59 (31)	35.7%	100%	19%
	$\overline{Combined}$: 7.84 (30)	35.7%	100%	25%
DP Hybrid	Urban: 8.40 (29)	28.4%	68.7%	61%
	Highway: 6.53 (36)	31.9%	91.5%	38%
	Combined: 7.28 (32)	30.5%	84.7%	45%
Upper bound Hybrid	$\overline{Urban}$: 4.61 (51)	35.7%	100%	183%
	$\overline{Highway}$: 6.03 (39)	35.7%	100%	50%
	$\overline{Combined}$: 5.61 (42)	35.7%	100%	91%

Table 8.3: Predicted powertrain efficiencies.

Moreover, the added accumulator allows the powertrain to recover the braking energy and to enable improved engine management.

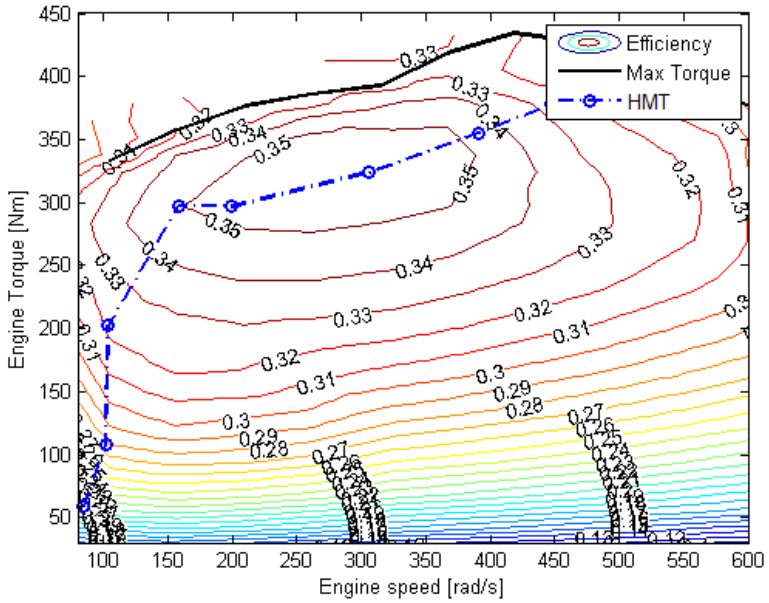

Figure 8.13: BSFC operating points for Generation II in `HMT` mode.

8.7 Transmission Optimization

As mentioned earlier, the Folsom HMT is designed to operate as a CVT without accumulators as energy storage. It is important to understand how fuel efficiency can be improved by optimizing the hybrid HMT transmission design. By applying the transmission design optimization methodology presented in Ch. 2, the potential fuel efficiency improvement can be predicted. The reference powertrain model is described in previous sections. Similarly, the Lagrange Multiplier method is applied to synthesize the energy management for the hybrid transmission, and operating modes are defined to simplify the optimization process. A constant system pressure of 13.8MPa (2000psi) is assumed in this case study. The Matlab `fminsearch` function is used to optimize the transmission design parameters $\nu = (G_\omega, D_{maxS}, D_{maxT})$. The combined drive cycle is used in this optimization study.

8.7.1 Operating Modes

Since the Folsom transmission does not include a clutch to separate the engine from the transmission, the operating modes for the Folsom HMT differ from the transmission defined in Sec. 2.4.1. `HMT` mode is not restricted to only one operating point but several points along the BSFC curve, shown in Fig. 8.13. `P/M-S only` mode requires locking up the engine, which is not feasible. Thus, `P/M-S only` mode is not considered. In `P/M-T only` mode, P/M-S is locked up and the engine is operated at its idling condition (84.75rad/s). `Parallel` mode operates the engine at maximum torque with P/M-S locked up. The operating modes used in this transmission optimization process are summarized in Tab. 8.4.

Table 8.4: Operating modes for Folsom HMT

Modes	Comments
HMT	Power-split, engine operates along BSFC
P/M-S only	Freespin P/M-T, engine lockup (not possible)
P/M-T only	Lock-up P/M-S, engine idles
Parallel	Lock-up P/M-S, engine operates at max torque

8.7.2 Optimization Results

The HMT optimization results are shown in Tab. 8.5. The results shown uses Lagrange Multiplier method without DP verification. The fuel economy results are significantly different for the Folsom HMT than shown in Tab. 8.3 because of the use of 'modes' in obtaining the results in Tab. 8.5. The optimized HMT design achieves 58.5% higher fuel economy than the original hybridized Folsom HMT design. The gain can be attributed to significantly smaller pump/motor sizes. For the optimized transmission design, P/M-S is 40% smaller and P/M-T is 66.7% smaller than those used in the Folsom HMT. This design implies that the original Folsom HMT is over-sized for the specified drive cycles. A Dynamic Programming verification step should be run on the optimized design to in order to compare the results with the results in Tab. 8.3.

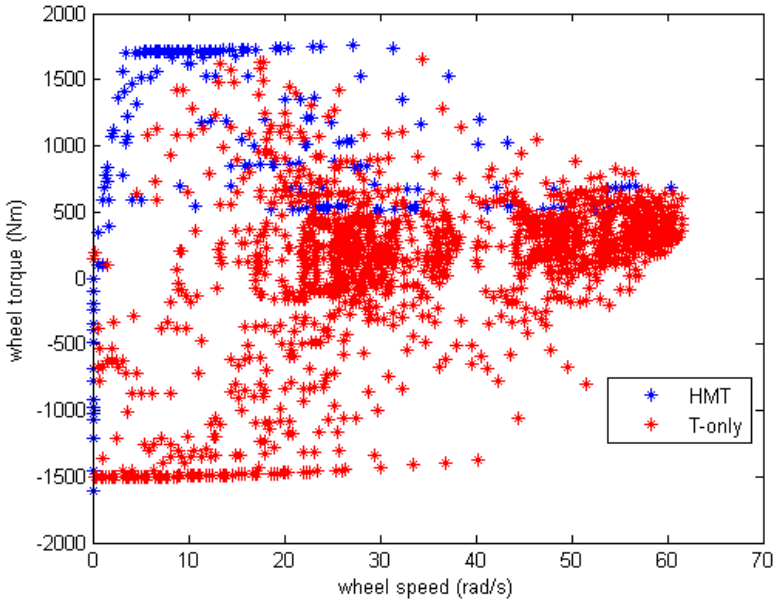

Figure 8.14: Operating modes distribution for the Folsom HMT.

Folsom HMT Design: The operating modes of the original Folsom HMT will be compared with the operating modes of the optimized HMT in the following paragraphs. Figure 8.14 shows the distribution of the operating modes for the Folsom HMT. `Parallel` mode is not utilized at all in the drive cycle. This is due to the high engine torque in `parallel` mode, where the pump/motors are not capable of achieving at the low system pressure, as seen in Eq. (8.6). `HMT` mode occurs at high torque while `P/M-T only` mode occurs frequently, especially during regenerative braking events. The pump/motor operating points are shown in Fig. 8.15. P/M-T operates at lower speeds and wide range of displacements, and P/M-S operates at a narrower range of speeds and displacements.

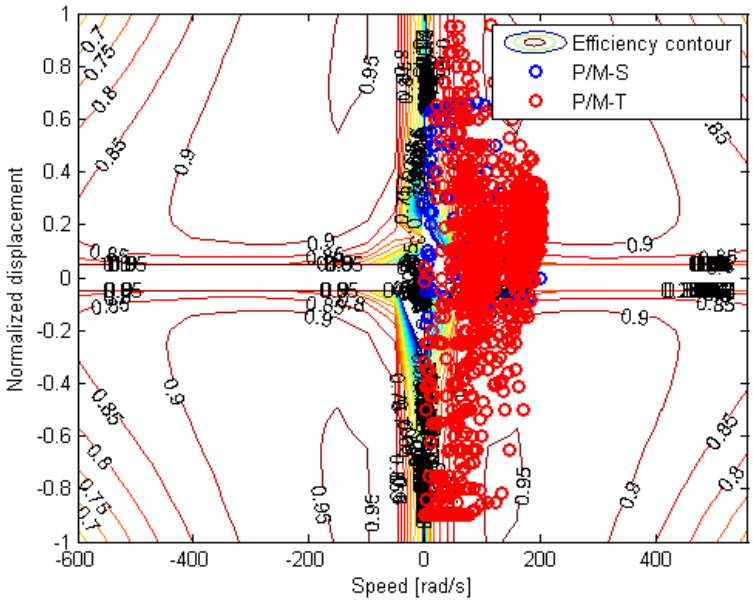

Figure 8.15: Pump/motors operating points for the Folsom HMT.

Table 8.5: Comparison of fuel economy between the Folsom HMT and transmission optimized using the Lagrange Multiplier method for various drive cycles.

Design	Folsom HMT
G matrix	$\begin{pmatrix} -1.49 & 1.00 \\ 0 & 1.00 \end{pmatrix}$
P/M sizes	P/M-S=222cc P/M-S=222cc
Urban/Highway/Combined	6.47 / 7.08 / 6.77 L/100km
	36.4 / 33.2 / 34.7 mpg
Design	Optimized HMT
G matrix	$\begin{pmatrix} -0.39 & 1.84 \\ 0 & 2.58 \end{pmatrix}$
P/M sizes	P/M-S=133cc P/M-S=74cc
Urban/Highway/Combined	5.64 / 3.67 / 4.27 L/100km
	41.7 / 64.1 / 55.0 mpg

Optimized HMT design: Figure 8.16 shows the distribution of the operating modes for the optimized HMT design. Similar to the Folsom HMT, `P/M-T` mode occurs widely throughout the drive cycle. `HMT` mode occurs at high wheel speed but low torque conditions, and also at high braking torque. Figure 8.17 shows that P/M-S operates in two clusters (high displacement low speed, and low displacement high speed), and P/M-T operates over a broad range of positive speed. The $G_{1,1}$ ratio is reduced such that P/M-S speed is reduced for a specific engine speed, and the $G_{1,2}$ is increased such that the P/M-S speed can be increased for a specific vehicle speed. The optimized $G_{1,1}$ and $G_{1,2}$ leads to higher fuel efficiency for Highway conditions. $G_{2,2}$ is increased in the optimized design such that P/M-T can be operated at higher speed lower torque, leading to a smaller P/M-T size.

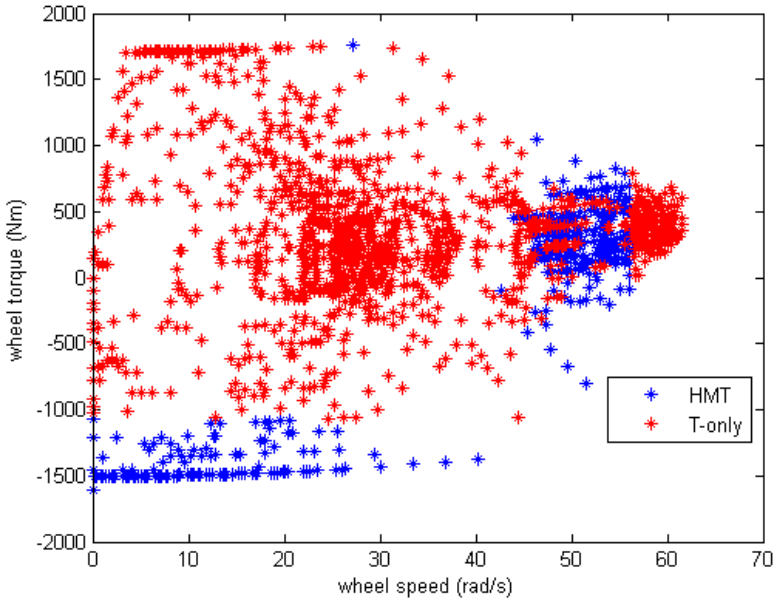

Figure 8.16: Operating modes distribution for the optimized HMT design.

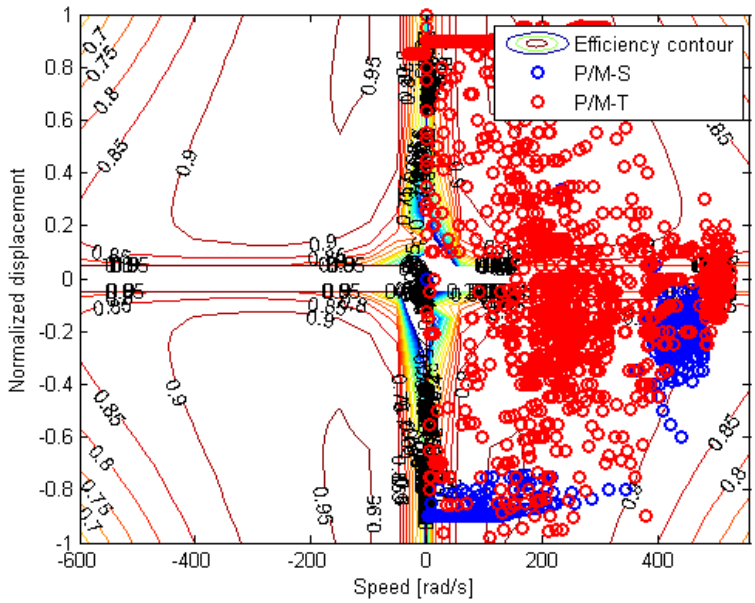

Figure 8.17: Pump/motors operating points for the optimized HMT design.

8.8 Concluding Remarks

This chapter introduced the Folsom Technology International (FTI) developed transmission and presented a model to describe the dynamics and efficiency of the powertrain. Unlike the Generation I vehicle, the Folson HMT is an output coupled architecture, where P/M-S controls the engine torque directly instead of the transmission output torque. This will affect the control strategy of the powertrain which will be presented in Ch. 9.

In this chapter, the basic operation of the transmission is explained. During CVT mode, basic functionalities of a conventional transmission can be achieved by controlling the pump/motors accordingly. On the other hand, the engine is operated more efficiently during hybrid mode operation. However, the transmission configuration with only single directional valve could cause restricted engine operation on the transmission. This issue is proved to be negligible in simulation.

Simulation conducted to predict the fuel efficiency improvement achievable by the hybrid HMT has shown promising results of up to 55% fuel economy improvement compared to the original 6-speed transmission. This improvement can be attributed to the regenerative braking and engine management. However, the fuel economy improvement on the highway cycle is expected to be less than of the urban cycle. This is because most of the power from the engine is already transmitted through the efficient mechanical path.

The transmission design optimization methodology proposed in Ch. 2 is utilized to optimize the Folsom HMT design. This is done to investigate the potential fuel efficiency improvement achievable by the hybrid HMT transmission design. The optimized transmission pump/motors are sized more than 40% smaller than the original Folsom HMT design. This is achieved by optimizing the kinematic relation matrix such that lower pump/motor torques are needed. This case study concluded that the Folsom HMT can be improved significantly, leading to 58.5% fuel economy improvement over the hybrid powertrain using original Folsom HMT.

Chapter 9

Powertrain Control and Preliminary Testing of Generation II Vehicle

With the powertrain model presented in Ch. 8, the overall powertrain control strategy can be synthesized similarly using the approach described in Ch. 6, where the controller is decomposed into a three-level hierarchical control structure. Also, the dynamic decomposition approach can be applied to the Generation II powertrain to understand the dynamics. However, the engine controller and pump/motor actuation are different from the Generation I vehicle.

As a preliminary test for the Folsom transmission, the transmission is tested under near zero load to ensure safety and stability. Thus, the wheels of the vehicle are lifted up from the ground. This test is also to verify the communication between the engine ECU and the DSpace MicroAutobox controller unit.

The rest of the chapter will be organized as follows. Section 9.1 focuses on the low level controller of the powertrain as the high and mid level controllers are identical to the Generation I powertrain. Results from the preliminary free-spinning test of the powertrain are presented in Sec. 9.2. Section 9.3 discusses the future work and experiments for Generation II. Section 9.4 contains some concluding remarks for this chapter.

9.1 Powertrain Controls

By adding the accumulator for energy storage, the engine power can be decoupled from the required wheel power. Hybrid powertrain control offers extra flexibility in engine management to improve overall fuel efficiency of the powertrain. Recall from Ch. 6, the mid-level controller translates statically the high-level's decision Q_{acc} and demand vehicle torque T_{out} into optimal operating points for the engine and hydraulics. For the given accumulator flow Q_{acc} (from high level), desired vehicle torque T_{out} (from driver), the current vehicle speed ω_{out} and system pressure P_{sys}, the mid-level controller determines the optimal engine speed/torque $(\omega^*_{eng}, T^*_{eng})$.

As the Generation II powertrain will adopt the identical control architecture as the Generation I three-level hierarchical control strategy, synthesis of the High-level and Mid-level controller will be omitted in this chapter. Instead, this section will focus on the Low-level controller to achieve $(\omega^*_{eng}, T^*_{eng})$. The powertrain actuation system of Generation II is different from the Generation I powertrain system.

Firstly, as mentioned earlier in Ch. 8, even though the Generation II transmission is a powersplit hybrid architecture, it is configured as output coupled (Generation I uses an input coupled power-split). Hence, the role of each hydraulic unit is reversed, where P/M-S couples to the engine torque and P/M-T augments the transmission output torque. Details will be presented in Sec. 9.1.1.

Secondly in Sec. 9.1.2, the engine controller can be simplified due to the embedded Engine Controller Unit (ECU). The engine torque is electronically linked to the accelerator pedal position and determined by the ECU. However, the engine output torque can be modified through the ECU's CAN communication[1] . Alternatively, the engine speed can be controlled using the built-in speed regulation control in the ECU.

Thirdly, the hydraulic pump/motors' displacement is controlled using stepper motors, as will be discussed in Sec. 9.1.3. Together with the measurement of the pump/motors' displacement angle, a feedback loop is applied to ensure the desired displacement is achieved.

[1] The CAN (Controller Area Network) communication is a standard message-based communication protocol that has high reliability of data transfer, often used in automation technology [36].

9.1.1 Dynamic Decomposition

For control purposes, the dynamic equations can be decomposed into internal and external coordinates for intuitive analysis. The dynamic decomposition technique identical to Ch. 6 will be used. The Generation II vehicle dynamics (Eq. (8.11)) are:

$$\underbrace{\begin{pmatrix} \hat{J}_{eng} & \hat{J}_{coup} \\ \hat{J}_{coup} & \hat{J}_{veh} \end{pmatrix}}_{J} \begin{pmatrix} \dot{\omega}_{eng} \\ \dot{\omega}_{out} \end{pmatrix} = \underbrace{\begin{pmatrix} T_{eng} - (1+\rho)T_S \\ T_S + T_T - T_{load} \end{pmatrix}}_{T}$$

where $\hat{J}_{eng} = J_{eng} + (1+\rho)^2 J_S$, $\hat{J}_{veh} = J_{veh} + (1+\rho)^2 J_T + J_S$, and $\hat{J}_{coup} = -(1+\rho)J_S$ is the coupling term. Then, define transformation matrix S to separate the dynamics between $(\omega_{eng}, \omega_{out})$ and $(\omega_{int}, \omega_{ext})$,

$$S = \begin{pmatrix} 1 & 0 \\ a & 1 \end{pmatrix}$$

$(\omega_{eng}, \omega_{out})$ and $(\omega_{int}, \omega_{ext})$ are related by:

$$\begin{pmatrix} \omega_{eng} \\ \omega_{out} \end{pmatrix} = \begin{pmatrix} 1 & 0 \\ a & 1 \end{pmatrix} \begin{pmatrix} \omega_{int} \\ \omega_{ext} \end{pmatrix}$$

Then, the coordinate transformation with the new variables is defined as:

$$S^T J S = \begin{pmatrix} 1 & a \\ 0 & 1 \end{pmatrix} \begin{pmatrix} \hat{J}_{eng} & \hat{J}_{coup} \\ \hat{J}_{coup} & \hat{J}_{veh} \end{pmatrix} \begin{pmatrix} 1 & 0 \\ a & 1 \end{pmatrix} \tag{9.1}$$

$$= \begin{pmatrix} \overbrace{\hat{J}_{eng} + 2a\hat{J}_{coup} + a^2\hat{J}_{veh}}^{J_{int}} & \hat{J}_{coup} + a\hat{J}_{veh} \\ \hat{J}_{coup} + a\hat{J}_{veh} & \underbrace{\hat{J}_{veh}}_{J_{ext}} \end{pmatrix} \tag{9.2}$$

and by setting $a = -\frac{\hat{J}_{coup}}{\hat{J}_{veh}} \approx 6.897 \times 10^{-4}$, the original dynamic system Eq. (8.11) is decomposed and becomes:

$$S^{\intercal} J S = \begin{pmatrix} J_{int} & 0 \\ 0 & J_{ext} \end{pmatrix} \tag{9.3}$$

$$\begin{pmatrix} J_{int} & 0 \\ 0 & J_{ext} \end{pmatrix} \begin{pmatrix} \dot{\omega}_{int} \\ \dot{\omega}_{ext} \end{pmatrix} = \begin{pmatrix} T_{eng} - (1+\rho)T_S + a(T_S + T_T - T_{load}) \\ \underbrace{T_S + T_T}_{T_{out}} - T_{load} \end{pmatrix} \tag{9.4}$$

where T_{out} is the vehicle torque demand, $\omega_{int} = \omega_{eng}$ and $\omega_{ext} = \omega_{out} - a\omega_{eng}$. Since the value of a is small, the coupling effect to the transmission load is relatively negligible. Using this coordinate transformation, the output speed can be controlled to satisfy the desired value specified by the drive cycle and the internal coordinate can be used to optimize the drive train operation and achieve maximum fuel economy.

The low level controller is designed to actuate T_{eng}, x_S, and x_T such that the vehicle torque demand T_{out} is fulfilled, and the desired engine operation $(\omega^*_{eng}, T^*_{eng})$ specified by the mid-level controller is achieved. Ideally, the driver's demand T_{out} is determined by the accelerator pedal. However,since the engine's output torque is directly coupled to the vehicle's accelerator pedal, it is desired to utilize a different device such that the engine controller is not affected. A joystick is proposed here as the driver's signal input to specify the vehicle torque demand T_{out}.

9.1.2 Engine Control

Currently, the engine output torque is directly coupled to the accelerator pedal position. In order to allow computer control of the engine via the ECU, there are two options: (i) modify the engine output torque specified by the accelerator pedal position, (ii) utilize the built-in engine speed regulation controller in the ECU.

Modifying the engine output torque requires specifying the maximum allowable torque via the CAN communication with the ECU. Since modifying engine output torque requires human input to the accelerator pedal, this mode of control is not selected.

Another option for engine control is to use the built-in speed controller in the ECU

for speed regulation. This mode is activated when the accelerator pedal is not depressed, when the engine is idling, or when the cruise control is active. This mode of operation appears to be the safest approach for the initial testing of the powertrain. By specifying the desired engine speed ω^*_{eng} (in rpm) via CAN communication to the ECU, the ECU speed controller will regulate the engine speed at ω^*_{eng}. Figure 9.1 shows the performance of the ECU engine speed controller: the engine is regulated at 83.8rad/s (800rpm) with only a brief fluctuation when subjected to a torque disturbance from the transmission. The engine torque is increased to maintain the engine speed at constant speed, even though the output speed is changing.

9.1.3 Pump/Motor Control

As previously mentioned, the transmission is configured as output coupled. The role of each hydraulic unit is opposite that of the input coupled configuration described in Sec. 6.2.3, where P/M-S determines the engine torque and P/M-T augments the transmission output torque, as seen in Eq. (8.6).

From Eq. (8.6), to achieve the desired engine torque T^*_{eng}, the desired P/M-S torque is determined as:

$$T_S(t) = \frac{1}{(1+\rho)} T^*_{eng} \tag{9.5}$$

To achieve the vehicle torque demand T_{out} for the specified desired engine torque T^*_{eng}, the desired P/M-T torque can be determined as:

$$T_T(t) = -\frac{1}{(1+\rho)} T^*_{eng} - T_{out} \tag{9.6}$$

To attained the desired pump/motor torques T_S, T_T, the pump/motor displacements x_S, x_T are actuated. Alternatively, one can specify x_S and x_T to solve for Q_{acc} (in Eq. (6.17)) and T_{out} (in Eq. (8.6)). In this transmission, the hydraulic pump/motor displacements are controlled using stepper motors to actuate spool valves within the transmission, which in turn change the bent axis angle (P/M displacement) via a piston-linkage assembly.

The stepper motors are driven by motor drivers that utilize the Serial RS232 communication protocol. Using the angular measurements from each hydraulic unit, a simple

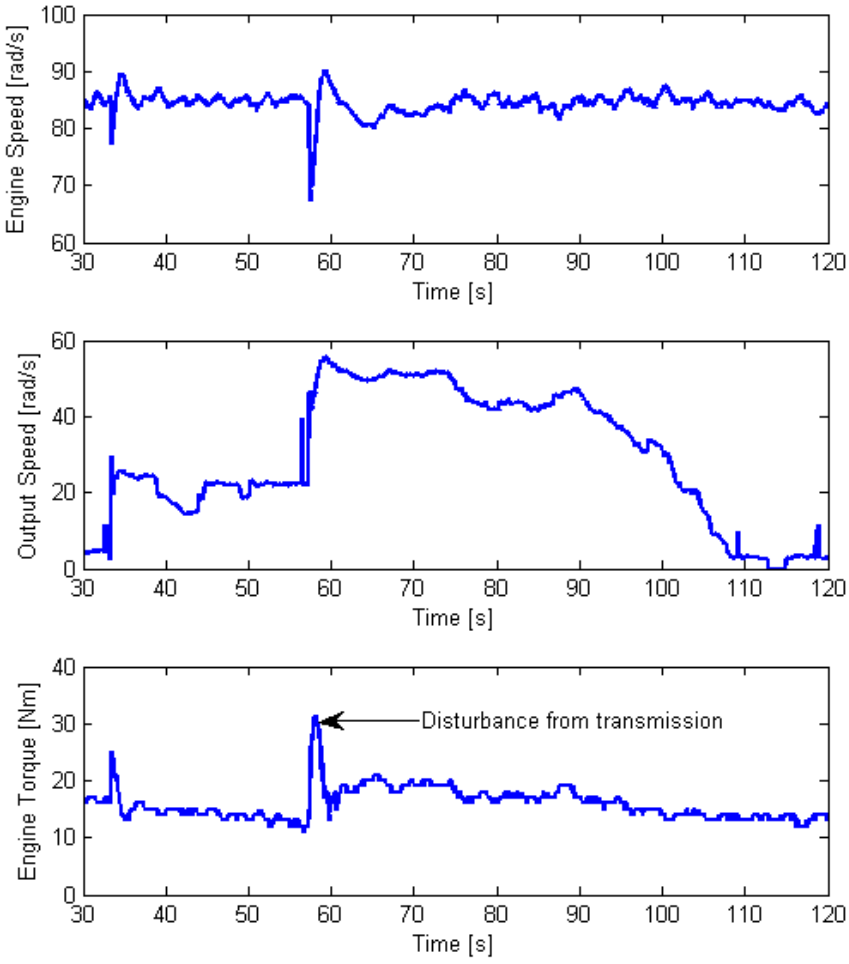

Figure 9.1: Engine speed regulated at 83.8rad/s (800rpm) with varying transmission output speed.

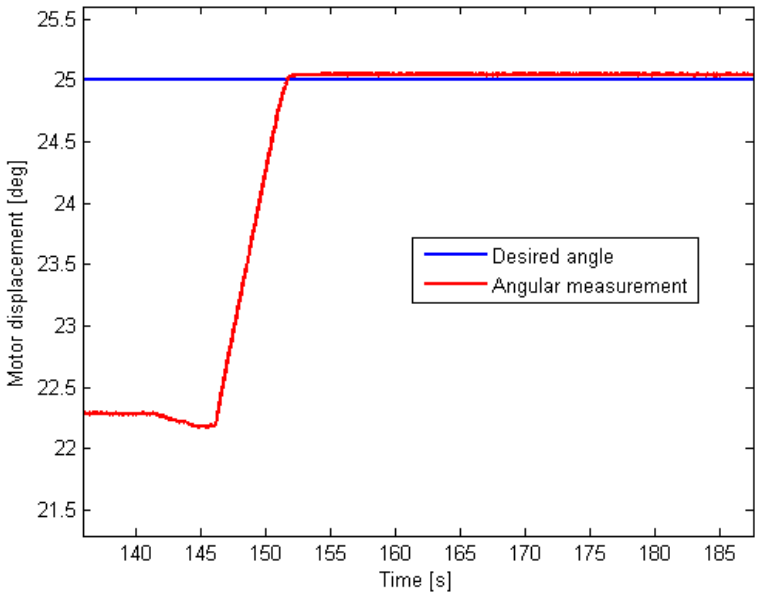

Figure 9.2: Step response of pump/Motor-T bent-axis angle tracking with proportional controller, with the controller activated at t=146s.

proportional feedback loop is designed such that the stepper motors will actuate automatically to achieve the specified pump/motor displacement. For each sampling time, the controller decides the number of micro-steps in order to reach the desired angle.

Figure 9.2 illustrates a step response of the stepper motor to actuate the pump/motor bent-axis displacement using the proportional controller. The controller achieves the desired position with steady state error of $0.05deg$. The controller shown in this example is tuned to have very low bandwidth (time constant of approximately 4 seconds) to ensure safety and stability during preliminary testing. The stepper motor controller must be further fine-tuned to higher bandwidth in order to be utilized for transmission control.

9.2 Preliminary Free-spinning Experiment

A preliminary test is conducted to ensure the low level controllers are operational and stable. Section 9.1.2 and 9.1.3 have shown that the engine speed controller and

pump/motors displacements are actuated successfully. During this test, all the wheels are off the ground, thus the transmission is under near zero load (hence free-spinning). Due to the malfunctioning pressure sensors, uncharged accumulator bladder, and malfunctioning shut-off valves, the powertrain cannot be tested as a hybrid transmission. Instead, stand-alone hydro-mechanical transmission mode, with accumulators shut off, is tested to ensure basic functions of the transmission are achievable.

In this free-spinning test, the transmission is operated to achieve 'Neutral', 'Drive', and 'Overdrive', where $\gamma \in [\frac{1}{1+\rho}, \infty)$. The engine is maintained at a constant speed of 83.8rad/s (800rpm) using the ECU built-in speed controller. The desired engine speed and pump/motor displacements are specified manually via DSpace MicroAutobox. Since the transmission is under zero load, the engine is only required to overcome the friction within the transmission.

Figure 9.3(a) shows the normalized pump/motor's displacements. At infinite transmission ratio (in Neutral 'N' mode), P/M-S is set to zero displacement, $x_S = 0$ and P/M-T is set to full displacement, $x_T = 1$. To reduce the transmission ratio (in Drive 'D' mode), P/M-S is stroked from zero to full displacement, $x_S = 0 \rightarrow 1$ while keeping $x_T = 1$ (t = 125 to 133s). After that, P/M-T is stroked from full displacement to zero displacement, $x_T = 1 \rightarrow 0$ while keeping $x_S = 1$ (t = 137 to 165s). Once $x_S = 1$ and $x_T = 0$, the transmission is operating at the mechanical point, where all power from the engine is transmitted through the mechanical path (in Overdrive mode). Figure 9.3(b) depicts the transmission output speed while maintaining the engine speed at 83.8rad/s (800rpm).

Figure 9.3(c) shows the transmission varying from high transmission ratio to low transmission ratio in CVT mode. The predicted transmission ratio is calculated based on:

$$\gamma_{pred} = \frac{x_T}{x_S} + \frac{1}{1+\rho} \tag{9.7}$$

The actual transmission ratio is defined as:

$$\gamma = \frac{\omega_{in}}{\omega_{out}} \tag{9.8}$$

As seen in the plot, the difference between the predicted and actual transmission ratio decreases as the transmission is operating near mechanical point region. The difference

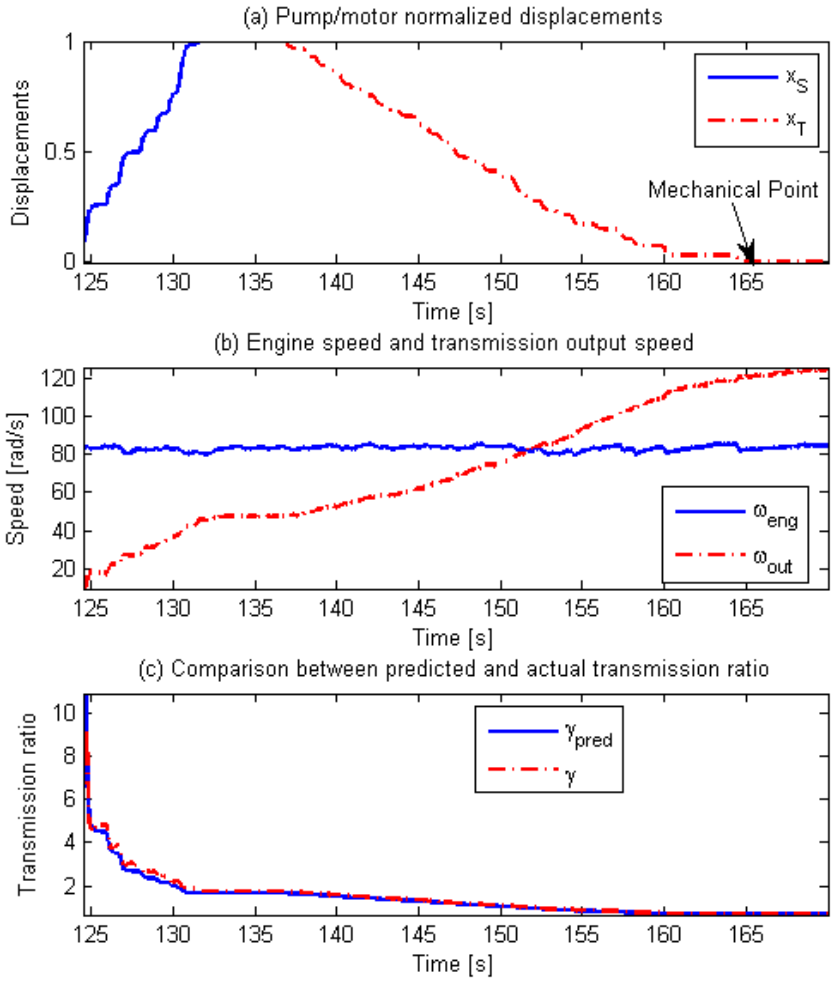

Figure 9.3: Trajectories of the powertrain throughout the free-spinning experiment. (a) Transmission pump/motor displacements. (b) Engine and transmission output speed trajectories. (c) Comparison between predicted and measured transmission ratio.

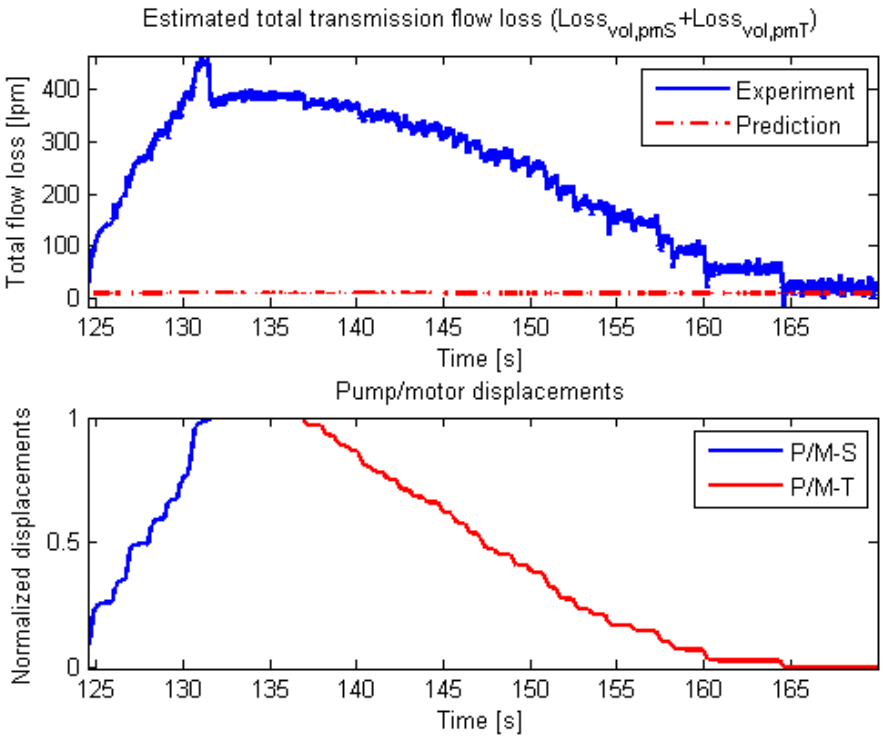

Figure 9.4: Estimated transmission flow loss at various transmission ratio.

between the predicted and actual ratio is due to leakage of the pump/motors, thus the mechanical point is expected to operate most efficiently.

Based on Eq. (8.16), the total flow leakage ($Q_{tot,loss} = Loss_{vol,pmS} + Loss_{vol,pmT}$) can be calculated as:

$$Q_{tot,loss} = \omega_T D_{max} x_S ((1+\rho)\frac{\omega_{eng}}{\omega_{out}} - \frac{x_T}{x_S} - 1) \tag{9.9}$$

Since flow measurements are not available for the transmission, the total flow loss of the transmission throughout the preliminary experiment is estimated according to Eq. (9.9). Figure 9.4 depicts the comparison between the estimated flow loss using Eq. (9.9) and the predicted flow loss using the pump/motor performance map in Sec. 8.3. Due to near zero flow through the pump/motors at the mechanical point, the total flow loss is minimum at that point. The maximum total flow loss occurs when both pump/motors are at full displacement.

A significant flow leakage of $460lpm$ is estimated, and this is substantially higher than the predicted flow. This indicates that the transmission is suffering from great internal leakage, and the pump/motor performance map in Sec. 8.3 has significantly under-estimated the flow losses.

9.3 Future Test

This preliminary test has confirmed the basic functionality of the transmission. Unfortunately, at the time of writing, some hardware issues have prevented further testing. These include: malfunctioning speed, pressure, and transmission output torque sensors, and hydraulic valves. In addition, the hydraulic accumulators have not been charged.

Once these issues have been corrected, future testing should be done to verify the drivability of the Generation II vehicle and the fuel economy throughout EPA drive cycles as predicted in Ch. 9.

Future tests for Generation II should proceed as follows:

1. **Fine-tune the pump/motor displacement actuation bandwidth.** As presented earlier, the time constant of the stepper motor actuation is tuned to approximately 4 seconds for safety concerns. The proportional control should be tuned to achieve at least 3rad/s (time constant of 0.33 second) such that the transmission is responsive to controller.

2. **Implement the joystick input as driver's input.** As mentioned previously, the engine output torque T_{eng} is directly coupled to the accelerator pedal. In order to separate T_{eng} from the vehicle torque demand T_{out}, a joystick is proposed to be utilized as the driver's input. Without pressing the accelerator pedal with the use of joystick, the built-in engine speed control can be used.

3. **Conduct a simplified CVT test.** In the simplified CVT test, the engine speed is regulated at a constant speed using the ECU built-in engine speed controller, with the accumulators shut off. The control objective becomes determining the transmission ratio γ according to the vehicle speed ω_{out} and vehicle torque demand T_{out}.

4. **Conduct CVT test with pressure regulation control.** Using a similar CVT strategy as described in Ch. 6 with pressure regulation control while operating the engine along the best BSFC curve, a baseline control strategy that utilizes the three-level hierarchical control structure can be tested. No regenerative braking will be used in this test.

5. **Conduct mild hybrid strategy test.** This strategy utilizes a similar control scheme as the CVT test, except braking energy will be recovered and utilized for vehicle launching. The testing of this strategy will demonstrate the benefits of hybridizing the hydo-mechanical transmission.

6. **Conduct full hybrid strategy test.** Different energy management strategies can be explored, for instance Modified Lagrange Multiplier strategy, stochastic dynamic programming strategy, thermostatic control strategy, etc., such that fuel economy improvements can be evaluated. In order to evaluate the fuel economy, this test will be conducted on a dynamometer.

9.4 Concluding Remarks

This chapter presents the adaptation of the three-level hierarchical control strategy onto the Generation II vehicle. Dynamic decomposition of the vehicle dynamics is also presented. While the structure of the control strategy is similar, the low level control scheme is different from the input coupled configuration. The desired engine torque is achieved by determining the P/M-S torque, while the vehicle torque demand is achieved by the torque summation of both pump/motor S and T.

The engine control is done by communicating with the ECU and specifying the desired engine speed. The speed regulation controller of the built-in ECU is capable of maintaining the engine speed but not with high bandwidth. Nevertheless, this is the safest and most reliable approach to operate the engine. Basic functions of the transmission have been tested using DSpace MicroAutobox. A preliminary experiment was conducted for a large range of transmission ratios in order to ensure the low level actuation is operational and stable. While the basic functions of the transmission are verified, significant flow loss in the transmission is estimated. The estimated flow loss is

also substantially higher than the flow loss predicted using the pump/motor performance model provided by FTI.

Since only a preliminary experiment was conducted so far using DSpace MicroAutobox, future tests for the Generation II vehicle can proceed by fine-tuning the pump/motor actuation bandwidth and implementing a joystick for the user input. Once the hardware issues are corrected, several control strategies can be tested including simplified CVT, CVT with pressure regulation, mild hybrid, and other full hybrid strategies. These hybrid strategies can be utilized to demonstrate the fuel economy improvement achievable by hybridizing the HMT with accumulators.

Chapter 10

Conclusions and Future Work

This dissertation covers the hydraulic hybrid powersplit powertrain design optimization, analysis, and experimental implementation. Hydraulic hybrid vehicle is a proven technology to improve fuel efficiency of a heavy duty powertrain due to its high power density. This is in pursuit of highly fuel efficient propulsion systems and to reduce harmful emissions due to concerns about energy availability and environmental impacts. This is accomplished by optimizing the engine operation to higher efficiency and recovering the kinetic energy from regenerative braking.

Among various types of hybrid architectures, hydraulic hybrid powersplit transmission is selected to be the focus of this study. Power-split hybrids combines the advantages of both the series and parallel hybrids. In addition to being able to decouple engine operation from vehicle load/speed requirements, they also transfer a flexible fraction of power through the efficient mechanical shaft. This architecture preserves the full engine management capability of a series hybrid, and yet it is less susceptible to hydraulics efficiency similar to the parallel architecture.

The rest of this chapter is organized as follows: Section 10.1 summarizes the work done in this dissertation. Section 10.2 presents the contributions made in this research, and Sec. 10.3 recommends some future work for this research.

10.1 Summary

This research extends the investigation of hydraulic hybrid powersplit transmission design optimization conducted in Van de Ven et al. (2008) [12], and Li and Mensing (2010,2011) [11, 22], that focus on passenger-sized hydraulic powertrains. In Ch. 2, a simplified and configuration-based generalized model of the hydraulic hybrid power-split transmission is developed. A systematic approach is proposed to optimize the power-split transmission design for fuel efficiency. By assuming constant system pressure and unconstrained accumulator capacity, the Lagrange Multiplier method can be used for energy management synthesis to significantly reduce the computational time for the transmission optimization process. Compared to the Dynamic Programming method, the Lagrange Multiplier method is 450 times faster.

Apart from fuel efficiency, vehicle acceleration is another performance criteria to be considered due to higher power density of hydraulics compared to electrical machines. Using the Weighted-sum method in Ch. 3, a classical multi-objective method to integrate the acceleration performance into fuel efficiency optimization, a set of Pareto Frontier optimum design with trade-offs between the objectives is generated. The ϵ-Constraint method is utilized to complement the Weighted-Sum method in order to generate a complete Pareto Frontier. The generated Pareto Frontier provides an important guideline for trading off fuel economy to improve the acceleration performance.

Meanwhile, the methodology proposed to optimize the power-split transmission design does not account for uncertainty. Realistically, feasibility and efficiency sensitivity of the transmission against design parameters and operating conditions variations must be addressed. In order to design the transmission to be robust against the operating conditions or model uncertainties, a worst-case variation design optimization approach is proposed in Ch. 4 to ensure the feasibility of the design. This will ensure the transmission design to be feasible within the prescribed uncertainty range. Efficiency sensitivity with respect to uncertainties is also minimized, by using the Weighted-sum method, to reduce the effect of operating conditions and powertrain loss variations.

The Generation I test bed is an experimental platform built to validate the input-coupled power-split hydraulic hybrid powertrain's effectiveness and evaluate its fuel economy. In Ch. 5, a quasi-static hybrid powertrain model is developed to predict the

potential fuel economy and dynamic behavior of the powertrain components including the engine and pump/motors. The three-level hierarchical control structure first proposed in [11], and the mid-level and low level controller is fully developed in Ch. 6. This control structure is implemented on the powertrain model, fuel economies of the Generation I vehicle under several energy management strategies are predicted. Experimental results in Ch. 7 show significant friction loss through the gearbox which was initially assumed frictionless in the model. A linear viscous friction model is empirically deduced to compensate for the lower transmission output torque. Experimental data also shows that the vehicle output torque is substantially lower than the driver demand torque. The error in translating the driver's demand will lead to erroneous engine operation, leading to less fuel efficient engine operation.

The Generation II vehicle is another hydraulic power-split architecture experimental platform. As explained in Ch. 8, the architecture of the Generation II transmission is output coupled power-split, the opposite of Generation I. The powertrain model is also developed for the Generation II vehicle. The hybrid vehicle control strategy developed in Generation I is adopted for this test bed as discussed in Ch. 9. This test vehicle will also prove the benefits of a hybrid hydro-mechanical powertrain on a commercially available pick-up truck. Simulation shows substantial fuel efficiency gain of up to 55% increase in fuel economy by replacing the 6-speed automatic transmission with the hybridized Folsom HMT. Preliminary tests verified the basic functionality of the transmission as a stand-alone CVT using DSpace MicroAutoBox. A study to optimize the Generation II transmission is also conducted, and showed that 58.5% fuel economy improvement can be achieved.

The research in this dissertation has provided a system level optimization of transmissions for hydraulic hybrid passenger vehicle. However, detailed transmission design requires extensive analysis on dynamic modeling, components stress analysis, system integration, etc. which has not been addressed here. While this research study targets the robust optimization of a passenger-sized hydraulic hybrid vehicle, the developed optimization procedure is not restricted to hydraulic hybrid but also hybrid electric vehicle.

10.2 Contributions

This research focuses on developing systematic and time-efficient methodology to optimize the hydraulic hybrid transmission design. The analysis aims to combine deterministic optimization and robust optimization for hybrid transmission design. The contributions of the work presented in this dissertation can be summarized as follows:

1. Development of generalized kinematic transmission modeling for power-split configuration. This computational efficient method utilizes the insight that there are many design configurations that are mechanically distinct but kinematically equivalent, redundant evaluation is avoided without considering each mechanical configuration.

2. Development of time-efficient hybrid transmission optimization methodology, by using the generalized kinematic transmission model and Lagrange Multiplier method for hybrid powertrain energy management synthesis. This systematic approach is significantly (> 400 times) faster than the traditional Dynamic Programming method.

3. Solving a multi-objective (MO) problem requires generating a complete Pareto Frontier solution set. In this study, the MO problem is solved using the classic Weighted-Sum method and complemented with the ϵ-Constraint method. This proposed methodology generates a complete Pareto Frontier solution set without using advanced solvers and sacrificing computation efficiency. Acceleration performance criteria is incorporated into fuel efficient transmission design optimization using this approach and a set of equally optimal design is successfully generated.

4. Development of robust optimal design methodology by using the worst-case variation to guarantee the feasibility of the transmission design. Minimization of fuel efficiency sensitivity with respect to uncertainty variation is incorporated by formulating both the worst-case optimal objective and efficiency sensitivity objective into multi-objective problem. The transmission design is made to be robustly feasible within the prescribed uncertainty variation.

5. Development of the previously proposed three-level hierarchical control strategy, and experimental implementation of the control structure on test hardware. Two

different energy management strategies are experimentally implemented without modifying the Mid-level controller. The effectiveness and modularity of this hierarchical control structure is validated.

10.3 Future Works

Despite the effort to analyze the transmission design, energy management strategies and effects of uncertainties, several assumptions are made to simplify the problem. There are several analysis and hardware improvements and directions that should be pursued. Previously, the comparison between Hybrid Electric Vehicle (HEV) and Hydraulic Hybrid Vehicle (HHV) is limited to static optimization where the power electronics efficiency and dynamics are neglected. Electrical machines and energy storage devices have very different benefits and limitations compared to hydraulics. For instance, electric motors have high torque bandwidth but also large inertia compared to same power-rated hydraulic pump/motors. Also, electric motors can be overloaded for short periods of time for extra power, potentially lowering the transmission weight. With these dynamics incorporated into the powertrain model, the comparison between the hybrid transmissions can be completed.

The uncertainty model and analysis requires further development. The results in this dissertation are limited to power loss variation due to torque uncertainty. Apart from power loss uncertainty, there are two other variations that are particularly of interest, i.e. the pressure variation and driver's demand variation. System pressure is assumed to be constant in the process of design optimization. However, also shown by dynamic programming results, the optimal pressure trajectory fluctuates between 13.8MPa (2000psi) to 34.5MPa (5000psi). The constant pressure assumption can be removed if the pressure probability distribution (non-Gaussian) is incorporated. The significance of the driver's demand uncertainty is reflected by the unpredictable driver's behavior.

As discussed in Sec. 7.2, the discrepancy between the demanded output torque and the measured transmission output torque has caused the engine to operate at lower efficiency region. Refining the transmission gearbox loss model will improve the output torque accuracy, hence lead to higher fuel efficiency. This can be done by applying the

viscous model developed to compensate for the friction loss. A more direct approach is to test the transmission gearbox on a separate test rig to isolate the uncertainties from other components, such as the engine.

Chapter 7 presented the implementation of CVT and Rule-based energy management strategies. Experimental testing of other strategies, including Dynamic Programming (DP) and Modified Lagrange Multiplier (MLM) strategies should be continued. These strategies shall demonstrate the benefit of hybrid powertrains, and the importance of engine management for fuel efficiency.

System pressure rating is an important design trade-off between efficiency and power density for a light-weight vehicle. The test hardware is designed to operate at maximum pressure of 34.5MPa (5000psi), hence the hydraulic hoses, valves and manifolds are steel-based instead of aluminum. As found out previously from the energy management strategy, the operating system pressure of the transmission is desired to operate at lower pressure for efficiency. This leads to the heavy, high pressure rated hydraulic units to be utilized infrequently. On the other hand, 20.7MPa (3000psi) rated aluminum-based plumbing would reduce the weight significantly but leads to larger pump/motor units to compensate for lower pressure rating.

Pump/motor selection requires further consideration for system integration, compactness, efficiency and controls. In this study, a set of variable displacement bent-axis axial piston pump/motors are used. Due to the lack of over-center capability, a pair of directional valves are installed to allow four-quadrant operation, adding weight, plumbing and controls complexity while lowering efficiency. In contrast, using over-center units, pump geometrical size would be larger for bent-axis type (or similar size for swash-plate type), and transition through over-center is continuous. Meanwhile, the two pump/motors types are not constrained to be identical. For example, the 'speeder' unit could be swash-plate or radial-piston type due to its low speed high torque characteristics, and the 'torquer' unit could be bent-axis or swash-plate type for its high efficiency.

Even though this dissertation focus only on fuel efficiency gain using hydraulic hybrid transmission, the engine performance plays significant role in transmission optimization. The diesel engine used in the Generation I vehicle has low power density. This 1.5L diesel engine produces only $26.5kW$, as compared to $80 \sim 97kW$ for a typical 4 cylinder

gasoline engine in a compact-sized vehicle (e.g. Honda Fit or Toyota Yaris). The difference in power could potentially improve the acceleration performance and fuel efficiency due to higher power-to-weight ratio.

The test hardware is configured as a rear-wheel drive transmission. However, it is not a compact nor practical for a passenger-sized vehicle. If a new experimental platform were to be built, front-wheel drivetrain configuration will offer compactness, light-weight and integration simplicity, hence it is adopted for majority of the commercial passenger vehicles. Meanwhile, with both the engine and transmission located at the front of the vehicle, transmission fluid conditioning can be combined with the engine radiator easily. Other hardware upgrade recommendation includes installation of speed sensor at output shaft, two speed gearbox, and soft-switching directional valves.

With additional effort to understand the hybrid powertrain energy management, improve the efficiency and packaging of the hydraulic transmission, and to reduce the cost of the components, hydraulic hybrid power-split powertrain will be a viable form of efficient, affordable and driver friendly propulsion system. As internal combustion engine will persevere for several decades, hydraulic hybrid powertrain will continue to be a versatile propulsion system.

References

[1] Tomaz Katrasnik, "Analysis of Fuel Consumption Reduction Due to Powertrain Hybridization and Downsizing of ICE," in *SAE International*, 2006-01-3262, 2006.

[2] Hong Chen and Bongzhao Gao, "Nonlinear estimation and control of automotive drivetrains," published by *Springer*, 2014.

[3] Volkswagen AG, The DSG Dual-Clutch Gearbox, Environmental Commendation Background Report, `http://en.volkswagen.com/content/medialib/vwd4/vw_international/4_company/4_3_overview_sustainability/Nachhaltigkeit/Data_Sheets/umweltpraedikatepar0034file-pdf/_jcr_content/renditions/rendition.file/umweltpraedikate_par_0034_file.pdf`

[4] ZF Friedrichshafen AG Website, `http://www.zf.com/corporate/en_de/products/product_range/cars/cars_7_speed_dual_clutch_transmission.shtml#tabs1-1`

[5] Environmental Protection Agency Website, `http://yosemite.epa.gov/opa/admpress.nsf/6424ac1caa800aab85257359003f5337/e1470abd2835dd10852573b40073a08f!opendocument`

[6] Eric Jacobson, Joe Wright, and Torsten Kohmasher, "Hydro-Mechanical Power Split Transmission (HMT) - Superior Technology to Solve the Conflict: Tier 4 vs. Machine Performance," in *Proceedings of the 52nd National Conference on Fluid Power (NCFP),* number 5.3, 2011.

[7] Environmental Protection Agency Website, "Hydraulic Hybrid Research, website: http://www.epa.gov/otaq/technology/research/research-hhvs.htm,'' June,2006.

[8] Advanced Technology Division, "Progress Report on Clean And Efficient Automotive Technologies Under Development at EPA," in *EPA Interim Technical Report*, year 2004.

[9] Eaton Hydraulic Launch Assist System, http://www.eaton.com/Eaton/ProductsServices/Hydraulics/HydraulicLaunchAssist/

[10] Bosch Rexroth Hydraulic Flywheel System, http://www.boschrexroth.com/en/xc/products/product-groups/mobile-hydraulics/systems-and-functional-modules/hydraulic-flywheel-hfw/index#

[11] Perry Y. Li and Felicitas Mensing, "Optimization and Control of a Hydro-Mechanical Transmission based Hybrid Hydraulic Passenger Vehicle," in *7th International Fluid Power Conference,* Aachen, Germany, 2010.

[12] Van de Ven, J., Olson, M., Li, P.Y.Development of a Hydro-Mechanical Hydraulic Hybrid Drive Train with Independent Wheel Torque Control for an Urban Passenger Vehicle, in *IFPE 2008*, Las Vegas, NV, 2008.

[13] Z. Du, K. L. Cheong, P. Y. Li and T. R. Chase, "Fuel Economy Comparisons of Series, Parallel and HMT Hydraulic Hybrid Architectures", in *Proc. of 2013 American Control Conference*, pp.5974–5979, 2013.

[14] John M. Miller, "Hybrid Electric Vehicle Propulsion System Architectures of the e-CVT Type," *IEEE Transactions on Power Electronics,* volume 21, number 3, May 2006.

[15] John Deere IVT Transmission, http://salesmanual.deere.com/sales/salesmanual/en_NA/tractors/2006/feature/transmissions/7020lf/7020lf_transmissions_ivt.html

[16] Bosch Rexroth Hydromechanical Variable Transmission, http://www.boschrexroth.com/en/xc/products/product-groups/

mobile-hydraulics/systems-and-functional-modules/
hydromechanical-variable-transmission-hvt/index

[17] PSA Peugeot Citroen Hybrid Air System, http://www.psa-peugeot-citroen.com/en/automotive-innovation/innovation-by-psa/hybrid-air-engine-full-hybrid-gasoline

[18] Center for Compact and Efficient Fluid Power (CCEFP) official website, http://www.ccefp.org/

[19] Stephen J. Sedler, *Design of a Hydromechanical Transmission with Regeneration for a Passenger Vehicle*. M.S. Plan-A thesis, Department of Mechanical Engineering, University of Minnesota, 2012.

[20] James H. Kress, "Hydrostatic Power-Splitting Transmission for Wheeled Vehicles - Classification and Theory of Operation," in *Society of Automotive Engineers,* number 680549, 1965.

[21] Blake Carl, Monika Ivantysynova, and Kyle Williams, "A Comparison of Operational Characteristic in Power Split Continuously Variable Transmission," in *SAE International,* number 2006-01-3468, 2006.

[22] Felicitas Mensing, and Perry Y. Li, "Sizing and Optimal Operation of a Power Split Hydraulic Hybrid Drive Train," in *International Fluid Power Exhibition (IFPE),* Las Vegas, NV, March 2011.

[23] Chiao-Ting Li and Huei Peng, "Optimal Configuration Design for Hydraulic Split Hybrid Vehicles", in *American Control Conference,* volume 14, pages 1-22, 2010.

[24] G. Paganelli et. al., "Optimizing control strategy for hybrid fuel cell," in *SAE*, number 2002-01-0102, 2002.

[25] Sciarretta, A., Dabadie, J-C. and Albrecht, "Control-Oriented Modeling of Power Split devices in Combined Hybrid-Electric Vehicles", in *SAE International,* number 2008-01-131, 2008.

[26] Gilbert Strang, "Linear Algebra and its Applications," published by *Thomson Learning, Inc.*, 4th Edition, 2005.

[27] Environmental Protection Agency Website, http://www.epa.gov/otaq/carlabel/regulations.htm#test-methods"

[28] A. Bryson and Y.-C. Ho, Applied Optimal Control, published by *Taylor and Francis Group*, 1975.

[29] Stephen Boyd and Lieven Vandenberghe, "Convex Optimization," published by *Cambridge University Press*, 2009.

[30] Eligius M.T. Hendrix and Boglarka G.-Toth, "Introduction to Nonlinear and Global Optimization," published by *Springer Science+Business Media, LLC.*, 2010.

[31] Matlab Help Website, http://www.mathworks.com/help/matlab/ref/fminsearch.html

[32] Kai Loon Cheong, Perry Y. Li, and Thomas R. Chase, "Optimal Design Power-Split Transmissions for Hydraulic Hybrid Passenger Vehicles", in *American Control Conference,* 2011.

[33] Kai Loon Cheong, Perry Y. Li, Stephen Sedler, and Thomas R. Chase, "Comparison between input coupled and output coupled power-split configurations in hybrid vehicles," in *International Fluid Power Exhibition (IFPE),* Las Vegas, NV, March 2011.

[34] Donald E. Kirk, "Optimal Control Theory - An Introduction", published by *Dover Publications, Inc.*, 2004.

[35] Bertsekas, D. P., "Dynamic Programming and Optimal Control," published by *Athena Scientific*, 1995.

[36] Bosch, "Automotive Handbook," in *SAE International*, 8th Edition, 2011.

[37] Richard Stone, "Introduction to Internal Combustion Engines," published by *SAE International*, 3rd Edition, 1999.

[38] A. Pourmovahed, N.H.Beachley, and F.J.Fronczak, "Modeling of a Hydraulic Energy Regeneration System - Part 1: Analytical Treatment," in *Journal of Dynamic System, Measurement, and Control*, volume 114, March, 1992.

[39] H.W.Cooper and J.C.Goldfrank, "B-W-R Constants and New Correlations," in *Hydrocarbon Processing*, volume 46, 1967.

[40] "ADVISOR - ADvanced VehIcle SimulatOR v. 3.0", National Renewable Energy Laboratory (NREL), Department of Energy, USA, 2000.

[41] Michael Duoba, Henry Ng and Robert Larsen, "Characterization and Comparison of Two Hybrid Electric Vehicles (HEVs) - Honda Insight and Toyota Prius," in *SAE International*, 2001-01-1335, 2001.

[42] Toyota Website, `http://www.toyota.com/prius`

[43] Zhijian Lu, "Acceleration Simulation of a Vehicle with a Continuously Variable Power Split Transmission," M.S. thesis, College of Engineering and Mineral Resources, West Virginia University, 1998.

[44] A. Haj-Fraj and F. Pfeiffer, "Optimization of Gear Shift Operations in Automatic Transmission," in *Proceeding of Advanced Motion Control,* IEEE, 2000.

[45] Chiao-Ting Li, Xiaowu Zhanga, and Huei Peng, "Design of Power-Split Hybrid Vehicles with a Signle Planetary Gear," in *ASME 2012 5th Annual Dynamic Systems and Control Conference*, Fort Lauderdale, Florida, 2012.

[46] Xiaowu Zhang, Huei Peng, Jing Sun, and Shengbo Li, "Automated Modeling and Mode Screening for Exhaustive Search of Double-Planetary-Gear Power Split Hybrid Powertrains," in *ASME 2014 Dynamic Systems and Control Conference,* San Antonio, Texas, 2014.

[47] Minkuk Kang, Hyunjun Kim, and Dongsuk Kum, "Systematic Configuration Selection Methodology of Power-Split Hybrid Electric Vehicles with a Single Planetary Gear," in *ASME 2014 Dynamic Systems and Control Conference,* San Antonio, Texas, 2014.

[48] Pareto, V., "Manuale di Economia Politica," Societa Editice Labraria, Milano, Italy, 1906. Translated into English by A.S. Schwier as "Manual of Political Economy", Macmillan, New York, 1971.

[49] Kaisa M. Miettinen, "Nonlinear Multiobjective Optimization," in *Springer Science+Business Media, LLC*, 1998.

[50] Petri Eskelinen, Kaisa Miettinen, Kathrin Klamroth, and Jussi Hakanen, "Pareto navigator for interactive nonlinear multiobjective optimization," in *Springer OR Spectrum,* 2010, Vol.32(1), pp.211-227

[51] Dr. Anas Alfaris, "ESD.77 / 16.888 Multidisciplinary System Design Optimization (MSDO) Lecture Slides," in *MIT Online Courseware*, Lecture 14, 2010.

[52] Patrick Ngatchou, Anahita Zarei, and M.A. El-Sharkawi, "Pareto Multi Objective Optimization," in *Proceedings of the 13th International Conference on, Intelligent Systems Application to Power Systems*, pp.84-91, 2005.

[53] Jrgen Branke, Kalyanmoy Deb, Kaisa Miettinen, and Roman Slowinski, "Multiobjective Optimization - Interactive and Evolutionary Approached," in *Springer Science+Business Media, LLC*, 2008.

[54] David L. Craft, et. al., "Approximating convex Pareto surfaces in multiobjective radiotherapy planning," in *American Association of Physicists in Medicine*, 2006.

[55] Yakov Ben-Haim, "Robust Reliability in the Mechanical Sciences," published by *Springer-Verlag*, 2nd edition, 1996.

[56] A. Parkinson, "Robust Mechanical Design Using Engineering Models," in *Transactions of the ASME,* volume 117, June 1995.

[57] Gerald Steiner, Andreas Weber, and Christian Magele, "Managing Uncertainties in Electromagnetic Design Problems With Robust Optimization", in *IEEE Transactions on Magnetics*, volume 40, number 2, March 2004.

[58] Sang-Baeck Yoon et. al., "Robust Shape Optimization of Electromechanical Devices", in *Transactions of the ASME*, volume 117, June 1995.

[59] QingHui Yuan and Perry Y. Li, "Robust Optimal Design of Unstable Valves", in *IEEE Transactions on Control System Technology*, volume 15, number 6, November 2007.

[60] Michael Kokkolaras et. al., "Design Under Uncertainty and Assessment of Performance Reliability of a Dual-Use Medium Truck with Hydraulic-Hybrid Powertrain and Fuel Cell Auxiliary Power Unit", in *SAE International*, number 2005-01-1396, 2005.

[61] Jinming Liu and Huei Peng, "Modeling and Control of a Power-Split Hybrid Vehicle," in *IEEE Transactions on Control Systems Technology*, Vol. 16, No. 6, November 2008.

[62] Zoran Filipi, Jonathan Hagena, and Hosam Fathy, "Investigating the Impact of In-Vehicle Transients on Diesel Soot Emissions," in *Thermal Science*, Vol. 12 (2008), No.1, pp. 53-71, 2008.

[63] Filipi, Z., et. al., Engine-in-the-Loop Testing for Evaluating Hybrid Propulsion Concepts and Transient Emissions HMMWV Case Study," in *SAE Transactions, Journal of Commercial Vehicles*, 2006-01-0443, 2006.

[64] Ramakrishnan, B. and Rao, S.S., "A Robust Optimization Approach Using Taguchi's Loss Function for Solving Nonlinear Optimization Problems," in *ASME Advanced in Design Automation*, Vol. DE-Vol. 32-1, 1991, pp. 241-248.

[65] Christopher A. Mattson and Achille Messac, "Handling Equality Constraints in Robust Design Optimization," in *American Institute of Aeronautics and Astronautics Paper*, 2003-1780.

[66] Sirisha Rangavajhala, Anoop Mullur and Achille Messac, "The Challenge of Equality Constraints in Robust Design Optimization: Examination and New Approach," in *Struct Multidisc Optim*, 2007.

[67] A. Messac and A. Ismail-Yahaya, "Multiobjective robust design using physical programming," in *Struct Multidisc Optim 23*, 357-371, 2002.

[68] H. Kohring, *Design and Construction of a Hydrostatic Dynamometer for Testing a Hydraulic Hybrid Vehicle*. M.S. Plan-A thesis, Department of Mechanical Engineering, University of Minnesota, 2012.

[69] Z. Du, P. Y. Li, K. L. Cheong and T. R. Chase, "Design and Experimental Validation of a Virtual Vehicle Control Concept for Testing Hybrid Vehicles Using a Hydrostatic Dynamometer", in *Proc. of ASME Dynamic Systems and Control Conference*, Paper No. DSCC2014-6290, 2014.

[70] John B. Heywood, "Internal Combustion Engine Fundamentals," published by *McGraw-Hill, Inc.*, 1st Edition, 1988.

[71] K.L. Cheong and P.Y. Li, "Control Oriented Modeling and System Identification of a Diesel Generator Set (Genset)," in *American Control Conference*, 2010.

[72] David R. Grandall, "The Performance and Efficiency of Hydraulic Pumps and Motors", *MSME dissertation*, Department of Mechanical Engineering, University of Minnesota, 2010.

[73] D. McCandlish and R.E. Dorey, "The Mathematical Modelling of Hydrostatic Pumps and Motors," in *Proc. Instn. Mech. Engs.*, Vol 198B, No. 10, 1984.

[74] G. Paganelli et. al., "Optimizing control strategy for hybrid fuel cell", SAE, Warrendale, PA, tech. Rep. 2002-01-0102, 2002.

[75] Namwook Kim, Suk Won Cha, and Huei Peng, "Optimal Equivalent Fuel Consumption for Hybrid Electric Vehicles," in *IEEE Trans. on Control Systems Technology*, Vol.20, No.3, May 2012.

[76] Dac Viet Ngo, Theo Hofman, Maarten Steinbuch, and Alex F. A. Serrarens, "An Optimal Control-Based Algorithm for Hybrid Electric Vehicle Using Preview Route Information," in *American Control Conference*, Baltimore, MD, 2010.

[77] B. Wu et. al., "Optimization of Power Management Strategies for a Hydraulic Hybrid Medium Truck", Proceedings of the 2002 Adv. Vehicle Control Conf., Hiroshima, Japan, Sep. 2002.

[78] Lorenzo Serrao, Simona Onori and Giorgio Rizzoni, "ECMS as a realization of Pontryagin's minimum principle for HEV control," in *American Control Conference*, FrA01.5, St. Louis, MO, 2009.

[79] Z. Filipi and Y.J. Kim, "Hydraulic Hybrid Propulsion for Heavy Vehicles: Combining the Simulation and Engine-In-the-Loop Techniques to Maximize the Fuel Economy and Emission Benefits," in *Oil and Gas Science and Technology*, Rev. IFP, Vol.65 (2010), No.1.

[80] Rajneesh Kumar, "A Power Management Strategy for Hybrid Output Coupled Power-split Transmission to Minimize Fuel Consumption", Ph.D dissertation, Purdue University, December 2010.

[81] Sim, T.P. and Li, P.Y., "Analysis and Control Design of Hydro-Mechanical Hydraulic Hybrid Passenger Vehicle," in *ASME DSCC/Bath Symposium*, number 2763, Hollywood, CA, 2009.

[82] Kai Loon Cheong, Zhekang Du, Perry Y. Li, and Thomas R. Chase, "Hierarchical Control Strategy for a Hybrid Hydro-mechanical Transmission (HMT) Power-Train", in *American Control Conference,* 2014.

[83] Lee, D.J., Li, P.Y., Passive Decomposition for Formation and Maneuver Control of Multiple Rigid-Bodies, in *ASME JDSMC.* pp. 662-677, 2007.

[84] Franklin, G. F., Powell, J. D., and Emami-Naeini, A., "Feedback Control of Dynamic Systems," 3rd ed., published by *Addison-Wesley*, 1994.

[85] J. Meyer, "Developing an Energy Management Strategy for Hydraulic Hybrid Passenger Vehicles", Ph.D dissertation, Department of Mechanical Engineering, University of Minnesota, 2014.

[86] Petra Heingartner and David Mba, "Determining Power Losses in Helical Gear Mesh: Case Study,", in *ASME/AGMA 9th International Power Transmission and Gearing Conference*, Chicago, IL, 2003.

[87] Anderson, N.E., and S.H. Loewenthal, Efficiency of nonstandard and high contact ratio involute spur gears, in *Journal of Mechanisms, Transmissions, and Automation in Design*, Vol. 108, March 1986, pp. 119126.

[88] Project Summary: TB3 Hydraulic Hybrid Passenger Vehicle (P.Y.Li and T.R.Chase), Center for Compact and Efficient Fluid Power Annual Report, Univesity of Minnesota, 2012.

[89] Lino Guzzella and Antonio Sciarretta, "Vehicle Propolsion Systems - Introduction to Modeling and Optimization," in *Springer Science+Business Media, LLC*, 2005.

[90] Laura Tribioli and Angela Fumarola, "Methodology Procedure for Hybrid Electric Vehicles Design", in *SAE International*, 2011-24-0071, 2011.

[91] M. Duoba, H.Lohse-Busch, R. Carlson, T. Bohn and S. Gurski,"Analysis of Power-Split HEV Control Strategies Using Data from Several Vehicles," in *SAE Internation Technical Paper Series*, 2007-01-0291.

Appendix A

Hydraulic Circuit

The schematic of the hydraulic hybrid vehicle hydraulic circuitry is shown in Fig. A.1.

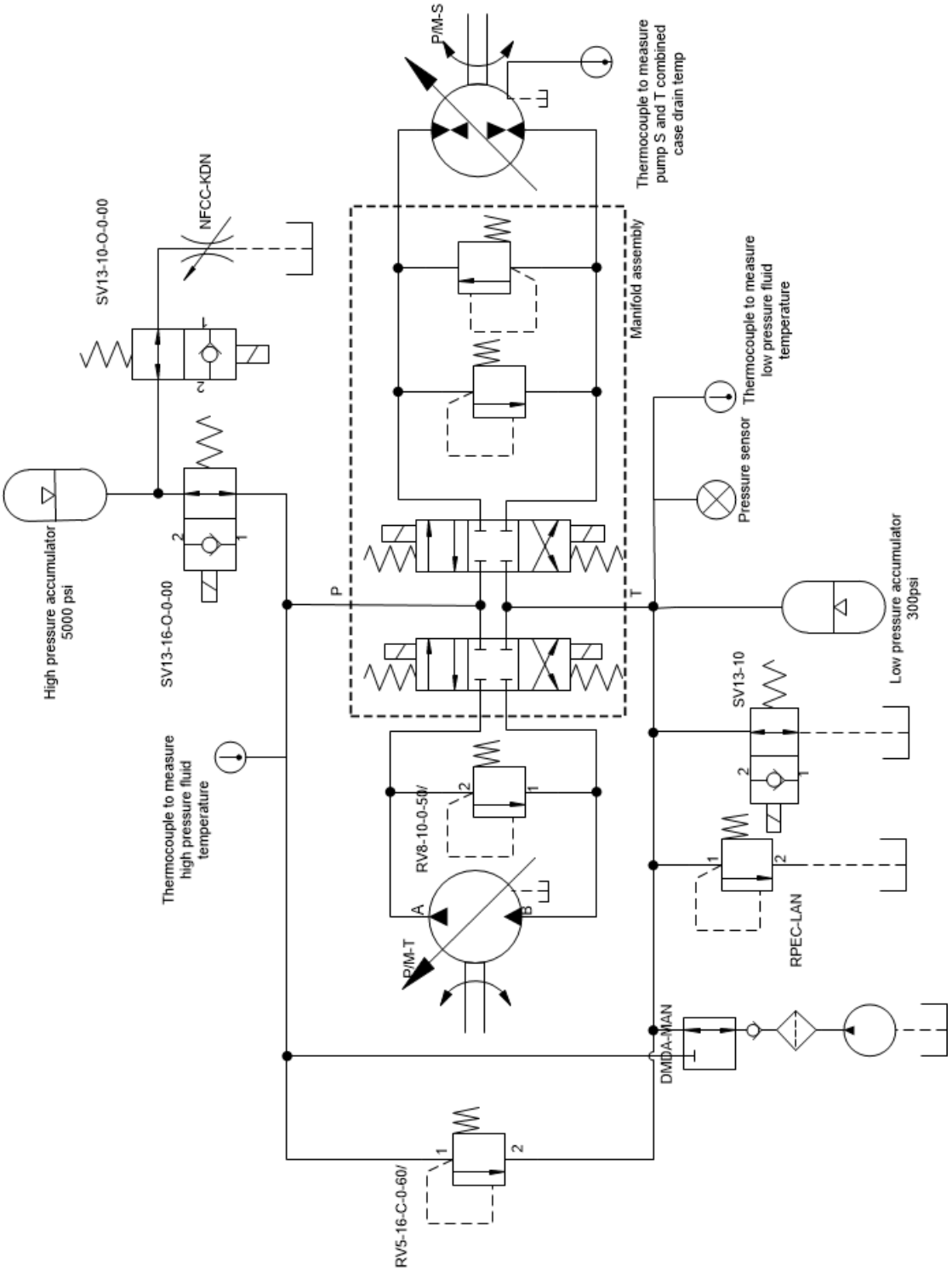

Figure A.1: 'Generation I' hydraulic hybrid circuit.

Appendix B

Generation II Transmission Characterization

As the pump/motors in the Folsom transmission will dominate the losses of the transmission, characterizing the pump/motors' efficiency is crucial in order to operate the transmission more efficiently. However, this integrated transmission design couples the two pump/motors hydraulically together, posing great challenge to characterize the hydraulic units individually. Hence, the efficiency of the pump/motors will be obtained by testing the transmission as a unit.

Standard dynamometer test procedures, as applied to a standard manual or automatic transmission to evaluate the efficiency at various gear ratios, generally do not provide sufficient performance information to operate hybrid transmissions optimally. Without hybridizing the transmission with an accumulator for energy storage, a hydromechanical transmission operates as an continuously variable transmission (CVT). Setting the pump/motors' displacement influences the effective transmission ratio, while the pressure is directly related to the torque transmitted through the transmission and the ratio between the two pump/motors' displacement.

For a hybrid transmission, however, the transmission ratio does not carry sufficient information to uniquely determine the system pressure due to the energy storage. The hybrid transmissions can operate in conditions where a stand-alone HMT could not. Having an extra hydraulic power source effectively decouples the input and output shaft

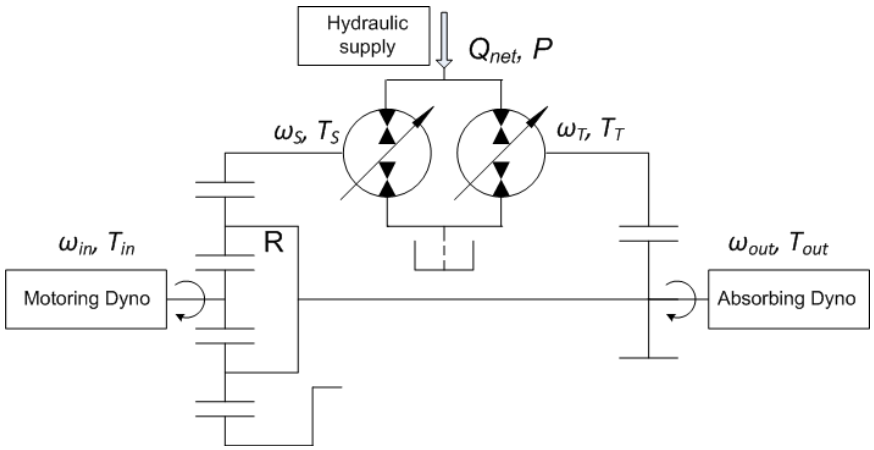

Figure B.1: Schematic of desired dynamometer test set-up.

operating conditions. Thus, similar to the Generation I transmission, individual loss maps on mechanical and volumetric flow efficiencies are required to properly characterize the entire hybrid transmission. In this case, a pressure source is needed to maintain the hydraulic pressure at the desired conditions on the dynamometer test stand. The ideal test set-up shown in Fig. B.1.

However, due to the inability to decouple the pump/motors in the transmission, several constraints and challenges are imposed on the experimental set-up in order to extract useful information from the dynamometer test. Moreover, the FTI facility lacks the required hydraulic power supply. The experimental set-up and restrictions are briefly described below:

I. The transmission is tested as shown in Fig. B.1 but without the hydraulic supply. The input shaft is connected to a motoring dynamometer that acts as an engine, delivering power to the transmission. The output shaft is coupled to an absorbing dynamometer as a power sink. The absorbing dynamometer is also capable of motoring the transmission to mimic regenerative braking events.

II. The motoring dynamometer's speed and absorbing dynamometer's torque or vice-versa can be specified but not speed and torque simultaneously on both dynamometers due to causality of the system.

III. There are limited access ports to the hydraulics. Only the high pressure and

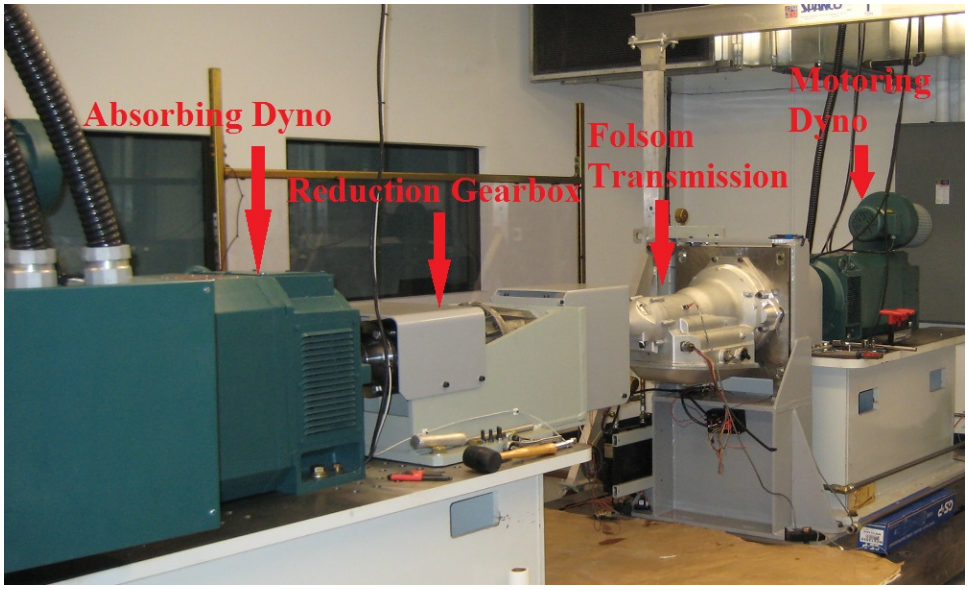

Figure B.2: The actual dynamometer set-up in FTI facility.

low pressure ports are available to be connected to accumulators. Due to this restriction, individual flow measurement between the two pump/motors is not available.

IV. The pump/motors has limited over-center displacements. The P/M-S unit has fractional displacement, x_S, of -0.1 to 1.0 and the P/M-T unit has only positive fractional displacement, x_T, of 0 to 1.0.

V. The make-up (charge) pump integrated to supply the lubrication for the transmission and to maintain a non-zero low pressure threshold in the transmission is directly coupled to the input shaft. Thus, the input shaft is required to spin in the proper direction to prevent any potential damage due to loss of lubrication.

VI. Available measurements are the input speed ω_{in}, input torque T_{in}, output speed ω_{out}, output torque T_{out}, P/M-S displacement x_S, P/M-T displacement x_T, high pressure P_{hi}, and low pressure P_{lo}.

VII. Quantities that cannot be measured includes 'speeder' speed ω_S, torque T_S, flow rate Q_S, P/M-S torque T_T, flow rate Q_T, and charge pump losses (mechanical and hydraulic).

VIII. With ω_{in} and ω_{out} directly measured, therefore ω_S can be deduced according to Eq. (8.5). Input shaft speed is constrained to be higher than 500 rpm (due to charge pump operation) but lower than 1750rpm (to reduce the risk of transmission overheating), $500rpm < \omega_{in} < 1750rpm$.

IX. Due to the lack of measurement on the charge pump losses, P/M-S and T torque (T_S and T_T) can only be estimated from measurements on input and output torque according to Eq. (8.6).

X. Because an external hydraulic supply is not available, hydraulic power within the HMT can only be obtained from mechanical power from the input shaft. This leads to limitations on maintaining the pressure of the hydraulics in various operating conditions.

It is desirable to identify all four quadrants of operational performance of the pump/motors, as shown in Fig. B.3. For consistency of sign convention with 'Generation 1' vehicle, as labeled in the figure, quadrant 1 and 3 implies motoring mode while quadrant 2 and 4 are pumping mode for an individual hydraulic unit.

However, due to the limited over-center displacement operation and the restriction that the input shaft must always be rotating in the same direction to maintain charge pressure, each hydraulic unit is not able to operate in all four quadrants. In addition, the transmission is designed with identical maximum flow displacement for both pump/motors, $D_S = D_T = D_{max}$. This leads to an assumption that P/M-S and P/M-T exhibit identical torque and flow characteristics, which significantly simplifies the characterization procedures.

To quantify the losses and efficiency of the pump/motors into a static map, the mechanical and hydraulic relationships are expressed as follows:

$$T_S = \frac{P_{sys} D_S x_S}{2\pi} - sgn(\omega_S) T_{S,loss}(x_S, \omega_S, P_{sys}) \quad \text{(B.1)}$$

$$T_T = \frac{P_{sys} D_T x_T}{2\pi} - sgn(\omega_T) T_{T,loss}(x_T, \omega_T, P_{sys}) \quad \text{(B.2)}$$

$$Q_S = \omega_S D_S x_S + Q_{S,loss}(x_S, \omega_S, P_{sys}) \quad \text{(B.3)}$$

$$Q_T = \omega_T D_T x_T + Q_{T,loss}(x_T, \omega_T, P_{sys}) \quad \text{(B.4)}$$

$$Q_{net} = Q_S + Q_T \quad \text{(B.5)}$$

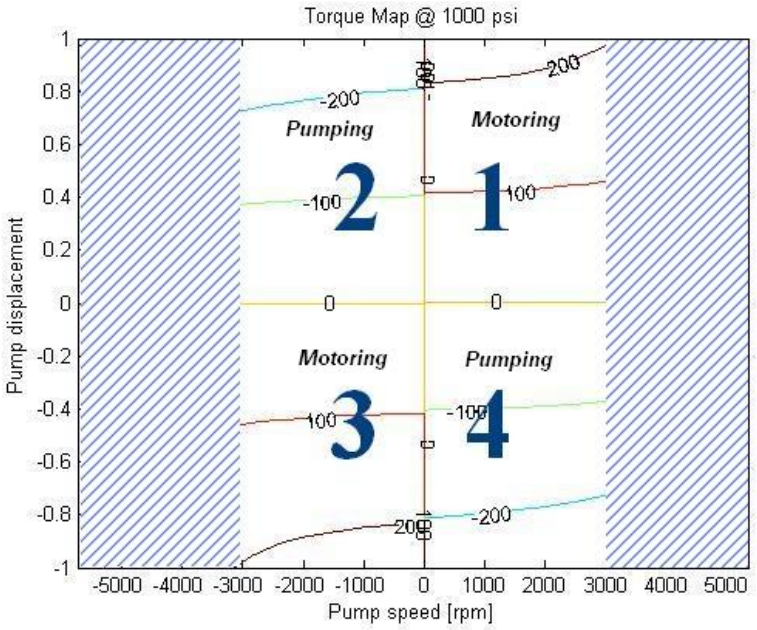

Figure B.3: Four-quadrant pump/motor operation sign convention.

where P_{sys} is the system pressure and is defined as the difference between the high and low pressure line ($P_{sys} := P_{hi} - P_{lo}$). ω_S, T_S are the P/M-S speed and torque, ω_T, T_T are the P/M-T speed and torque. x_S, x_T are P/M-S and P/M-T fractional displacements from the maximum flow displacement of each unit, D_S and D_T. Q_S, Q_T are P/M-S and P/M-T volumetric flow rate. $Q_{S,loss}$, $Q_{T,loss}$ are P/M-S and P/M-T volumetric flow losses. $T_{S,loss}$ and $T_{T,loss}$ are P/M-S and P/M-T mechanical losses. Q_{net} is the net flow rate in or out of the accumulator. The main difference between a hybrid and a non-hybrid transmission is the ability to store energy. Under such circumstances, Q_{net} represents the volumetric flowrate being stored or discharged for a hybrid transmission, and $Q_{net} = 0$ for the non-hybrid case.

In order to determine each quadrant of the pump/motor efficiency map, several assumptions are necessary as a result of the restrictions on the physical system. (1) Both pump and motor are identical in design and characteristics. Thus, maximum displacement of pump and motor are the same, $D_S = D_T = D_{max}$. (2) Quadrants 2 and 3 can be identified through the characteristics of P/M-S whereas quadrant 1 and 4 are determined by P/M-T. Different portion of the map can then be merged into a

overall efficiency characteristic map for both pump/motors. (3) Charge pump losses are negligible, thus input torque is completely transmitted into the planetary gear set. (4) A heat exchanger is available to maintain hydraulic fluid temperature, hence temperature of the fluid is assumed constant throughout the test at steady-state. Fluid properties (viscosity, bulk modulus, etc.) do not vary.

The main objective of conducting dynamometer tests on the hydro-mechanical transmission is to identify the torque and flow loss maps (hence efficiencies) of the pump/motors. Each map is a function of the volumetric displacement (x_{pm}), speed (ω_{pm}) and system pressure (P_{sys}). Thus, data obtained from transmission testing takes the form of a three-dimension lookup table. By combining Eq. (8.6) with Eqs. (B.1) and (B.2), the losses are expressed as follows:

$$sgn(\omega_S)T_{S,loss}(x_S,\omega_S,P_{sys}) = \frac{P_{sys}D_{max}x_S}{2\pi} - \frac{T_{in}}{1+\rho} \tag{B.6}$$

$$sgn(\omega_T)T_{T,loss}(x_T,\omega_T,P_{sys}) = \frac{P_{sys}D_{max}x_T}{2\pi} + \frac{T_{in}-(1+\rho)T_{out}}{(1+\rho)^2} \tag{B.7}$$

$$\begin{aligned} Q_{com,loss}(x_S,\omega_S,x_T,\omega_T,P_{sys}) &= Q_{S,loss}+Q_{T,loss} \\ &= \omega_S D_{max}x_S + \omega_T D_{max}x_T + Q_{net} \end{aligned} \tag{B.8}$$

where $Q_{com,loss}$ is the combined losses from the two pump/motor units.

B.1 Torque map identification

The main obstacle for obtaining the loss maps is the coupling effect between the two hydraulic pump/motors when the external hydraulic supply is unavailable. However, torque loss identification can be achieved without the need of an external hydraulic supply, i.e. shut off hydraulic ports. In this case, the net flow from the hydraulic components is zero ($Q_{net} = 0$), meaning all the flow generated by P/M-S must be consumed by P/M-T plus a relatively small amount of leakage into the sump.

$$(\omega_S D_{max}x_S + Q_{S,loss}) + (\omega_T D_{max}x_T + Q_{T,loss}) = 0 \tag{B.9}$$

where ω_S, and x_S are the P/M-S speed and control displacement, ω_T, and x_T are the P/M-T speed and control displacement. $Q_{S,loss}$ and $Q_{T,loss}$ are the P/M-S and P/M-T

flow losses.

From Eq. (B.9), the relationship between the hydraulic units' speed and displacement can be rearranged as:

$$\frac{\omega_S}{\omega_T} = -\frac{x_T}{x_S} - \frac{Q_{S,loss} + Q_{T,loss}}{\omega_T D_{max} x_S} \tag{B.10}$$

According to Eqs. (8.5), the pump/motor speed and input/output speed is expressed by

$$\frac{\omega_S}{\omega_T} = \frac{1}{1+\rho} - \frac{\omega_{in}}{\omega_{out}} \tag{B.11}$$

Thus, combining Eqs. (B.12) and (B.11), the pump/motor displacement, input and output shaft speed are related by

$$\frac{x_T}{x_S} = \frac{\omega_{in}}{\omega_{out}} - \frac{1}{1+\rho} - \frac{Q_{S,loss} + Q_{T,loss}}{\omega_T D_{max} x_S} \tag{B.12}$$

Combining Eqs. (8.6), (B.1), (B.5), and (B.11), the system pressure can be related to output torque as:

$$\begin{aligned} P_{sys} \quad = \quad & \frac{2\pi}{D_{max} x_S} \frac{1}{(\omega_{in}/\omega_{out} - (Q_{S,loss} + Q_{T,loss})/\omega_T D_{max} x_S} \\ & \left[\frac{1}{1+\rho} T_{out} + sgn(\omega_T) T_{T,loss} + \frac{1}{1+\rho} sgn(\omega_S) T_{S,loss} \right] \end{aligned} \tag{B.13}$$

Thus according to Eq. (B.13), the pump/motor displacements and output torque can be calculated to maintain the desired pressure. Generally, it is beneficial to set $\frac{\omega_{in}}{\omega_{out}} = 1 + \frac{1}{1+\rho}$, so that displacements of both pump/motors are evenly distributed throughout different input speeds.

As there are three variables that influence the pump/motors' torque efficiency, i.e. the unit's displacement, speed and pressure, to obtain the torque performance map, it is necessary to sweep through every combination possible.

To identify the torque map, one specifies different combinations of input speed and pump/motors' displacement hence pump/motor speeds specified, with a fixed input-output speed ratio, then the output torque (or input torque) is adjusted by trial and error until the pressure is regulated to the desired value (according to Eq. (B.13)). With the input and output torque measured, the pump/motors' torque, T_S and T_T,

can then be computed according to Eq. (8.6), and therefore the torque losses for each pump/motor can be computed according to the equations above.

The procedure for **Quadrant 1 and 2** can be summarized as follows:

1. Discretize the variable grid points (pump/motor displacement, speed, and pressure)

2. Determine desired input and output shaft speed ratio , ω_{in}/ω_{out} based on

$$\gamma = \frac{\omega_{in}}{\omega_{out}} = \frac{x_T}{x_S} + \frac{1}{(1+\rho)}$$

   and by setting $x_T/x_S = 1$ for evenly distributed data points.

3. For a specific ω_S and γ, determine the input speed, ω_{eng} using Eq. (8.5) and use the input dynamometer to maintain the desired input speed.

$$\omega_S = -(1+\rho)\omega_{in} + \omega_{out}$$

4. Set x_S to the grided displacement and set $x_T = x_S$.

5. Increase output loading torque, T_{out}, such that $\omega_{eng}/\omega_{out} = \gamma$.

6. Since the system pressure will not be at the desired pressure due to losses, adjust x_T and T_{out} iteratively according to Eq. (B.13) to achieve the desired output speed and system pressure.

7. Record input and output torque, T_{in},T_{out}.

8. Compute torque loss according to Eq. (B.6) and (B.7):

$$\begin{aligned} T_{S,loss}(x_S, \omega_S, P_{sys}) &= \frac{P_{sys} D_{max} x_S}{2\pi} - sgn(\omega_S)\frac{T_{in}}{1+\rho} \\ T_{T,loss}(x_T, \omega_T, P_{sys}) &= \frac{P_{sys} D_{max} x_T}{2\pi} - sgn(\omega_T)\frac{-T_{in} + (1+\rho)T_{out}}{(1+\rho)^2} \end{aligned}$$

The procedure for **Quadrant 4** can be summarized as follows, this quadrant is characterized with P/M-T only. Relief valve is required to be connected between the high and low pressure port

1. Discretize the variable grid points (pump/motor displacement, speed, and pressure)
2. Determine desired output shaft speed, ω_{out} with Eqs. (8.5) and maintain ω_{out} by motoring output dynamometer.

$$\omega_T = (1+\rho)\omega_{out}$$

3. Set x_T to desired displacement.
4. Adjust system pressure using the relief valve.
5. Input speed is set at minimum speed required (in order to run charge pump) and x_s is set to zero displacement.
6. Record input and output torque, T_{in},T_{out}.
7. Compute torque loss according to Eq. (B.7):

$$T_{T,loss}(x_T, \omega_T, P_{sys}) = \frac{P_{sys} D_{max} x_T}{2\pi} - sgn(\omega_T)\frac{-T_{in} + (1+\rho)T_{out}}{(1+\rho)^2}$$

Thus, with torque loss for all four quadrants identified, this section can be concluded by computing the mechanical efficiency of the pump/motor:

$$\eta_{pm,mech} = \frac{T_{pm} - T_{pm,loss}}{T_{pm}} \quad \text{for pumping} \tag{B.14}$$

$$\eta_{pm,mech} = \frac{T_{pm}}{T_{pm} + T_{pm,loss}} \quad \text{for motoring} \tag{B.15}$$

B.2 Volumetric flow map identification

Continuing the volumetric efficiency map identification is relatively difficult compared to torque mapping as flow to each pump/motor can not be measured. As mentioned previously, separating flow losses of each individual pump/motor is not possible and additionally, the net flow measurement from pump to motor is not available due to lack of an accessible port.

Without external hydraulic supply: Theoretically, without any modification to the hydraulics, the combined flow losses can be deduced from the difference between the ideal and measured displacement for a specific transmission ratio when there is no net flow ($Q_{net} = 0$), i.e.

$$\begin{aligned} Q_{com,loss}(x_S, \omega_S, x_T, \omega_T, P) &= Q_S, loss + Q_T, loss \\ &= \omega_S D x_S + \omega_T D x_T \end{aligned} \tag{B.16}$$

where $Q_{com,loss}$ is the combined volumetric flow loss, and ω_S and ω_T can be obtained from ω_{in} and ω_{out} measurements, according to Eq. (8.5). Assume the pump/motor maximum displacements are known, and control displacements are measured. However, this method of flow loss identification without external hydraulic supply depends on highly accurate speed measurement. Typically, to measure the transmission operating around 95% efficiency, speed measurements require accuracy of at least $\pm 2.2\%$ with displacements known perfectly in order to detect the loss difference. To overcome this issue, a minor modification to the hydraulic circuit is proposed and a staircase method is developed to simplify the testing procedure.

With external hydraulic supply: If an external hydraulic supply were available for the dynamometer test, as shown in Fig. B.1, then the supply pressure would be connected to the high pressure access port of the transmission and the low pressure line would be connected to the sump. This configuration enables maintaining system pressure at constant level and sufficient flow is supplied to decouple the input and output speed. Theoretically, with this configuration, arbitrary test conditions can be conducted, whether the net flow is in or out of the transmission.

With relief valve: Instead of using an external hydraulic supply, another approach to decouple the input and output speed is by using a relief valve. A pressure relief valve and a flow meter is installed between the high pressure and low pressure port, as seen in Fig. B.4.

As the flow through the relief valve is measured ($Q_{net} = Q_{relief}$), the flow relationship of the transmission is then re-formulated from Eq. (B.8):

$$Q_{com,loss}(x_S, \omega_S, x_T, \omega_T, P) = \omega_S D x_S + \omega_T D x_T + Q_{relief} \tag{B.17}$$

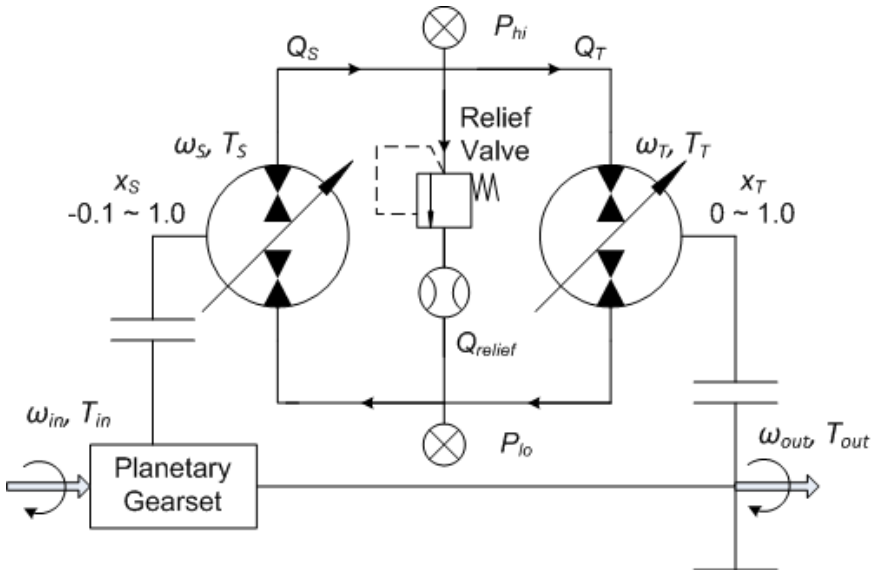

Figure B.4: Modified hydraulic circuit with relief valve and flow meter.

where Q_{relief} is the measured flow rate through the relief valve[1] .

To determine the combined volumetric flow loss, $Q_{com,loss}$, the direct approach is to test every possible operating point of the transmission, i.e. the total search approach. However, this method is tedious and still not able to test all desired operating points as a result of the system constraints. Moreover, high input speed points require high pressure and high flow rate, hence potentially damaging the transmission. High flow indicates high power through the relief valve, causing temperature to increase if heat exchanger is not present.

The staircase method is based on extrapolating the data points with common testing conditions. This method is depicted in Fig. B.5. Axes represent various combinations of displacement fraction and speed of the two hydraulic units at a constant pressure. For example, point 1 represents pump speed of $209 rad/s$ ($2000 rpm$) and fractional displacement of 0.1, point 2 represents $209 rad/s$ ($2000 rpm$) and 0.2 fractional displacement on P/M-S, and point 3 represents $314 rad/s$ ($3000 rpm$) and 0.1 displacement. As illustrated in the figure, this method proposes that instead of conducting experiments on all operating conditions, one need only to evaluate conditions where one unit is varying

[1] Negative flow through the relief valve is considered infeasible test points.

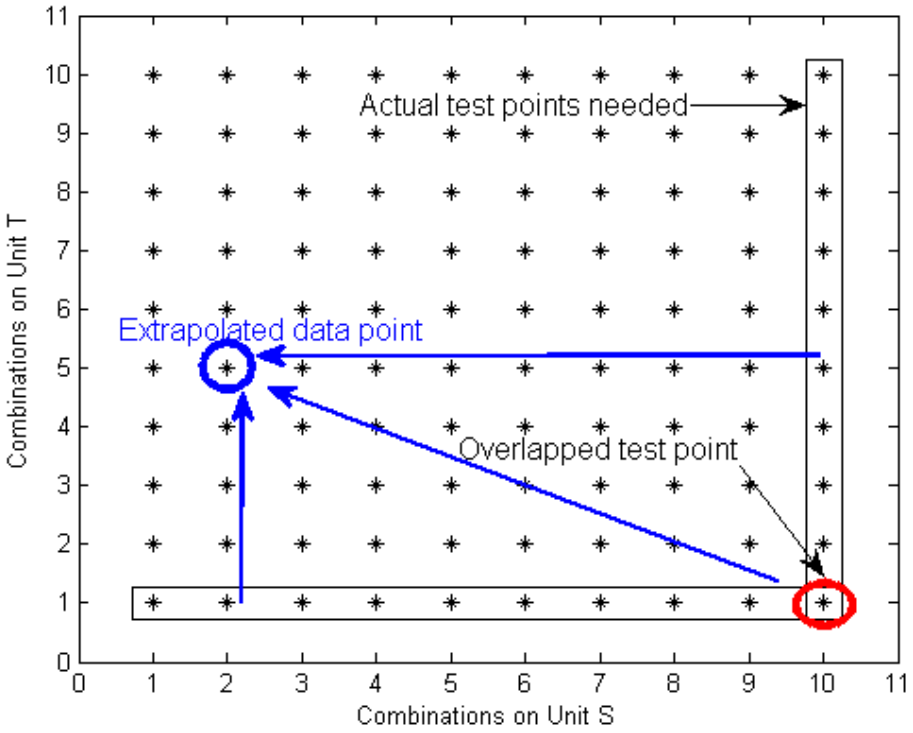

Figure B.5: Illustration of one step of the staircase method. For example, from point (10,1) to (10,10), x_S, ω_S, P_{sys} remains the same, any variation in flow is attributed to the varying conditions of x_T, ω_T.

while the other is held constant. Test points covered between the two perpendicular lines of actual experimental data can be extrapolated from the available information.

Below shows the mechanism behind this approach. q^* represents the pump/motor settings that are held constant while q represents the settings that are varied. Then the

net flow (or the relief valve flow) can be expressed in:

$$\begin{aligned} Q_{relief} &= Q_S(x_S, \omega_S, P) + Q_T(x_T, \omega_T, P) \\ &= Q_S(qs) + Q_T(qt) \\ Q_{relief}(qs^*, qt) &= Q_S(qs^*) + Q_T(qt) \\ Q_{relief}(qs, qt^*) &= Q_S(qs) + Q_T(qt^*) \\ Q_{relief}(qs^*, qt^*) &= \underbrace{Q_S(qs^*) + Q_T(qt^*)}_{\text{Overlapping test point}} \end{aligned}$$

If $Q_{relief}(qs^*, qt)$ is measured for all conditions on unit T and $Q_{relief}(qs, qt^*)$ is measured for all conditions on unit S, then any relief valve conditions in the range can be extrapolated as follows:

$$\begin{aligned} Q_{relief}(qs, qt) &= Q_{relief}(qs^*, qt) + Q_{relief}(qs, qt^*) \\ &\quad - \underbrace{Q_{relief}(qs^*, qt^*)}_{\text{Overlapped test point}} \qquad \text{(B.18)} \\ &= Q_s(qs) + Q_T(qt) \qquad \text{(B.19)} \end{aligned}$$

Equation (B.19) shows that to extrapolate a point within a map, one can sum the corresponding test points and subtract the overlapping test point.

Thus, in order to extrapolate the combined flow loss for a specific test condition for both pump/motor units Q_{com} with (qs, qt),

$$\begin{aligned} Q_{com,loss}(qs, qt) &= \omega_S Dx_S + \omega_T Dx_T + Q_{relief}(qs^*, qt) \\ &+ Q_{relief}(qs, qt^*) - Q_{relief}(qs^*, qt^*) \qquad \text{(B.20)} \end{aligned}$$

where the Q_{relief}s are all directly measured from the flow meter and ω_S and ω_T are indirectly evaluated from ω_{in} and ω_{out} measurements.

With the relief valve installed, the system pressure can be regulated according to demand. In reality, the relief valve volumetric flow rating is finite. If the flow capacity is exceeded, even the total search method will not be capable of determining all test points. For example, with P/M-T at low speed, $52 rad/s$ ($500 rpm$) and P/M-S at high speed $314 rad/s$ ($3000 rpm$), Q_{relief} would be substantially higher than the relief valve

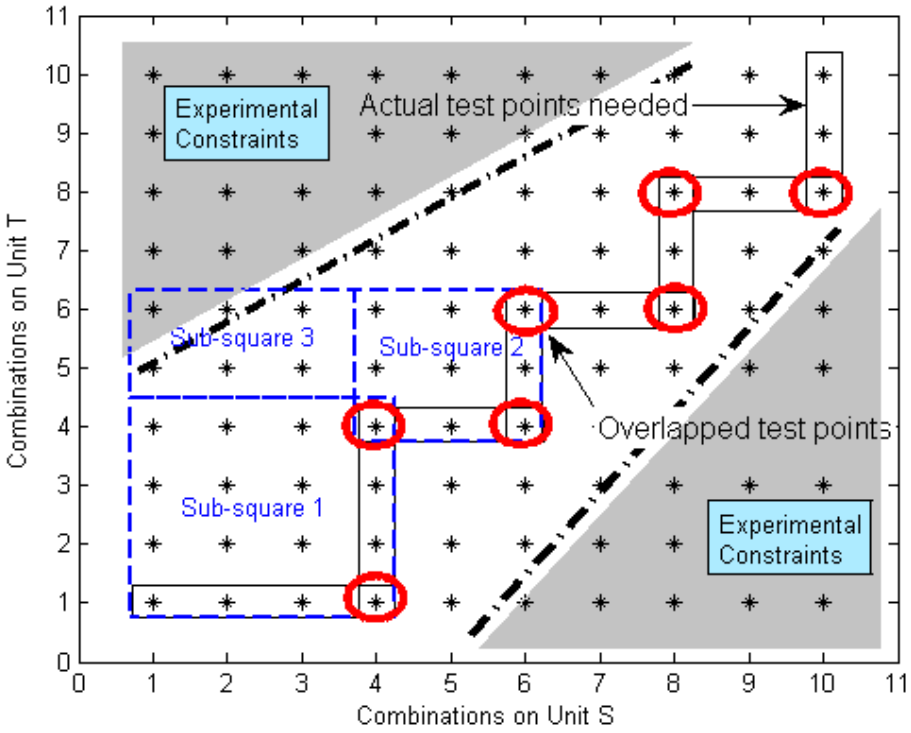

Figure B.6: Illustration of the staircase method.

flow rating.

A complete staircase method is needed to overcome such difficulties. Instead of testing all points in the lowest row and rightmost column, the process can be divided into several sub-steps, as depicted in Fig. B.6. At each sub-step, the same method as the one-step staircase is used to extrapolate the sub-square area data points. In Fig. B.6, sub-square 1 and 2 can be obtained from extrapolating the first and second sub-steps from the left. Consequently, sub-square 3 can be extrapolated from results of sub-square 1 and 2. This process is then propagated throughout the entire upper triangle of the map.

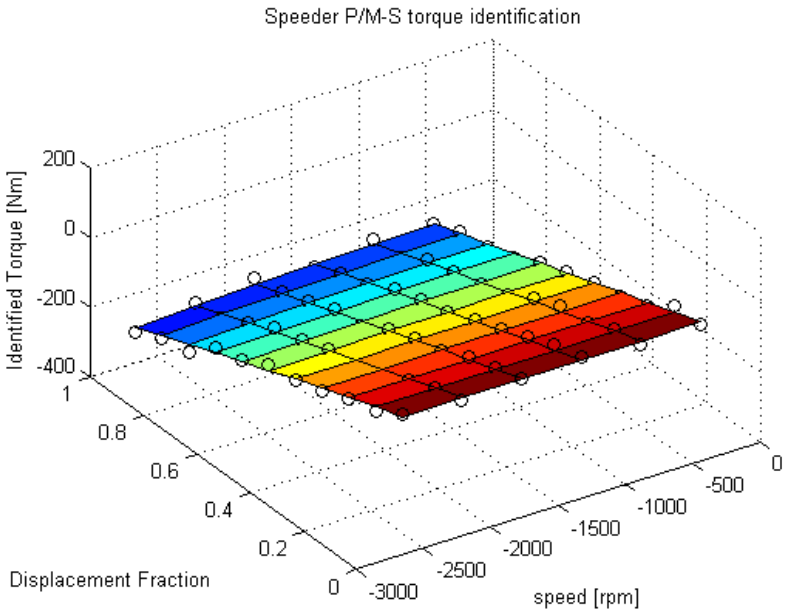

Figure B.7: Example of identification of 'speeder' torque map.

B.3 Illustration examples of torque and flow map identification

To illustrate the effectiveness of this extrapolation method, this method is simulated using the Folsom transmission pump/motor map of a developed hydro-mechanical transmission. The target transmission to be identified in this example, ρ (the ratio between the sun gear and ring gear number of teeth) is 34/70, and a relief valve with a flow rating of 0.0057 m^3/s (90 gpm) is assumed. Both hydraulic units have maximum volumetric displacement of 222 cc/rev. The hydraulic unit's displacement is discretized into 10 even intervals (0.1 to 1.0) and input speed is discretized between 500 rpm to 3000 rpm with a step size of 500 rpm.

Figures B.7 and B.8 show the results of the torque performance map identification method proposed in Sec. B.1 at a constant pressure of 1000 psi. The surfaces represent the pump torque model maps (obtained from FTI) and the circles represent the simulated results with 10 Nm standard deviation uncertainty assumed. The identification method successfully generated the torque map that matches the baseline map within

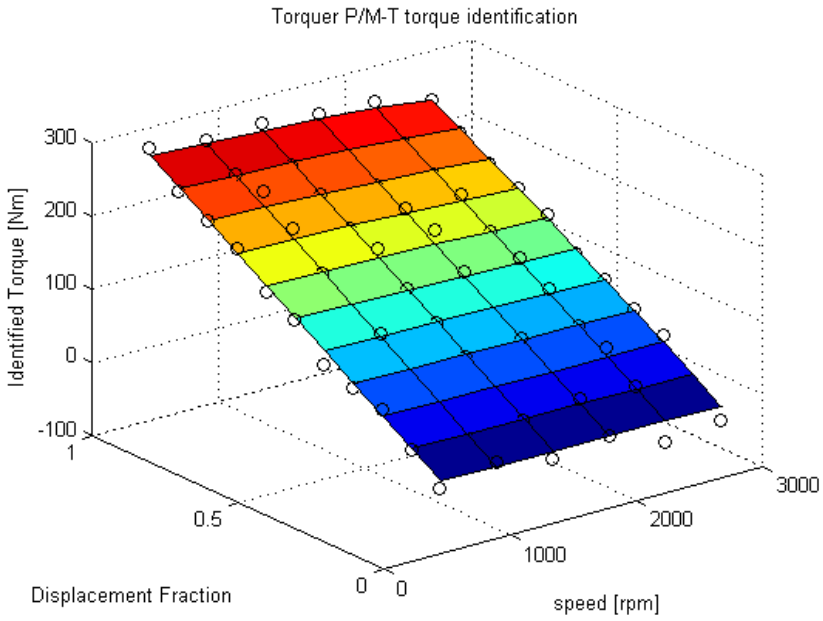

Figure B.8: Example of identification of 'torquer' torque map.

$2Nm$.

Next, the same HMT model is used for volumetric flow identification by applying the staircase method as described in Section B.2. The result of applying the method is shown in Fig. B.9.

The contour lines represent the flow rate through the relief valve if the pump/motors were to operate in such corresponding conditions. The black crosses illustrate all feasible[2] test conditions using the test set-up described previously. The red dots represent the trace of the test points of the applied staircase method. This method shows significant simplification of the experimental processes. From this example, the amount of test points required to fully characterize the loss maps is significantly reduced from approximately 3600 points per pressure condition from doing total search, to merely 126 points per pressure by staircase method. [3]

Various noise levels ($0.00001\ m^3/s$ [$0.158\ gpm$], $0.0001\ m^3/s$ [$1.58\ gpm$], $0.0002\ m^3/s$

[2] Conditions where Q_{relief} is higher than relief valve flow rating are considered infeasible.

[3] Moreover, this method can be automated based on the relief valve rating and defined test conditions. However, this will not be discussed in this paper.

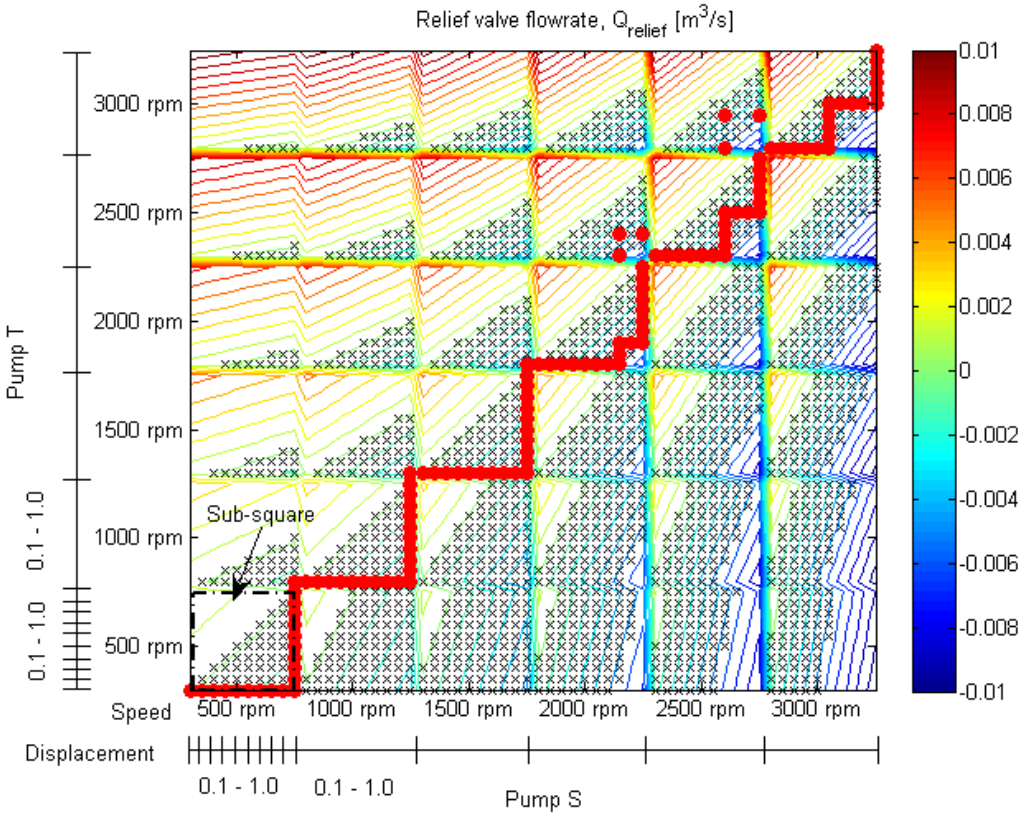

Figure B.9: Flow-rate distribution for various combinations of displacements and speed [contour: desired test points, x: feasible test points, o: Staircase method].

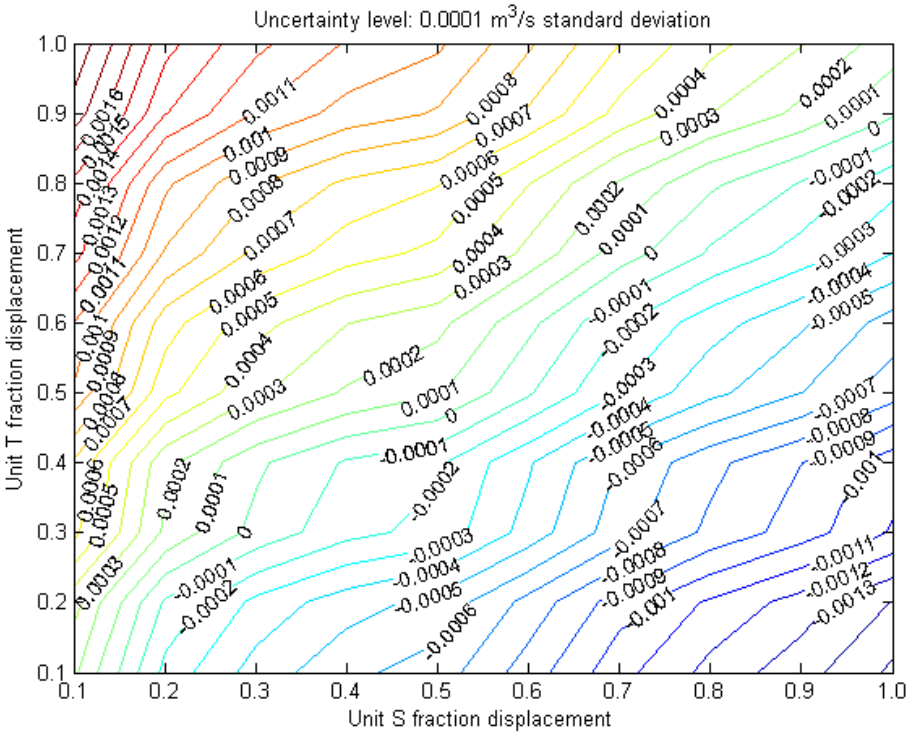

Figure B.10: Effect of noise and uncertainty on measurement results.

[3.16 gpm]) are simulated, with P/M-S and P/M-T operated at $52.3 rad/s$ ($500 rpm$) (Sub-square in Fig. B.9), to investigate the propagation of noise and error throughout the entire map. As seen in Fig. B.10, as long as the flow rate measurement is better than 0.0001 m^3/s accuracy, the generated combined flow loss map will have accuracy of 0.0001 m^3/s.

Appendix C

Glossary and Acronyms

C.1 Conversion Factors

$$\begin{aligned} 1ft-lb &= 1.3558Nm \\ 1psi &= 6894.75Pa \\ 1rpm &= 2\pi/60rad/s \\ 1gallon &= 3.7854litres \\ 1HP &= 745.7Watts \\ 1km &= 0.621miles \end{aligned}$$

C.2 Fuel Properties

Diesel fuel:

- Density, $\rho_{diesel} = 0.832kg/litre$
- Specific energy, $LHV_{diesel} = 45.9MJ/kg$
- Volumetric energy density, $= 38.2MJ/liter$

Gasoline fuel:

- Density, $\rho_{gas} = 0.745 kg/litre$
- Specific energy, $LHV_{gas} = 46.7 MJ/kg$ **
- Volumetric energy density, $= 34.4 MJ/liter$